

AWARD NUMBER: W81XWH-13-1-0269

TITLE: Fusion of Ultrasound Tissue-Typing Images with Multiparametric MRI for Image-guided Prostate Cancer Radiation Therapy

PRINCIPAL INVESTIGATOR: Xiaofeng Yang, PhD

CONTRACTING ORGANIZATION: Emory University
Atlanta, GA 30322

REPORT DATE: October 2014

TYPE OF REPORT: Annual

PREPARED FOR: U.S. Army Medical Research and Materiel Command
Fort Detrick, Maryland 21702-5012

DISTRIBUTION STATEMENT: Approved for Public Release;
Distribution Unlimited

The views, opinions and/or findings contained in this report are those of the author(s) and should not be construed as an official Department of the Army position, policy or decision unless so designated by other documentation.

REPORT DOCUMENTATION PAGE

Form Approved
OMB No. 0704-0188

Public reporting burden for this collection of information is estimated to average 1 hour per response, including the time for reviewing instructions, searching existing data sources, gathering and maintaining the data needed, and completing and reviewing this collection of information. Send comments regarding this burden estimate or any other aspect of this collection of information, including suggestions for reducing this burden to Department of Defense, Washington Headquarters Services, Directorate for Information Operations and Reports (0704-0188), 1215 Jefferson Davis Highway, Suite 1204, Arlington, VA 22202-4302. Respondents should be aware that notwithstanding any other provision of law, no person shall be subject to any penalty for failing to comply with a collection of information if it does not display a currently valid OMB control number. **PLEASE DO NOT RETURN YOUR FORM TO THE ABOVE ADDRESS.**

1. REPORT DATE October 2014			2. REPORT TYPE Annual		3. DATES COVERED 30 Sep 2013 - 29 Sep 2014
4. TITLE AND SUBTITLE Fusion of Ultrasound Tissue-Typing Images with Multiparametric MRI for Image-guided Prostate Cancer Radiation Therapy					5a. CONTRACT NUMBER W81XWH-13-1-0269
					5b. GRANT NUMBER W81XWH-13-1-0269
					5c. PROGRAM ELEMENT NUMBER
6. AUTHOR(S) PI: Xiaofeng Yang, PhD, Mentors: Tian Liu, PhD, Jani Ashesh, MD, Hui Mao, PhD, Walter Curran, MD. E-mail: xyang43@emory.edu					5d. PROJECT NUMBER
					5e. TASK NUMBER
					5f. WORK UNIT NUMBER
7. PERFORMING ORGANIZATION NAME(S) AND ADDRESS(ES) Emory University 1599 Clifton Road Atlanta, GA 30322					8. PERFORMING ORGANIZATION REPORT NUMBER
9. SPONSORING / MONITORING AGENCY NAME(S) AND ADDRESS(ES) U.S. Army Medical Research and Materiel Command Fort Detrick, Maryland 21702-5012					10. SPONSOR/MONITOR'S ACRONYM(S)
					11. SPONSOR/MONITOR'S REPORT NUMBER(S)
12. DISTRIBUTION / AVAILABILITY STATEMENT Approved for Public Release; Distribution Unlimited					
13. SUPPLEMENTARY NOTES					
14. ABSTRACT Purpose: We propose to generate 3-D prostate cancer map through the fusion of ultrasound tissue-typing (UTT) onto the multiparametric MR images. This translational research brings our innovative image registration method into the clinic for an image-guided tumor-targeted prostate radiotherapy. Major research accomplishments: A prostate segmentation method has been developed to improve the accuracy of prostate contour. Based on this segmentation, a novel registration method based on patient-specific biomechanical model was developed. We created image registration and fusion methods that could be used to combine UTT and multiparametric MR images. We demonstrated the feasibility of combining the two modalities for image-guided radiotherapy for prostate cancer. Major training accomplishments: Under the guidance of a highly distinguished mentor team, the PI had a very productive year, in which he published 26 abstracts, 6 conference papers, 8 journal papers and two pending patents. In addition, the PI received research awards from Emory University, American Association of Physicists in Medicine and International Society for Optics and Photonics. Impact: With this research, we hope to offer radiation oncologists a new approach that delivers higher doses to tumor-bearing regions to improve local control and survival while maintaining or reducing doses to surrounding normal tissues, such as the rectum and bladder.					
15. SUBJECT TERMS Prostate cancer, image-guided intervention, image registration, multiparametric MRI, ultrasound tissue-typing (UTT), radiotherapy.					
16. SECURITY CLASSIFICATION OF:			17. LIMITATION OF ABSTRACT	18. NUMBER OF PAGES	19a. NAME OF RESPONSIBLE PERSON USAMRMC
a. REPORT Unclassified	b. ABSTRACT Unclassified	c. THIS PAGE Unclassified	Unclassified	129	19b. TELEPHONE NUMBER (include area code)

Table of Contents

	<u>Page</u>
1. Introduction.....	4
2. Keywords.....	4
3. Overall Project Summary.....	4
4. Key Research Accomplishments.....	7
5. Conclusion.....	8
6. Publications, Abstracts, and Presentations.....	8
7. Inventions, Patents and Licenses.....	13
8. Reportable Outcomes.....	13
9. Other Achievements (Awards).....	14
10. References.....	16
11. Appendices.....	18

Introduction

Radiation therapy is an important modality in the treatment of localized advanced prostate cancer. However, a subset of these patients will not be cured, and long-term follow-up shows half of them will suffer relapse. In conventional radiotherapy, physicians use CT images to identify the prostate, plan treatment, and deliver the radiation to cure the patient. A limitation of CT imaging is its inability to identify cancerous regions within the prostate gland; therefore the whole prostate is irradiated with a tumoricidal dose.

Recent studies have shown that ultrasound tissue-typing (UTT) and multiparametric MR imaging can identify cancer or aggressive cancer inside the prostate. Each modality has shown encouraging potential for improved imaging of prostate cancer when used alone; combining parameters derived from each modality may provide superior sensitivity and specificity for prostate cancer. To achieve such combination, image registration of the prostate gland of the UTT and MR images is the most critical step.

The proposed project is to combine UTT and MR imaging to develop an image-guided tumor-targeted radiation therapy, in which higher radiation dose will be delivered to the aggressive tumors to improve long-term survival. We propose a novel registration technology of UTT and multiparametric MR images based on a patient-specific biomechanical model. We will test our registration technique to a set of 20 patients' ultrasound and MR images. Through registration between ultrasound and MRI, the generated 3D cancer mapping shows the location, volume and aggressiveness of the tumor foci. Success in this research program will offer radiation oncologists a new approach that delivers higher doses to tumor-bearing regions to improve local control and survival while maintaining or reducing doses to surrounding normal tissues, such as the rectum and bladder.

Keywords

Prostate cancer, image-guided intervention, image registration, MRI, ultrasound tissue-typing (UTT), radiotherapy.

Overall Project Summary

During this funding period, I have accomplished the training and research plan proposed for year 1. My career development was comprised of mentored research, advanced coursework, seminars and conferences. I was fortunate to work under the guidance of an outstanding mentor team at Emory Winship Cancer Institute. I took three courses (Medical Health Physics, Radiation Dosimetry and Radiation Therapy Physics) between September 2013 and May 2014, and go straight "A"s. I attended weekly chart rounds and monthly journal club at the Department of Radiation Oncology. I attended monthly research seminars and prostate tumor boards at the Winship Cancer Institute. I also attended seminars on manuscript and grant writing organized by Emory Postdoctoral Education Office. I attended five international conferences, and gave 7 oral and 9 poster presentations during this funding period.

As for the proposed research, my specialized role is to develop image registration techniques. I participated in most, if not all, research aspects of image-guided prostate cancer radiation therapy through combination of UTT images with multiparametric MR (Yang *et al.*, 2013c; Yang *et al.*, 2013a; Lin *et al.*, 2013b; Lin *et al.*, 2013a; Wang *et al.*, 2013; Yang *et al.*, 2014c, b; Yang *et al.*, 2014d; Yang *et al.*, 2014g; Yang *et al.*, 2014a; Yang *et al.*, 2014e; Yang and Liu, 2014;

Yang *et al.*, 2015c; Yang *et al.*, 2015a; Yang *et al.*, 2015b). The following paragraphs outline the training and research associated with the tasks described in the Statement of Work.

As for the Task 1 in Aim 1 of 3D prostate segmentation, we have developed and refined a prostate segmentation method (Yang *et al.*, 2011; Yang *et al.*, 2012; Yang *et al.*, 2014d; Yang *et al.*, 2014e; Yang *et al.*, 2015c, b) based on the patch-based anatomical features, as shown in Fig.1. Patient-specific anatomical features are extracted from the aligned training images and adopted as signatures for each voxel. The more robust and informative features are identified by the feature selection process to train the machine learning classifier (MLC). The well-trained MLC was used to localize the prostate of the patient. Many studies have shown that transrectal ultrasound (TRUS) prostate images provide accurate prostate volumes as compared with pathological specimens; hence we proposed to utilize these TRUS images to create prostate contours for radiation therapy treatment planning. We first used our previously developed TRUS segmentation method to segment the prostate from the ultrasound (US) images, and then we used the deformable registration based on catheter locations to deform the segmented prostate volume on the ultrasound images to planning CT images to improve the prostate delineation in radiotherapy. Our prostate segmentation research on improving the accuracy of prostate volume delineation in radiation therapy received the Science Council Research Award at the 55th annual meeting of American Association of Physicists in Medicine (AAPM), Indianapolis, IN, in October, 2013.

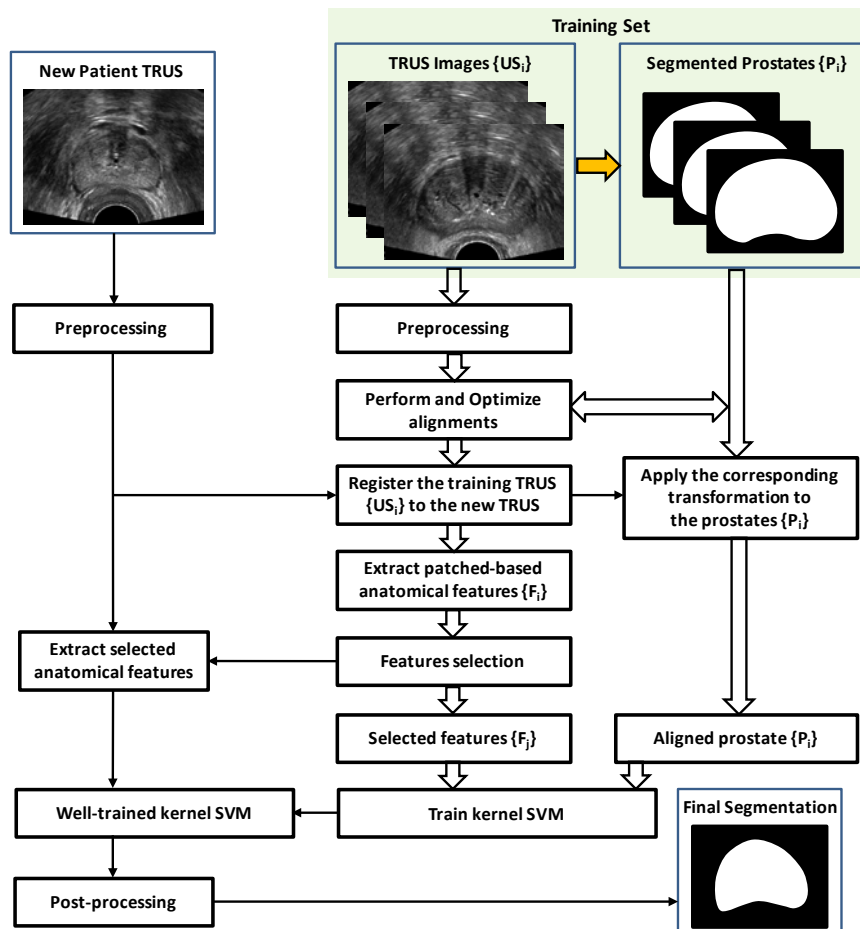


Figure 1. Schematic flow chart of the 3D US prostate segmentation.

As for the Task 2 in Aim 1 of prostate image registration, we have developed a novel registration method for ultrasound (US) and MR prostate images (Yang *et al.*, 2014a; Yang *et al.*, 2014c, b; Yang *et al.*, 2014g; Yang *et al.*, 2015a). We introduced a new MR-US registration method that combined a subject-specific biomechanical model with the B-spline-based transformation, as shown in Fig.2. In particular, we exploited the US elastography concept, in which a detailed 3D elasticity map of the prostate was generated for each patient. The B-spline transformation was calculated by minimizing the Euclidean distance between the normalized attribute vectors of surface landmarks of MR and TRUS prostate surfaces. The biomechanical mode was subsequently used to constrain the B-spline-based deformation to achieve an accurate internal volumetric deformation. Our biomechanical model took into account the wide variations among patients and within each prostate gland – normal prostatic tissue, cysts, cancers and calcifications all have different elastic properties. We are the first group to utilize the ultrasound elastography to generate a subject-specific biomechanical model to improve the volumetric deformation in MR-US prostate registration. Because of our registration work on the ultrasound-guided prostate radiotherapy I was honored with the Young Scientist Award by the SPIE Medical Imaging, San Diego, CA, in February, 2014.

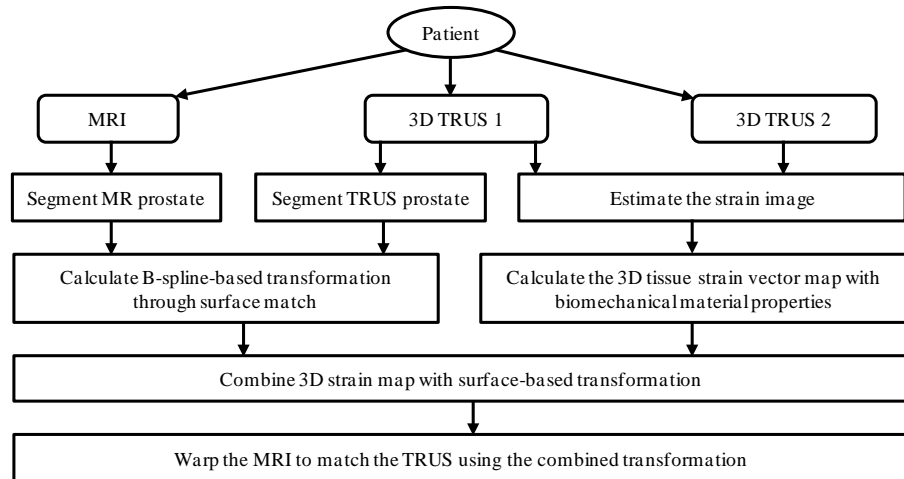


Figure 2. Schematic flow chart of the MR-TRUS prostate registration.

As for the Task 3 and 4 in Aim 2 of acquiring the US and MR scans of a prostate phantom and evaluating the accuracy of our registration method with this phantom, we conducted a prostate-mimicking phantom study. Three to five metal seeds were implanted inside the prostate phantom as land markers. A series of 3D ultrasound scans were obtained under the various pressure applied by the ultrasound probe. One MRI scan was obtained without prostate deformation. All phantom data have been analyzed and mean target registration error (TRE) was 1.29 mm. The achieved TRE less than 2 mm meets our defined error and shows the success of our registration method.

As for the Task 5 in the Aim 3, we have obtained the IRB approval for the study “Prostate Cancer Radiotherapy” and are working on evaluating the performance of our registration technique (Task 6 and 7 in Aim 3) using 20 patients’ UTT and MR images. To date, we have enrolled 7 patients in our study. So, we have a bit ahead of the proposed research schedule and we anticipate a successful completion of the proposed research in year 2.

Key Research Accomplishments

1. We have developed prostate segmentation method for prostate radiation therapy (Yang *et al.*, 2013a; Yang *et al.*, 2013c; Yang *et al.*, 2014d; Yang *et al.*, 2014e; Yang *et al.*, 2015b). It is significant because it improves prostate contours utilizing intra-operative US-based prostate volume in prostate treatment planning. This technique could improve prostate delineation, and enable accurate dose planning and delivery.
2. We have developed MR-US image registration method (Yang and Liu, 2014; Yang *et al.*, 2014a; Yang *et al.*, 2014b; Yang *et al.*, 2014e; Yang *et al.*, 2014g; Yang *et al.*, 2015c; Yang *et al.*, 2015a) that could be used for the tumor-guided prostate radiotherapy. It is important because it could help radiation oncologists better locate and target tumors regions for prostate treatment planning and, potentially, improve prostate-cancer treatment outcome.
3. We have developed image visualization software for prostate image segmentation, registration and analysis (Yang *et al.*, 2013a; Yang and Liu, 2014; Yang *et al.*, 2014d; Yang *et al.*, 2014e). This byproduct is a very useful image analysis tool with multiple visualization displays. It also allows physicians to quantitatively measure prostate and tumor size, prostate movement and deformation.
4. We have refined MR prostate imaging techniques using multiparametric T2, DCE and DWI images. Since the imaging techniques well delineate the prostate and the potential tumor region, they could possibly be used for the prostate cancer screening and other clinical applications such as image-guided prostate radiotherapy (Yang *et al.*, 2014b; Yang *et al.*, 2014g; Yang *et al.*, 2014k).
5. We have developed ultrasound imaging techniques for the acquisition of B-mode and RF prostate images. Since the B-mode images well delineate the prostate and UTT images provide the potential tumor region (Liu *et al.*, 2007; Liu *et al.*, 2009). They also could possibly be used for the prostate cancer screening and other clinical applications (Yang *et al.*, 2013b; Yang *et al.*, 2014i; Yang *et al.*, 2014j).
6. We have designed fast imaging techniques for interventional transrectal ultrasound (TRUS) imaging of the prostate (Yang *et al.*, 2014c; Yang *et al.*, 2014e). This is very important because the technique can acquire prostate images in real-time and thus potentially provide image guidance during interventional procedure.
7. We have performed image registration and fusion experiments using retrospective ultrasound and MR images from patients with prostate cancer (Yang *et al.*, 2014c; Yang *et al.*, 2015a). Registration and fusion of the two modalities could improve the diagnosis of prostate tumors, the accuracy of dose delivery and potentially enhance prostate cancer radiotherapy treatment outcome.
8. We have conducted a variety of pelvic phantom experiments to test registration accuracy of MR and US image (Yang *et al.*, 2013c; Yang *et al.*, 2014c; Yang *et al.*, 2015a). These experiments provided some baseline for accuracy evaluation and simulation.
9. We have tested the registration accuracy and clinical feasibility (Yang *et al.*, 2014c, b; Yang *et al.*, 2014g; Yang *et al.*, 2015a) with *in vivo* patient data. We planned to use more patients' data to test our registration method. These experiments will test a variety of possible conditions in potential application and thus provide useful information and guidance for future clinical trial.

Conclusion

In this funding period, I have accomplished the proposed research for year 1. Specifically, I have completed the Tasks 1 and 2 in Aim 1, the Tasks 3 and 4 in Aim 2 and the Task 5 in the Aim 3 outlined in the Statement of Work. I have had a very productive funding period, in which we have published 26 abstracts, 6 conference papers, 8 peer-reviewed journal papers and two pending patents. I achieved 9 key research accomplishments and 8 reportable outcomes. In addition, I received the Science Council Research Award from American Association of Physicists in Medicine (AAPM), the Young Scientist Award from the International Society for Optics and Photonics (SPIE) and the Emory Outstanding Postdoctoral Award. I am looking forward to working on the Tasks 6 and 7 in Aim 3 and successful completing the proposed research in the coming funding year.

Publications, Abstracts, and Presentations

a. Publication and abstracts

Peer Review Journal Papers

1. **Yang X**, Rossi P, Ogunleye T, Marcus D, Jani A, Mao H, Curran W, and Liu T. "Prostate CT Segmentation Method Based on Deformable Registration in Ultrasound-Guided CT-Based HDR Prostate Brachytherapy", *Medical Physics*, 41(11), November 2014 (In Press).
2. **Yang X**, Cheng G, Wu N, Zhou Z, Curran W, and Liu T, " Automated Segmentation of the Parotid Gland based on Atlas Registration and Machine Learning: A Longitudinal MRI Study in Head-and-Neck Radiotherapy ", *International Journal of Radiation Oncology • Biology • Physics (IJROBP)*, October 2014 (Online).
3. Wang Y, Liu T, Rossi P, Cooper S, **Yang X**, and Jani A. "Influence of Vascular Comorbidities and Race on Erectile Dysfunction after Prostate Cancer Radiotherapy", *Journal of Sexual Medicine*, 10(8), 2108-14, 2013
4. Lin Y, Liu T, **Yang X**, Wang Y, and Khan M. "Respiratory Induced Prostate Motion Using Wavelet Decomposition of the Real Time Electromagnetic Tracking Signal", *International Journal of Radiation Oncology • Biology • Physics (IJROBP)*, 87(2), 370-4, 2013.
5. Lin Y, Liu T, Wang W, **Yang X**, and Khan M. "The Non-Gaussian Nature of Prostate Motion Based on Real-Time Intra-fraction Tracking", *International Journal of Radiation Oncology • Biology • Physics (IJROBP)*, 87(2), 363-9, 2013.
6. **Yang X**, Tridandapani S, Beitler J, Yu D, Wu N, Bruner D, Curran W and Liu T. "Ultrasonic Nakagami-Parameter Characterization of Parotid-Gland Injury Following Head-and-Neck Radiotherapy", *Medical Physics*, 41, 022903, 2014.
7. **Yang X**, Beitler J, Tridandapani S, Yu D, Cheng Z, Bruner D, Curran W and Liu T. "Quantitative Ultrasound Evaluation of Acute and Late Parotid-Gland Injury in Head-and-Neck Radiotherapy: Pilot Study of Sonographic Features Based on Echo-Histogram Analysis", *Academic Radiology*, 21(10), 2014.
8. Gao Y, Tanenbaum A, Chen H, Torres M, Yoshida E, **Yang X**, Curran W and Liu T. "Development of automated skin segmentation in ultrasonic evaluation of skin toxicity in breast-cancer radiotherapy", *Ultrasound in Medicine and Biology*, 39(11), 2166-75, 2013

Peer Review Conference Papers

1. **Yang X**, Rossi P, Ogunleye T, Curran W and Liu T. "A CT Prostate Segmentation for Ultrasound-Guided CT-Based HDR Brachytherapy", *Proc. SPIE* 90362K-90362K-9 (2014).
2. **Yang X**, Rossi P, Bruner D, Tridandapani S and Liu T. "3D Ultrasound Nakagami Imaging for Radiation-induced Vaginal Fibrosis", *Proc. SPIE* 90401B-90401B-7 (2014).
3. **Yang X**, Torres M, Kirkpatrick S, Curran W and Liu T. "Ultrasound 2D Strain Estimator Based on Non-rigid Registration for Ultrasound Elastography", *Proc. SPIE* 904018-904018-10 (2014).
4. **Yang X**, Rossi P, Ogunleye T, Jani B, Curran W and Liu T. "A New 3D Neurovascular Bundles (NVB) Segmentation Method based on MR-TRUS Deformable Registration", Accepted by SPIE Medical Imaging 2015.
5. **Yang X**, Rossi P, Ogunleye T, Jani B, Curran W and Liu T. "MR-TRUS Registration Based on Subject-Specific Biomechanical Model for Image-Guided Prostate Interventions", Accepted by SPIE Medical Imaging 2015.
6. **Yang X**, Rossi P, Ogunleye T, Jani B, Curran W and Liu T. "3D Prostate Segmentation in Ultrasound Images Using Patch-Based Anatomical Feature", Submitted by SPIE Medical Imaging 2015.

Abstracts

1. **Yang X**, Cheng G, Wu N, Curran W and Liu T. "Development of Automatic Segmentation Algorithm to Assess Parotid-Gland Volume Changes Following Radiotherapy for Head-And-Neck Malignancies: A Longitudinal Study", *Medical Physics*, 40(6):346, 2013.
2. **Yang X**, Rossi P, Ogunleye T, Curran W and Liu T. "Improved the Accuracy of Prostate Delineation for Ultrasound-Guided CT-Based Treatment Planning in Prostate HDR Brachytherapy: A Pilot Study with MRI Validation", *Medical Physics*, 40(6):480, 2013.
3. Liu T, Yu D, Beitler J, Tridandapani S, Bruner D, Curran W and **Yang X**. "Ultrasonic Tissue Characterization of Parotid-Gland Injury Following Head-And-Neck Radiotherapy Using Nakagami-Parameter Imaging: A Feasibility Study", *Medical Physics*, 40(6):498, 2013.
4. Liu T, **Yang X**, Liu Y, Wang Y, Curran W and Torres M. "A Prospective Longitudinal Study with Ultrasound Nakagami Imaging to Evaluate the Relationship Between Acute and Late Normal-Tissue Toxicity in Breast-Cancer Radiotherapy", *Medical Physics*, 40(6):379, 2013.
5. **Yang X**, Liu T, Curran W and Torres M. "Hypofractionated Breast-Cancer Radiotherapy Does Not Increase Cutaneous Toxicity: A Prospective Comparative Study between Standard and Hypofractionated Radiotherapy Using Quantitative Ultrasound Imaging", *International Journal of Radiation Oncology • Biology • Physics (IJROBP)*, 87(2):S48, 2013.
6. Liu T, **Yang X**, Y Liu, Wang Y, Curran W and Torres M. "Acute Toxicity Can Be Used to Predict Late Toxicity In Breast-cancer Radiotherapy: A Prospective Longitudinal Study with Quantitative Ultrasound Imaging", *International Journal of Radiation Oncology • Biology • Physics (IJROBP)*, 87(2):S237-238, 2013.
7. **Yang X**, Rossi P, Ogunleye T, Curran W and Liu T. "Integration of Intra-operative

- Ultrasound-volume Into CT-based Treatment Planning in Prostate HDR Brachytherapy: A Pilot Study", *International Journal of Radiation Oncology • Biology • Physics (IJROBP)*, 87(2):S372, 2013.
8. **Yang X**, Beitler J, Yu D, Tridandapani S, Bruner D, Curran W and Liu T. "Quantitative Ultrasound Evaluation of Post-Radiotherapy Sialadenitis and Fibrosis of the Parotid Glands in Patients following Head-and-Neck Radiotherapy", *International Journal of Radiation Oncology • Biology • Physics (IJROBP)*, 87(2):S459, 2013.
 9. **Yang X**, Shelton J, Rossi P, Bruner D, Tridandapani S and Liu T. "Multi-parametric Ultrasound Imaging of Vaginal Fibrosis Following Radiotherapy for GYN Malignancies", *International Journal of Radiation Oncology • Biology • Physics (IJROBP)*, 87(2):S459, 2013.
 10. Wang Y, Liu T, Rossi P, Bruner D, Hsiao W, Cooper S, **Yang X** and Jani A. "Influence of Vascular Comorbidities and Race on Erectile Dysfunction after Prostate Cancer Radiotherapy", *International Journal of Radiation Oncology • Biology • Physics (IJROBP)*, 87(2):S371, 2013.
 11. Lin Y, Liu T, **Yang X**, Wang Y and Khan M. "Respiratory Induced Prostate Motion Using Wavelet Decomposition of the Real-Time Electromagnetic Tracking Signal", *International Journal of Radiation Oncology • Biology • Physics (IJROBP)*, 87(2):S369, 2013.
 12. Lin Y, Liu T, Wang W, **Yang X** and Khan M. "The Non-Gaussian Nature of Prostate Motion Based on Real-Time Intra-fraction Tracking", *International Journal of Radiation Oncology • Biology • Physics (IJROBP)*, 87(2):S363, 2013.
 13. Eaton B, Liu T, **Yang X**, Mister D, Zhao Y, Miller A, Long Q, and Torres M. "Perceived Stress Predicts for Acute Radiation-Induced Skin Toxicity: Evidence for the Mind-Body Connection", *Journal of Clinical Oncology* 31 (S26), 2013
 14. Lee A, **Yang X**, Mister D, Liu T and Torres M. "Cutaneous toxicity and recovery: Is there a difference between breast cancer patients treated with daily radiotherapy in the morning versus the afternoon?" *Cancer Research* 73(24):P3, 2013.
 15. **Yang X**, Rossi P, Bruner D, Tridandapani S and Liu T. "Development of 2D and 3D Quantitative Ultrasound Method to Assess Radiation-Induced Vaginal Fibrosis in Women Following Radiotherapy for GYN Cancers", *Journal of Ultrasound in Medicine* 33(suppl):S1–S124, 2014.
 16. **Yang X**, Torres M, Kirkpatrick S, Curran W and Liu T. "Quantitative Assessment of Arm Lymphedema Using Ultrasound 2D Strain Estimate Based on Non-Rigid Registration: A Feasibility Study", *Journal of Ultrasound in Medicine* 33(suppl):S1–S124, 2014.
 17. Liu T, **Yang X**, Curran W and Torres M. "A Prospective Comparative Study of Skin Toxicity between Standard and Hypofractionated Breast-Cancer Radiotherapy using Quantitative Ultrasound Imaging", *Journal of Ultrasound in Medicine* 33(suppl):S1–S124, 2014.
 18. **Yang X**, Liu T, Marcus D, Jani A, Ogunleye T, Curran W and Rossi P. "A Novel Ultrasound-CT Deformable Registration Process Improves Physician Contouring during CT-based HDR Brachytherapy for Prostate Cancer", *Brachytherapy*, 13, S67-68, 2014.
 19. **Yang X**, Rossi P, Ogunleye T, Curran W and Liu T. "3D Localization of Neurovascular Bundles through MR-TRUS Registration in Prostate Radiotherapy", *Medical Physics* 41 (6), 123-123, 2014.
 20. **Yang X**, Rossi P, Marcus D, Jani A, Ogunleye T, Curran W and Liu T. "MR-TRUS

- Prostate Registration Using Patient-Specific Tissue Elasticity Property Prior for MR-targeted, TRUS-guided HDR Brachytherapy", *Medical Physics* 41 (6), 470-471, 2014.
21. Liu T, Yu D, Beitler J, Tridandapani S, Bruner D, Curran W and **Yang X**. " Gaussian mixture model analysis of radiation-induced parotid-gland injury: an ultrasound study of acute and late xerostomia in head-and-neck radiotherapy", *Medical Physics* 41 (6), 571-571, 2014.
 22. Liu T, **Yang X**, Curran W and Torres M. "GLCM Texture Analysis for Normal-tissue Toxicity: A Prospective Ultrasound Study of Acute Toxicity in Breast-Cancer Radiotherapy", *Medical Physics* 41 (6), 482-482, 2014.
 23. Gao Y, Lee A, Fishman K, **Yang X** and Liu T. "Semi-automatic Segmentation of Skin Cancer in High-frequency Ultrasound Images: Initial Comparison with Histology", *Medical Physics* 41 (6), 448-448, 2014.
 24. Lee A, Johnson J, **Yang X**, Torres M, Curran W and Liu T. "Inter- and Intra-operator Reproducibility of Cutaneous Toxicity Measurements Using Quantitative Ultrasound", *International Journal of Radiation Oncology • Biology • Physics (IJROBP)*, 90(1):S265-266, 2014.
 25. **Yang X**, Torres M, Curran W and Liu T. "Ultrasound Texture Features as Potential Early Imaging Biomarkers for Normal-tissue Toxicity in breast-cancer radiotherapy", *International Journal of Radiation Oncology • Biology • Physics (IJROBP)*, 90(1):S242-243, 2014.
 26. **Yang X**, Rossi P, Marcus D, Jani A, Ogunleye T, Wang Y, Curran W and Liu T. "Integration of MR images into ultrasound for 3D Doppler imaging of the neurovascular bundle in prostate radiotherapy: A pilot study", *International Journal of Radiation Oncology • Biology • Physics (IJROBP)*, 90(1):S440, 2014.
- b. International Conference Presentations**
- (*Means the presentations will or produced manuscripts)
1. **Yang X**, Rossi P, Ogunleye T, Curran W and Liu T. "Improved the Accuracy of Prostate Delineation for Ultrasound-Guided CT-Based Treatment Planning in Prostate HDR Brachytherapy: A Pilot Study with MRI Validation", AAPM annual meeting, 2013. (Oral)*
 2. **Yang X**, Cheng G, Wu N, Curran W and Liu T. "Development of Automatic Segmentation Algorithm to Assess Parotid-Gland Volume Changes Following Radiotherapy for Head-And-Neck Malignancies: A Longitudinal Study", AAPM annual meeting, 2013. (Oral)*
 3. Liu T, Yu D, Beitler J, Tridandapani S, Bruner D, Curran W and **Yang X**. "Ultrasonic Tissue Characterization of Parotid-Gland Injury Following Head-And-Neck Radiotherapy Using Nakagami-Parameter Imaging: A Feasibility Study", AAPM annual meeting, 2013. (Oral)*
 4. Liu T, **Yang X**, Liu Y, Wang Y, Curran W and Torres M. "A Prospective Longitudinal Study with Ultrasound Nakagami Imaging to Evaluate the Relationship Between Acute and Late Normal-Tissue Toxicity in Breast-Cancer Radiotherapy", ASTRO annual meeting, 2013.*
 5. **Yang X**, Liu T, Curran W and Torres M. "Hypofractionated Breast-Cancer Radiotherapy Does Not Increase Cutaneous Toxicity: A Prospective Comparative Study between

Standard and Hypofractionated Radiotherapy Using Quantitative Ultrasound Imaging", ASTRO annual meeting, 2013. (Oral)*

6. Liu T, **Yang X**, Y Liu, Wang Y, Curran W and Torres M. "Acute Toxicity Can Be Used to Predict Late Toxicity In Breast-cancer Radiotherapy: A Prospective Longitudinal Study with Quantitative Ultrasound Imaging", ASTRO annual meeting, 2013.
7. **Yang X**, Rossi P, Ogunleye T, Curran W and Liu T. "Integration of Intra-operative Ultrasound-volume Into CT-based Treatment Planning in Prostate HDR Brachytherapy: A Pilot Study", ASTRO annual meeting, 2013. *
8. **Yang X**, Beitler J, Yu D, Tridandapani S, Bruner D, Curran W and Liu T. "Quantitative Ultrasound Evaluation of Post-Radiotherapy Sialadenitis and Fibrosis of the Parotid Glands in Patients following Head-and-Neck Radiotherapy", ASTRO annual meeting, 2013. *
9. **Yang X**, Shelton J, Rossi P, Bruner D, Tridandapani S and Liu T. "Multi-parametric Ultrasound Imaging of Vaginal Fibrosis Following Radiotherapy for GYN Malignancies", ASTRO annual meeting, 2013. *
10. Wang Y, Liu T, Rossi P, Bruner D, Hsiao W, Cooper S, **Yang X** and Jani A. "Influence of Vascular Comorbidities and Race on Erectile Dysfunction after Prostate Cancer Radiotherapy", ASTRO annual meeting, 2013. *
11. Lin Y, Liu T, **Yang X**, Wang Y and Khan M. "Respiratory Induced Prostate Motion Using Wavelet Decomposition of the Real-Time Electromagnetic Tracking Signal", ASTRO annual meeting, 2013. *
12. Lin Y, Liu T, Wang W, **Yang X** and Khan M. "The Non-Gaussian Nature of Prostate Motion Based on Real-Time Intra-fraction Tracking", ASTRO annual meeting, 2013. *
13. Eaton B, Liu T, **Yang X**, Mister D, Zhao Y, Miller A, Long Q, and Torres M. "Perceived Stress Predicts for Acute Radiation-Induced Skin Toxicity: Evidence for the Mind-Body Connection", ASCO annual meeting, 2014.
14. Lee A, **Yang X**, Mister D, Liu T and Torres M. "Cutaneous toxicity and recovery: Is there a difference between breast cancer patients treated with daily radiotherapy in the morning versus the afternoon?" ASCO annual meeting, 2014.
15. **Yang X**, Rossi P, Bruner D, Tridandapani S and Liu T. "Development of 2D and 3D Quantitative Ultrasound Method to Assess Radiation-Induced Vaginal Fibrosis in Women Following Radiotherapy for GYN Cancers", AIUM annual meeting, 2014. (Oral)*
16. **Yang X**, Torres M, Kirkpatrick S, Curran W and Liu T. "Quantitative Assessment of Arm Lymphedema Using Ultrasound 2D Strain Estimate Based on Non-Rigid Registration: A Feasibility Study", AIUM annual meeting, 2014. (Oral)*
17. Liu T, **Yang X**, Curran W and Torres M. "A Prospective Comparative Study of Skin Toxicity between Standard and Hypofractionated Breast-Cancer Radiotherapy using Quantitative Ultrasound Imaging", AIUM annual meeting, 2014. (Oral)*
18. **Yang X**, Liu T, Marcus D, Jani A, Ogunleye T, Curran W and Rossi P. "A Novel Ultrasound-CT Deformable Registration Process Improves Physician Contouring during CT-based HDR Brachytherapy for Prostate Cancer", ABS annual meeting, 2014. *
19. **Yang X**, Rossi P, Ogunleye T, Curran W and Liu T. "3D Localization of Neurovascular Bundles through MR-TRUS Registration in Prostate Radiotherapy", AAPM annual meeting, 2014. (Oral)*

20. **Yang X**, Rossi P, Marcus D, Jani A, Ogunleye T, Curran W and Liu T. "MR-TRUS Prostate Registration Using Patient-Specific Tissue Elasticity Property Prior for MR-targeted, TRUS-guided HDR Brachytherapy", AAPM annual meeting, 2014. (Oral)*
21. Liu T, Yu D, Beitler J, Tridandapani S, Bruner D, Curran W and **Yang X**. " Gaussian mixture model analysis of radiation-induced parotid-gland injury: an ultrasound study of acute and late xerostomia in head-and-neck radiotherapy", AAPM annual meeting, 2014. (Oral)*
22. Liu T, **Yang X**, Curran W and Torres M. "GLCM Texture Analysis for Normal-tissue Toxicity: A Prospective Ultrasound Study of Acute Toxicity in Breast-Cancer Radiotherapy", AAPM annual meeting, 2014. (Oral)*
23. Gao Y, Lee A, Fishman K, **Yang X** and Liu T. "Semi-automatic Segmentation of Skin Cancer in High-frequency Ultrasound Images: Initial Comparison with Histology", AAPM annual meeting, 2014. (Oral)*
24. Lee A, Johnson J, **Yang X**, Torres M, Curran W and Liu T. "Inter- and Intra-operator Reproducibility of Cutaneous Toxicity Measurements Using Quantitative Ultrasound", ASTRO annual meeting, 2014.*
25. **Yang X**, Torres M, Curran W and Liu T. "Ultrasound Texture Features as Potential Early Imaging Biomarkers for Normal-tissue Toxicity in breast-cancer radiotherapy", ASTRO annual meeting, 2014.
26. **Yang X**, Rossi P, Marcus D, Jani A, Ogunleye T, Wang Y, Curran W and Liu T. "Integration of MR images into ultrasound for 3D Doppler imaging of the neurovascular bundle in prostate radiotherapy: A pilot study", ASTRO annual meeting, 2014. *
27. **Yang X**, Rossi P, Ogunleye T, Curran W and Liu T. "A CT Prostate Segmentation for Ultrasound-Guided CT-Based HDR Brachytherapy", SPIE annual meeting, 2014. *
28. **Yang X**, Rossi P, Bruner D, Tridandapani S and Liu T. "3D Ultrasound Nakagami Imaging for Radiation-induced Vaginal Fibrosis", SPIE annual meeting, 2014. *
29. **Yang X**, Torres M, Kirkpatrick S, Curran W and Liu T. "Ultrasound 2D Strain Estimator Based on Non-rigid Registration for Ultrasound Elastography", SPIE annual meeting, 2014. *

Inventions, Patents and Licenses

1. **Yang X**, Liu T and Rossi P. "Systems, Methods and Computer Readable Storage Media Storing Instructions for Generating Planning Images Based on Prostate HDR Applicators", filed in Oct. 2013. (61/986,410, Pending)
2. **Yang X**, and Liu T. "System and Method for Using Medical Image Fusion in Image-Guided Prostate Interventions", filed in March. 2014. (Emory Ref: 14094, Pending)

Reportable Outcomes

1. Our paper entitled "Prostate CT Segmentation Method Based on Deformable Registration in Ultrasound-Guided CT-Based HDR Prostate Brachytherapy (Yang *et al.*, 2014e)" was accepted for publication in the *Medical Physics*, the scientific journal of the American Association of Physicists in Medicine (AAPM) and is an official science journal of the

Canadian Organization of Medical Physicists, the Canadian College of Physicists in Medicine, and the International Organization for Medical Physics (IOMP), which was the top physics journal in the radiation oncology field.

2. Two papers entitled “Respiratory Induced Prostate Motion Using Wavelet Decomposition of the Real Time Electromagnetic Tracking Signal (Lin *et al.*, 2013b)” and “The Non-Gaussian Nature of Prostate Motion Based on Real-Time Intra-fraction Tracking (Lin *et al.*, 2013a)” were published in *the International Journal of Radiation Oncology • Biology • Physics (IJROBP)*, the official journal of American Society for Radiation Oncology (ASTRO). ASTRO’s Annual Meeting is the premier radiation oncology scientific event in the world and draws more than 11,000 attendees each year. One paper entitled “Influence of Vascular Comorbidities and Race on Erectile Dysfunction after Prostate Cancer Radiotherapy” (Wang *et al.*, 2013) was published in *Journal of Sexual Medicine*.
3. Our three conference papers entitled “A new CT prostate segmentation for CT-based HDR brachytherapy (Yang *et al.*, 2014d)”, “Ultrasound 2D strain estimator based on image registration for ultrasound elastography (Yang *et al.*, 2014h)”, and “3D ultrasound Nakagami imaging for radiation-induced vaginal fibrosis (Yang *et al.*, 2014f)” were published in the *Proceeding of SPIE on Medical Imaging* in 2014.
4. Three conference papers entitled “MR-TRUS Registration Based on Subject-Specific Biomechanical Model for Image-Guided Prostate Interventions (Yang *et al.*, 2015a)” and “A New 3D Neurovascular Bundles (NVB) Segmentation Method based on MR-TRUS Deformable Registration (Yang *et al.*, 2015c)” and “3D Prostate Segmentation in Ultrasound Images Using Patch-Based Anatomical Feature (Yang *et al.*, 2015b)” was submitted to the *SPIE Medical Imaging 2015*. Currently, two papers have been accepted and one is under review.
5. Two patents entitled “Systems, Methods and Computer Readable Storage Media Storing Instructions for Generating Planning Images Based on prostate HDR Applicators (Yang *et al.*, 2013a)” and “System and Method for Using Medical Image Fusion in Image-Guided Prostate Interventions (Yang and Liu, 2014)” were filed between 2013 and 2014.
6. I gave 16 presentations at five international conferences, the annual meeting of American Society for Radiation Oncology (ASTRO) in Atlanta, GA in October 2013, the annual meeting of American Association of Physicists in Medicine (AAPM) in Austin, TX in July 2014, the annual meeting of the annual meeting of The International Society for Optical Engineering (SPIE) on Medical Imaging in San Diego, CA in February 2014, the annual meeting of American Brachytherapy Society (ABS) in San Diego, CA in April 2014, and the annual meeting of American Institute of Ultrasound in Medicine (AIUM), Las Vegas, NV, in April, 2014.
7. My work on prostate segmentation and registration was awarded the “Science Council Research Award” by AAPM in 2013 and “Young Scientist Award” by SPIE Medical Imaging in 2014. Because of my productive research achievements, I was awarded the Emory Outstanding Postdoctoral Award (<1%) in 2013.

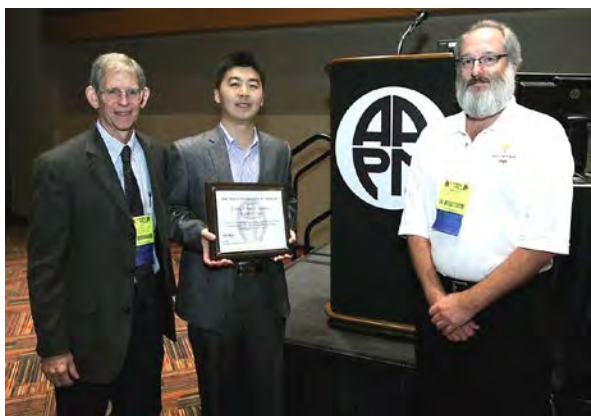
Other Achievements (Awards)

During this funding period, I received the following scientific awards:

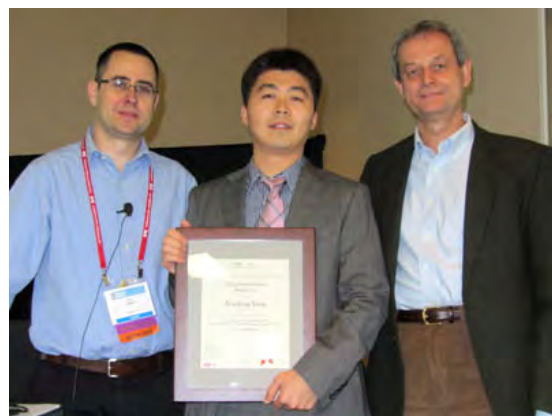
1. **Science Council Research Award:** Our prostate segmentation research on improving the accuracy of prostate volume delineation during prostate radiotherapy received the Science

Council Research Award at the 55th annual meeting of American Association of Physicists in Medicine (AAPM), Indianapolis, IN, in October, 2013;

2. **Young Scientist Award:** I was honored with the Young Scientist Award for my prostate registration work on the image-guided prostate brachytherapy by the SPIE Medical Imaging, San Diego, CA, in February, 2014;
3. **Outstanding Postdoctoral Award:** In November 2013, I was awarded the Emory Outstanding Post-doctoral Award (top 4 out of 700+) because of my productive research achievements.
4. **Finalist for the Young Investigator Award:** I was selected as one of the finalists of the Young Investigator Award for our novel ultrasound imaging work on evaluating radiation-induced toxicity following cancer radiotherapy by American Institute of Ultrasound in Medicine (AIUM), Las Vegas, NV, in April, 2014.



The Science Council Research Award at 55th annual meeting of the AAPM (October, 2013)



Young Scientist Award at the 2014 annual meeting of the SPIE Medical Imaging (February, 2014)

References

- Lin Y T, Liu T, Yang W, Yang X F and Khan M K 2013a The Non-Gaussian Nature of Prostate Motion Based on Real-Time Intrafraction Tracking *Int J Radiat Oncol* **87** 363-9
- Lin Y T, Liu T, Yang X F, Wang Y N and Khan M K 2013b Respiratory-Induced Prostate Motion Using Wavelet Decomposition of the Real-Time Electromagnetic Tracking Signal *Int J Radiat Oncol* **87** 370-4
- Liu T, Lizzi F L, Ketterling J A, Silverman R H and Kutcher G J 2007 Ultrasonic tissue characterization via 2-D spectrum analysis: Theory and in vitro measurements *Med Phys* **34** 1037-46
- Liu T, Mansukhani M M, Benson M C, Ennis R, Yoshida E, Schiff P B, Zhang P P, Zhou J and Kutcher G J 2009 A feasibility study of novel ultrasonic tissue characterization for prostate-cancer diagnosis: 2D spectrum analysis of in vivo data with histology as gold standard *Med Phys* **36** 3504-11
- Wang Y F, Liu T, Rossi P J, Watkins-Bruner D, Hsiao W, Cooper S, Yang X and Jani A B 2013 Influence of Vascular Comorbidities and Race on Erectile Dysfunction after Prostate Cancer Radiotherapy *J Sex Med* **10** 2108-14
- Yang X, Halig L V and Fei B 2012 3D Prostate Segmentation of Ultrasound Images Combining Longitudinal Image Registration and Machine Learning *Proc SPIE* **8316** 831620
- Yang X and Liu T 2014 System and Method for Using Medical Image Fusion in Image-Guided Prostate Interventions (Emory Ref: 14094, Pending).
- Yang X, Liu T, Marcus D M, Jani A B, Ogunleye T, Curran W J and Rossi P J 2014a A Novel Ultrasound-CT Deformable Registration Process Improves Physician Contouring during CT-based HDR Brachytherapy for Prostate Cancer *Brachytherapy* **13** S67-S8
- Yang X, Liu T and Rossi P 2013a Systems, Methods and Computer Readable Storage Media Storing Instructions for Generating Planning Images Based on HDR Applicators (61/986,410, Pending).
- Yang X, Rossi P, Bruner D W, Tridandapani S, Shelton J and Liu T 2013b Noninvasive evaluation of vaginal fibrosis following radiotherapy for gynecologic malignancies: A feasibility study with ultrasound B-mode and Nakagami parameter imaging *Med Phys* **40**
- Yang X, Rossi P, Mao H, Ogunleye T, Jani A, Curran W and Liu T 2015a A New MR-TRUS Registration for Ultrasound-Guided Prostate Interventions *Accepted by SPIE Medical Imaging 2015: Image-Guided Procedures, Robotic Interventions, and Modeling*, 9415
- Yang X, Rossi P, Ogunleye T, Curran W J and Liu T 2013c Integration of Intraoperative Ultrasound Volume Into CT-Based Treatment Planning in Prostate HDR Brachytherapy: A Pilot Study *Int J Radiat Oncol* **87** S372-S
- Yang X, Rossi P, Ogunleye T, Jani A, Curran W and Liu T 2014b 3D Localization of Neurovascular Bundles Through MR-TRUS Registration in Prostate Radiotherapy *Med Phys* **41** 123-
- Yang X, Rossi P, Ogunleye T, Jani A, Curran W and Liu T 2014c MR-US Prostate Registration Using Patient-Specific Tissue Elasticity Property Prior for MR-Targeted, TRUS-Guided HDR Brachytherapy *Med Phys* **41** 470-1
- Yang X, Rossi P, Ogunleye T, Jani A, Curran W and Liu T 2015b 3D Prostate Segmentation in Ultrasound Images Using Patch-Based Anatomical Feature *Submitted to SPIE Medical Imaging*
- Yang X, Rossi P, Ogunleye T, Jani A, Curran W and Liu T 2015c A New 3D Neurovascular Bundles (NVB) Segmentation Method based on MR-TRUS Deformable Registration *Accepted by SPIE Medical Imaging*
- Yang X, Rossi P, Ogunleye T, Jani A B, Curran W J and Liu T 2014d A new CT prostate segmentation for CT-based HDR brachytherapy *Proc. SPIE, Medical Imaging 2014: Image-Guided Procedures, Robotic Interventions, and Modeling*, **9036** 90362K-K-9

- Yang X, Rossi P, Ogunleye T, Marcus D, Jani A, Mao H, Curran W and Liu T 2014e Prostate CT Segmentation Method Based on Deformable Registration in Ultrasound-Guided CT-Based HDR Prostate Brachytherapy *Med Phys* **In Press**
- Yang X, Rossi P, Shelton J, Bruner D, Tridandapani S and Liu T 2014f 3D ultrasound Nakagami imaging for radiation-induced vaginal fibrosis *Proc. SPIE, Medical Imaging 2014: Ultrasonic Imaging and Tomography* **9040** 90401B-B-7
- Yang X, Rossi P J, Ogunleye T B, Wang Y, Curran W J and Liu T 2014g Integration of MR Images Into Ultrasound for 3D Doppler Imaging of the Neurovascular Bundle in Prostate Radiation Therapy: A Pilot Study *International Journal of Radiation Oncology • Biology • Physics* S440
- Yang X, Schuster D, Master V, Nieh P, Fenster A and Fei B 2011 Automatic 3D Segmentation of Ultrasound Images Using Atlas Registration and Statistical Texture Prior *Proc SPIE* **7964**
- Yang X, Torres M, Kirkpatrick S, Curran W J and Liu T 2014h Ultrasound 2D strain estimator based on image registration for ultrasound elastography *Proc. SPIE, Medical Imaging 2014: Ultrasonic Imaging and Tomography* **9040** 904018--10
- Yang X, Tridandapani S, Beitler J J, Yu D S, Chen Z J, Kim S, Bruner D W, Curran W J and Liu T 2014i Diagnostic Accuracy of Ultrasonic Histogram Features to Evaluate Radiation Toxicity of the Parotid Glands: A Clinical Study of Xerostomia Following Head-and-Neck Cancer Radiotherapy *Acad Radiol* **21** 1304-13
- Yang X, Tridandapani S, Beitler J J, Yu D S, Wu N, Wang Y F, Bruner D W, Curran W J and Liu T 2014j Ultrasonic Nakagami-parameter characterization of parotid-gland injury following head-and-neck radiotherapy: A feasibility study of late toxicity *Med Phys* **41** 0229031-8
- Yang X, Wu N, Cheng G, Zhou Z, Yu D, Beitler J, Curran W and Liu T 2014k Automated Segmentation of the Parotid Gland based on Atlas Registration and Machine Learning: A Longitudinal MRI Study in Head-and-Neck Radiotherapy *Int J Radiat Oncol Online*

Appendices

Peer-review publications:

1. **Yang X**, Rossi P, Ogunleye T, Marcus D, Jani A, Mao H, Curran W, and Liu T. "Prostate CT Segmentation Method Based on Deformable Registration in Ultrasound-Guided CT-Based HDR Prostate Brachytherapy", *Medical Physics*, 2014. (In Press).
2. **Yang X**, Cheng G, Wu N, Zhou Z, Curran W, and Liu T, " Automated Segmentation of the Parotid Gland based on Atlas Registration and Machine Learning: A Longitudinal MRI Study in Head-and-Neck Radiotherapy ", *International Journal of Radiation Oncology • Biology • Physics (IJROBP)*, 2014 (Online).
3. Wang Y, Liu T, Rossi P, Cooper S, **Yang X**, and Jani A. "Influence of Vascular Comorbidities and Race on Erectile Dysfunction after Prostate Cancer Radiotherapy", *Journal of Sexual Medicine*, 10(8), 2108-14, 2013
4. Lin Y, Liu T, **Yang X**, Wang Y, and Khan M. "Respiratory Induced Prostate Motion Using Wavelet Decomposition of the Real Time Electromagnetic Tracking Signal", *International Journal of Radiation Oncology • Biology • Physics (IJROBP)*, 87(2), 370-4, 2013.
5. Lin Y, Liu T, Wang W, **Yang X**, and Khan M. "The Non-Gaussian Nature of Prostate Motion Based on Real-Time Intra-fraction Tracking", *International Journal of Radiation Oncology • Biology • Physics (IJROBP)*, 87(2), 363-9, 2013.
6. **Yang X**, Tridandapani S, Beitler J, Yu D, Wu N, Bruner D, Curran W and Liu T. "Ultrasonic Nakagami-Parameter Characterization of Parotid-Gland Injury Following Head-and-Neck Radiotherapy", *Medical Physics*, 41, 022903, 2014.
7. **Yang X**, Beitler J, Tridandapani S, Yu D, Cheng Z, Bruner D, Curran W and Liu T. "Quantitative Ultrasound Evaluation of Acute and Late Parotid-Gland Injury in Head-and-Neck Radiotherapy: Pilot Study of Sonographic Features Based on Echo-Histogram Analysis", *Academic Radiology*, 21(10), 2014.
8. Gao Y, Tanenbaum A, Chen H, Torres M, Yoshida E, **Yang X**, Curran W and Liu T. "Development of automated skin segmentation in ultrasonic evaluation of skin toxicity in breast-cancer radiotherapy", *Ultrasound in Medicine and Biology*, 39(11), 2166-75, 2013

Peer-review International Conference Proceeding:

1. **Yang X**, Rossi P, Ogunleye T, Jani B, Curran W and Liu T. "MR-TRUS Registration Based on Subject-Specific Biomechanical Model for Image-Guided Prostate Interventions", Accepted by SPIE Medical Imaging 2015.
2. **Yang X**, Rossi P, Ogunleye T, Curran W and Liu T. "A CT Prostate Segmentation for Ultrasound-Guided CT-Based HDR Brachytherapy", *Proc. SPIE* 90362K-90362K-9 (2014).
3. **Yang X**, Rossi P, Ogunleye T, Jani B, Curran W and Liu T. "A New 3D Neurovascular Bundles (NVB) Segmentation Method based on MR-TRUS Deformable Registration", Accepted by SPIE Medical Imaging 2015.
4. **Yang X**, Rossi P, Ogunleye T, Jani B, Curran W and Liu T. "3D Prostate Segmentation in Ultrasound Images Using Patch-Based Anatomical Feature", Submitted by SPIE Medical Imaging 2015.
5. **Yang X**, Rossi P, Bruner D, Tridandapani S and Liu T. "3D Ultrasound Nakagami Imaging

- for Radiation-induced Vaginal Fibrosis”, Proc. SPIE 90401B-90401B-7 (2014).
6. **Yang X**, Torres M, Kirkpatrick S, Curran W and Liu T. “Ultrasound 2D Strain Estimator Based on Non-rigid Registration for Ultrasound Elastography”, *Proc. SPIE* 904018-904018-10 (2014).

1 Prostate CT segmentation method based on nonrigid registration 2 in ultrasound-guided CT-based HDR prostate brachytherapy

3 Xiaofeng Yang,^{a)} Peter Rossi, Tomi Ogunleye, David M. Marcus, and Ashesh B. Jani
4

5 Department of Radiation Oncology and Winship Cancer Institute, Emory University, Atlanta, Georgia 30322
6

7 Hui Mao
8

9 Department of Radiology and Imaging Sciences, Emory University, Atlanta, Georgia 30322
10

11 Walter J. Curran and Tian Liu
12

13 Department of Radiation Oncology and Winship Cancer Institute, Emory University, Atlanta, Georgia 30322
14

15 (Received 7 March 2014; revised 22 September 2014; accepted for publication 24 September 2014;
16 published XX XX XXXX)

17 **Purpose:** The technological advances in real-time ultrasound image guidance for high-dose-rate
18 (HDR) prostate brachytherapy have placed this treatment modality at the forefront of innovation
19 in cancer radiotherapy. Prostate HDR treatment involves placing the HDR catheters (needles) into
20 the prostate gland under the transrectal ultrasound (TRUS) guidance, then generating a radiation
21 treatment plan based on CT prostate images, and subsequently delivering high dose of radiation
22 through these catheters. The main challenge for this HDR procedure is to accurately segment the
23 prostate volume in the CT images for the radiation treatment planning. In this study, the authors
24 propose a novel approach that integrates the prostate volume from 3D TRUS images into the treatment
25 planning CT images to provide an accurate prostate delineation for the prostate HDR treatment.
26

27 **Methods:** The authors' approach requires acquisition of 3D TRUS prostate images in the operating
28 room right after the HDR catheters are inserted, which takes 1–3 min. These TRUS images are then
29 used to create prostate contours. The HDR catheters are reconstructed from the intraoperative TRUS
30 and postoperative CT images, and subsequently used as landmarks for the TRUS–CT image fusion.
31 After TRUS–CT fusion, the TRUS-based prostate volume is deformed to the CT images for treatment
32 planning. This method was first validated with a prostate-phantom study. In addition, a pilot study
33 of ten patients undergoing HDR prostate brachytherapy was conducted to test its clinical feasibility.
34 The accuracy of their approach was assessed through the locations of three implanted fiducial (gold)
35 markers, as well as previous T2-weighted MR images of patients.
36

37 **Results:** For the phantom study, the target registration error (TRE) of gold-markers was 0.41 ± 0.11 mm. For the ten patients, the TRE of gold markers was 1.18 ± 0.26 mm; the prostate volume
38 difference between the authors' approach and the MRI-based volume was $7.28\% \pm 0.86\%$, and the prostate volume Dice overlap coefficient was $91.89\% \pm 1.19\%$.

39 **Conclusions:** The authors have developed a novel approach to improve prostate contours utilizing
40 intraoperative TRUS-based prostate volume in CT-based prostate HDR treatment planning, demon-
41 strated its clinical feasibility, and validated its accuracy with MRIs. The proposed segmentation
42 method would improve prostate delineations, enable accurate dose planning and treatment delivery,
43 and potentially enhance the treatment outcome of prostate HDR brachytherapy. © 2014 American
44 Association of Physicists in Medicine. [<http://dx.doi.org/10.1118/1.4897615>]

45 Key words: prostate, CT, segmentation, transrectal ultrasound (TRUS), HDR brachytherapy

46 1. INTRODUCTION

47 Radiotherapy is an important treatment modality for localized
48 prostate cancer. The past few decades have witnessed a signif-
49 icant evolution in radiation techniques, such as the intensity-
50 modulated radiation therapy (IMRT) and high-dose-rate
51 (HDR) brachytherapy. In particular, the technological advances
52 in real-time ultrasound (US) image guidance for HDR pro-
53 state brachytherapy have placed this treatment modality at the
54 forefront of innovation in the field of cancer radiotherapy.¹

55 HDR prostate brachytherapy involves using a radiation
56 source (Iridium-192) to deliver high radiation dose to the pros-

57 tate gland through a series of catheters that are temporarily
58 placed within the prostate transperineally under transrectal
59 ultrasound (TRUS) guidance.² This HDR procedure allows
60 the dose delivered to surrounding normal tissues to be mini-
61 mized, thereby permitting safe dose escalation to the prostate
62 gland.^{3–6} Recent data clearly show an improved efficacy of
63 this treatment approach in patients with locally advanced can-
64 cer when compared with conventional 3D external beam and
65 IMRT techniques.⁷ As a result, an increasing number of men,
66 many of younger ages, are undergoing prostate HDR brachy-
67 therapy instead of radical prostatectomy for localized prostate
68 cancer.^{8,9}

The key to the success of HDR prostate brachytherapy is the accurate segmentation of the prostate in treatment-planning CT images. If the prostate is not accurately localized, high therapeutic radiation dose could be delivered to the surrounding normal tissues (e.g., rectum and bladder) during the treatment, which may cause severe complications such as rectal bleeding. More importantly, this may also lead to an undertreatment of cancerous regions within the prostate gland, and therefore, result in poor treatment outcome.

In the clinic, physicians' manual segmentation of the prostate on CT images is a common practice and the gold standard in prostate radiotherapy.^{10,11} Prostate CT segmentation is challenging mainly due to the low image contrast between the prostate and its surrounding tissues and the uncertainty in defining the prostate base and apex on CT images. It is well-known that the accuracy and reproducibility of prostate volume manually contoured on CT images are poor.^{10–15} Dubois *et al.* showed that a large variation and inconsistency existed in CT-based prostate contours among physicians.¹¹ Hoffelt *et al.* reported that CT consistently overestimated the prostate volume by approximately 50% compared with TRUS.¹⁵ Roach *et al.* found that CT-defined prostate volume was on average 32% larger (range 5%–63%) than MRI-defined prostate volume.¹³ Rasch *et al.* demonstrated that CT-derived prostate volumes were larger than MR-derived volumes, and the average ratio between the CT and MR prostate volumes was 1.4, which was significantly different from 1 ($p < 0.005$).¹⁴

Many CT prostate segmentation technologies have been investigated in recent years, such as the models-based,^{16–21} classification-based,^{22–27} and registration-based^{28,29} methods (detailed in Sec. 4). Most of these segmentation approaches are based on the appearance and texture of the prostate gland on CT images. In prostate HDR brachytherapy, prostate CT images are acquired after the insertions of the HDR catheters. The frequently used metal catheters introduce considerable artifacts to the CT images, as shown in Fig. 1. These artifacts often smear the appearance and texture of the CT prostate images; therefore, these previous methods may not work well for the prostate HDR application.

Studies have shown that TRUS and MRI are superior imaging modalities in terms of prostate contour as compared with CT;^{30,31} and both TRUS-defined and MRI-defined prostate volumes have been shown to correlate closely with the

prostate volume on pathologic evaluation.^{30,32} In this paper, we propose a new approach that integrates an intraoperative TRUS-based prostate volume into treatment planning through TRUS–CT fusion based on catheter locations.

2. METHODS AND MATERIALS

2.A. Prostate segmentation method

Our prostate segmentation approach for the HDR prostate brachytherapy involves five major steps (Fig. 2): (1) The 3D TRUS prostate images are captured after the catheter insertions during the HDR procedure; (2) A postoperative CT scan is obtained with all catheters for the brachytherapy treatment planning; (3) The prostate volume is contoured (segmented) in the TRUS images; (4) The HDR catheters in the 3D TRUS and CT images are reconstructed; (5) The TRUS–CT image registration is performed using HDR catheters as landmarks, and the TRUS-based prostate volume is integrated into the 3D CT images for HDR treatment planning.

2.A.1. 3D intraoperative TRUS image acquisition

The TRUS scan was performed in the operating room after the catheter insertions. The 3D TRUS images were captured with a clinical ultrasound scanner (HI VISION Avius, Hitachi Medical Group, Japan) and a transrectal 7.5 MHz prostate biplane probe (UST-672-5/7.5). During the data acquisition, the transrectal probe was held with a mechanical SurePoint stepper (Bard Medical, Inc., GA) to allow for a manual step-wise movement along the longitudinal axis. The patient was scanned in the lithotomy position and a series of parallel axial (transverse) scans were captured from the apex to the base with a 1 or 2 mm step size to cover the entire prostate gland plus 5–10 mm anterior and posterior margins. For a typical prostate, 30–40 TRUS images would cover 60–80 mm in the longitudinal direction (with a 2 mm step size).

2.A.2. CT image acquisition for HDR treatment planning

After the catheter insertion and TRUS scan, the patient was then transferred to a CT simulation room to obtain 3D CT images for HDR treatment planning (Electra Oncentra

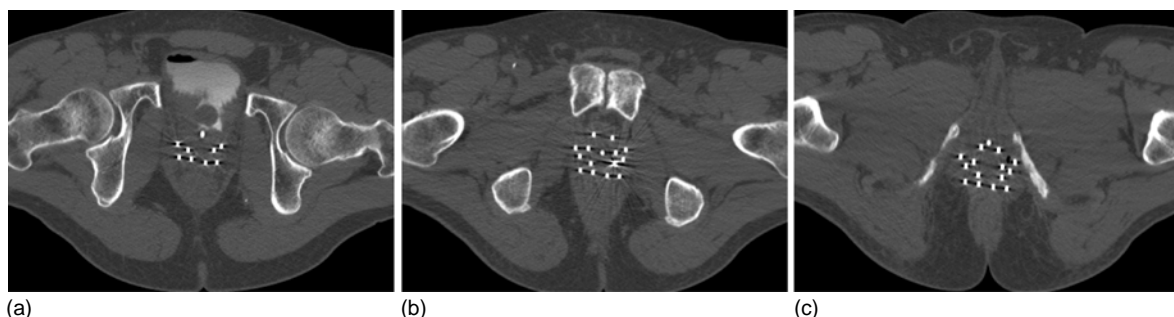


Fig. 1. Significant artifacts induced by the HDR metal catheters (white dots) in axial CT prostate images: (a) prostate base, (b) prostate midgland, and (c) prostate apex.

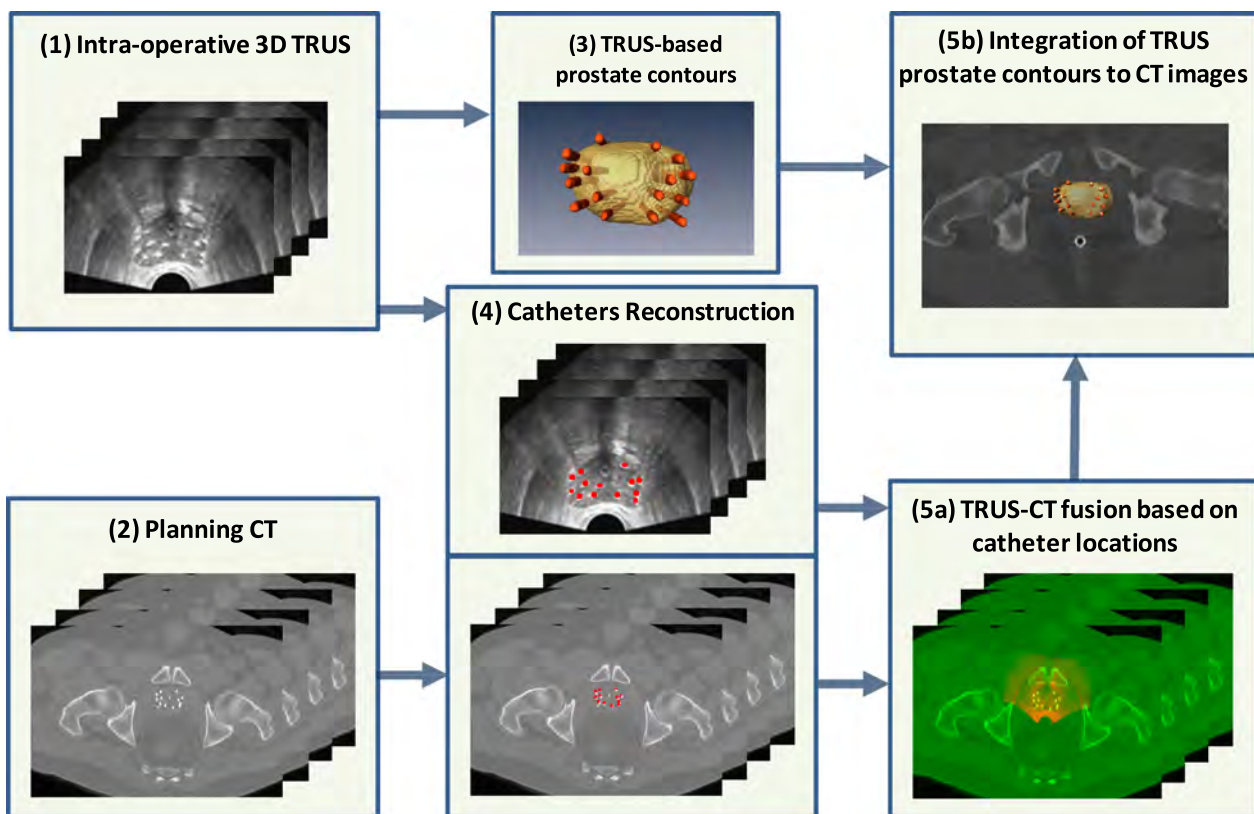


FIG. 2. Flow chart of integrating TRUS-based prostate volume into CT-based HDR treatment planning.

v4.3). Even though MRI has better soft tissue contrast than CT,³³ using the MR images for treatment planning is, however, problematic.¹ For example, most HDR catheters are not MRI compatible and catheter reconstructions can be difficult with MRIs. MRI is more expensive and less available as compared with CT, therefore, CT is still the most-commonly used image modality for radiotherapy dose calculation.¹ The treatment planning CT was acquired following standard CT protocol. A helical CT scan was taken after 40 mL of contrast was injected into the bladder and a rectal marker was placed into the rectum. All patients were scanned in head first supine, feet-down position without the probe or immobilization device. The slice thickness was 1.0 mm through the whole pelvic region, and the matrix size was 512×512 pixels with 0.68×0.68 mm² pixel size.

2.A.3. Prostate volume contour in TRUS images

A radiation oncologist manually contoured the prostate volumes using TRUS prostate images. For a typical prostate of 50 mm, with 2 mm slide thickness, approximately 25 TRUS slides needed to be contoured. In general, it takes 5–15 min to contour a prostate volume. Although this might be time consuming, because the TRUS images are greatly degraded due to the HDR catheter insertion, we feel manual contours would provide the most accurate prostate volumes.

2.A.4. Catheter reconstruction in TRUS and CT images

For TRUS images, catheter reconstruction is challenging due to the artifacts induced by the multiple scattering from HDR catheters. As shown in Fig. 3, bright band/tail

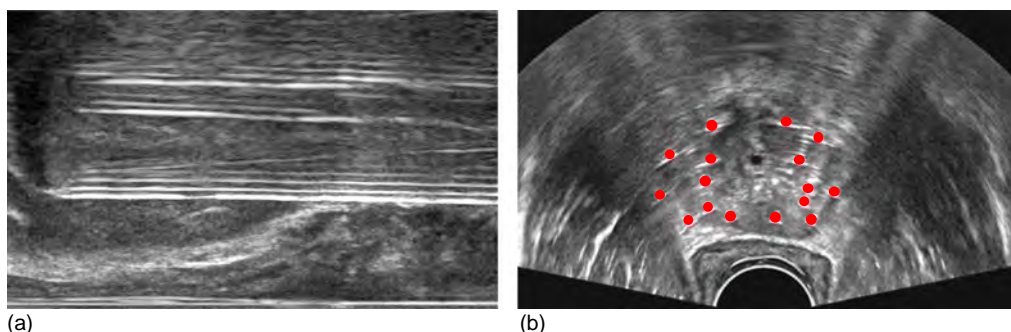


FIG. 3. Catheter artifacts on TRUS images. (a) Bright band artifacts seen on a longitudinal TRUS image, and (b) HDR catheters reconstruction on the axial TRUS image.

and dark shadow artifacts³⁴ are present on the longitudinal [Fig. 3(a)] and axial [Fig. 3(b)] TRUS images. To deal with these artifacts, we used a manual catheter reconstruction method. Specifically, we first located the tips of all catheters located close to the base of the prostate. We then identified the brightest point of each catheter and placed 2 mm circles on an axial TRUS image. Such operation was repeated on every three to four slides, and catheter locations on the skipped slides were interpolated. The final step was 3D catheter reconstruction for the TRUS prostate images. For CT images, we were able to use the threshold method to automatically detect the HDR catheters because of the high contrast between the HDR catheters and soft tissue. We tested a range of HU thresholds in this study and the best threshold of 950 HU was determined by matching the catheter diameter on the CT image to the real catheter diameter of 2 mm.

2.A.5. TRUS-CT registration

2.A.5.a. *Landmarks similarities.* In this study, we used HDR catheters as landmarks for image registration. In general, the catheters were uniformly and symmetrically distributed inside the prostate gland except for regions near the urethra where catheters were placed at least 5 mm away from the urethra. In other words, the catheters followed uniform spacing along the periphery with several interior catheters. After catheter insertion, the catheters were locked onto a needle template which was fixed onto the patient throughout the HDR brachytherapy. This is critically to ensure no relative displacement among the catheters and no catheter movement inside the prostate gland during intraoperative TRUS scan, planning CT scan, and final dose delivering. Such evenly distributed catheters will provide exceptional landmarks for the TRUS-CT registration to capture the nonrigid prostate deformation between TRUS and CT images. The corresponding catheter pairs in CT and TRUS images with the same number were used as landmarks to improve our registration accuracy.

Our TRUS-CT registration method was performed by matching the catheter locations, where x_i^{CT} and y_i^{TRUS} are the landmark point sets on the catheter surface from the planning CT and TRUS images, respectively. We assumed the detected catheters' surface is $\{x| i=1, \dots, I\}$ in the CT image, and $\{y| j=1, \dots, J\}$ in the TRUS image. The correspondences between x_i^{CT} and y_i^{TRUS} are described by a fuzzy correspondence matrices P . We defined a binary corresponding matrix P with dimension $(I+1) \times (J+1)$

$$P = \left\{ \begin{array}{ccc|c} p_{11} & \cdots & p_{1J} & p_{1,J+1} \\ \vdots & \ddots & \vdots & \vdots \\ p_{I1} & \cdots & p_{IJ} & p_{I,J+1} \\ \hline p_{I+1,1} & \cdots & p_{I+1,J} & 0 \end{array} \right\}. \quad (1)$$

The matrix $P = \{p_{ij}\}$ consists of two parts. The $I \times J$ inner submatrix defines the correspondences of X and Y . It is worth noting that p_{ij} have real values between 0 and 1, which denote the fuzzy correspondences between the landmarks.³⁵ If x_i is

mapped to y_j , then $p_{ij} = 1$, otherwise $p_{ij} = 0$. The $(J+1)$ th column and the $(I+1)$ th row define the outliers in X and Y , respectively. If a landmark cannot find its correspondence, it is regarded as an outlier and the extra entry of this landmark will be set as 1. That is, if x_i is an outlier, then there is $p_{i,J+1} = 1$. Similarly, if y_j is an outlier, then there is $p_{I+1,j} = 1$. P satisfies the row and column normalization conditions, and P is subject to $\{\sum_{i=1}^{I+1} p_{ij} = 1 (j=1, \dots, J); \sum_{j=1}^{J+1} p_{ij} = 1 (i=1, \dots, I); p_{ij} \in [0, 1]\}$.

2.A.5.b. *Similarity function.* In this study, the similarity between two sets of catheter landmarks x_i and y_j in TRUS and CT images can be defined by a Euclidean distance between their point sets. We used a soft assign technique allowing P to take values from interval $[0, 1]$ in energy function.³⁶ The continuous property of P acknowledges the ambiguous matches between X and Y . For the catheter landmarks, our registration task is to find an optimal correspondence matrix P and an optimal spatial transform f , which matches these two points' sets, X and Y , as closely as possible. Therefore, the following energy function for registration between TRUS and CT images is minimized.^{35,37}

$$E(f) = \alpha \sum_{i=1}^I \sum_{j=1}^J p_{ij} \left(\|y_j^{\text{TRUS}} - f(x_i^{\text{CT}})\|^2 \right) + \delta \sum_{i=1}^I \sum_{j=1}^J p_{ij} \log(p_{ij}) - \xi \sum_{i=1}^I \sum_{j=1}^J p_{ij} + \lambda \left\| \iiint_{(x,y,z) \in \Omega_M} \left(\frac{\partial^2 f}{\partial x^2} + \frac{\partial^2 f}{\partial y^2} + \frac{\partial^2 f}{\partial z^2} \right)^2 dx dy dz \right\|^2, \quad (2)$$

where α , δ , ξ , and λ are the weights for the energy terms. p_{ij} is the fuzzy correspondence matrix. f denotes the transformation between the TRUS and CT images. The first term is the geometric feature-based energy term defined by the Euclidean distance. Similarly the space between x_i^{CT} and y_i^{TRUS} is measured by the Euclidean distance—a smaller distance indicates a higher similarity between them. The second term is an entropy term that comes from the deterministic annealing technique,³⁸ which is used to directly control the fuzziness of P . δ is called the temperature parameter. The third term is used to direct the correspondences matrices P converging to binary, and is used to balance the outlier rejection. As δ is gradually reduced to zero, the fuzzy correspondences become binary. The first three terms constitute the similarity metric on both catheter landmarks in TRUS and CT images. The last term is the regularization of the transformation, which is described by the bending energy of f . In a nonrigid registration, smoothness is necessary to restrict the mappings from not being too arbitrary. The local deformation ought to be characterized as a smooth function to discourage arbitrary unrealistic shape deformation. So this smoothness penalty term is introduced to regularize the local deformation by the second order spatial derivatives. For the registration, parameter α in Eq. (2) was set to 0.5, and δ , ξ , and λ were three dynamic parameters that were initially set as 1 and decreased to 0.05 with the progress of iterations.^{35,37,39}

The overall similarity function can be minimized by an alternating optimization algorithm that successively updates

289 the correspondences matrix p_{ij} and the transformation function f . First, with the fixed transformation f , the correspondence matrices between the landmarks are updated by minimizing $E(f)$. The updated correspondence matrices are then treated as the temporary correspondences between the landmarks. Second, with the fixed temporary correspondence matrix p_{ij} , the transformation function f is updated. The two steps are alternatively repeated until there are no updates of the correspondence matrices P . By optimizing an overall similarity function that integrates the similarities between the landmarks and the smoothness constraints on the estimated transformation between the TRUS and CT images, the correspondences between the landmarks and importantly the dense transformation between the TRUS and CT images can be simultaneously obtained.

304 *2.A.5.c. Transformation model.* The transformation between TRUS and CT images are represented by a general 305 function, which can be modeled by various function bases 306 (e.g., multiquadratic,⁴⁰ thin-plate spline (TPS),^{41,42} radial 307 basis,⁴³ or B-spline⁴⁴). In this study, we chose the B-splines 308 as the transformation basis. Unlike the TPS or the elasticbody 309 splines, the B-splines translation of a point is only deter- 310 mined by the area immediately surrounding the control point, 311 resulting in locally controlled transformation. In the case of 312 the HDR procedure, the major deformations are caused by 313 a transrectal probe, and are spatially localized; therefore, a 314 locally controlled transformation would be advantageous for 315 registering TRUS images, and result in smooth transforma- 316 tion fields.⁴⁵

318 2.B. Prostate-phantom experiments

319 In order to validate the prostate segmentation method, 320 we first conducted experiments with a multimodality prostate 321 phantom (CIRS Model 053). In this phantom, a tissue- 322 mimicking prostate, along with structures simulating the rectal 323 wall, seminal vesicles, and urethra, is contained within an 324 $11.5 \times 7.0 \times 9.5 \text{ cm}^3$ clear plastic container. For the US scan, 325 a HI VISION Avius US machine (Hitachi Medical Group, 326 Japan) with a 7.5 MHz prostate biplane probe (UST-672-5/7.5) 327 was used. To mimic a prostate HDR procedure, 14 HDR 328 catheters were implanted into the prostate under US guidance 329 and the prostate was deformed by the pressure of the US 330 probe during the ultrasound scan. The voxel size of the 3D 331 US dataset was $0.08 \times 0.08 \times 0.50 \text{ mm}^3$. Figure 4(a) shows the 332 axial, coronal, and sagittal US images of the prostate phantom. 333 For the CT scan, a Philips CT scanner (Philips, The Netherlands) 334 was used, and the prostate was not deformed during the CT 335 scan. The voxel size of the 3D CT dataset was $0.29 \times 0.29 \times 0.80 \text{ mm}^3$. Figure 4(b) shows the axial, coronal, 336 and sagittal CT images of the prostate phantom. 337

338 The registration accuracy was evaluated using the fiducial 339 localization error (FLE) and target registration error (TRE). 340 The registration's accuracy depends on the FLE, which is the 341 error in locating the fiducials (points) employed in the regis- 342 tration process.⁴⁶ In this study, we used reconstructed cathe- 343 ters from TRUS and CT images as fiducials (landmarks) to

344 perform the registration, so the mean surface distances of the 345 corresponding catheters between the CT and postregistration 346 TRUS images were used to quantify the FLE. The TRE is an 347 important measure of the accuracy of the performed registra- 348 tion, which is the distance, after registration, between a pair 349 of corresponding fiducials that are not used in the registration 350 process.⁴⁶ In this study, the displacements of gold markers 351 between the CT and postregistration TRUS images were used 352 to quantify the TRE.

353 To evaluate the segmentation accuracy, we compared the 354 surface, and absolute and DICE volume difference of anatom- 355 ical structures (prostate and urethra) between the CT and 356 postregistration TRUS images, which are the two essential 357 measurements in the morphometric assessments. The segmen- 358 tation accuracy was quantified with three surface measures 359 (average surface distance, root-mean square (RMS), and 360 maximum surface distance) and two volume measures (abso- 361 lute volume difference and Dice volume overlap).

362 2.C. Preliminary clinical study

363 We conducted a retrospective clinical study with ten pa- 364 tients who had received HDR brachytherapy for localized pros- 365 tate cancer between January and June 2013. In this group of ten 366 patients, 12–16 catheters (mean \pm STD: 14.6 ± 1.4) were im- 367 planted. The same Hitachi US machine and Philips CT scanner 368 detailed in the phantom study were used to image the patients. 369 For TRUS images, the voxel size was $0.12 \times 0.12 \times 1.00 \text{ mm}^3$ 370 for three patients and $0.12 \times 0.12 \times 2.00 \text{ mm}^3$ for the remaining 371 seven patients. For the planning CT images, the voxel size was 372 $0.68 \times 0.68 \times 1.00 \text{ mm}^3$ for all patients. The accuracy of our 373 approach is assessed through the locations of three implanted 374 gold markers, as well as previous T2-weighted MR images of 375 the patients. To evaluate the accuracy of the prostate registra- 376 tion, we calculated the TRE and FLE.

377 In this pilot study, all patients had previous diagnostic MR 378 scans of the prostate. As compared with CT, MRI has high 379 soft tissue contrast and clear prostate boundaries.³³ Studies 380 have shown that accurate prostate volumes can be obtained 381 with both MRI and US.^{30,31,47} Hence, in this study, we used 382 prostate contours from the MR images as the gold standard 383 to evaluate our prostate segmentation method. All patients 384 were scanned in feet-down supine position with a body coil using 385 a Philips MRI with a voxel size of $1.0 \times 1.0 \times 2.00 \text{ mm}^3$. All 386 prostates were manually segmented from the T2-weighted 387 MR images. Because of various patients' positioning during 388 CT and MR scans, the prostate shape and size may vary be- 389 between the MR and CT images. To compute the volume differ- 390 ence and Dice overlap between the MRI-defined prostate and 391 our TRUS-based segmented prostate, we registered the MR 392 images to CT images^{48–50} and then applied the correspond- 393 ing deformation to the respective prostates of MR images to 394 obtain the MRI-based prostate volume.

395 To evaluate interobserver reliability of the prostate manual 396 contours, three observers (two radiologists and one US phys- 397 icist) were asked to independently contour the prostate US

398

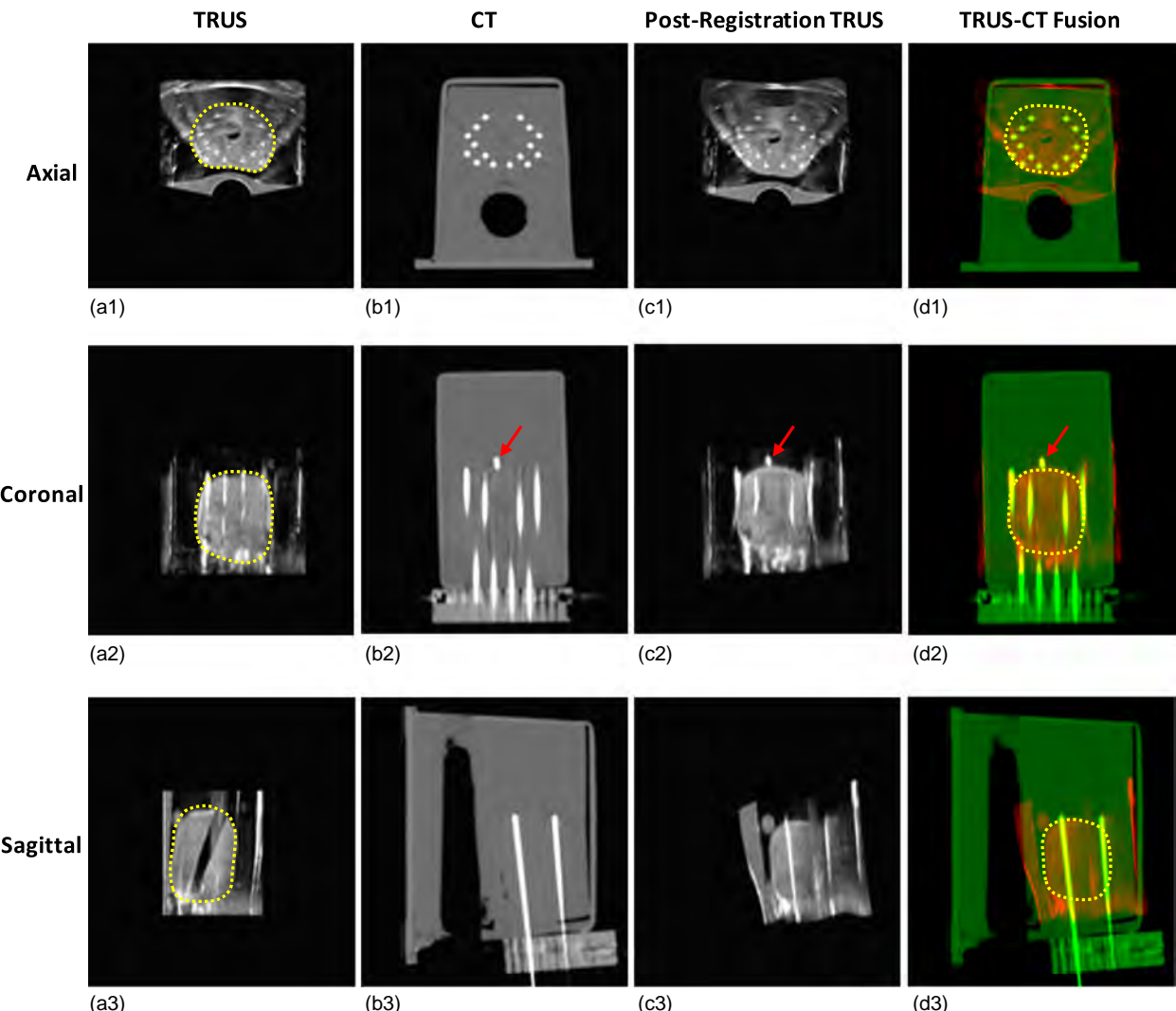


Fig. 4. 3D TRUS-CT registered results of the prostate phantom. (a1)–(a3) are TRUS images in the axial, coronal, and sagittal directions; (b1)–(b3) are CT images in three directions; (c1)–(c3) are the postregistration TRUS images; (d1)–(d3) are the TRUS-CT fusion images, where the prostate volume is transformed from original preregistration TRUS images. The close match between the gold marker (red arrows) and catheters in TRUS and CT demonstrates the accuracy of our method.

and MR images of six subjects. Each observer was blinded to other observers' contours. The variations of the prostate volume were calculated for assessment of consistency among measurements by the three observers. In addition, the effect of interobserver segmentation was further evaluated by comparing the variations of our automated segmentation results based on each observer's contours.

To evaluate intraobserver reliability of the prostate manual contours, one observer was asked to contour the prostate of the six sets of US and MR images twice. The time between the first and second contours was roughly 5 months, which was long enough to reduce recall bias. From these contours, the variations of the prostate volume were computed for assessment of consistency among measurements by the same observer. In addition, the effect of intraobserver segmentation was further evaluated by comparing the variations of our automated segmentation results based on the same observer's contours performed at two different times.

3. RESULTS

3.4. Prostate-phantom study

3.4.1. Registration accuracy

The prostate [Fig. 4(a), yellow dotted line] and the urethra were manually contoured on the TRUS images. The catheters were reconstructed on both TRUS and CT images. Figure 4(c) shows the postregistration TRUS images, and Fig. 4(d) shows the fusion images between the postregistration TRUS and CT images. From Fig. 4, we can obtain a visual assessment of the catheter and gold-marker match between the postregistration TRUS and CT images. To further quantify the accuracy of the registration, we calculated the three gold markers between the postregistration TRUS and CT images. The length of each gold marker is 3 mm, therefore the gold marker was often seen on two to three consecutive postregistration TRUS and CT images (0.8 mm slice thickness) and we used the center position (x , y , and z coordinates) to calculate the TRE of

444 TABLE I. TRE between the centers of three gold markers for prostate
 445 phantom.

Gold markers	ΔX	ΔY	ΔZ	Distance (mm)
1	1	2	0	0.51
2	0	1	0	0.29
3	1	1	0	0.42
Mean \pm STD				0.41 \pm 0.11

456 each gold marker between the CT and postregistration TRUS
 457 images. Table I illustrates the TRE for three gold markers,
 458 and the mean TRE is 0.41 ± 0.11 mm. For the FLE, the mean
 459 surface distance of the catheter pairs between the CT and
 460 postregistration TRUS images is 0.18 ± 0.15 mm.

3.A.2. Segmentation accuracy

462 Figure 5 provides a 3D visualization comparison of the
 463 prostate and urethra between our segmentation results and the
 464 gold standards (manual segmentations from CT images). The
 465 quantitative evaluations of the surface distance and volume
 466 difference between the prostate and urethra of TRUS and CT
 467 images of the prostate phantom are shown in Table II. The
 468 volume of the phantom prostate is 53.53 cm^3 . For both prostate
 469 and urethra, the mean surface distance, RMS, and maximum
 470 surface distance between our segmentations and the gold stan-
 471 dards are in submillimeter or millimeter range. The less than
 472 2% absolute volume difference and the more than 97% Dice
 473 volume overlap for both structures demonstrate the accurate
 474 volume segmentation of our proposed TRUS-based seg-
 475 mentation method. Not only can the proposed method accurately
 476 segment the prostate, it can also accurately segment the
 477 urethra—a smaller structure, located in the center of prostate,
 478 which further indicates the robustness of our proposed method.

3.B. Preliminary clinical study

3.B.1. Registration accuracy—comparison of gold 480 markers

482 Here, we used the case of a 58-yr-old patient who received
 483 HDR treatment for the intermediate prostate cancer to demon-
 484 strate our proposed segmentation method. Figure 6(a) shows

490 TABLE II. Surface distance and volume difference between our segmentations
 491 and CT-defined structures.

	Surface distance (mm)			Volume difference (%)																																	
	Mean \pm STD	RMS	Max	Absolute volume difference	Dice volume overlap																																
				494	495	496	497	498	499																												
Prostate	0.39 ± 0.25	0.41	1.32	1.65	97.84	500	501	502	503	504	505	506	507	508	509	510	511	512	513	514	515	516	517	518	519	520	521	522	523	524	525	526	527	528	529	530	531
Urethra	0.20 ± 0.16	0.21	0.68	1.83	97.75	500	501	502	503	504	505	506	507	508	509	510	511	512	513	514	515	516	517	518	519	520	521	522	523	524	525	526	527	528	529	530	531

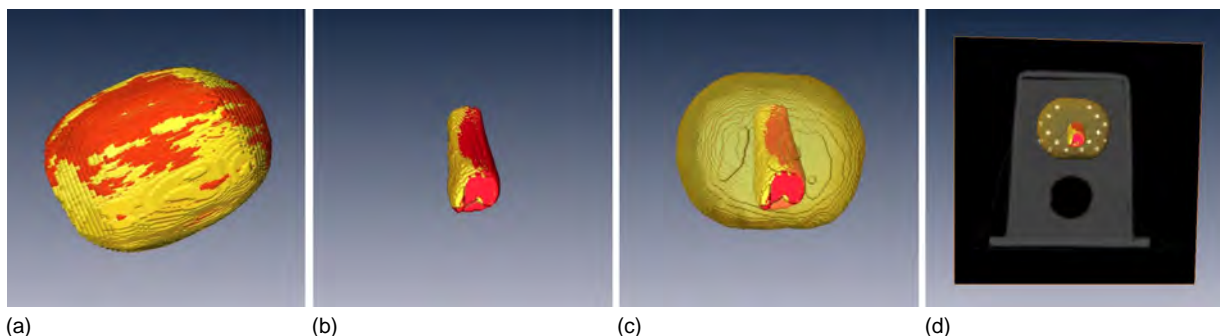
501 the intraoperative TRUS images and Fig. 6(b) displays the
 502 treatment planning CT images after catheter insertion. The
 503 fusion images between the planning CT and postregistration
 504 TRUS [Fig. 6(c)] are shown in Fig. 6(d). The prostate contour
 505 in the intraoperative TRUS image [Fig. 6(a)] was deformed to
 506 the postregistration TRUS, based on a deformable TRUS-CT
 507 registration. Finally, the prostate volume in TRUS images was
 508 integrated into the treatment planning CT.

509 Seven patients received combined radiotherapy (external
 510 beam radiotherapy plus HDR brachytherapy) for prostate can-
 511 cer treatment, while three patients received HDR monotherapy.
 512 For patients receiving combined radiotherapy, three gold
 513 markers were implanted before their external beam radio-
 514 therapy for the prostate localization during treatment. For
 515 patients receiving monotherapy, three gold markers were im-
 516 planted during the HDR procedure for the prostate localiza-
 517 tion. Three gold markers were placed at the base, middle, or
 518 apex of the prostate under the TRUS guidance.

519 We calculated the TRE of the gold markers and the FLE
 520 of the HDR catheters in CT and postregistration TRUS im-
 521 ages to evaluate the accuracy of our registration, as shown in
 522 Fig. 7. This figure shows the TRE and FLE for ten patients.
 523 Overall, the TRE of the gold markers for all patients was
 524 1.18 ± 0.26 mm, and the FLE (mean surface distance) of the
 525 HDR catheters for all patients was 0.33 ± 0.09 mm. The close
 526 match between the gold markers and the HDR catheters in
 527 the TRUS and CT demonstrated the accuracy of our method.

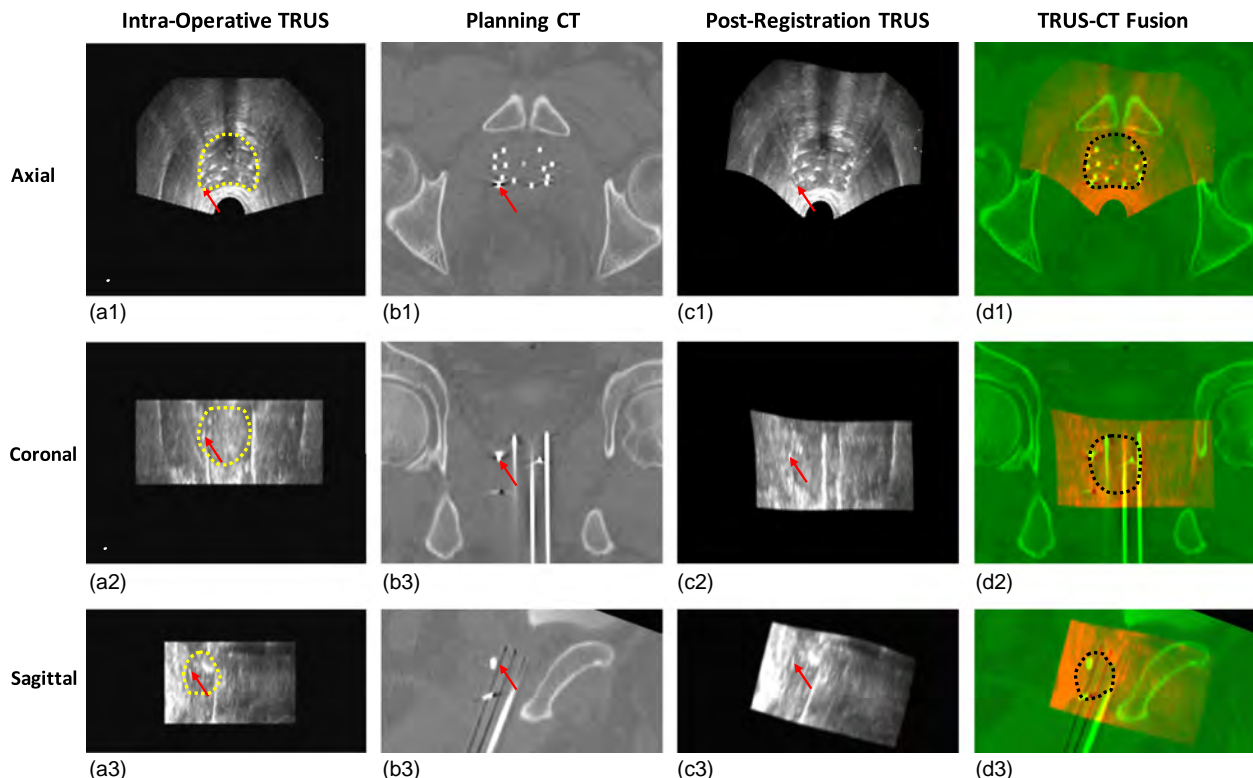
3.B.2. Segmentation accuracy—comparison with MR 528 prostate volume

529 Here, we used the same 58-yr old patient, shown in Fig. 6,
 530 to illustrate the comparison between our TRUS-based prostate



531 Fig. 5. 3D comparison of segmented prostate and urethra with the gold standards. (a) 3D prostate overlap comparison between the postregistration TRUS (red)
 532 and gold-standard CT (yellow); (b) 3D urethra overlap between the postregistration TRUS (red) and CT (yellow); (c) 3D overlap of the urethra inside the
 533 prostate; (d) 3D result of the prostate and urethra in 3D CT image.

532



533

534

535

536

537

538

539 Fig. 6. Integration of TRUS-based prostate volume into postoperative CT images. (a1)–(a3) are TRUS images in axial, coronal, and sagittal directions; (b1)–(b3) 540 are the postoperative CT; (c1)–(c3) are the postregistration TRUS images; (d1)–(d3) are the TRUS–CT fusion images, where the prostate volume is 541 integrated. The close match between the gold markers (red arrows) in the TRUS and CT demonstrates the accuracy of our method.

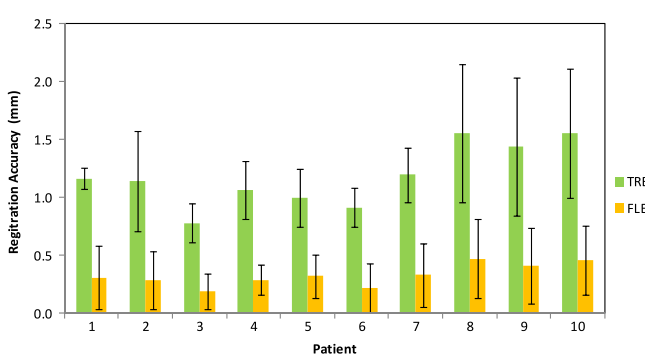
542 segmentation and the MR-defined prostate volume. Figure 8(a) 543 shows the treatment planning CT images. Figure 8(b) 544 shows the CT images with the MRI-defined prostate volume and the 545 MRI-defined prostate volume of this patient is 40.9 cm^3 . Figure 546 8(c) shows the CT images with our TRUS-based segmented 547 prostate volume, and our segmented prostate volume for this 548 patient is 38.2 cm^3 . Figure 8(d) displays the 3D overlap shown 549 in yellow between our TRUS-based prostate volume, shown 550 in red, and MR-based prostate volume, shown in green. The 551 absolute prostate volume difference of this patient is 6.51% 552 and the Dice volume overlap is 92.77%. Large yellow overlap 553 areas at three directions show a close match of the prostate 554 contours obtained from our prostate segmentation and the 555 MRI-defined boundary (ground truth). In particular, our 556 segmentation matched very well with the MR-defined prostate at the

564 base and apex, which is usually a difficult area to segment on 565 CT images.

566 In Table III, the mean surface distance, absolute prostate 567 volume differences, and Dice volume overlaps between 568 our segmented prostate and MR-defined prostate of all ten 569 patients are displayed. The average prostate-surface differ- 570 ence between our approach and the corresponding MRI was 571 around 0.60 mm, the average absolute prostate-volume differ- 572 ence was less than 10%, and the average Dice volume overlap 573 was over 90%. The small surface and volume difference and 574 high volume overlap demonstrated the prostate volume con- 575 tour accuracy of our TRUS–CT-based registration method. 576 The Bland–Altman analysis⁵¹ is a method for statistical eval- 577 uation of agreement between two measurements. Figure 9 578 shows the systematic differences and estimate bias and limits 579 of agreement between the TRUS-based and MRI-based pros- 580 state volumes. The relative bias in the TRUS-based volume 581 over the MRI-based volume was 1.7%, which may be due to 582 the prostate swelling from the implant needles.

3.B.3. Inter- and intraobserver reliability

583 Inter- and intraobserver reliability of the prostate contours 584 is demonstrated in Fig. 10. Among the manual segmentations 585 of the three observers, the mean prostate volume difference 586 was $-1.13\% \pm 8.40\%$, $1.11\% \pm 4.70\%$ and $0.31\% \pm 4.94\%$ for 587 the TRUS, and $1.79\% \pm 6.16\%$, $-0.85\% \pm 3.32\%$, and $1.12\% \pm 3.16\%$ for the MRI. Between the two measurements of 588 the same observer, the mean prostate volume difference was 589



590 Fig. 7. The TRE of the gold markers and the FLE of the HDR catheters for 591 ten patients.

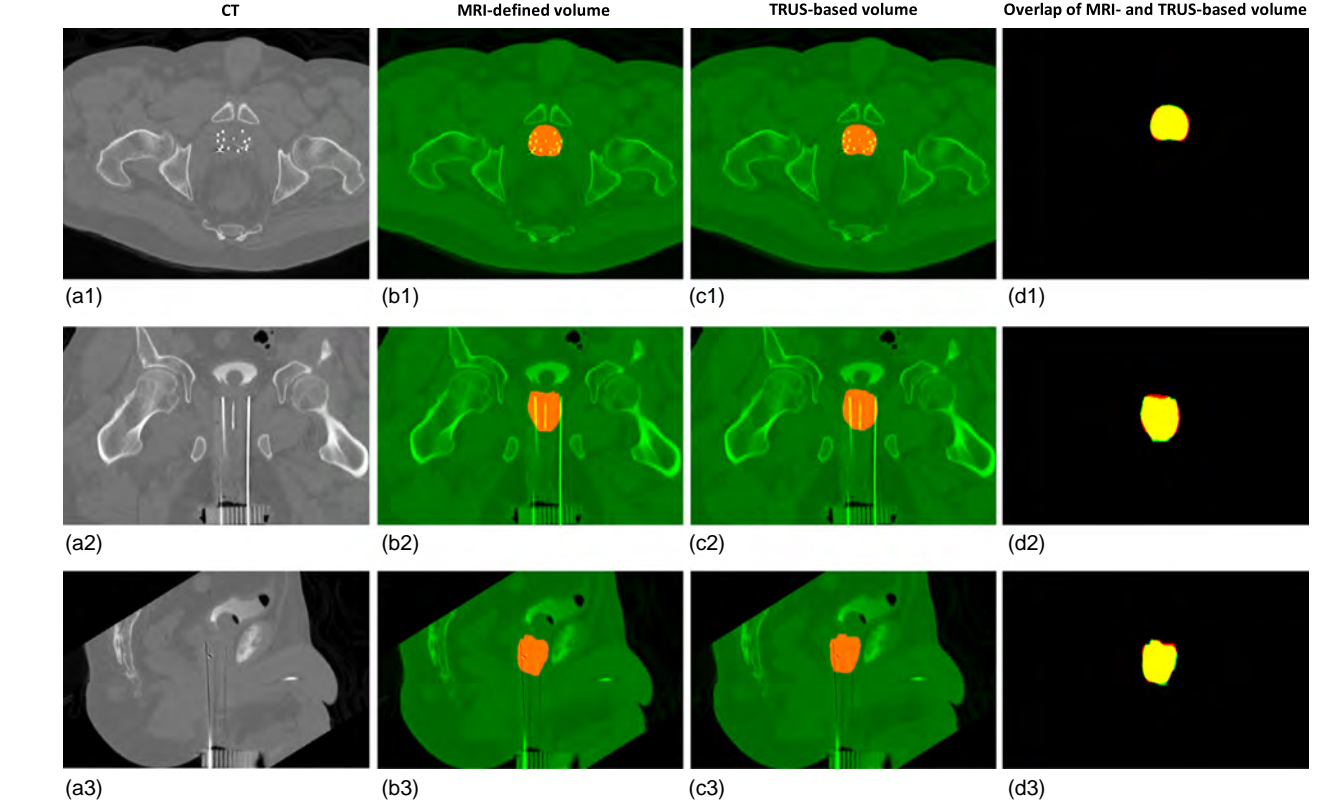


FIG. 8. Comparison of the TRUS-based prostate segmentation and MR-defined prostate volume. (a1)–(a3) are the axial, coronal, and sagittal CT images; (b1)–(b3) are the CT images with MRI-defined prostate volume; (c1)–(c3) are the CT images with our TRUS-based segmented prostate volume; (d1)–(d3) are the volume overlap (yellow) between our TRUS-based segmented prostate volume (red) and MRI-based prostate volume (green).

–0.93% \pm 3.19% for the TRUS, and –0.07% \pm 3.56% for the MRI. Figure 11 compares the automated segmented prostate CT volumes based on the three observers' segmentations and the same observer's segmentations at two different times. The mean prostate volume difference for our automated CT segmentation was –1.95% \pm 7.50%, 1.64% \pm 4.51%, and 0.05% \pm 4.85% based on the manual segmentations of three observers, and –0.04% \pm 3.30% based on the manual segmentations of the same observer at two different times. The inter- and intraobserver reliability study showed the consistency in the manual segmentations, as well as in our automated segmentations based on various sets of manual segmentations.

Figure 12 shows the volume difference between our automated segmentation volumes and the MR-defined prostate volumes for three observers. There are no significant prostate volume differences among these three observers (p -values = 0.43, 0.32, and 0.28 between any two observers). Figure 13 shows the volume difference between our automated segmentation volumes and the MR-defined prostate volumes for the

same observer. There is no significant volume difference between the two measurements (p -value = 0.37).

4. DISCUSSIONS

We proposed a novel CT prostate segmentation approach through TRUS–CT deformable registration based on the HDR catheter locations, which may significantly improve the prostate contour accuracy in US-guided CT-based prostate HDR treatment. This method was tested through a prostate-phantom study and a pilot clinical study. In the prostate-phantom study, the mean displacement of the three implanted gold markers was less than 0.5 mm. In addition, the small surface and volume difference of both the prostate and the urethra further demonstrated that our approach not only captured the external deformation (prostate contour) but also the internal deformation (urethra). In the clinical study, we further demonstrated its clinical feasibility and validated the segmentation accuracy with the patients' MRIs.

TABLE III. Prostate surface and volume comparison between our segmentation and the MR-defined prostate.

Patient	P01	P02	P03	P04	P05	P06	P07	P08	P09	P10	Mean \pm STD
Mean surface distance (mm)	0.58	0.61	0.59	0.57	0.49	0.63	0.73	0.57	0.61	0.56	0.61 \pm 0.06
Absolute volume difference (%)	7.13	7.75	6.97	6.71	6.51	6.23	7.35	8.19	8.04	8.35	7.28 \pm 0.86
Dice volume overlap (%)	92.72	91.27	93.89	92.97	92.77	92.54	91.41	90.69	91.14	90.36	91.89 \pm 1.19
TRUS prostate volume (CC)	41.51	42.03	43.14	39.02	38.19	44.11	58.87	29.21	38.68	28.94	40.37 \pm 8.40

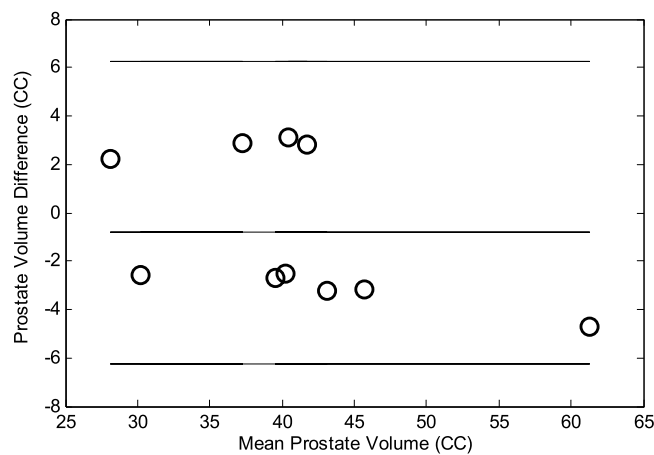


FIG. 9. Bland-Altman analysis between our segmentation and the MR-defined prostate. The lines indicate the mean difference (the middle line), the mean difference + 2SD (the top line), and the mean difference - 2SD (the bottom line).

The novelty of our approach is to integrate TRUS-based prostate volume into CT-based prostate HDR treatment planning. To the best of our knowledge, this is the first study on CT prostate segmentation with catheters based on the TRUS volume in HDR brachytherapy. This approach has three distinctive strengths. (1) We utilize 3D TRUS images to provide accurate prostate delineation and improve prostate contours for CT-based HDR treatment planning. (2) The TRUS and planning CT images both are acquired post catheter insertions, so these HDR catheters uniformly and symmetrically distributed inside the prostate gland provide exceptional landmarks for the later TRUS-CT registration to capture the nonrigid prostate

deformation between the TRUS and CT modalities. (3) Our approach is clinically feasible and can be easily adapted into the HDR procedure. The 3D TRUS data are acquired in the operating room during a HDR procedure; and the patient scan takes 1–3 min. Therefore no prior TRUS or additional patient visits for imaging are required. In addition, these TRUS images acquired during the HDR procedure provide the most authentic prostate volume for HDR treatment planning as compared with patients' previous TRUS or MRI.

The robustness of the proposed prostate segmentation was resulted from the accurate registration between the TRUS and CT images. The registration between CT and US images of the prostate is often very challenging, mainly because the anatomical structures in the US images are embedded in a noisy and low contrast environment with little distinctive information regarding the material density measured in the CT images. To overcome these difficulties, many approaches were proposed to achieve prostate registration between CT and US. For example, Fallavollita *et al.* reported an intensity-based registration method using TRUS and CT. Their registration error was 0.54 ± 0.11 mm in the phantom study and 2.86 ± 1.26 mm in the clinical study.^{52,53} Using a similar registration method, Dehghan *et al.* reported 0.70 ± 0.20 mm error in the implanted seed locations for the phantom study and 1.80 ± 0.90 mm registration error for the clinical study.^{52,53} Even *et al.* used 1–2 fiducial markers and 3–4 needle tips to perform a rigid registration between TRUS and cone-beam CT and their registration errors were within 3 mm for 85% of their patients.⁵⁴ Yang *et al.* presented a hybrid approach that simultaneously optimized the similarities from the point-based registration and the volume matching method. In a phantom study, a target

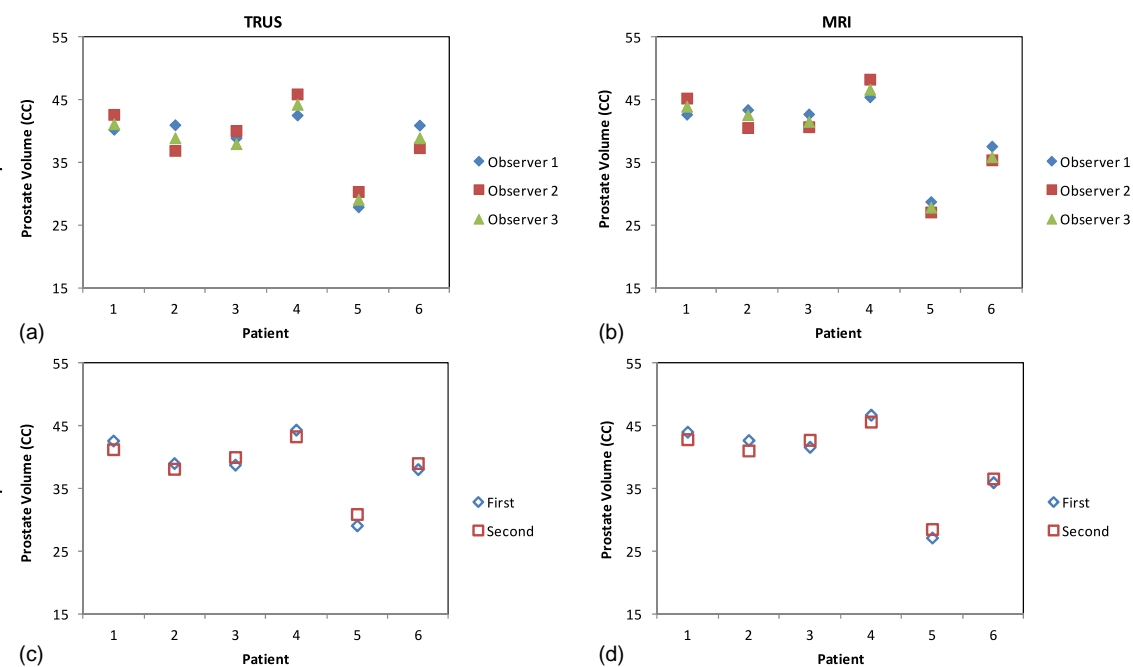


FIG. 10. Inter- and intraobserver reliability of the prostate contours. Among three observers, prostate volume comparison for TRUS (a) and MRI (b); between the two measurements of the same observer, prostate volume comparison for TRUS (c) and MRI (d). Interobserver reliability was demonstrated by the agreement between three observers' prostate volumes. And intraobserver reliability was demonstrated by the agreement between the two sets of prostate volumes performed by one observer.

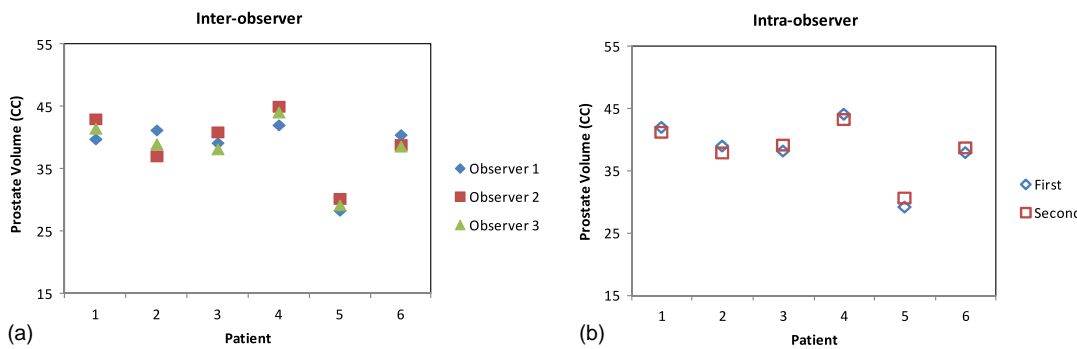


FIG. 11. Prostate volume comparison of our automated segmentations based on the three observer's segmentations (a) and the same observer's segmentations at two different times (b).

registration error of 3-voxels (1.5 mm) was reported.³⁹ Firle *et al.* used the segmented structures (e.g., prostate or urethra) for US and CT prostate registration. Their prostate-phantom study demonstrated 0.55–1.67 mm accuracy, but no clinical study was reported.⁵⁵ In this study, we proposed a catheter-based registration method. In the HDR procedure, the catheters were fixed with the needle template after the completion of the catheter insertion in the operating room to ensure no catheter movement or displacement relative to the prostate gland throughout the brachytherapy procedure. In order to deliver a uniform dose to the prostate and spare the surrounding normal tissues such as the bladder and the rectum, the catheters were evenly placed to cover the entire prostate. Such uniformly and symmetrically distributed catheters provide exceptional landmarks to capture the nonrigid prostate deformation between the TRUS and CT images. Even though some catheters may be curved due to the deflection, manual catheter segmentation can easily capture the curvatures. In addition, we chose a B-splines transformation model, therefore, the translation of a point is only determined by the area immediately surrounding the control points to ensure locally controlled transformation.⁵⁶ Because the deformations caused by a transrectal probe are spatially localized, this locally controlled transformation could be advantageous for registering TRUS images and result in smooth transformation fields. As a result, our registration between the CT and US prostate images has achieved submillimeter accuracy in the phantom study, and 1.18 ± 0.26 mm accuracy in the clinical study.

In recent years, many prostate segmentation methods based on CT images have been proposed and these approaches can be broadly classified into three main categories: model-based, classification-based, or registration-based methods.²⁶ Model-based methods^{16–21} construct the statistical models based on the prostate shape or appearance to guide segmentation in a new set of images. Feng *et al.* presented a deformable-model-based segmentation method by using both the shape and appearance information learned from the previous images to guide automatic segmentation of the new CT images.¹⁷ Chowdhury *et al.* proposed a linked statistical shape model that links the shape variations of a structure of interest across MR and CT imaging modalities to concurrently segment the prostate on the MRI and CT images.²¹ In the classification-based methods,^{21–27} the segmentation process is formulated as a classification problem, where classifiers are trained from the training images and based on which voxel-wise classification is performed for each voxel in the new image to determine whether it belongs to the prostate or the nonprostate region. Li *et al.* presented an online-learning and patient-specific classification method based on the location-adaptive image context to achieve the segmentation of the prostate in CT images.²² In Liao's paper, a patch-based representation in the discriminative feature space with logistic sparse LASSO was used as the anatomical signature to deal with the low contrast problem in the prostate CT images, and a multiatlases label fusion method formulated under sparse representation framework was designed to segment

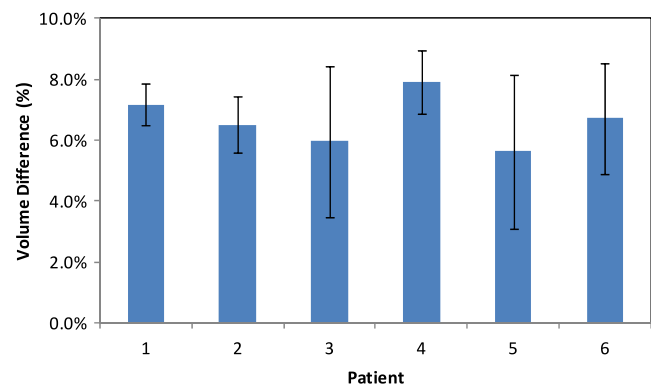


FIG. 12. The volume difference between our automated segmentation volumes and the MR-defined prostate volumes for three interobservers.

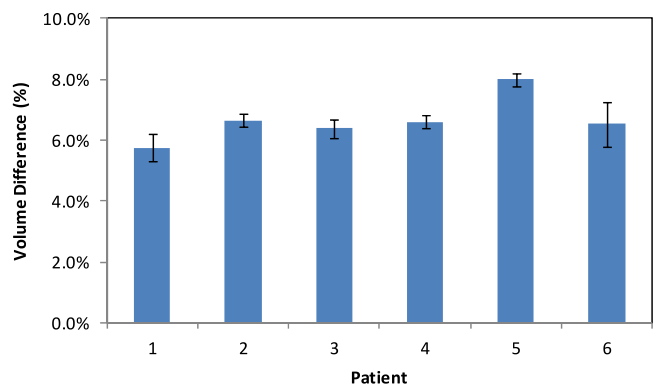


FIG. 13. The volume difference between our automated segmentation volumes and the MR-defined prostate volumes for the same intraobserver.

the prostate.²⁶ Finally, registration-based methods^{28,29} explicitly estimate the deformation field from the planning image to the treatment image so that the segmented prostate in the planning image can be warped to the treatment image space to localize the prostate in the treatment images. Davis *et al.*'s paper exemplifies the registration method by combining a large deformation image registration with a bowel gas segmentation and deflation algorithm for adaptive radiation therapy of the prostate.²⁸

We compared our method with six previous prostate CT segmentation methods proposed by Chen *et al.*,¹⁶ Feng *et al.*,¹⁷ Li *et al.*,²² Liao *et al.*,^{23,26} and Davis *et al.*²⁸ The mean Dice volume overlap of these 6 methods ranged between 82.0% and 90.9%. In contrast, our approach integrated accurate TRUS prostate volume into the CT images, and the average Dice volume overlap between our segmentation and the MRI-based prostate volume was 91.89%. The volume discrepancies mostly occurred at the base and apex of the prostate. The prostate boundary on the MRI is sometimes not clear around the prostate base and apex. Therefore, the volume discrepancies may be related to the MRI-based manual segmentation error. Of course, many other factors, such as patient position, rectal probe, and catheter-induced prostate swelling, could also contribute to the discrepancies.

For future studies, we will either decrease the number of catheters used in the deformable registration or incorporate automatic catheter recognition in TRUS images to speed up registration and segmentation. We will also introduce automatic segmentation methods for TRUS prostate images to eliminate physicians' manual contours.⁵⁷⁻⁶⁴ Meanwhile, we are conducting a clinical study with a larger cohort to further investigate treatment outcomes (e.g., cancer control and side effects) in the clinic.

5. CONCLUSION

Accurate segmentation of the prostate volume in the treatment planning CT is a key step to the success of CT-based HDR prostate brachytherapy. We have developed a novel segmentation approach to improve prostate contours utilizing intraoperative TRUS-based prostate volume in the treatment planning. In a preliminary study of ten patients, we demonstrated its clinical feasibility and validated the accuracy of our segmentation method with MRI-defined prostate volumes. Our multimodality technology, which incorporates accurate TRUS prostate volume, and fits efficiently with the HDR brachytherapy workflow, could improve prostate contours in planning CT, enables accurate dose planning and delivery, and potentially enhance the prostate HDR treatment outcomes.

ACKNOWLEDGMENTS

This research is supported in part by the DOD Prostate Cancer Research Program (PCRP) Award W81XWH-13-1-0269 and the National Cancer Institute (NCI) Grant No. CA114313. The authors report no conflicts of interest in conducting the research.

- ^{a)}Author to whom correspondence should be addressed. Electronic mail: xyang43@emory.edu; Telephone: (404)778-8622; Fax: (404)778-4139.
- ¹A. Challapalli, E. Jones, C. Harvey, G. O. Hellawell, and S. A. Mangar, "High dose rate prostate brachytherapy: An overview of the rationale, experience and emerging applications in the treatment of prostate cancer," *Br. J. Radiol.* **85**, S18–S27 (2012).
- ²S. G. Williams, J. M. G. Taylor, N. Liu, Y. Tra, G. M. Duchesne, L. L. Kestin, A. Martinez, G. R. Pratt, and H. Sandler, "Use of individual fraction size data from 3756 patients to directly determine the alpha/beta ratio of prostate cancer," *Int. J. Radiat. Oncol.* **68**, 24–33 (2007).
- ³M. Sato, T. Mori, S. Shirai, K. Kishi, T. Inagaki, and I. Hara, "High-dose-rate brachytherapy of a single implant with two fractions combined with external beam radiotherapy for hormone-naïve prostate cancer," *Int. J. Radiat. Oncol.* **72**, 1002–1009 (2008).
- ⁴T. M. Pisansky, D. G. Gold, K. M. Furutani, O. K. Macdonald, R. H. McLaren, L. A. Mynderse, T. M. Wilson, J. R. Hebl, and R. Choo, "High-dose-rate brachytherapy in the curative treatment of patients with localized prostate cancer," *Mayo Clin. Proc.* **83**, 1364–1372 (2008).
- ⁵B. A. Jereczek-Fossa and R. Orecchia, "Evidence-based radiation oncology: Definitive, adjuvant and salvage radiotherapy for non-metastatic prostate cancer," *Radiat. Oncol.* **84**, 197–215 (2007).
- ⁶A. J. Stewart and B. Jones, *Radiobiologic Concepts for Brachytherapy* (Williams & Wilkins, Philadelphia, PA: Lippincott, 2002).
- ⁷"Prostate cancer," NCCN clinical practice guidelines in oncology, V.2.2009 (2009) (available URL: http://www.nccn.org/professionals/physician_gls/PDF/prostate.pdf).
- ⁸C. J. Mettlin, G. P. Murphy, C. J. McDonald, and H. R. Menck, "The National Cancer Data base Report on increased use of brachytherapy for the treatment of patients with prostate carcinoma in the U.S.," *Cancer* **86**, 1877–1882 (1999).
- ⁹M. R. Cooperberg, D. P. Lubeck, M. V. Meng, S. S. Mehta, and P. R. Carroll, "The changing face of low-risk prostate cancer: Trends in clinical presentation and primary management," *J. Clin. Oncol.* **22**, 2141–2149 (2004).
- ¹⁰O. Acosta, J. Dowling, G. Drean, A. Simon, R. Crevoisier, and P. Haigron, "Multi-atlas-based segmentation of pelvic structures from CT scans for planning in prostate cancer radiotherapy," in *Abdomen and Thoracic Imaging*, edited by A. S. El-Baz, L. Saba, and J. Suri (Springer, NY, 2014), pp. 623–656.
- ¹¹D. F. Dubois, B. R. Prestidge, L. A. Hotchkiss, J. J. Prete, and W. S. Bice, "Intraobserver and interobserver variability of MR imaging- and CT-derived prostate volumes after transperineal interstitial permanent prostate brachytherapy," *Radiology* **207**, 785–789 (1998).
- ¹²X. Yang, T. Liu, D. M. Marcus, A. B. Jani, T. Ogunleye, W. J. Curran, and P. J. Rossi, "A novel ultrasound-CT deformable registration process improves physician contouring during CT-based HDR brachytherapy for prostate cancer," *Brachytherapy* **13**, S67–S68 (2014).
- ¹³M. Roach, P. FaillaceAkazawa, C. Malfatti, J. Holland, and H. Hricak, "Prostate volumes defined by magnetic resonance imaging and computerized tomographic scans for three-dimensional conformal radiotherapy," *Int. J. Radiat. Oncol.* **35**, 1011–1018 (1996).
- ¹⁴C. Rasch, I. Barillot, P. Remeijer, A. Touw, M. van Herk, and J. V. Lebesque, "Definition of the prostate in CT and MRI: A multi-observer study," *Int. J. Radiat. Oncol.* **43**, 57–66 (1999).
- ¹⁵S. C. Hoffelt, L. M. Marshall, M. Garzotto, A. Hung, J. Holland, and T. M. Beer, "A comparison of CT scan to transrectal ultrasound-measured prostate volume in untreated prostate cancer," *Int. J. Radiat. Oncol.* **57**, 29–32 (2003).
- ¹⁶S. Q. Chen, D. M. Lovelock, and R. J. Radke, "Segmenting the prostate and rectum in CT imagery using anatomical constraints," *Med. Image Anal.* **15**, 1–11 (2011).
- ¹⁷Q. J. Feng, M. Foskey, W. F. Chen, and D. G. Shen, "Segmenting CT prostate images using population and patient-specific statistics for radiotherapy," *Med. Phys.* **37**, 4121–4132 (2010).
- ¹⁸J. V. Stough, R. E. Broadhurst, S. M. Pizer, and E. L. Chaney, "Regional appearance in deformable model segmentation," *Lect. Notes Comput. Sci.* **4584**, 532–543 (2007).
- ¹⁹D. Freedman, R. J. Radke, T. Zhang, Y. Jeong, D. M. Lovelock, and G. T. Y. Chen, "Model-based segmentation of medical imagery by matching distributions," *IEEE Trans. Med. Imaging* **24**, 281–292 (2005).
- ²⁰M. H. Smitsmans, J. W. Wolthaus, X. Artignan, J. de Bois, D. A. Jaffray, J. V. Lebesque, and M. van Herk, "Automatic localization of the prostate for on-line or off-line image-guided radiotherapy," *Int. J. Radiat. Oncol., Biol., Phys.* **60**, 623–635 (2004).

- ⁹³²²¹N. Chowdhury, R. Toth, J. Chappelow, S. Kim, S. Motwani, S. Punekar, H. B. Lin, S. Both, N. Vapiwala, S. Hahn, and A. Madabhushi, "Concurrent segmentation of the prostate on MRI and CT via linked statistical shape models for radiotherapy planning," *Med. Phys.* **39**, 2214–2228 (2012).
- ⁹³³²²W. Li, S. Liao, Q. J. Feng, W. F. Chen, and D. G. Shen, "Learning image context for segmentation of the prostate in CT-guided radiotherapy," *Phys. Med. Biol.* **57**, 1283–1308 (2012).
- ⁹³⁴²³S. Liao and D. G. Shen, "A feature-based learning framework for accurate prostate localization in CT images," *IEEE Trans. Image Process.* **21**, 3546–3559 (2012).
- ⁹³⁵²⁴B. Haas, T. Coradi, M. Scholz, P. Kunz, M. Huber, U. Oppitz, L. Andre, V. Lengkeek, D. Huyskens, A. Van Esch, and R. Reddick, "Automatic segmentation of thoracic and pelvic CT images for radiotherapy planning using implicit anatomic knowledge and organ-specific segmentation strategies," *Phys. Med. Biol.* **53**, 1751–1771 (2008).
- ⁹³⁶²⁵P. Ghosh and M. Mitchell, "Segmentation of medical images using a genetic algorithm," in *GECCO 2006: Genetic and Evolutionary Computation Conference* (■, ■, 2006), Vols. 1 and 2, pp. 1171–1178.
- ⁹³⁷²⁶S. Liao, Y. Z. Gao, J. Lian, and D. G. Shen, "Sparse patch-based label propagation for accurate prostate localization in CT images," *IEEE Trans. Med. Imaging* **32**, 419–434 (2013).
- ⁹³⁸²⁷P. Ghosh and M. Mitchell, "Prostate segmentation on pelvic CT images using a genetic algorithm," *Proc. Soc. Photo.-Opt. Instrum.* **6914**, 91442–■ (2008).
- ⁹³⁹²⁸B. C. Davis, M. Foskey, J. Rosenman, L. Goyal, S. Chang, and S. Joshi, "Automatic segmentation of intra-treatment CT images for adaptive radiation therapy of the prostate," in *Medical Image Computing and Computer-Assisted Intervention - Miccai 2005* (■, ■, 2005), Vol. 3749, pp. 442–450.
- ⁹⁴⁰²⁹M. Foskey, B. Davis, L. Goyal, S. Chang, E. Chaney, N. Strehl, S. Tomei, J. Rosenman, and S. Joshi, "Large deformation three-dimensional image registration in image-guided radiation therapy," *Phys. Med. Biol.* **50**, 5869–5892 (2005).
- ⁹⁴¹³⁰J. S. Lee and B. H. Chung, "Transrectal ultrasound versus magnetic resonance imaging in the estimation of prostate volume as compared with radical prostatectomy specimens," *Urol. Int.* **78**, 323–327 (2007).
- ⁹⁴²³¹B. E. Weiss, A. J. Wein, S. B. Malkowicz, and T. J. Guzzo, "Comparison of prostate volume measured by transrectal ultrasound and magnetic resonance imaging: Is transrectal ultrasound suitable to determine which patients should undergo active surveillance?," *Urol. Oncol.: Semin. Orig. Invest.* **31**, 1436–1440 (2013).
- ⁹⁴³³²A. Tewari, R. Indudhara, K. Shinohara, E. Schalow, M. Woods, R. Lee, C. Anderson, and P. Narayan, "Comparison of transrectal ultrasound prostatic volume estimation with magnetic resonance imaging volume estimation and surgical specimen weight in patients with benign prostatic hyperplasia," *J. Clin. Ultrasound* **24**, 169–174 (1996).
- ⁹⁴⁴³³Y. Mazaheri, A. Shukla-Dave, A. Muellner, and H. Hricak, "MR imaging of the prostate in clinical practice," *Magn. Reson. Mater. Phys.* **21**, 379–392 (2008).
- ⁹⁴⁵³⁴M. Peikari, T. K. Chen, A. Lasso, T. Heffter, G. Fichtinger, and E. C. Burdette, "Characterization of ultrasound elevation beamwidth artifacts for prostate brachytherapy needle insertion," *Med. Phys.* **39**, 246–256 (2012).
- ⁹⁴⁶³⁵H. Chui and A. Rangarajan, "A new point matching algorithm for non-rigid registration," *Comput. Vis. Image Und.* **89**, 114–141 (2002).
- ⁹⁴⁷³⁶S. Belongie, J. Malik, and J. Puzicha, "Shape matching and object recognition using shape contexts," *IEEE Trans. Pattern Anal.* **24**, 509–522 (2002).
- ⁹⁴⁸³⁷Y. Zhan, Y. Ou, M. Feldman, J. Tomaszewski, C. Davatzikos, and D. Shen, "Registering histologic and MR images of prostate for image-based cancer detection," *Acad. Radiol.* **14**(11), 1367–1381 (2007).
- ⁹⁴⁹³⁸A. L. Yuil and J. J. Kosowsky, "Statistical physics algorithms that converge," *Neural Comput.* **6**, 341–356 (1994).
- ⁹⁵⁰³⁹X. F. Yang, H. Akbari, L. Halig, and B. W. Fei, "3D non-rigid registration using surface and local salient features for transrectal ultrasound image-guided prostate biopsy," *Proc. SPIE* **7964**, ■–■ (2011).
- ⁹⁵¹⁴⁰R. L. Hardy, "Hardy's multiquadric-biharmonic method for gravity field predictions II," *Comput. Math. Appl.* **41**, 1043–1048 (2001).
- ⁹⁵²⁴¹F. L. Bookstein, "Principal warps - thin-plate splines and the decomposition of deformations," *IEEE Trans. Pattern Anal.* **11**, 567–585 (1989).
- ⁹⁵³⁴²T. Stammberger, J. Hohe, K. H. Englmeier, M. Reiser, and F. Eckstein, "Elastic registration of 3D cartilage surfaces from MR image data for detecting local changes in cartilage thickness," *Magn. Reson. Med.* **44**, 592–601 (2000).
- ⁹⁵⁴⁴³N. Arad and D. Reisfeld, "Image warping using few anchor points and radial functions," *Comput. Graph. Forum* **14**, 35–46 (1995).
- ⁹⁵⁵⁴⁴Z. Y. Xie and G. E. Farin, "Image registration using hierarchical B-splines," *IEEE Trans. Vis. Comput. Graph.* **10**, 85–94 (2004).
- ⁹⁵⁶⁴⁵Y. Mazaheri, L. Bokacheva, D. J. Kroon, O. Akin, H. Hricak, D. Chamudot, S. Fine, and J. A. Koutcher, "Semi-automatic deformable registration of prostate MR images to pathological slices," *J. Magn. Reson. Imaging* **32**, 1149–1157 (2010).
- ⁹⁵⁷⁴⁶M. H. Moghari and P. Abolmaesumi, "Distribution of target registration error for anisotropic and inhomogeneous fiducial localization error," *IEEE Trans. Med. Imaging* **28**, 799–813 (2009).
- ⁹⁵⁸⁴⁷W. L. Smith, C. Lewis, G. Bauman, G. Rodrigues, D. D'Souza, R. Ash, D. Ho, V. Venkatesan, D. Downey, and A. Fenster, "Prostate volume contouring: A 3D analysis of segmentation using 3DTRUS, CT, and MR," *Int. J. Radiat. Oncol., Biol., Phys.* **67**, 1238–1247 (2007).
- ⁹⁵⁹⁴⁸C. J. Dean, J. R. Sykes, R. A. Cooper, P. Hatfield, B. Carey, S. Swift, S. E. Bacon, D. Thwaites, D. Sebag-Montefiore, and A. M. Morgan, "An evaluation of four CT–MRI co-registration techniques for radiotherapy treatment planning of prone rectal cancer patients," *Br. J. Radiol.* **85**, 61–68 (2012).
- ⁹⁶⁰⁴⁹A. Betgen, F. Pos, C. Schneider, M. van Herk, and P. Remeijer, "Automatic registration of the prostate on MRI scans to CT scans for radiotherapy target delineation," *Radiother. Oncol.* **84**, S119–■ (2007).
- ⁹⁶¹⁵⁰D. Levy, E. Schreibmann, B. Thorndyke, T. Li, Y. Yang, A. Boyer, and L. Xing, "Registration of prostate MRI/MRSI and CT studies using the narrow band approach," *Med. Phys.* **32**, 1895–■ (2005).
- ⁹⁶²⁵¹J. M. Bland and D. G. Altman, "Statistical methods for assessing agreement between two methods of clinical measurement," *Lancet* **1**, 307–310 (1986).
- ⁹⁶³⁵²P. Fallavollita, Z. K. Aghaloo, E. C. Burdette, D. Y. Song, P. Abolmaesumi, and G. Fichtinger, "Registration between ultrasound and fluoroscopy or CT in prostate brachytherapy," *Med. Phys.* **37**, 2749–2760 (2010).
- ⁹⁶⁴⁵³E. Dehghan, J. Lee, P. Fallavollita, N. Kuo, A. Deguet, E. C. Burdette, D. Song, J. L. Prince, and G. Fichtinger, "Point-to-volume registration of prostate implants to ultrasound," in *Medical Image Computing and Computer-Assisted Intervention (Miccai 2011)* (■, ■, 2011), Vol. 6892, pp. 615–622.
- ⁹⁶⁵⁵⁴A. J. Even, T. T. Nuver, H. Westendorp, C. J. Hoekstra, C. H. Slump, and A. W. Minken, "High-dose-rate prostate brachytherapy based on registered transrectal ultrasound and in-room cone-beam CT images," *Brachytherapy* ■, ■–■ (2013).
- ⁹⁶⁶⁵⁵E. A. Firle, W. Chen, and S. Wesarg, "Registration of 3D U/S and CT images of the prostate," in *Cars 2002: Computer Assisted Radiology and Surgery, Proceedings* (■, ■, 2002), pp. 527–532.
- ⁹⁶⁷⁵⁶X. Yang, P. Rossi, T. Ogunleye, A. B. Jani, W. J. Curran, and T. Liu, "Image-guided procedures, robotic interventions, and modeling," *Proc. SPIE* (2014) (unpublished).
- ⁹⁶⁸⁵⁷X. Yang and B. Fei, "3D prostate segmentation of ultrasound images combining longitudinal image registration and machine learning," *Proc. SPIE* **8316**, 83162O (2012).
- ⁹⁶⁹⁵⁸X. Yang, D. Schuster, V. Master, P. Nieh, A. Fenster, and B. Fei, "Automatic 3D segmentation of ultrasound images using atlas registration and statistical texture prior," *Proc. SPIE* **7964**, 796432 (2011).
- ⁹⁷⁰⁵⁹P. Yan, S. Xu, B. Turkbey, and J. Kruecker, "Adaptively learning local shape statistics for prostate segmentation in ultrasound," *IEEE Trans. Biomed. Eng.* **58**, 633–641 (2011).
- ⁹⁷¹⁶⁰Y. Zhan and D. Shen, "Deformable segmentation of 3-D ultrasound prostate images using statistical texture matching method," *IEEE Trans. Med. Imaging* **25**, 256–272 (2006).
- ⁹⁷²⁶¹J. A. Noble and D. Boukerroui, "Ultrasound image segmentation: A survey," *IEEE Trans. Med. Imaging* **25**, 987–1010 (2006).
- ⁹⁷³⁶²D. Shen, Y. Zhan, and C. Davatzikos, "Segmentation of prostate boundaries from ultrasound images using statistical shape model," *IEEE Trans. Med. Imaging* **22**, 539–551 (2003).
- ⁹⁷⁴⁶³Y. Q. Zhan and D. G. Shen, "Automated segmentation of 3D US prostate images using statistical texture-based matching method," in *Medical Image Computing and Computer-Assisted Intervention - Miccai 2003* (■, ■, 2003), Vol. 2878, pp. 688–696.
- ⁹⁷⁵⁶⁴W. Qiu, J. Yuan, E. Ukwatta, Y. Sun, M. Rajchl, and A. Fenster, "Prostate segmentation: An efficient convex optimization approach with axial symmetry using 3-D TRUS and MR images," *IEEE Trans. Med. Imaging* **33**, 947–960 (2014).

Physics Contribution

Automated Segmentation of the Parotid Gland Based on Atlas Registration and Machine Learning: A Longitudinal MRI Study in Head-and-Neck Radiation Therapy

¹⁵ **Xiaofeng Yang, PhD,* Ning Wu, MD,† Guanghui Cheng, MD, PhD,†**
Zhengyang Zhou, MD, PhD,‡ David S. Yu, MD, PhD,§
²⁰ **Jonathan J. Beitler, MD,|| Walter J. Curran, MD,* and Tian Liu, PhD***

**Radiation Oncology and Winship Cancer Institute, Emory University, Atlanta, Georgia; †Radiation Oncology, Jilin University, Changchun, Jilin, China; and ‡Radiology, Nanjing University, Nanjing, Jiangsu, China*

Received Mar 20, 2014, and in revised form Aug 8, 2014. Accepted for publication Aug 28, 2014.

Summary

Parotid gland volume reduction has been associated with decreased saliva production and xerostomia (dry mouth) in head and neck cancer radiation therapy. In this study, an automated parotid segmentation method, based on atlas registration and machine learning, was developed to accurately quantify radiation-induced parotid gland change, using pre- and post-treatment magnetic resonance imaging. This automated segmentation tool will be valuable to carry out

Purpose: To develop an automated magnetic resonance imaging (MRI) parotid segmentation method to monitor radiation-induced parotid gland changes in patients after head and neck radiation therapy (RT).

Methods and Materials: The proposed method combines the atlas registration method, which captures the global variation of anatomy, with a machine learning technology, which captures the local statistical features, to automatically segment the parotid glands from the MRIs. The segmentation method consists of 3 major steps. First, an atlas (pre-RT MRI and manually contoured parotid gland mask) is built for each patient. A hybrid deformable image registration is used to map the pre-RT MRI to the post-RT MRI, and the transformation is applied to the pre-RT parotid volume. Second, the kernel support vector machine (SVM) is trained with the subject-specific atlas pair consisting of multiple features (intensity, gradient, and others) from the aligned pre-RT MRI and the transformed parotid volume. Third, the well-trained kernel SVM is used to differentiate the parotid from surrounding tissues in the post-RT MRIs by statistically matching multiple texture features. A longitudinal study of 15 patients undergoing head and neck RT was conducted: baseline MRI was acquired prior to RT, and the post-RT MRIs were acquired at 3-, 6-, and 12-month follow-up examinations. The resulting segmentations were compared with the physicians' manual contours.

This work was supported by National Institutes of Health, National Cancer Institute grant CA114313 and US Department of Defense grant W81XWH-13-1-0269.

Conflict of interest: none.

Supplementary material for this article can be found at www.redjournal.org.

Reprint requests to: Tian Liu, PhD, Department of Radiation Oncology, Emory University School of Medicine, 1365 Clifton Rd NE, Atlanta, GA 30322, Tel: (404)778-1848; E-mail: tlu34@emory.edu

This work was presented in part at the 55th Annual Meeting and Exhibition of the American Association of Physicists in Medicine, August 2013.

Int J Radiation Oncol Biol Phys, Vol. ■, No. ■, pp. 1–9, 2014
0360-3016/\$ - see front matter © 2014 Elsevier Inc. All rights reserved.
<http://dx.doi.org/10.1016/j.ijrobp.2014.08.350>

125
126 longitudinal or large-scale
127 clinical studies to understand
128 toxicity of the parotid gland
129 and treat radiation-induced
130 xerostomia.
131
132
133
134
135
136
137
138

Results: Successful parotid segmentation was achieved for all 15 patients (42 post-RT MRIs). The average percentage of volume differences between the automated segmentations and those of the physicians' manual contours were 7.98% for the left parotid and 8.12% for the right parotid. The average volume overlap was $91.1\% \pm 1.6\%$ for the left parotid and $90.5\% \pm 2.4\%$ for the right parotid. The parotid gland volume reduction at follow-up was 25% at 3 months, 27% at 6 months, and 16% at 12 months. **Conclusions:** We have validated our automated parotid segmentation algorithm in a longitudinal study. This segmentation method may be useful in future studies to address radiation-induced xerostomia in head and neck radiation therapy.
© 2014 Elsevier Inc.

Introduction

141 Xerostomia (dry mouth) is a common debilitating adverse
142 effect in patients who have received radiation therapy (RT)
143 for head and neck malignancies (1-8). Severe xerostomia is
144 associated with oral discomfort, increased rates of dental
145 caries, oral infection, and difficulty in speaking and swal-
146 lowing (6, 8). Several studies have shown that changes in
147 parotid gland morphology (eg volume reduction) are
148 associated with decreased saliva production and xerostomia
149 (1-8). Nevertheless, longitudinal imaging studies with
150 larger cohorts are needed to better understand this debili-
151 tating side effect, monitor its progression, and evaluate its
152 response to interventions such as partial parotid sparing
153 (available with intensity modulated RT).
154

155 Longitudinal imaging studies of radiation-induced parotid
156 toxicity require an accurate, reliable, and validated imaging
157 method to segment the parotid glands. In the clinic, manual
158 segmentation remains the gold standard for parotid delin-
159 ection with magnetic resonance images (MRI). However, it
160 is impractical to apply the manual segmentation method to
161 longitudinal or large-scale studies due to time constraints. In
162 addition, manual segmentations are also prone to rater drift
163 and bias. A number of CT-based parotid gland segmentation
164 methods have been investigated (9-16), yet few studies have
165 been conducted using MRIs. Therefore, the goal of this
166 study was to develop an automated, reliable, and robust
167 segmentation method to monitor radiation-induced parotid
168 gland changes by using multiple MRIs.
169

170 We proposed combining atlas registration, which cap-
171 tures global variations of anatomy, with machine learning,
172 which captures local statistical features, using kernel sup-
173 port vector machine (SVM), to automatically segment the
174 parotid glands in MR images. This method uses the base-
175 line parotid contours as the atlas and automates the parotid
176 segmentation for post-RT MRIs. Our technology was tested
177 in a longitudinal study of 15 head and neck patients with
178 1-year follow-up examinations.
179

Methods and Materials

180 Our segmentation method consisted of 3 major steps: (1)
181 atlas-based registration; (2) feature SVM training; and (3)
182

183 parotid gland volume segmentation using trained feature
184 SVM.
185

Step 1: Atlas-based registration

186 A hybrid deformable image registration combining a
187 normalized mutual information (NMI) metric with a
188 normalized sum-of-squared-differences (NSSD) metric was
189 used to map the pre-RT MR to the post-RT MRI. The
190 transformation was then applied to the parotid gland binary
191 volume manually contoured from pre-RT MR images
192 (Fig. 1).
193

194 The term "atlas" in the context of this work is defined as
195 the pairing of structural MRI volumes with their corre-
196 sponding segmented parotid gland binary volumes. We
197 built a subject-specific atlas for each patient, which
198 included the patient's baseline (pre-RT) MR images and the
199 manually contoured parotid binary volume. The advantage
200 of using the pre-RT MR as the basis for the SVM approach
201 is that the pre-RT MRI often shows anatomy structure that
202 is clearer than that of post-RT MRI, where radiation dam-
203 age may occur. The MR parotid segmentations at various
204 follow-up times for a specific patient were based on this
205 atlas. Using this patient's post-RT MR scan obtained at
206 follow-up, we aligned the pre-RT MRI to the post-RT MRI,
207 using deformable registration (detailed in the following
208 section) and applied the transformation to the parotid gland
209 binary volume of the pre-RT MRI.
210

211 In order to handle the local intensity contrast induced by
212 RT (17) and inhomogeneity changes associated with
213 various MR scans (18, 19), we applied a hybrid image
214 matching metric (10), which is a combination of NMI and
215 NSSD metrics.
216

$$E(I, J) = \alpha \cdot \text{NSSD}(I, J) - \beta \cdot \text{NMI}(I, J) \\ = \alpha \cdot \frac{1}{N} \sum_x \left\| \frac{I(x) - \mu_{I(x)}}{\sigma_{I(x)}} - \frac{J(x) - \mu_{J(x)}}{\sigma_{J(x)}} \right\| \\ - \beta \cdot \frac{H(I(x)) + H(J(x))}{H(I(x), J(x))} \quad (1)$$

217 where I and J denote the pre-RT and follow-up images;
218 $H(I)$ and $H(J)$ denote the marginal entropies I and J ; and
219 $H(I, J)$ denotes their joint entropy, which is calculated from
220

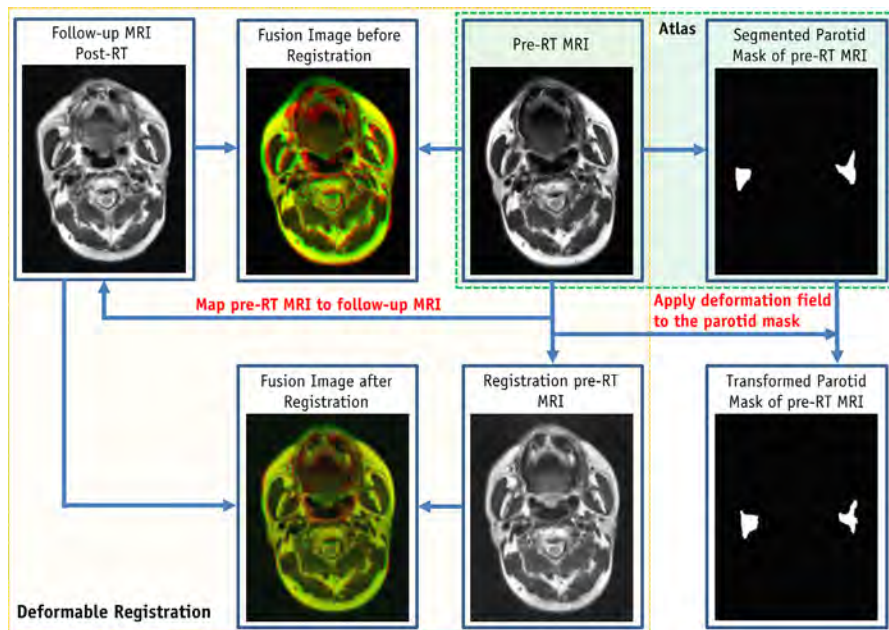
249
250
251
252
253
254
255
256
257
258
259
260
261
262
263
264
265
266
267
268
269
270
271
272
273
274
275
276
277
278
279
280
281
282
283
284
285
286
287
288
289
290
291
292
293
294
295
296
297
298
299
300
301
302
303
304
305
306
307
308
309
310
311
312
313
314
315
316
317
318
319
320
321
322
323
324
325
326
327
328
329
330
331
332
333
334
335
336
337
338
339
340
341
342
343
344
345
346
347
348
349
350
351
352
353
354
355
356
357
358
359
360
361
362
363
364
365
366
367
368
369
370
371
372

Fig. 1. Flow chart of atlas registration (Step 1).

the joint histogram of I and J . α and β are the relative weighting of the two terms $\alpha = \beta = 0.5$. $\mu_I = G_s * I$ denotes the local intensity mean, and $\sigma_I = G_s * (I - \mu_I)^2$ denotes the local intensity variation of image, I . The same denotations are for the target image J, G_s , which denotes a Gaussian filter with the kernel size s (the kernel size s was chosen to be 2-3 times the image voxel size). The hybrid matching metric provides a better image alignment than the NSSD or NMI because they are sensitive only to edges or local image contrast, respectively (10).

After this atlas registration, the registered baseline (pre-RT) MRI had similar global anatomy information as the follow-up MRI. However, the size and intensity of the parotid glands in MRI often change over time after RT (17). In order to capture local changes (intensity contrast variation) of parotid glands and improve the segmentation accuracy, we used this pair with large similarity as the follow-up MRI to train the kernel-based SVM.

Step 2: Support vector machine training

Multiple operators (gradient, enhanced Sobel and Gabor wavelets) were used to extract the local features from registered baseline MRI, and multiple different features were extracted to aid in the kernel-based SVM classification process (Fig. 2). A total of 41 features, some sensitive to the boundary and some sensitive to the microstructures, were made up of the original intensity feature, gradient features, enhanced Sobel features, and Gabor features. Four gradient and Sobel operators were convolved with aligned pre-RT MR images to detect horizontal, vertical, and diagonal edges and strength of edges (20). We also obtained a total of 32 Gabor features on 4 levels and 4 rotations for the original

intensity image. Gabor wavelet was used to capture image features in multiple scales and multiple orientations (21, 22). The mother function of the 2-dimensional Gabor wavelet is.

$$g(x, y) = \frac{1}{2\pi\sigma_x\sigma_y} \exp \left[-\frac{1}{2} \left(\frac{x^2}{\sigma_x^2} + \frac{y^2}{\sigma_y^2} \right) + 2\pi\sqrt{-1}Wx \right] \quad (2)$$

with the corresponding Fourier transformation as.

$$G(u, v) = \exp \left[-\frac{1}{2} \left(\frac{(u - W)^2}{\sigma_u^2} + \frac{v^2}{\sigma_v^2} \right) \right] \quad (3)$$

where $\sigma_u = 1/(2\pi\sigma_x)$ and $\sigma_v = 1/(2\pi\sigma_y)$ and σ_x and σ_y characterize the spatial extent and frequency bandwidth of the Gabor wavelet, and W is a shifting parameter along the u axis in the frequency domain. The Gabor wavelet can be obtained by dilation and rotation of the mother function. Use of the Gabor wavelet offers at least 2 advantages for parotid gland segmentation. First, with the Gaussian factor in the Gabor wavelet, the noise in the MRI (19) can be smoothed or removed. Second, the multiscale and multi-orientation structure of the Gabor wavelet enables the extractions of edge direction as well as edge strength. The Gabor wavelet provides rich edge maps that correspond to a variety of directions, rather than a single "maximum edge intensity" map.

SVM is a popular, supervised machine learning model with associated statistical learning algorithms that analyze data and recognize patterns for classification and regression analysis (23). The idea behind SVMs is to map the original data points from the input space to a high-dimension (hyperplane) feature space such that the classification problem becomes simpler in the hyperplane space. The training phase of SVMs looks for a linear, optimal separating

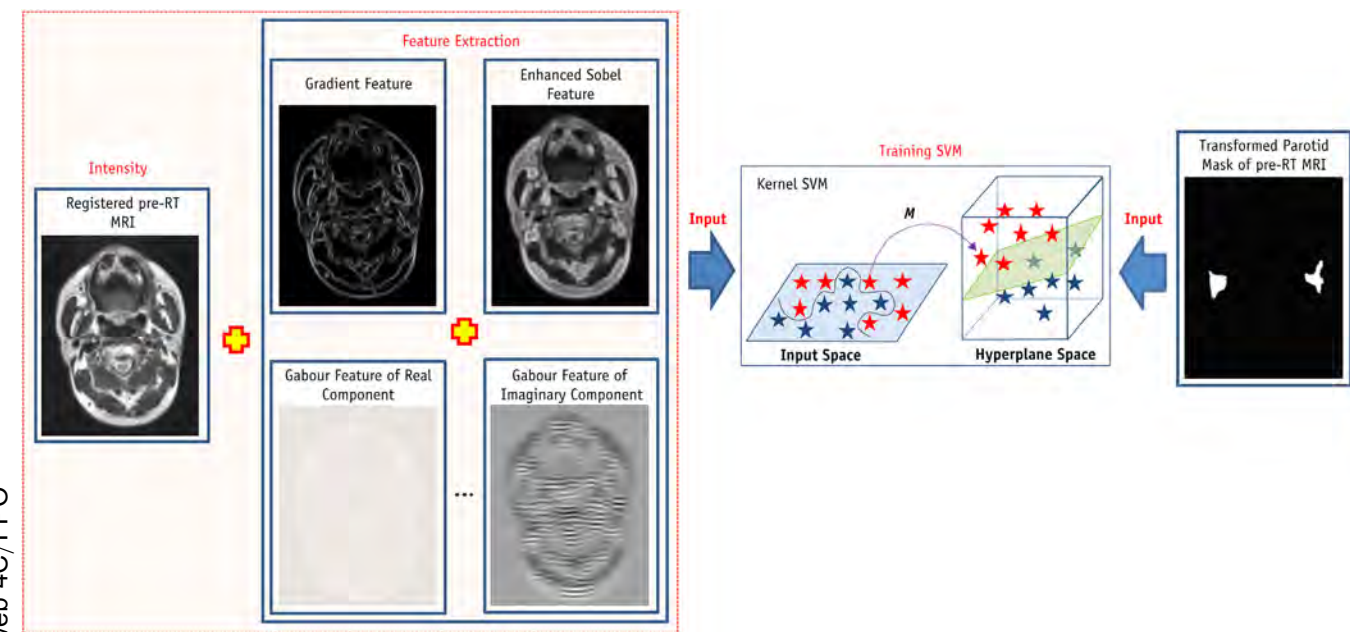


Fig. 2. Flow chart of SVM training (Step 2). SVM = support vector machine.

hyperplane as the maximum margin classifier with respect to the training data (24). Because the training data are not linearly separable, kernel-based SVM methods are used to classify these features. Kernel-based SVM methods map data from an original input feature space to a kernel feature space of higher dimensionality and then solve a linear problem in that space. In this study, kernel-based SVM was used to identify the features of parotid gland tissue. Although these features may vary greatly among various follow-up MR scans, the kernel-based SVM nonlinearly classifies subjects by extracting different features. The method defines a hyperplane to classify the subjects by minimizing the following function.

$$\frac{1}{2} (w^T w + b^2) - C \sum_{i=1}^N \xi_i \quad (4)$$

subject to.

$$y_i(w^T k(x_i) + b) \geq 1 - \xi_i, \quad \xi_i \geq 0 \text{ and } i \in N \quad (5)$$

where C is a penalty parameter and ξ_i is a slack variable to measure the deviation of training samples. w is the vector of coefficients, and b is a constant offset. To find the optimal input parameter values, the grid search method is used. The index i labels the N training cases. $y_i \in \pm 1$ is the class label, and x_i is the independent variable. The kernel k is used to transform data from the input to the feature space. There are a number of kernels that can be used in SVM models. In our implementation, radial basis function (RBF) was used as follows

$$k(x_i, x_j) = \exp(-\gamma \|x_i - x_j\|^2), \quad \gamma = 1/(2\sigma^2) \quad (6)$$

We used the registered pre-RT MRI with multiple features (gradient, Sobel, and Gabor features), as well as the transformed parotid binary volume, to train the RBF kernel-based SVM.

Step 3: Volume segmentation

In order to segment the parotid glands, we performed the same feature extraction process for the follow-up MRIs (Fig. 3). The follow-up MR images and their multiple features (gradient, Sobel, and Gabor features) were the input of trained kernel-based SVM, and the trained SVM adaptively labeled the parotid tissue based on its texture and location. The output of trained SVM is a binary image (volume) consisting of many “0” (nonparotid tissues) and “1” (parotid tissue) points. The 3D parotid segmentation was obtained from the classification-based binary volume using the following steps: (1) the pre-RT segmented parotid volume plus 10-mm margin was defined as the volume of interest (VOI); (2) the VOI was applied to the binary volume to set the volume outside the VOI to 0; (3) a 3D filter was applied to smooth the binary volume; (4) a 0.5 threshold was applied to the filtered volume; and (5) 3D morphology operation was used to eliminate the holes or disconnections in the parotid glands.

Reliability evaluation of the segmentation algorithm

The automatic parotid segmentation results were compared with the gold standards of physicians' manual contours. A common evaluation measure for a segmentation method is the Dice overlap ratio. The Dice overlap ratio is defined as follows.

$$\text{Dice} \left(\text{Vol}_1, \text{Vol}_2 \right) = \frac{2|\text{Vol}_1 \cap \text{Vol}_2|}{|\text{Vol}_1| + |\text{Vol}_2|} \quad (7)$$

where Vol_1 represents the voxels of the parotid gland segmented by the automated algorithm, and Vol_2 represent the voxels of the corresponding manual segmentation of the experts.

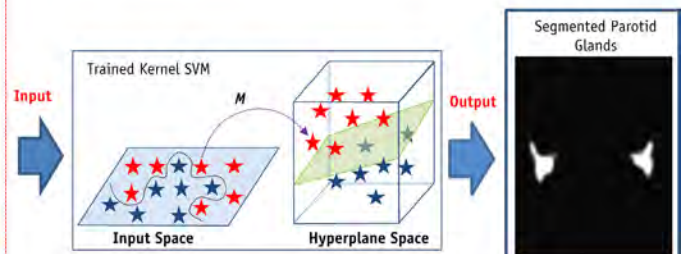
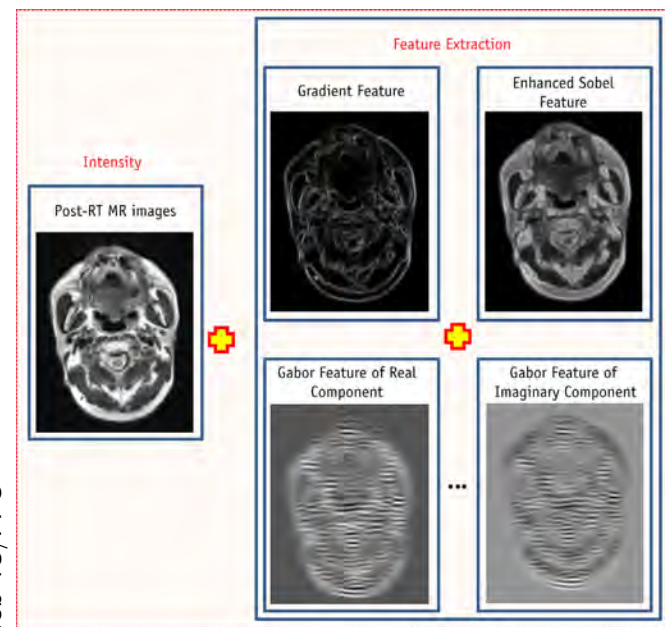


Fig. 3. Flow chart of parotid volume segmentation (Step 3).

Results

Subjects

We conducted a longitudinal study of 15 patients receiving radiation therapy for head and neck malignancies, such as laryngeal and oropharyngeal cancers. This MR imaging study was approved by the Ethics Committee of our university. The 15 patients (10 men and 5 women) ranged in age from 40 to 65 years old (mean, 49.5 ± 6.6 years old). The median radiation dose to the left parotid gland was 50.3 Gy (43.1-61.1 Gy) and 51.9 Gy (38.5-63.2 Gy) to the right parotid gland. All patients received a baseline MR scan prior to RT and an additional 3 MR scans post-RT at 3- and 6-month and 1-year follow-up examinations. Among the 15 patients, 2 patients missed the 6-month follow-up scan, and 1 patient missed the 1-year follow-up scan. A total of 57 MR scans were included in this study.

MRI scan

All MRI examinations were performed with a dedicated head and neck coil, with a Signa model HDxt 1.5-T machine (GE Healthcare). T1-and T2-weighted MR sequences were obtained after intravenous injection of contrast material (gadopentetate dimeglumine). The parameters for the T2-weighted sequence were TR/TE/ETL = 3000 ~ 4000/90 ~ 120/8 ~ 16 ms, 3.0-mm slice thickness, 256 × 256 matrix, maximum voxel resolution of $0.8 \times 0.8 \times 3.0$ mm³.

Interobserver reliability study

The interobserver reliability study showed consistency in physicians' manual baseline contours, which were used as

the ground truth, as well as in the automatic parotid segmentations, using the 2 different sets of baseline contours.

Parotid gland segmentation: a case report

Figure 4 shows the case of a 41-year-old patient who received intensity modulated RT for laryngeal cancer. The mean dose to the right parotid was 55.26 Gy, and the mean dose to the left parotid was 53.05 Gy. Prior to RT, the baseline volume of the right parotid was 28.14 cc and 26.98 cc of the left parotid. Post-RT, the right parotid gland volumes obtained from the automatic segmentation compared to those from manual segmentation (Dice volume overlap) were 21.55 versus 22.82 cc (89.9%), respectively, at 3-month follow-up; 20.86 versus 22.26 cc (91.3%), respectively, at 6-month follow-up; and 23.35 versus 25.29 cc (89.6%), respectively, at 1-year follow-up. Similarly, the left parotid gland volumes obtained from the automatic compared to those of the manual segmentations were 19.90 versus 21.14 cc (91.8%), respectively, at 3 months; 19.71 versus 18.93 cc (90.4%), respectively, at 6 months; and 22.96 versus 24.77 cc (90.1%), respectively, at 1-year follow-up. Differences between automatically segmented parotid gland volumes and the physicians' manual contours ranged between -8.3% and 7.7% at the 3 follow-up time points.

Parotid gland segmentation: first follow-up study for all patients

Fifteen pre-RT MR image volumes corresponding to 15 patients were first manually contoured by an experienced radiation oncologist (NW) to obtain respective left and right parotid gland binary volumes (masks). We built 15 atlases (pre-RT T2-weighted MRI volume plus

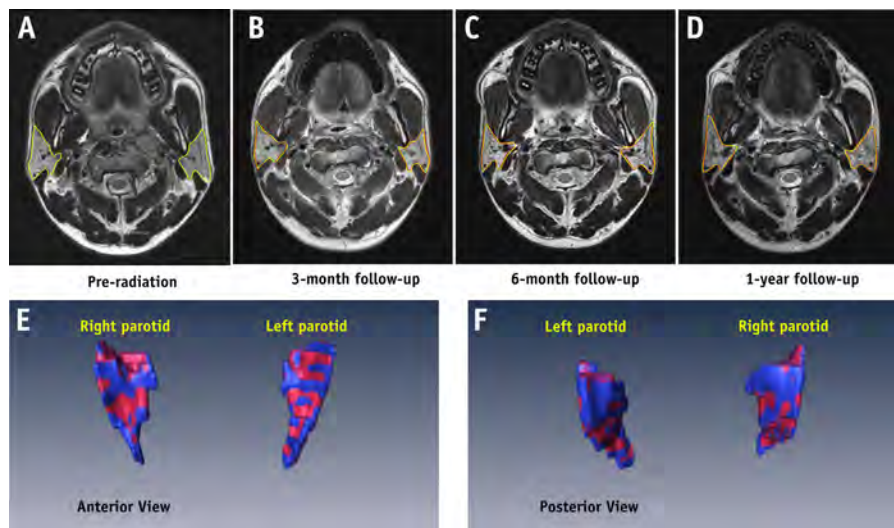


Fig. 4. An example of parotid gland volume reduction post-RT. (Top row) MR images of the pre-RT parotid glands (a) and at 3-month (b), 6-month (c), and 1-year (d) follow-up examinations. The automatic segmentation is shown in red, and the manual contour is shown in yellow. (Bottom row) 3D visualization and comparison between automatic (red) and manual (blue) parotid gland segmentation 3 months post-RT. A color version of the figure is available at www.redjournal.org.

corresponding parotid gland binary volume comprised an atlas for each patient) for 15 patients in our longitudinal study.

We compared the automatic parotid gland segmentations with the physicians' manual contours for the 42 follow-up MRIs. Figure 5 shows the Dice volume overlap, maximum, and mean surface distance comparisons of the first follow-up time point for the 15 patients. The averaged volumes obtained from the automatic segmentations compared to the manual contours were 20.56 ± 7.63 versus 22.23 ± 8.39 cc, respectively, for the left parotid glands; and 21.31 ± 6.16 versus 23.01 ± 7.87 cc, respectively, for the right ones. The averaged Dice volume overlap was $91.1 \pm 1.6\%$ (left) and $90.5 \pm 2.4\%$ (right); the averaged absolute volume difference was 7.98% (left) and 8.12% (right); the averaged maximum surface distance was 3.46 ± 1.22 (left) and 3.79 ± 1.47 mm (right); and the averaged surface distance was 0.29 ± 0.11 mm (left) and 0.32 ± 0.17 mm (right).

Parotid gland segmentation: all follow-up studies for all patients

For the longitudinal study, the pre-RT parotid gland volume was used as the reference with which to observe the parotid gland volume reduction in all patients at various follow-up times. Figure 6 shows a comparison of the average percentage of volume reduction in the 15 patients, obtained by automatic and manual segmentations. For the manual and automatic segmentations, the percentage of parotid volume reduction was $24.9\% \pm 8.2\%$ and $26.1\% \pm 8.4\%$, respectively, at 3 months post-RT ($P=.42$); $27.4\% \pm 7.9\%$ and $27.9\% \pm 9.3\%$, respectively, at 6 months post-RT ($P=.83$); and $16.1\% \pm 15.6\%$ and $17.3\% \pm 15.2\%$, respectively, at 1 year post-RT ($P=.55$). There were no significant

differences ($P=.37$) between parotid gland volume reductions at 3 and 6 months post-RT, whereas there were significant difference in volume reductions between the 3-month and 1-year follow-up examinations ($P=.019$) and the 6-month and 1-year follow-up examinations ($P=.014$).

Discussion

We proposed an automatic MR parotid gland segmentation algorithm with which to study RT-induced parotid volume changes in head and neck cancer RT. In this algorithm, an atlas registration combined the NMI with the NSSD and was used to register the pre-RT MRI to the post-RT MRI, and multiple features were extracted from the registered pre-RT MRI to train the kernel SVM. The trained kernel SVM was subsequently used to perform the segmentation for the post-RT MRI. In this automatic segmentation, the atlas registration was used to capture the radiation-induced global anatomical variation of the parotid glands, whereas the trained SVM with multiple features was used to capture the local statistical structural variation. Automatic segmentation results were compared with physicians' manual contours (gold standard). The average Dice volume overlaps between our segmentations and the manual contours of bilateral parotid glands were more than 90%. Compared to the pre-RT parotid gland volume, the percentage of parotid volume reduction was 25% at 3 months post-RT, 27% at 6 months post-RT, and 16% at 1 year post-RT.

Parotid gland volume reduction was observed in all 15 patients after RT, which is consistent with previous studies (6-8, 17, 25, 26). Wu et al (8) demonstrated that the post-RT parotid glands had an average of 35% volume reduction compared with normal glands. Vasquez et al (25)

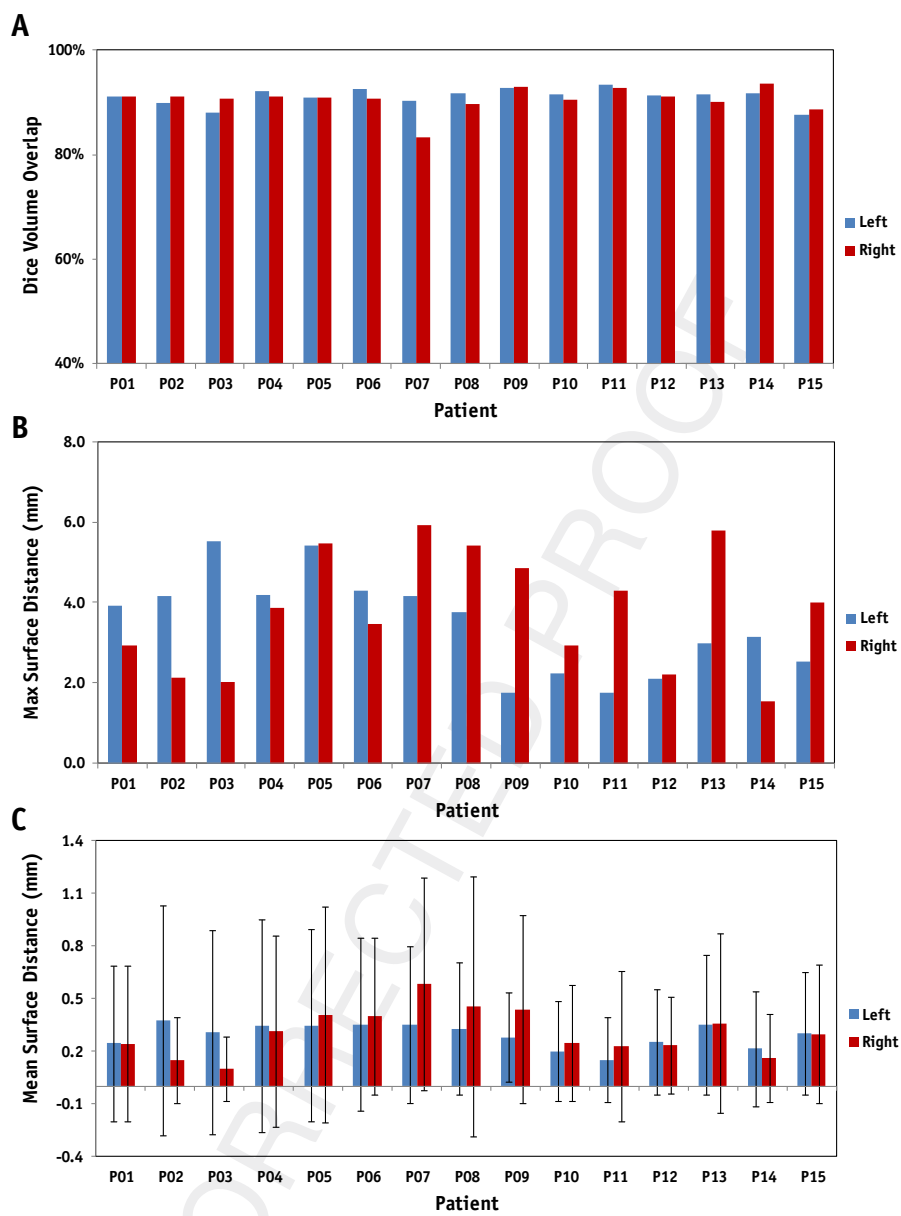


Fig. 5. Dice volume overlap (a), maximum (b) and mean surface distance (c) comparisons of left and right parotid glands for 15 patients at the first follow-up time between the automatic and manual segmentation.

observed that the average parotid volume reduction was 14% to 17% at the end of the treatment. In a clinical study of 82 patients, Wang et al (6) indicated the average parotid gland volume loss was 20.1% after 3 weeks of RT; 26.93% upon completing RT; and 27.21% at 2 months post-RT.

Histologically, normal parotid glands consist entirely of serous cells with densely packed translucent secretory granules (3, 27). Radiation doses of more than 26 Gy can cause a significant loss of serous acini and reduce the volume of parotid glands (6) during the treatment and at the early follow-up examinations after RT. The percentage of parotid gland volume reduction produced big difference among those studies, which may be caused by (1) different mean doses to parotid glands correlated with parotid damage; and (2) different follow-up times. In the current

study, no significant differences in gland volumes were observed between the 3- and 6-month follow-up examinations, which is consistent with reports by Wang et al (6) and Nomayr et al (17). The parotid volume increase between 6-month and 1-year follow-up examinations may indicate the parotid recovery after radiation therapy (27).

Due to the complexity of head and neck MRI, most MR-based segmentation methods rely on single or multiple atlases. Single - or multiple-atlas-based segmentation methods include 2 key steps: (1) how to register single or multiple atlases to the images that need to be segmented; and (2) how to refine a segmented boundary or surface for the single-atlas-based method and how to combine or select the multiple aligned atlases for the multi-atlas-based method. Therefore, a good atlas-based segmentation

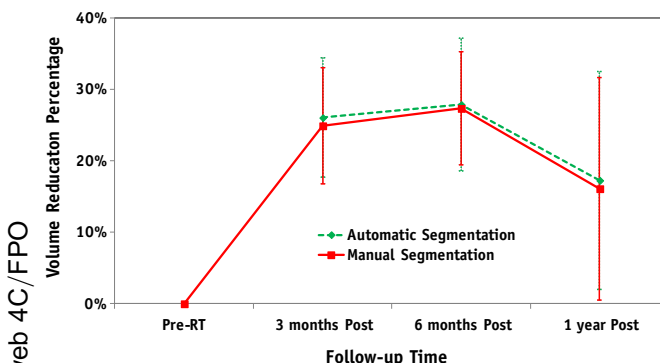


Fig. 6. Comparison of average percentages of volume reduction in 15 patients between the automatic and manual segmentation at different follow-up times.

system requires not only a robust registration algorithm but also an effective scheme to select the optimal atlas templates that are close to the segmenting image. In our single-atlas-based method, a hybrid deformable registration algorithm based on the NMI and NSSD was used to register the atlas (pre-RT MRI) to the post-RT MR image. This algorithm could capture the variations of anatomy and cope well with the local image contrast changes associated with radiation-induced tissue damage. A kernel SVM was used to combine multiple features extracted from an aligned subject-specific atlas. Our kernel SVM mapped the feature data from the aligned atlas space to the kernel feature space of higher dimensionality and then solved a linear problem separating the parotid and nonparotid tissues. Multiple features from subject-specific atlas pairs were used to train the kernel SVM, and the well-trained SVM based on RBF kernel could then robustly differentiate the parotid tissue from the surrounding tissues by statistically matching multiple texture features.

Future areas of study include speeding up the SVM training and segmentation by testing the sensitivity of multiple features and decreasing the number of feature numbers. Meanwhile, we are conducting a clinical longitudinal study with a larger cohort to further investigate the relationship between parotid volume changes and parotid gland function and validate if volume changes could predict xerostomia.

Conclusions

Studies have shown that volume changes of the parotid glands are correlated with the severity of radiation damage and may serve as a predictor for xerostomia. To better monitor radiation-induced volume change of the parotid gland and fully understand xerostomia in head and neck cancer radiation therapy, we developed a novel automatic MR parotid gland segmentation algorithm based on atlas registration and machine learning. We also demonstrated the feasibility and accuracy of our automatic segmentation algorithm in a clinical study. This segmentation method

may be useful as we try to address xerostomia in patients after radiation therapy for head and neck malignancies.

References

1. Chao KS, Deasy JO, Markman J, et al. A prospective study of salivary function sparing in patients with head-and-neck cancers receiving intensity-modulated or three-dimensional radiation therapy: Initial results. *Int J Radiat Oncol Biol Phys* 2001;49:907-916.
2. Eisbruch A, Kim HM, Terrell JE, et al. Xerostomia and its predictors following parotid-sparing irradiation of head-and-neck cancer. *Int J Radiat Oncol Biol Phys* 2001;50:695-704.
3. Eisbruch A, Rhodus N, Rosenthal D, et al. How should we measure and report radiotherapy-induced xerostomia? *Semin Radiat Oncol* 2003;13:226-234.
4. Braam PM, Roesink JM, Raaijmakers CP, et al. Quality of life and salivary output in patients with head-and-neck cancer five years after radiotherapy. *Radiat Oncol* 2007;2:3.
5. Ying M, Wu VWC, Kwong DLW. Comparison of sonographic appearance of normal and postradiotherapy parotid glands: a preliminary study. *Ultrasound Med Biol* 2007;33:1244-1250.
6. Wang ZH, Yan C, Zhang ZY, et al. Radiation-induced volume changes in parotid and submandibular glands in patients with head and neck cancer receiving postoperative radiotherapy: A longitudinal study. *Laryngoscope* 2009;119:1966-1974.
7. Teshima K, Murakami R, Tomita E, et al. Radiation-induced parotid gland changes in oral cancer patients: correlation between parotid volume and saliva production. *Jpn J Clin Oncol* 2010;40:42-46.
8. Wu VW, Ying MT, Kwong DL. Evaluation of radiation-induced changes to parotid glands following conventional radiotherapy in patients with nasopharyngeal carcinoma. *Br J Radiol* 2011;84:843-849.
9. Han X, Hoogeman MS, Levendag PC, et al. Atlas-based auto-segmentation of head and neck CT images. *Med Image Comput Comput Assist Interv* 2008;2008(5242):434-441.
10. Han X, Hibbard L, O'Connell N, Willcut V. Automatic segmentation of parotids in head and neck CT images using multi-atlas fusion. *MICCAI 2010 Grand Challenges in Medical Image Analysis: Head & Neck Autosegmentation Challenge*. Beijing; 2010.
11. Daisne JF, Blumhofer A. Atlas-based automatic segmentation of head and neck organs at risk and nodal target volumes: a clinical validation. *Radiat Oncol* 2013;8:154.
12. Gorthi S, Cuadra M, Schick U, et al. Multi-atlas based segmentation of head and neck CT images using active contour framework. *MICCAI 2010 grand challenges in medical image analysis: head & neck autosegmentation challenge*. Beijing; 2010.
13. Qazi AA, Pekar V, Kim J, et al. Auto-segmentation of normal and target structures in head and neck CT images: A feature-driven model-based approach. *Med Phys* 2011;38:6160-6170.
14. Hollensen C, Hansen MF, Hojgaard L, et al. Segmenting the parotid gland using registration and level set methods. *MICCAI: Grand challenges in medical image analysis: head & neck autosegmentation challenge* Beijing; 2010.
15. Yang J, Zhang Y, Zhang L, et al. Automatic segmentation of parotids from CT scans using multiple atlases. *MICCAI workshop proceedings: medical image analysis for the clinic—A grand challenge* Beijing; 2010. pp. 323-330.
16. Pekar V, Allaire S, Qazi A, et al. Head and neck auto-segmentation challenge: segmentation of the parotid glands. *MICCAI 2010 grand challenges in medical image analysis: Head & neck autosegmentation challenge*. Beijing; 2010.
17. Nomayr A, Lell M, Sweeney R, et al. MRI appearance of radiation-induced changes of normal cervical tissues. *Eur Radiol* 2001;11: 1807-1817.
18. XXX.
19. XXX.
20. Lindeberg T. Edge detection and ridge detection with automatic scale selection. *Int J Comput Vis* 1998;30:117-154.

931
932
933
934
935
936
937
938
939
940
941
942
943
944
945
946
947
948
949
950
951
952
953
954
955
956
957
958
959
960
961
962
963
964
965
966
967
968
969
970
971
972
973
974
975
976
977
978
979
980
981
982
983
984
985
986
987
988
989
990
991
992

1003
1004
1005
1006
1007
1008
1009
1010
1011
1012

- 993 21. Manjunath BS, Ma WY. Texture features for browsing and retrieval of
994 image data. *IEEE Trans Pattern Anal Mach Intell* 1996;18:837-842.
- 995 22. Han J, Ma KK. Rotation-invariant and scale-invariant Gabor features
996 for texture image retrieval. *Image Vis Comput* 2007;25:1474-1481.
- 997 23. Meyer D, Leisch F, Hornik K. The support vector machine under test.
998 *Neurocomputing* 2003;55:169-186.
- 999 24. Boser BE, Guyon IM, Vapnik VN. A Training algorithm for optimal
1000 margin classifiers. Proceedings of the 5th Annual ACM Workshop
1001 on Computational Learning Theory. City, State. ACM Press; 1992:
1002 144-152. Q14
25. Vasquez Osorio EM, Hoogeman MS, Al-Mamgani A, et al. Local
anatomic changes in parotid and submandibular glands during radio-
therapy for oropharynx cancer and correlation with dose, studied in
detail with nonrigid registration. *Int J Radiat Oncol Biol Phys* 2008;
70:875-882.
26. Roesink JM, Moerland MA, Battermann JJ, et al. Quantitative dose-
volume response analysis of changes in parotid gland function after
radiotherapy in the head-and-neck region. *Int J Radiat Oncol Biol
Phys* 2001;51:938-946.
27. XXX₁

Influence of Vascular Comorbidities and Race on Erectile Dysfunction after Prostate Cancer Radiotherapy

Yuefeng Wang, PhD,* Tian Liu, PhD,*† Peter J. Rossi, MD,*† Deborah Watkins-Bruner, PhD,*‡ Wayland Hsiao, MD,† Sherrie Cooper, BA,* Xiaofeng Yang, PhD,* and Ashesh B. Jani, MD, MSEE*‡

*Department of Radiation Oncology, Emory University, Atlanta, GA, USA; †Department of Urology, Emory University, Atlanta, GA, USA; ‡Winship Cancer Institute, Emory University, Atlanta, GA, USA

DOI: 10.1111/jsm.12215

ABSTRACT

Introduction. Vascular comorbidities (VC) (hypertension, diabetes, and hyperlipidemia) are known factors related to erectile dysfunction (ED) in men. However, no data are yet available for the effects of VC on ED incidence after prostate cancer radiotherapy (XRT).

Aim. To investigate the influence of VC on post-XRT ED incidence and to further characterize ED incidence by racial groups.

Main Outcome Measures. ED incidence.

Methods. We reviewed 732 charts of patients (267 Caucasian and 465 African American [AA]) who received prostate XRT (external beam radiotherapy and/or brachytherapy) with or without hormone therapy between 1999 and 2010. The number of pre-XRT VC (0, 1, 2, or 3) was determined by medical history and medication list. ED (defined by use of erectile aids or by documentation of moderate or high sexual dysfunction on patient history) was determined pre-XRT as well as 1, 2, and 4 years post-XRT.

Results. ED incidence progressively increased from 22% pre-XRT to 58% 4 years post-XRT ($P < 0.01$). Additionally, ED incidence significantly increased with number of VC—4-year incidence between patients with 1 vs. 0 ($P = 0.02$), 2 vs. 0 ($P < 0.01$), 3 vs. 0 ($P < 0.01$), 3 vs. 1 ($P < 0.01$), and 3 vs. 2 ($P = 0.04$). VC (2 vs. 1 VC was nonsignificant). Compared with the Caucasian patients, ED incidences were slightly higher for the AA group with 0, 1, 2, and 3 comorbidities at 4 years follow-up (but statistically nonsignificant).

Conclusions. The number of VCs have a significant effect on development of post-XRT ED. Pre- and post-XRT ED appear to be independent of race when number of VCs are considered. Our results can be used to guide physicians in counseling patients on the incidence of ED by number of VC and as preliminary data for prospective efforts aimed at reducing post-XRT ED. **Wang Y, Liu T, Rossi PJ, Watkins-Bruner D, Hsiao W, Cooper S, Yang X, and Jani AB. Influence of vascular comorbidities and race on erectile dysfunction after prostate cancer radiotherapy. J Sex Med 2013;10:2108–2114.**

Key Words. Prostate Cancer; Radiotherapy; Erectile Dysfunction; Vascular Comorbidity; Race

Introduction

With advances in diagnosis and treatment, over 2.35 million American men have currently survived prostate cancer [1]. As such, reduction of treatment-related side effects is increasingly important. Erectile dysfunction (ED) is a common complication of prostate cancer

radiotherapy (XRT) [2,3]. Depending on the population studied, up to 50% of men receiving radiotherapy for prostate cancer will suffer post-XRT ED [4]. Clearly, radiation-induced ED is a clinical problem of enormous magnitude.

The causes of radiation-induced ED are not fully understood, with several different proposed factors and mechanisms, including neurogenic, vascular, and psychogenic [5]. It has been proposed that dose-related vascular damage to the neurovascular bundles may be a critical causative factor [3].

Presented at the ASCO/ASTRO/SUO Genitourinary Cancers Symposium, San Francisco, CA, February 2012.

Several studies have been conducted to understand the radiation dose to penile structures (body and bulb) and radiation-induced ED [6,7].

Hypertension (HTN), diabetes (DM), and hyperlipidemia (HL) are the three most common vascular comorbidities (VC) associated with ED in the general population, most likely due to the common mechanism of vasculogenic damage [8]. However, the influence of these VC on post-XRT ED is poorly understood. The prevalence of HTN and DM is higher in African Americans (AAs) than Caucasians, and this has been found to translate to an overall higher age-matched prevalence of ED in AA men [9]; the higher prevalence of VC has in some cases served as an obstacle to enrollment of AA men on quality of life trials.

While vascular disease is clearly related to ED, little is known about the effect of XRT on ED, and no published reports to date exist on the effect of vascular disease on post-XRT ED. Therefore, we undertook this study to understand the impact of VC on post-XRT ED and to further characterize pre- and post-XRT ED by race.

Materials and Methods

After obtaining institutional review board approval, the charts of consecutive prostate cancer patients treated with radiation therapy at two affiliated hospitals in our department between 1999 and 2010 were reviewed. Patients with stage IV disease, patients who had radical prostatectomy, and patients with follow-up data less than 1 year were excluded. The remaining 732 patients (267 Caucasians and 465 AAs) comprise the study population. Our standard clinical practice is to have providers evaluate ED at each visit with questions from the provider. Patients were asked if they were having problems with obtaining erections adequate enough for sexual activity and were charted on a three-tiered system for having (i) no or minimal sexual dysfunction, (ii) moderate sexual dysfunction, or (iii) severe sexual dysfunction. Patients reporting moderate or severe problems with erectile function were referred for urologic evaluation and treatment of ED.

The medical records were used to abstract demographic, disease, and treatment information. Patient's VC (HTN, DM, and HL) status was determined by medications and past medical history recorded in patient chart during patients' initial consultation visit. Sexual function status

was also determined by medical record review. For our study, ED was defined as a dichotomous event occurring if (i) moderate or severe sexual dysfunction was documented in patient chart on physician-obtained history or (ii) if patients were using or prescribed any erectile aids that included phosphodiesterase type 5 inhibitors, transurethral prostaglandin, intracavernosal injection therapy, or vacuum erection device [10]. Of note, patients who reported diminished erections but were still firm enough for sexual activity were considered as potent. Sexual function status was determined at four specific time points: pre-XRT, and 1 year, 2 years, and 4 years post-XRT. The median follow-up for all patients is 33.6 months. Intention-to-treat analysis was applied; for those patients lost to follow-up, their sexual function status was determined at the last appointment.

External beam radiotherapy (EBRT) was performed using three-dimensional conformal or intensity-modulated technique. If EBRT was given alone (i.e., without brachytherapy [BT]), the total dose to the prostate was 67.0 to 81.0 Gy delivered in 1.8 to 2.0 Gy fractions. Planning target volume (PTV) included the prostate, seminal vesicles, and in some cases pelvic lymph nodes to define PTV1; PTV2 consisted of prostate alone. BT was a component of XRT for 190 patients. When BT was combined with EBRT, and dose of EBRT was 45.0 Gy delivered in 25 fractions to the prostate plus seminal vesicles; EBRT PTV margins in all cases were typically 0.8–1.0 cm circumferentially with a smaller margin (0.6–0.8 cm) posteriorly. The BT dose was 100–109 Gy when combined with EBRT and 125–145 Gy when given alone.

Statistical analyses were performed using SAS (version 9.3, SAS Institute Inc., Cary, NC, USA) and Minitab (version 16, Minitab Inc., State College, PA, USA). The age difference between Caucasians and AAs was tested using the Student's *t*-test. The chi-square independence test was applied to determine the difference in demographic, disease, and treatment factors based on race. In order to determine the impact of comorbidity on radiation-induced ED, the two sample proportion test was performed to assess the significance of ED differences between patients with different number of VC. A logistic regression model was used to analyze the effect of race on radiation-induced ED by number of VC. All *P* values reported are two-tailed, with *P* < 0.05 considered statistically significant.

Table 1 Patient characteristics

	Caucasian (total: 267)	AA (total: 465)	P value (t-test or chi-square)
Comorbidity			
HTN*	190 (71%)	372 (80%)	<0.01
DM*	37 (14%)	112 (24%)	<0.01
HL*	177 (44%)	167 (36%)	<0.01
Years (mean)	68.6 ± 8.05	63.4 ± 8.10	<0.01
Stage			
I	147 (55%)	324 (69%)	<0.01
II	102 (38%)	107 (23%)	
III	15 (6%)	31 (7%)	
Unknown	3 (1%)	3 (1%)	
PSA (ng/ml)			
<10	191 (74%)	256 (55%)	<0.01
≥10	76 (26%)	209 (45%)	
Gleason score			
Average	7.0 ± 0.88	7.0 ± 0.87	0.91
4–6	80 (30%)	147 (32%)	
7	130 (49%)	228 (49%)	
8–10	52 (21%)	88 (19%)	
Unknown	1 (<1%)	2 (<1%)	
Radiation treatment			
EBRT alone	192 (72%)	350 (75%)	0.10
BT ± EBRT	79 (28%)	116 (25%)	
Hormone therapy			
LHRH alone	78 (29%)	141 (30%)	0.35
LHRH/Antiandrogen	40 (15%)	100 (22%)	
Antiandrogen alone	3 (1%)	2 (<1%)	
None	146 (55%)	222 (48%)	

*Patient may or may not have other comorbidities.

Results

Mean follow-up for the entire cohort was 33.6 months (Caucasian: 38.4 months, AA: 30.0 months). The clinical characteristics of the study population are shown in Table 1. As shown, AA and Caucasian patients were generally balanced with respect to Gleason score, radiation treatment, and use of hormone therapy. However, the AA patients were on average approximately 5 years younger, had a higher pretreatment prostate-specific antigen (PSA), had a lower T-stage, and had higher incidence of HTN (80% vs. 71%, $P < 0.01$) and DM (24% vs. 14%, $P < 0.01$) than Caucasian patients. However, the HL incidence for AA patients was lower than for Caucasian patients (36% vs. 44%, $P < 0.01$). Notably, the HTN, DM, and HL incidence differences between two racial groups identified in our study was consistent with reported results in general population [11].

In order to investigate the impact of VC on ED incidence post radiotherapy, we identified each patient's HTN, DM, and HL status prior to radiation and stratified them into four subgroups based on the number of VC (0, 1, 2, and 3). Table 2 displays the number/percentage of patients by

number of VC across race groups. Overall there was a similar incidence of patients having 0, 1, or 2 VC, with the AA group having a higher percentage of patients with 3 VC.

Table 3a displays the incidence of ED as a function of number of VC and time. As shown, after radiotherapy, ED incidence increased in two manners: First, compared with the baseline levels (pre-XRT), ED incidence progressively increased from 1 year to 4 years post-XRT when patients had the same number of VC. Second, post-XRT

Table 2 Prevalence of vascular comorbidities for Caucasian and AA prostate cancer patients

	Caucasian (total: 267)	AA (total: 465)	P value*
Patients without comorbidity			
None	50 (19%)	67 (14%)	0.16
Patients with one comorbidity			
HTN	82 (31%)	179 (39%)	0.03
DM	2 (1%)	7 (2%)	0.33
HL	25 (10%)	15 (3%)	<0.01
Total	109 (41%)	201 (43%)	0.53
Patients with two comorbidities			
HTN and DM	16 (6%)	45 (10%)	0.06
HTN and HL	73 (27%)	92 (20%)	0.02
DM and HL	1 (<1%)	5 (1%)	N/A
Total	90 (34%)	142 (31%)	0.38
Patients with three comorbidities			
HTN, DM, and HL	18 (7%)	55 (12%)	0.02

*Obtained using t-test.

Table 3 Erectile dysfunction incidences by vascular comorbidities (VC)

a. ED incidence for whole group by VC and time point				
Number of VCs	Pre-XRT ED (%)	Post-XRT ED (%)		
		1 year	2 years	4 years
0	15	39	41	44
1	19	48	55	56
2	26	55	59	63
3	35	71	73	75
Overall	22	52	56	58

b. Pairwise comparisons of increase in ED incidence by number of VC				
VC	Pre-XRT		4 years post-XRT	
	Increase in ED incidence (%)	P value*	Increase in ED incidence (%)	P value*
1 vs. 0	4	0.41	12	0.02
2 vs. 1	7	0.08	7	0.12
3 vs. 2	9	0.09	12	0.04
2 vs. 0	11	0.03	19	<0.01
3 vs. 1	16	<0.01	19	<0.01
3 vs. 0	20	<0.01	31	<0.01

*Obtained using t-test.

Table 4 Erectile dysfunction incidence by race

a. Overall pre- and post-XRT ED incidences for Caucasian and AA patients

	Caucasian (%)	AA (%)	P value*
Pre-XRT ED	20	23	0.31
Post-XRT ED			
1 year	48	54	0.12
2 years	52	58	0.12
4 years	55	60	0.21

b. Logistic regression analyses of ED differences by time point, number of VC, and race

Number of VCs	Pre-XRT ED		1 year		2 years		4 years	
	Caucasian	AA	Caucasian	AA	Caucasian	AA	Caucasian	AA
0	14%	16%	38%	40%	38%	43%	40%	46%
1	18%	19%	46%	49%	52%	56%	55%	57%
2	22%	28%	52%	57%	56%	61%	60%	64%
3	33%	36%	67%	73%	67%	75%	71%	76%
P value [†]	0.37		0.53		0.30		0.25	

*Obtained using *t*-test.

†Obtained using chi-square test.

ED incidence increased with increasing number of comorbidities. Table 3b shows the results of pairwise comparisons of ED incidence by number of VC—these pairwise comparisons were done at two time points (pre-XRT and 4 years post-XRT). At 4 years post-XRT, the increases in ED incidence for all pairwise comparisons were statistically significant except the 2 vs. 1 comparison.

The analysis of ED incidence by race is shown in Table 4—Table 4a shows the comparisons by race at the 4 time points—pre-XRT and 1, 2, and 4 years post-XRT. As shown, although there was a

slightly higher ED incidence in AA men at all time points (due perhaps to the slightly higher VC incidence in AA men), these differences in ED rates did not reach statistical significance. Table 4b displays the results of the logistic regression analysis of ED incidence at each of the 4 time points by number of VC. None of these regression analyses at any time point demonstrated significant differences by race.

Figure 1 comprehensively displays the general results shown in Tables 3 and 4 visually. As shown, ED incidence steadily rises with time interval

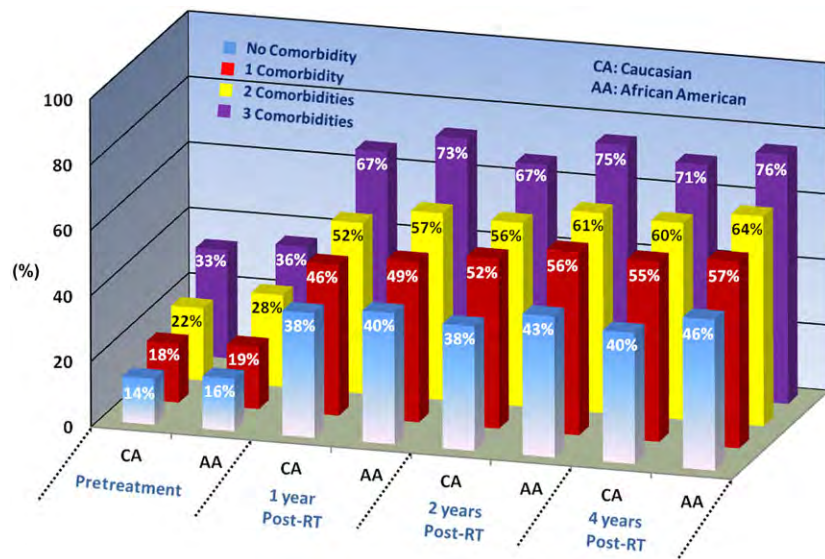


Figure 1 Pre-RT and post-RT ED incidences. At each time point, the ED incidences for each subgroup of patients with 0 (blue), 1 (red), 2 (yellow), and 3 (purple) vascular comorbidities are shown. For each time point, Caucasian patients are presented on the left and AA patients on the right.

post-XRT and with increasing number of VC, with only a slight difference by race within each interval/VC-based bin.

Discussion

Our study is the first to report pre- and post-XRT ED as a function of VCs and race. HTN, DM, and HL are well-known risk factors for ED in the general population [8], which was consistent with our finding that, prior to radiation treatment, ED incidence increased with increasing number of VC (Table 3). In the post-XRT setting, we found a progressive increase in ED with increasingly longer post-XRT time interval, regardless of number of VC. At 1-year follow-up, the overall ED incidence for all patients was 52%, which is similar to other series [12,13]. An important and novel finding in our study was that the number of VC had a profound impact on development of radiation-induced ED. Indeed, at all three post-XRT analysis time points (Table 3 and Figure 1), the post-XRT ED incidence increased substantially with increasing the number of VC. Also, as shown in Table 3, the majority of the pairwise ED incidence comparisons based on number of VC reached statistical significance. Furthermore, when the number of VC within each comparison differed by 2 or more (i.e., 3 vs. 0, 3 vs. 1, and 2 vs. 0), the differences in ED incidence were highly significant, further highlighting that number of VC plays a critical role in increasing the rate of post-XRT ED.

Our study results clearly demonstrate that radiation-induced ED incidence increases when patients have more VCs (HTN, HL, and DM). It will be quite interesting to understand the underlying mechanism. Our results may support the hypothesis that post-XRT ED is due to vasculogenic insufficiency [5]. Several studies have demonstrated (by Doppler ultrasound) a reduction of blood flow in the cavernosal artery in men with ED after radiotherapy [14,15]. It has been suggested that radiotherapy causes pathological changes in small- and medium-sized arteries, which decrease vascular inflow. These arterial changes resemble chronic, progressive atherosclerosis and may be due to a combination of intimal fibrosis, direct damage to the arterial wall, and acceleration of naturally occurring atherosclerosis [16]. The first animal study demonstrated fibrosis change in the arteries of rat corpora cavernosa after adequate irradiation [17]. In addition to vascular parameters, XRT may have a direct effect on endothelial cell function, which is an area of strong interest in ED

research [18]. Data from other body sites indicates that endothelial cells may be the initial target for damage during radiotherapy [19]. Perhaps radiation accelerates the process of atherosclerosis particularly if the patient has one or more VCs. This model is consistent with the findings of the present study, namely that post-XRT ED incidence increased when patients had more VCs.

Interventions that seek to minimize vascular damage during RT may be a reasonable strategy. Radiation Therapy Oncology Group (RTOG) 08-31 is a randomized, placebo-controlled trial currently examining the role of tadalafil for prophylaxis against XRT-induced ED [20]. As a follow-up to this study, perhaps future studies examining interventions should control for number and severity of VC.

Our study is also the first to analyze pre- and post-XRT ED incidence by race. Pre-XRT ED incidence was slightly higher in AA (Table 4), likely due to the higher number of VC. This finding is consistent with other studies. Our study further shows, though, that when accounting for VC, there are no significant differences in ED incidence as a function of race. This is an important finding and will facilitate further studies that can focus on the impact of VC (particularly DM and HTN) on patient selection for prostate cancer quality of life trials and to enhance enrollment of AA patients on these trials.

There are several limitations to our study. First, we did not assess severity of the VCs or whether they were controlled through medication or diet—this will be done in a future analysis. Second, the definition of ED for this study was dichotomous and was based on abstraction of medical record (history of ED documented on history or follow-up or use of medications/treatment aids for ED). The use of validated instruments [21] would certainly increase our ability to accurately assess sexual function. Indeed, in a subset analysis of the Massachusetts Male Aging Study, a single-question self-report was found to be able to identify ED as well as a urologic examination including a sexual history, medical history, psychosocial history, and physical exam [22]. However, it should be noted that our definition of ED was applied uniformly to all patients across subsets so any potential recruitment biases based solely on the ED definition would be minimal. Third, though the Caucasian and AA populations were balanced overall, unbalanced items (such as age and PSA) may be confounding factors; it should be noted, however, that no significant differences based on

race were demonstrated in any of the analyses based on time points or number of VC. Fourth, hormone treatment is a well-known factor to cause ED. Therefore, we investigated the hormone treatment rate among patients with different number of VC. As shown in Table 5, the hormone treatment percentage is not increasing as the number of VC increases. Fifth, the ED rates may vary as a function of radiation modality (EBRT alone vs. combination of EBRT with BT) [4,23], due in part perhaps to differences in radiobiological doses between these modalities [24]. However, results as a function of radiation modality (EBRT + BT) are shown in Table 6—as shown, the results seem to be consistent for patients with different numbers of VCs. Sixth, the dose to the penile structures may be another confounding factor because it has been shown to correlate with radiation-induced ED [6,25]. This is an ongoing area of investigation that we plan to analyze and report separately at a later date. Seventh, as our study population was in a single hospital system treated over a time period in which older radiotherapy techniques were used for some patients, our work requires validation in a larger study population treated with intensity-modulated radiotherapy, perhaps in the multi-institutional consortium setting [26,27]. Finally, the biases inherent to all retrospective analyses are understood by the investigators.

Despite these limitations, our study provides evidence that VC play an important role in the development of both pre- and post-XRT ED. Our results can be used to guide physicians in counseling patients on the incidence of ED by number of VC. Our results can also serve as preliminary data for prospective efforts aimed at reducing post-XRT ED and for future investigations focusing on the incorporation of VC into ED-related treatment management decisions.

Table 5 Hormone therapy use among patients by number of vascular comorbidities

	Caucasian (total: 267)	AA (total: 465)	P value*
Patients without comorbidity	50	67	
Hormone therapy	27 (54%)	39 (58%)	0.66
Patients with one comorbidity	109	201	
Hormone therapy	49 (45%)	113 (56%)	0.06
Patients with two comorbidities	90	142	
Hormone therapy	37 (41%)	65 (46%)	0.46
Patients with three comorbidities	18	55	
Hormone therapy	7 (39%)	24 (44%)	0.71

*Obtained by *t*-test.

Table 6 Brachytherapy use among patients by number of vascular comorbidities

	Caucasian (total: 267)	AA (total: 465)	P value*
Patients without comorbidity	50	67	
BT ± EBRT	16 (32%)	19 (28%)	0.69
Patients with one comorbidity	109	201	
BT ± EBRT	27 (25%)	42 (21%)	0.48
Patients with two comorbidities	90	142	
BT ± EBRT	23 (26%)	40 (28%)	0.76
Patients with three comorbidities	18	55	
BT ± EBRT	5 (28%)	12 (22%)	0.75

*Obtained by *t*-test.

BT = brachytherapy; EBRT = external beam radiotherapy

Conclusions

Our analysis represents the first effort in exploring post-XRT ED by VC and race. Our results suggest that number of VC have a significant effect on the development of post-XRT ED. Pre- and post-XRT ED appear to be independent of race when 1, 2, or 3 VC are considered. These findings can be useful for physicians in patient's consultation regarding post-XRT ED and as preliminary data for prospective efforts aimed at reducing post-XRT ED.

Acknowledgments

Dr. Wang was supported by the Emory Medical Scholar Award program. Dr. Jani is a Georgia Cancer Coalition Distinguished Cancer Clinician/Scientist and was supported in part by this program. The authors thank Ms. Xiaoyan Sun (Department of Biostatistics, Emory University) for the assistance with the statistical analyses.

Corresponding Author: Ashesh B. Jani, MD, MSEE, Department of Radiation Oncology, Emory University, 1365 Clifton Road, NE, Suite A 1300, Atlanta, GA 30322, USA. Tel: 1-404-778-3827; Fax: 1-404-778-4139; E-mail: abjani@emory.edu

Conflict of Interest: No authors have any conflicts of interest, financial or otherwise.

Statement of Authorship

Category 1

(a) Conception and Design

Yuefeng Wang; Tian Liu; Peter J. Rossi; Deborah Watkins-Bruner; Wayland Hsiao; Ashesh B. Jani

(b) Acquisition of Data

Yuefeng Wang; Tian Liu; Sherrie Cooper; Xiaofeng Yang; Ashesh B. Jani

(c) Analysis and Interpretation of Data

Yuefeng Wang; Tian Liu; Peter J. Rossi; Deborah Watkins-Bruner; Wayland Hsiao; Ashesh B. Jani; Sherrie Cooper; Xiaofeng Yang

Category 2**(a) Drafting the Article**

Yuefeng Wang; Tian Liu; Peter J. Rossi; Wayland Hsiao; Ashesh B. Jani

(b) Revising It for Intellectual Content

Yuefeng Wang; Tian Liu; Peter J. Rossi; Deborah Watkins-Bruner; Wayland Hsiao; Sherrie Cooper; Xiaofeng Yang; Ashesh B. Jani

Category 3**(a) Final Approval of the Completed Article**

Yuefeng Wang; Tian Liu; Peter J. Rossi; Deborah Watkins-Bruner; Wayland Hsiao; Sherrie Cooper; Xiaofeng Yang; Ashesh B. Jani

References

- 1 Howlader N, Noone AM, Krapcho M, Neyman N, Aminou R, Waldron W, Altekruse SF, Kosary CL, Ruhl J, Tatalovich Z, Cho H, Mariotto A, Eisner MP, Lewis DR, Chen HS, Feuer EJ, Cronin KA, Edwards BK, eds. *Seer cancer statistics review, 1975–2008*. Bethesda, MD: National Cancer Institute; 2011.
- 2 Jani AB, Hellman S. Early prostate cancer: Clinical decision-making. *Lancet* 2003;361:1045–53.
- 3 Bruner DW, Calvano T. The sexual impact of cancer and cancer treatments in men. *Nurs Clin North Am* 2007;42: 555–8.
- 4 Incrocci L, Slob AK, Levendag PC. Sexual (dys)function after radiotherapy for prostate cancer: A review. *Int J Radiat Oncol Biol Phys* 2002;52:681–93.
- 5 Kao J, Turian J, Meyers A, Hamilton RJ, Smith B, Vijayakumar S, Jani AB. Sparing of the penile bulb and proximal penile structures with intensity-modulated radiation therapy for prostate cancer. *Br J Radiol* 2004;77:129–36.
- 6 Roach M, Winter K, Michalski JM, Cox JD, Purdy JA, Bosch W, Lin X, Shipley WS. Penile bulb dose and impotence after three-dimensional conformal radiotherapy for prostate cancer on RTOG 9406: Findings from a prospective, multi-institutional, phase I/II dose-escalation study. *Int J Radiat Oncol Biol Phys* 2004;60:1351–6.
- 7 Roach M 3rd, Nam J, Gagliardi G, El Naqa I, Deasy JO, Marks LB. Radiation dose-volume effects and the penile bulb. *Int J Radiat Oncol Biol Phys* 2010;76(suppl):S130–4.
- 8 Bacon CG, Mittelman MA, Kawachi I, Giovannucci E, Glasser DB, Rimm EB. A prospective study of risk factors for erectile dysfunction. *J Urol* 2006;176:217–21.
- 9 Laumann EO, West S, Glasser D, Carson C, Rosen R, Kang JH. Prevalence and correlates of erectile dysfunction by race and ethnicity among men aged 40 or older in the United States: From the Male Attitudes Regarding Sexual Health survey. *J Sex Med* 2007;4:57–65.
- 10 Bergman J, Gore JL, Penson DF, Kwan L, Litwin MS. Erectile aid use by men treated for localized prostate cancer. *J Urol* 2009;182:649–54.
- 11 Fryar CD, Hirsch R, Eberhardt MS, Yoon SS, Wright JD. Hypertension, high serum total cholesterol, and diabetes: Racial and ethnic prevalence differences in U.S. adults, 1999–2006. *NCHS Data Brief* 2010;36:1–8.
- 12 Pinkawa M, Gagel B, Piroth MD, Fischedick K, Asadpour B, Kehl M, Klötz J, Eble MJ. Erectile dysfunction after external beam radiotherapy for prostate cancer. *Eur Urol* 2009;55:227–34.
- 13 Robinson JW, Moritz S, Fung T. Meta-analysis of rates of erectile function after treatment of localized prostate carcinoma. *Int J Radiat Oncol Biol Phys* 2002;54:1063–8.
- 14 Goldstein I, Feldman MI, Decker PJ, Babayan RK, Krane RJ. Radiation-associated impotence. A clinical study of its mechanism. *JAMA* 1984;251:903–10.
- 15 Mulhall J, Ahmed A, Parker M, Mohideen N. The hemodynamics of erectile dysfunction following external beam radiation for prostate cancer. *J Sex Med* 2005;2:432–7.
- 16 Kalman PG, Lipton IH, Provan JL, Walker PM, Miles JT, Yeung HP. Radiation-damage to large arteries. *Can J Surg* 1983;26:88–91.
- 17 van der Wielen GJ, Vermeij M, de Jong BW, Schuit M, Marnijssen J, Kok DJ, van Weerden WM, Incrocci L. Changes in the penile arteries of the rat after fractionated irradiation of the prostate: A pilot study. *J Sex Med* 2009;6:1908–13.
- 18 Aversa A, Rossi F, Francomano D, Bruzziches R, Bertone C, Santiemma V, Spera G. Early endothelial dysfunction as a marker of vasculogenic erectile dysfunction in young habitual cannabis users. *Int J Impot Res* 2008;20:566–73.
- 19 Hasleton PS, Carr N, Schofield PF. Vascular changes in radiation bowel-disease. *Histopathology* 1985;9:517–34.
- 20 Radiation Therapy Oncology Group Protocol 0831. A Randomized, Double-Blinded, Placebo-Controlled Phase III Trial to Evaluate the Effectiveness of a Phosphodiesterase 5 Inhibitor, Tadalafil, in Prevention of Erectile Dysfunction in Patients Treated with Radiotherapy for Prostate Cancer. 2008. Available at: <http://www.rtog.org> (accessed May 29, 2013).
- 21 Rosen RC, Althof SE, Giuliano F. Research instruments for the diagnosis and treatment of patients with erectile dysfunction. *Urology* 2006;68(suppl):6–16.
- 22 O'Donnell AB, Araujo AB, Goldstein I, McKinlay JB. The validity of a single-question self-report of erectile dysfunction. Results from the Massachusetts Male Aging Study. *J Gen Intern Med* 2005;20:515–9.
- 23 Snyder KM, Stock RG, Buckstein M, Stone NN. Long-term potency preservation following brachytherapy for prostate cancer. *BJU Int* 2012;110:221–5.
- 24 Wang JZ, Li XA. Evaluation of external beam radiotherapy and brachytherapy for localized prostate cancer using equivalent uniform dose. *Med Phys* 2003;30:34–40.
- 25 Fisch BM, Pickett B, Weinberg V, Roach M. Dose of radiation received by the bulb of the penis correlates with risk of impotence after three-dimensional conformal radiotherapy for prostate cancer. *Urology* 2001;57:955–9.
- 26 Watkins Bruner D, James JL, Bryan CJ, Pisansky TM, Rotman M, Corbett T, Speight J, Byhardt R, Sandler H, Bentzen S, Kachnic L, Berk L. Randomized, double-blinded, placebo-controlled crossover trial of treating erectile dysfunction with sildenafil after radiotherapy and short-term androgen deprivation therapy: Results of RTOG 0215. *J Sex Med* 2011;8:1228–38.
- 27 Koontz BF, Yan H, Kimura M, Vujaskovic Z, Donatucci C, Yin FF. Feasibility study of an intensity-modulated radiation model for the study of erectile dysfunction. *J Sex Med* 2011;8:411–8.

Physics Contribution

Respiratory-Induced Prostate Motion Using Wavelet Decomposition of the Real-Time Electromagnetic Tracking Signal

Yuting Lin, PhD,^{*} Tian Liu, PhD,[†] Xiaofeng Yang, PhD,[†] Yuenan Wang, PhD,[‡] and Mohammad K. Khan, MD, PhD[†]

^{*}Tu and Yuen Center for Functional Onco-Imaging, Department of Radiological Sciences, University of California, Irvine, California; [†]Department of Radiation Oncology, Emory University Hospital, Winship Cancer Institute, Atlanta, Georgia; and [‡]Center for Devices and Radiological Health, US Food and Drug Administration, Silver Spring, Maryland

Received Feb 13, 2013, and in revised form May 7, 2013. Accepted for publication May 9, 2013

Summary

The objective of this work is to characterize and quantify respiratory-induced prostate motion using wavelet transform of the Calypso tracking system. Our results show that prostate motion is influenced by respiration in most fractions, and this technique provides a tool that can be useful if one moves toward smaller margins (≤ 5 mm). This also opens up the possibility of being able to develop patient-specific margins, knowing that prostate motion is not unpredictable.

Purpose: The objective of this work is to characterize and quantify the impact of respiratory-induced prostate motion.

Methods and Materials: Real-time intrafraction motion is observed with the Calypso 4-dimensional nonradioactive electromagnetic tracking system (Calypso Medical Technologies, Inc. Seattle, Washington). We report the results from a total of 1024 fractions from 31 prostate cancer patients. Wavelet transform was used to decompose the signal to extract and isolate the respiratory-induced prostate motion from the total prostate displacement.

Results: Our results show that the average respiratory motion larger than 0.5 mm can be observed in 68% of the fractions. Fewer than 1% of the patients showed average respiratory motion of less than 0.2 mm, whereas 99% of the patients showed average respiratory-induced motion ranging between 0.2 and 2 mm. The maximum respiratory range of motion of 3 mm or greater was seen in only 25% of the fractions. In addition, about 2% patients showed anxiety, indicated by a breathing frequency above 24 times per minute.

Conclusions: Prostate motion is influenced by respiration in most fractions. Real-time intrafraction data are sensitive enough to measure the impact of respiration by use of wavelet decomposition methods. Although the average respiratory amplitude observed in this study is small, this technique provides a tool that can be useful if one moves to smaller treatment margins (≤ 5 mm). This also opens up the possibility of being able to develop patient specific margins, knowing that prostate motion is not unpredictable. © 2013 Elsevier Inc.

Introduction

Conformal external beam therapy can effectively enhance the local control of prostate cancer (1, 2). The knowledge of organ

motion is essential to ensure conformed dose delivery to the target and minimize toxicity to the surrounding organs at risk during prostate radiation therapy (3, 4). Prostate intrafraction motion causes the dose distribution to be smeared. Even with perfect external immobilization techniques and minimized whole pelvic

DOI of original article: 10.1016/j.ijrobp.2013.05.019.

Reprint requests to: Mohammad K. Khan, MD, PhD, Department of Radiation Oncology, Emory University Hospital, Winship Cancer Institute,

1365 Clifton Rd NE, Atlanta, GA 30345. Tel: (404) 778-4126 E-mail: drkhurram2000@gmail.com
Conflict of Interest: none.

motion controlled by patient consciousness, the intrafraction internal organ motion during treatment will contribute to smearing of the dose distribution and increase toxicity of surrounding tissue significantly (5, 6). In general, prostate motion is a combination of the contribution from bladder and rectum filling and respiratory motion. Currently, there is very limited understanding of how prostate movement is affected by the respiratory cycle because most intrafraction tracking techniques cannot separate the contribution from respiratory-induced prostate motion from the bladder and rectum filling. In this article we attempt to isolate the respiratory motion from the total prostate displacement and characterize the contribution of respiratory-induced prostate motion using a wavelet transform technique. To our knowledge, this is the first study of this type.

High-precision, real-time intrafraction motion is obtained with the Calypso 4-dimensional nonradioactive electromagnetic position tracking system (Calypso Medical Technologies, Inc. Seattle, Washington). Three electromagnetic transponders ("beacon") are implanted into the prostate. During daily radiation treatment, the beacon transponders communicate with the Calypso system through nonionizing radiofrequency signal, and the prostate isocenter displacement in the superoinferior, anteroposterior, and lateral directions is recorded at a frequency of 10 Hz. The objective of this work is to characterize and quantify the impact of respiratory-induced prostate motion from these tracking data. We report the results from a total of 1024 fractions from 31 prostate cancer patients who underwent daily intensity modulated radiation therapy (IMRT) treatment.

Methods and Materials

Patient and Calypso implantation procedure

A total of 31 subjects clinically diagnosed with prostate cancer and treated with IMRT at Winship Cancer Institute, Atlanta, Georgia, were included in the study. The real-time tracking technique, which was instrumental in initial Food and Drug Administration approval for the Calypso system, has been previously described (7-9). In brief, all patients underwent implantation of 3 beacon electromagnetic transponders into the prostate via transrectal ultrasound guidance before the radiation treatment. All patients were treated in the supine position as follows: a band was placed around the feet, a wedge under the knees, a ring for the hands on the chest, and a Vac-Loc bag for daily immobilization. All patients were instructed to drink 500 mL of fluid 4 hours before simulation and during daily treatments. No specific bowel preparation instructions were provided. A low-residue diet was encouraged during treatments, and patients were encouraged to have a bowel movement before daily treatments.

After daily localization with minimal initial residual, intrafractional motion of the prostate during the treatment is monitored at a 10-Hz frequency as the lateral (RL), anteroposterior (AP), and superoinferior (SI) displacement of the isocenter with the Calypso 4-dimensional tracking system (7, 8). An action threshold of 3 mm of prostate motion or greater lasting for more than 30 seconds was instituted. If this was exceeded, the beam and prostate tracking was stopped and the patient was repositioned with minimal residual before treatment was resumed. A typical IMRT course consisted of 38 to 39 fractions, and the mean fraction length was 7 minutes 6 seconds (426 seconds). Only the fractions consisting of

a minimum of 3 minutes of continuous tracking data were included in the analysis, resulting in a total of 1024 fractions. The tracking data obtained from the Calypso system and analyzed within this work are limited to intrafraction prostate motion obtained after initial prostate localization with near 0 initial residual.

Prostate motion characterization and quantification using wavelet analysis

Normally, Fourier transform is extremely useful for extracting frequency content of the respiratory sinusoidal signal. However, the major drawback is the requirement for the signal to be stationary. Unfortunately, prostate motion tracking data are non-stationary, characterized by drifting, abrupt changes, and multiple excursions (7). To overcome the limitation of Fourier transformation, wavelet transform is used as a more suitable tool. Wavelet analysis allows the use of stretched wavelets to extract low-frequency information and compressed wavelets to extract high-frequency information (10, 11). As a result, the particular power spectral band relevant to respiration motion can be effectively separated from high-frequency noise through this multi-resolution time-frequency analysis.

Uniform samples at 10 Hz were obtained from the real-time Calypso tracking data. Then, the data were wavelet transformed with the discontinuous wavelet transform algorithm to 5 levels by use of db4 wavelets (Daubechies wavelets) (13). The use of 10 Hz results in the following frequency bands: D5, 0.1563 to 0.3125 Hz; D4, 0.3125 to 0.625 Hz; D3, 0.625 to 1.25 Hz; D2, 1.25 to 2.5 Hz; and D1, 2.5 to 5 Hz. The frequency band corresponds to respiratory frequency as follows: D5, 10 to 20 times per minute; D4, 20 to 40 times per minute; D3, 40 to 80 times per minute; D2, 80 to 160 times per minute; and D1, 160 to 320 times per minute. The typical breathing pattern is around 10 to 24 breaths per minute, and thus extracted signals at D5 and D4 bands are mainly used for further analysis. It is essential to include the D4 band because some patients may have anxiety or respiratory distress during radiation, resulting in accelerated breathing frequency above 24 times per minute. On the other hand, the frequency ranges of D1 through D3 are apparently too high for respiratory motion. Power spectral density analysis was performed to extract the peak breathing frequency and the average total power. The average total power is defined as the area under the power spectral density curve.

Results

Prostate motion characterization and quantification using wavelet analysis

The general pattern of the prostate motion may not be predictable because the frequency and magnitude of the effect from bladder and rectum filling are unknown. Various excursion patterns have shown that it may be futile to predict the general prostate motion behavior (7). However, a closer look at the tracking data, as shown in Figure 1, clearly shows that there exists an oscillation pattern, especially in the AP and SI directions. This pattern exists in all fractions for all patients, and the difference is just a matter of magnitude rather than existence of the pattern. Graphically, the oscillation is about 16 to 18 times per minute and consistently

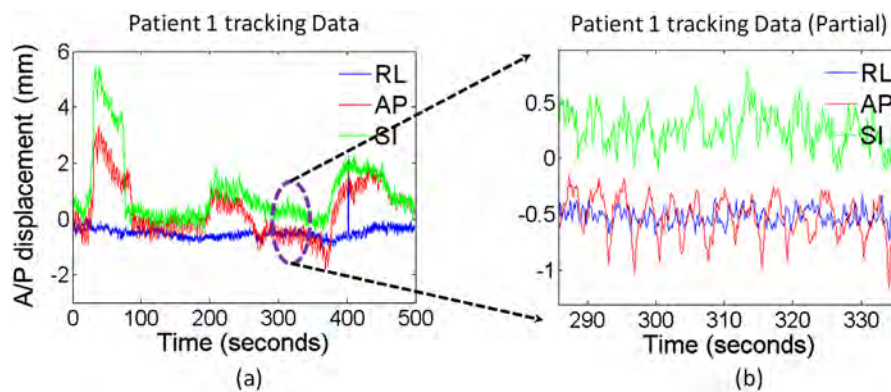


Fig. 1. (a) Example of tracking data. (b) A zoom-in view of a portion of the tracking data shows the respiratory-induced oscillation pattern especially in the anteroposterior (AP) and superoinferior (SI) directions. (RL, lateral.)

present throughout the entire tracking period. To effectively analyze this respiratory-induced prostate motion, this periodical signal must be extracted and separated from the general prostate motion. For that purpose, wavelet decomposition is used in our study because it is ideal for situations where a repetitive pattern caused by respiration exists amidst background noise caused by prostate drifting and bladder or rectal filling. We have shown in our previous publication (12) that the prostate motion in the AP/SI direction is highly correlated, which is consistent with the longitudinal oblique motion of the prostate, and likely due to the effect of respiration on an organ confined between the bladder and rectum. For this reason, the magnitude and peak frequency of the respiratory motion are extracted from the displacement in the oblique direction ($\sqrt{y^2 + z^2}$) (y-axis for AP and z-axis for SI).

An example of the wavelet decomposition is shown in Figure 2. The original signal is decomposed to a low-frequency approximation at level 5 (A5) and high-frequency details at 5 levels (D5-D1). It is obvious that details D1 through D3 are beyond the range of respiratory frequency, and the D4 and D5 frequency range (10-40 breaths per minute) represents the range for most of the patients. An example of the D4-plus-D5 oscillation superimposed on the A5 approximation in comparison to its original signal is shown in Figure 3. Detail at levels 4 and 5 (D4 plus D5) well represents the major oscillation pattern while disregarding the higher-frequency noises.

The power spectral density analysis for D3, D4, and D5 is shown in Figure 4. The total represents the sum of all 5 levels of details. D5 showed the highest and most dominant signal strength compared with signal at the D4 and D3 frequency range, indicating that the oscillation signal is mainly at the D5 frequency range. For a total of 1024 fractions, there are only 157 fractions (15%) during which the patient's respiratory frequency is above 20 times per minute. Moreover, only 24 fractions (2%) are higher than 24 times per minute, which may indicate the increased anxiety level of the patient due to the treatment.

The quantification of the respiratory motion amplitude is then determined by the average and maximum respiratory range of motion in the oblique direction. To isolate the total displacement and the impact of respiratory motion, we used the following steps (the notations can be found in Fig. 2): (1) The oscillation details (D4 plus D5) were extracted for both AP (y-axis) and SI (z-axis) directions. (2) Regardless of the displacement for the approximation component (A5), the respiratory motion in oblique direction is defined as $RM = \sqrt{y_{(D4+D5)}^2 + z_{(D4+D5)}^2}$. This way, we only

calculate the contribution of the amplitude from the respiratory motion rather than total displacement. (3) The average absolute amplitude (RM_{mean}) and the difference between maximum and minimum amplitude (RM_{max}) of the oblique motion obtained in step 2 is calculated for each fraction. (4) The average respiratory range of motion is then determined as $4 \times RM_{mean}$, taking into account the positive and negative signs of the data. For instance, an oscillation wave with an amplitude of 2 mm (± 1 mm) has an average absolute amplitude of 0.5 mm. Meanwhile, the maximum respiratory range of motion is RM_{max} . The results are shown in Table 1.

It is worth noting that the amplitude presented in this article is only the oscillation component of the tracking data. The actual average displacement of the signal can be much higher than 1 or 2 mm. For this reason, the amplitude reported in this article is much smaller than what is normally reported in the literature on deep breathing (14).

Discussion

The small amplitude of respiratory-induced prostate motion extracted from wavelet analysis should not be confused with the overall prostate motion, which has been investigated by several groups. The Calypso real-time tracking data showed that the continuous prostate motion can be unpredictable, ranging greatly from constant drifting, abrupt changes, or a combination thereof, given the unpredictability of bladder filling, rectum filling, and flatulence (7). Shah et al (15) reported prostate motion greater than 3 mm and greater than 5 mm for 12.6% and 2.9% of fractions in the supine position, respectively. Similarly, Langen et al (16) reported prostate motion greater than 3 mm and greater than 5 mm for 14% and 3% of fractions, respectively. Willoughby et al (8) reported prostate displacements of 0.9 ± 0.35 mm, 3.61 ± 3.13 mm, and 3.92 ± 4.32 mm in the lateral, AP, and SI directions, respectively.

Given the complexity of prostate motion, we present the first attempt to isolate the high-frequency respiratory-induced motion from the general prostate motion. The amplitude of respiratory motion alone will be the minimum amount of planning target volume margin required and is likely a function of how frequent prostate motion is imaged during treatment delivery (9). Malone et al (17) quantified and characterized the respiratory motion using implanted gold fiducial markers. A total length of a 20-second interval of fluoroscopy was analyzed, and the maximum

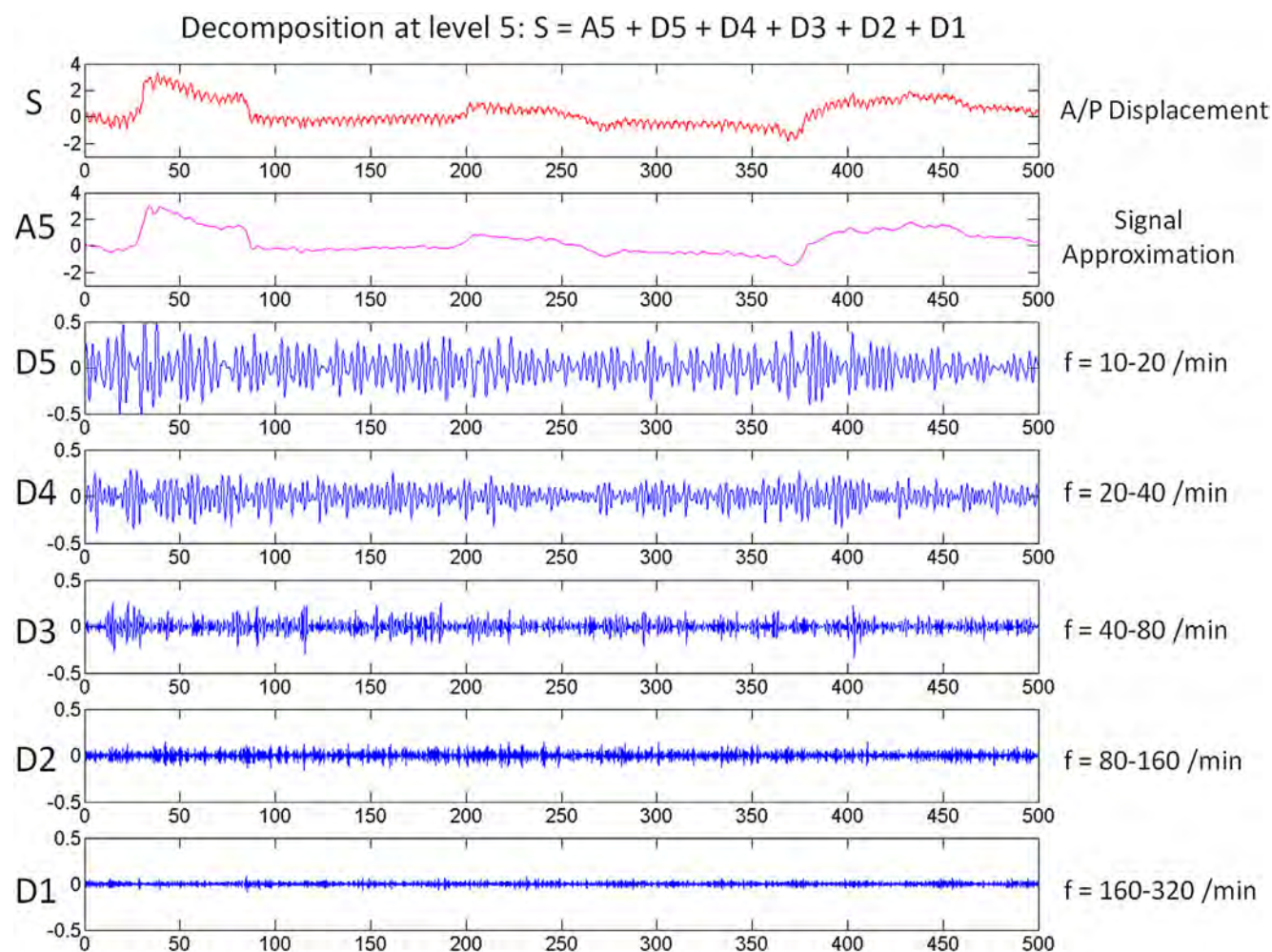


Fig. 2. Example of wavelet decomposition. The signal (S) is decomposed to 5 levels. (f, frequency.)

displacement in the AP and SI directions was measured. For a total of 20 patients, mean displacement was 1.6 mm and 2.9 mm in the AP and SI directions, respectively. Dinkel et al (14) evaluated

respiratory-induced prostate motion using cine-magnetic resonance imaging. The temporal resolution was 3 frames per second, and the total acquisition time was 15 seconds. From the magnetic

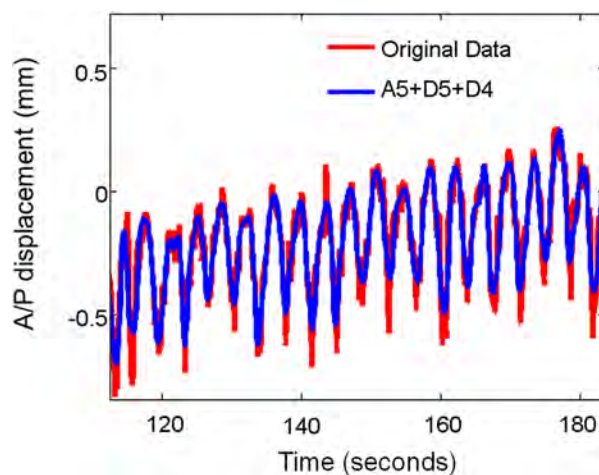


Fig. 3. D4-plus-D5 oscillation superimposed on A5 approximation in comparison to its original signal.

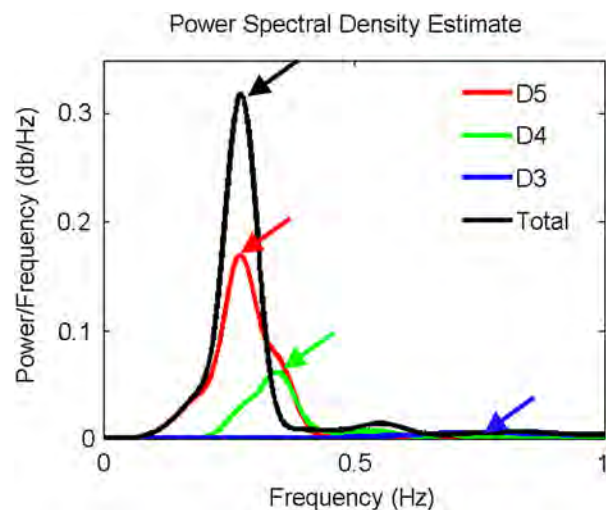


Fig. 4. Power spectral density analysis for D3, D4, and D5 and sum of details.

Table 1 Results for amplitude of respiratory prostate motion

	No. of fractions
Average respiratory range of motion	
0-0.2 mm	4 (<1%)
0.2-0.5 mm	322 (31%)
0.5-1.0 mm	688 (67%)
1.0-2.0 mm	10 (1%)
>2.0 mm	0 (0%)
Maximum respiratory range of motion	
0-0.5 mm	16 (2%)
0.5-1.0 mm	252 (25%)
1.0-2.0 mm	348 (34%)
2.0-3.0 mm	145 (14%)
>3.0 mm	263 (25%)

resonance imaging measurement, the mean displacement of the prostate during deep breathing in the SI and AP directions was 2.7 mm and 1.8 mm, respectively. The prostate displacement for abdominal contraction (via a coughing maneuver) was significantly higher: mean SI displacement was 8.4 mm, and mean AP movement was 8.3 mm. Our results show that most patients have a mean prostate motion below 1 mm, which is a much lower number than the numbers in previous studies. The 2 main reasons are (1) our data were acquired during the actual treatment with normal breathing, and thus deep breathing or conscious abdominal contraction is not included; and (2) the respiratory component is effectively extracted by use of wavelet decomposition, thus excluding the possible large displacement caused by other factors such as bladder/rectum filling or flatulence.

Udrescu et al (18) investigated respiratory prostate motion using 4-dimensional computed tomography and concluded that there is no respiratory motion observed. In this study the SI direction displacement is, in general, unattainable because of the 2.5-mm slice thickness. In both the AP and lateral directions, the prostate motion stayed below 1 mm, with an average of 0.27 mm for a period of 2 minutes. The amplitude of the respiratory motion is consistent with our results, where 99% patients had a mean prostate motion below 1 mm.

The use of high-frequency, real-time tracking data allowed us to evaluate the respiratory motion quantitatively. Our approach has several distinct improvements over respiratory-induced prostate motion analysis in the literature (13, 17, 18). First, the oscillation component of the prostate motion is identified through wavelet analysis, which effectively isolates the respiratory-induced prostate motion from the total prostate displacement. Second, previous publications reported the results from visual observation because of the limited length and sampling rate of data. The 10-Hz real-time tracking data during treatment give sufficient information to extract the frequency and amplitude of the respiratory-induced prostate motion through wavelet frequency-time analysis. Indeed, this is the first time wavelet analysis has been used to characterize respiratory-induced prostate motion during radiation therapy.

Conclusions

Prostate motion is influenced by respiration in most fractions. Real-time intrafraction data are sensitive enough to measure the impact of respiration by use of wavelet decomposition methods.

Although the average respiratory amplitude observed in this study is small, this technique provides a tool that can be useful if one moves to smaller treatment margins (≤ 5 mm). This also opens up the possibility of being able to develop patient-specific margins, knowing that prostate motion is not unpredictable. Moving toward 0-mm margins will only be possible if deformation change of the prostate is also taken into account.

References

- Pollack A, Zagars GK. External beam radiotherapy dose response of prostate cancer. *Int J Radiat Oncol Biol Phys* 1997;39:1011-1018.
- Nilsson S, Norlén BJ, Widmark A. A systematic overview of radiation therapy effects in prostate cancer. *Acta Oncol* 2004;43:316-381.
- Nederveen AJ, van der Heide UA, Dehnad H, et al. Measurements and clinical consequences of prostate motion during a radiotherapy fraction. *Int J Radiat Oncol Biol Phys* 2002;53:206-214.
- Huang E, Dong L, Chandra A, et al. Intrafraction prostate motion during IMRT for prostate cancer. *Int J Radiat Oncol Biol Phys* 2002;53:261-268.
- Zelefsky MJ, Levin EJ, Hunt M, et al. Incidence of late rectal and urinary toxicities after three-dimensional conformal radiotherapy and intensity-modulated radiotherapy for localized prostate cancer. *Int J Radiat Oncol Biol Phys* 2008;70:1124-1129.
- Guckenberger M, Ok S, Polat B, et al. Toxicity after intensity-modulated, image-guided radiotherapy for prostate cancer. *Strahlenther Onkol* 2010;186:535-543.
- Kupelian P, Willoughby T, Mahadevan A, et al. Multi-institutional clinical experience with the Calypso System in localization and continuous, real-time monitoring of the prostate gland during external radiotherapy. *Int J Radiat Oncol Biol Phys* 2007;67:1088-1098.
- Willoughby TR, Kupelian PA, Pouliot J, et al. Target localization and real-time tracking using the Calypso 4D localization system in patients with localized prostate cancer. *Int J Radiat Oncol Biol Phys* 2006;65:528-534.
- Curtis W, Khan M, Magnelli A, et al. Relationship of imaging frequency and planning margin to account for intrafraction prostate motion: analysis based on real-time monitoring data. *Int J Radiat Oncol Biol Phys* 2013;85:700-706.
- Houtveen JH, Molenaar PCM. Comparison between the Fourier and Wavelet methods of spectral analysis applied to stationary and nonstationary heart period data. *Psychophysiology* 2001;38:729-735.
- Pichot V, Gaspoz J-M, Molliex S, et al. Wavelet transform to quantify heart rate variability and to assess its instantaneous changes. *J Appl Physiol* 1999;86:1081-1091.
- Lin, Liu, Yang et al. The Non-Gaussian Nature of Prostate Motion Based on Real-Time Intrafraction Tracking. *Int J Radiat Oncol Biol Phys* 2013. Epub July 9.
- Daubechies I. Ten Lectures on Wavelets. Philadelphia, PA: Society for Industrial and Applied Mathematics; 1992.
- Dinkel J, Thieke C, Plathow C, et al. Respiratory-induced prostate motion. *Strahlenther Onkol* 2011;187:426-432.
- Shah AP, Kupelian PA, Willoughby TR, et al. An evaluation of intrafraction motion of the prostate in the prone and supine positions using electromagnetic tracking. *Radiother Oncol* 2011;99:37-43.
- Langen KM, Willoughby TR, Meeks SL, et al. Observations on real-time prostate gland motion using electromagnetic tracking. *Int J Radiat Oncol Biol Phys* 2008;71:1084-1090.
- Malone S, Crook JM, Kendal WS, et al. Respiratory-induced prostate motion: quantification and characterization. *Int J Radiat Oncol Biol Phys* 2000;48:105-109.
- Udrescu C, Jalade P, de Bari B, et al. Evaluation of the respiratory prostate motion with four-dimensional computed tomography scan acquisitions using three implanted markers. *Radiother Oncol* 2012;103:266-269.

Physics Contribution

The Non-Gaussian Nature of Prostate Motion Based on Real-Time Intrafraction Tracking

Yuting Lin, PhD,^{*} Tian Liu, PhD,[†] Wells Yang,[‡] Xiaofeng Yang, PhD,[†] and Mohammad K. Khan, MD, PhD[†]

^{*}Tu and Yuen Center for Functional Onco-Imaging, Department of Radiological Sciences, University of California, Irvine, California; [†]Department of Radiation Oncology Emory University Hospital, Winship Cancer Institute, Atlanta, Georgia; and [‡]Department of Biomedical Engineering, Georgia Institute of Technology, Atlanta, Georgia

Received Feb 13, 2013, and in revised form May 7, 2013. Accepted for publication May 9, 2013

Summary

The objective of this work is to test the validity of the Gaussian approximation for prostate motion through characterization of its spatial distribution using Calypso 4D nonradioactive electromagnetic tracking system. Our results showed that the prostate motion is highly correlated in the AP and SI directions. In addition, the spatial distribution of prostate motion is elongated in an oblique direction, indicating that the organ motion dosimetric modeling using Gaussian kernel may need to be modified.

Purpose: The objective of this work is to test the validity of the Gaussian approximation for prostate motion through characterization of its spatial distribution.

Methods and Materials: Real-time intrafraction prostate motion was observed using Calypso 4-dimensional (4D) nonradioactive electromagnetic tracking system. We report the results from a total of 1024 fractions from 31 prostate cancer patients. First, the correlation of prostate motion in right/left (RL), anteroposterior (AP), and superoinferior (SI) direction were determined using Pearson's correlation of coefficient. Then the spatial distribution of prostate motion was analyzed for individual fraction, individual patient including all fractions, and all patients including all fractions. The displacement in RL, AP, SI, oblique, or total direction is fitted into a Gaussian distribution, and a Lilliefors test was used to evaluate the validity of the hypothesis that the displacement is normally distributed.

Results: There is high correlation in AP/SI direction (61% of fractions with medium or strong correlation). This is consistent with the longitudinal oblique motion of the prostate, and likely the effect from respiration on an organ confined within the genitourinary diaphragm with the rectum sitting posteriorly and bladder sitting superiorly. In all directions, the non-Gaussian distribution is more common for individual fraction, individual patient including all fractions, and all patients including all fractions. The spatial distribution of prostate motion shows an elongated shape in oblique direction, indicating a higher range of motion in the AP and SI directions.

Conclusions: Our results showed that the prostate motion is highly correlated in AP and SI direction, indicating an oblique motion preference. In addition, the spatial distribution of prostate motion is elongated in an oblique direction, indicating that the organ motion dosimetric modeling using Gaussian kernel may need to be modified to account for the particular organ motion character of prostate. © 2013 Elsevier Inc.

Reprint requests to: Mohammad K. Khan, MD, PhD, 1365 Clifton Road NE, Department of Radiation Oncology, Emory University Hospital, Winship Cancer Institute, 1365 Clifton Rd NE, Atlanta, GA 30345. Tel: (404) 778-4126; E-mail: drkhurram2000@gmail.com

Conflict of Interest: none.

Supplementary material for this article can be found at www.redjournal.org.

Introduction

During prostate cancer external beam radiation therapy, the knowledge of organ motion is essential to ensure conformed dose

delivery to the target while minimizing toxicity to the surrounding organs at risk. Organ motion leads to smearing of dose distribution, causing reduced sharpness of intended dose conformality (1, 2). Interfraction motion will not cause blurring in a given

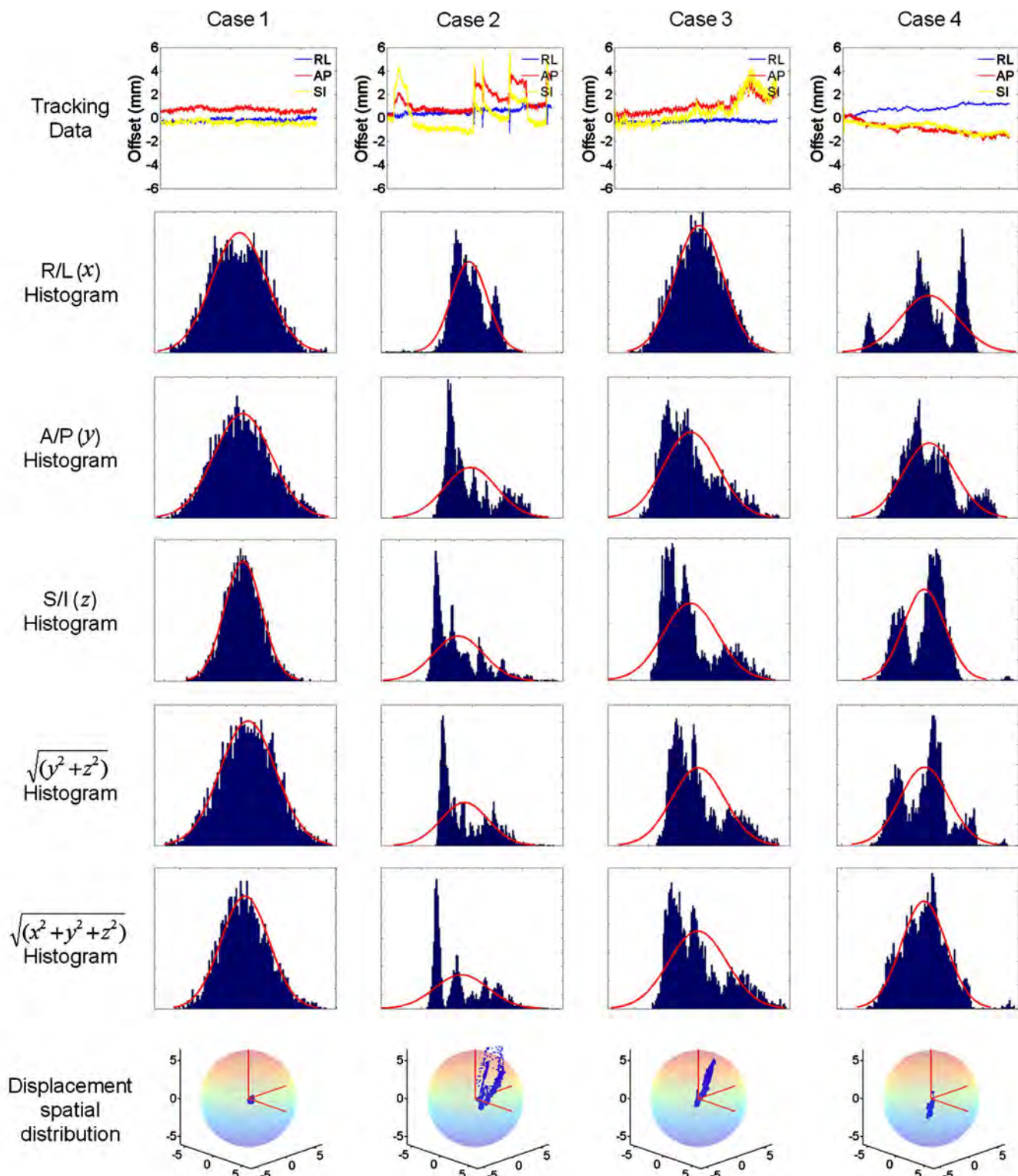


Fig. 1. Examples of prostate motion distribution analysis for individual fraction. (Row 1) Raw tracking data. (Rows 2-7) Histogram plot for right/left (RL), anteroposterior (AP), superoinferior (SI), oblique, and total directions. (Red line) Gaussian fit of the tracking data overlaid on the histogram. (Row 7) Spatial distribution of the transponder displacement. The upper limit of the x, y, and z axes are set to 6 mm.

Table 1 The result for correlation analysis

Correlation	RL/AP	RL/SI	AP/SI
Strong ($R \geq 0.7$)	123 (12%)	141 (14%)	401 (39%)
Medium ($0.5 \leq R < 0.7$)	202 (9%)	190 (18%)	231 (22%)
Weak ($0.3 \leq R < 0.5$)	273 (23%)	247 (26%)	173 (17%)
None ($R < 0.3$)	427 (42%)	447 (44%)	220 (21%)

Abbreviations: AP = anteroposterior; RL = right/left; SI = superoinferior.

The boldface red text emphasizes the strong correlation in AP/SI direction and weak correlation in the RL/AP and RL/SI directions.

fraction; rather, the total accumulated dose distribution will be blurred. To characterize and minimize the interfraction motion, various daily localization techniques have been developed, such as surface fiducial or 3-point surface alignment, implanted fiducial, or bony landmark with on board imaging, ultrasound, and kV/mV CBCT (3-5). Meanwhile, the daily intrafraction motion also plays an essential role in determining treatment planning margin (6), and may be a function of how frequent the prostate motion is sampled during a course of treatment (7).

Decreasing the planning target volume (PTV) margins can potentially reduce the radiation exposure to normal tissue and limit the toxicity and side effect for treatment. To decrease PTV margins in a safe manner, precise understanding and proper modeling of the interfraction motion is critical. High precision, real-time intrafraction prostate motion was obtained using Calypso 4D nonradioactive electromagnetic tracking system. Three electromagnetic transponders ("Beacon") were implanted into the prostate. During daily radiation treatments, the Beacon transponders communicated with the Calypso System through nonionizing radiofrequency signal and the prostate isocenter displacement in SI, AP, and lateral directions is recorded at a 10-Hz frequency. The availability of these measurements allows us to evaluate and characterize the intrafraction prostate motion in detail—in particular, whether or not the motion errors can be represented by a Gaussian function.

The objectives of this work were (1) to investigate the directional dependence and correlation of prostate motion; and (2) to characterize and quantify the spatial distribution of the prostate motion.

Methods and Materials

Patient and calypso implantation procedure

A total of 31 patients were included in this study. These subjects were clinically diagnosed with prostate cancer and treated with intensity modulated radiation therapy at the Taussig Cancer Institute at Cleveland Clinic. Three Beacon electromagnetic

transponders were implanted into the prostate via transrectal ultrasound guidance before the radiation treatment. Intrafractional motion of the prostate is monitored at 10-Hz frequency of the RL, AP, and SI displacement of the isocenter using the Calypso 4-dimensional (4D) tracking system. Our Calypso technique, which was instrumental in initial US Food and Drug Administration approval for the Calypso system, has been previously described (8, 9). Briefly, all patients were treated in the supine position with a band placed around the feet, a wedge under the knees, a ring for the hands on the chest, and a Vac-Loc bag for daily immobilization purposes. They were instructed to drink 500 mL of fluid 4 hours before the daily treatments. A low-residue diet was encouraged during treatments and patients were encouraged to have a bowel movement earlier during the day before treatments. Typical intensity modulated radiation therapy treatments included 38-39 daily fractions, and only the fractions consisting of a minimum of 3 minutes' continuous tracking data are included in the analysis, resulting in a total of 1024 fractions.

Prostate motion direction correlation

To characterize the directional dependency of prostate motion, the correlation in RL, AP, and SI direction from tracking data were determined using Pearson's correlation of coefficient. The magnitude of correlation coefficient ≥ 0.7 indicates a strong correlation between 2 directions. Medium correlation is defined by the magnitude of correlation coefficient between 0.5 and 0.7. The magnitude of correlation coefficient between 0.3 and 0.5 indicates a low correlation, and little if any correlation exists for those data pairs whose magnitude of coefficient is < 0.3 . A 99% confidence interval for the correlation coefficient is required.

Prostate motion distribution analysis: individual fraction

The procedure to account for motion and setup error in dose calculation uses Gaussian approximation to describe the blurring effect. Because it has been long believed that prostate motion and setup errors are random, Gaussian approximation is considered to be good without loss of generality, especially after multiple fractions based on the central limit theorem (2, 10). To evaluate the validity of the Gaussian approximation assumption, the prostate motion was characterized using real-time tracking data during radiation treatment.

For each fraction of each patient, the tracking data indicating displacement in RL (x axis) direction, AP (y axis) direction, and SI (z axis) direction was obtained. The total displacement in the oblique direction ($\sqrt{y^2 + z^2}$) and the total displacement in all directions ($\sqrt{x^2 + y^2 + z^2}$) were also calculated. Afterward, the displacement was fitted into

Table 2 The result of prostate motion distribution analysis for individual fractions

	RL x axis	AP y axis	SI z axis	Oblique $\sqrt{(x^2 + y^2)}$	Total $\sqrt{(x^2 + y^2 + z^2)}$
Number of fractions with Gaussian distribution	139	77	85	89	89
Percentage of total fractions with Gaussian distribution	13.6	7.5	8.3	8.7	8.7

A total of 1024 fractions were included in the analysis.

Abbreviations: AP = anteroposterior; RL = right/left; SI = superoinferior.

Table 3 The result of prostate motion distribution analysis for individual patient including all fractions

	RL x axis	AP y axis	SI z axis	Oblique $\sqrt{(x^2 + y^2)}$	Total $\sqrt{(x^2 + y^2 + z^2)}$
Number of patients with Gaussian distribution	8	3	2	2	4
Percentage of patients with Gaussian distribution	33	12.5	8.3	8.3	16.7

A total of 24 patients were included in the analysis.

Abbreviations: AP = anteroposterior; RL = right/left; SI = superoinferior.

a Gaussian distribution and was used to evaluate the validity of the hypothesis that the distribution is normally distributed. The Lilliefors test was used when the null distribution is unknown and has to be estimated (11). This was suitable for our study because we were interested in whether or not the distribution is Gaussian with any mean and variance.

Prostate motion distribution measurement: total fractions of one patient

We evaluated the validity of the Gaussian approximation assumption of accumulative fractions of prostate motion from a single patient. Only those patients who had more than 30 valid fractions were included in this analysis, resulting in 24 patients in total. All the fractions of displacement tracking data were combined into a single array, and displacement in RL, AP, SI, oblique, and all directions were calculated for each patient. The same Gaussian distribution test was used to quantify the displacement on an individual patient level.

Prostate motion distribution measurement: total fractions from all patients

Last, we evaluated the validity of Gaussian approximation assumption of accumulative fractions of prostate motion from all patients on a population level. The recorded displacements from all 24 patients who had more than 30 fractions of tracking data were combined into one large array. Again, the same Gaussian distribution test was used to quantify the displacement at an all-fraction, all-patient level.

Results

Prostate motion correlation in AP and SI directions

Visually, the AP and SI displacement tends to move together as shown in the first row in Figure 1. The result for the correlation analysis is shown in Table 1. Thirty-nine percent of the fractions show strong correlation in the AP/SI direction, whereas only 12% and 14% of the fractions show strong correlation in RL/AP and RL/SI directions. Moreover, 42% and 44% of the fractions show no correlation in RL/AP and RL/SI directions. The high percentage of correlation in the AP/SI direction (61% medium or strong correlation) is consistent with the longitudinal oblique motion of the prostate, and likely from the effect of respiration on an organ confined within the genitourinary dia-phragm with the rectum sitting posterior and the bladder sitting superiorly.

Prostate motion distribution measurement: individual fraction

The results are shown in Table 2. Four examples were selected for presentation as shown in Figure 1.

Case 1 (first column): This case shows relatively small and stable prostate motion throughout the fraction. The histograms revealed that the displacement in all directions are normally distributed, indicating a random motion in all directions. The 3-dimensional displacement spatial distribution shown in the last row indicates a uniform, small motion in all directions. This is the ideal case where the patient has both constrained physical movement and little internal organ motion.

Case 2 (second column): This case shows high range of motion with several excursions. In contrast to case 1, the histogram reveals that none of the displacement in any direction is normally distributed. All of them have multiple peaks on their histogram plots. Accordingly, there is no clear pattern of the spatial distribution of the transponder displacement in all directions as shown in the last row.

Case 3 (third column): This case shows an overall stable motion with a period of excursion toward the end of the treatment. The histogram reveals that the displacement in RL directions shows a nice Gaussian distribution. However, the displacements are not normally distributed in all other directions. As shown in Table 2, 13.6% of all 1024 available fractions had Gaussian distribution in the RL directional the percentage is higher than other directions. The spatial distribution of the transponder displacement shows an elongated pattern in oblique direction, indicating a larger range of motion in AP and SI directions.

Case 4 (fourth column): This case shows an overall stable but drifting prostate motion. The histogram reveals that the displacement in RL, AP, SI, and oblique directions are not normally distributed where multiple peaks in histogram are observed. However, the displacement in total direction is normally distributed. As shown in the last row, the spatial distribution of the transponder displacement shows an overall uniform distribution in all directions regardless of the non-Gaussian distribution in each individual direction.

In all directions, the non-Gaussian distribution is more common. The RL direction has a higher percentage of Gaussian distribution than other directions.

Prostate motion distribution measurement: total fractions of one patient

The results are shown in Table 3. Three examples were selected for presentation as shown in Figure 2. The number of tracking data is large, and the plot in the first row is downsampled to select every tenth data for presentation purpose.

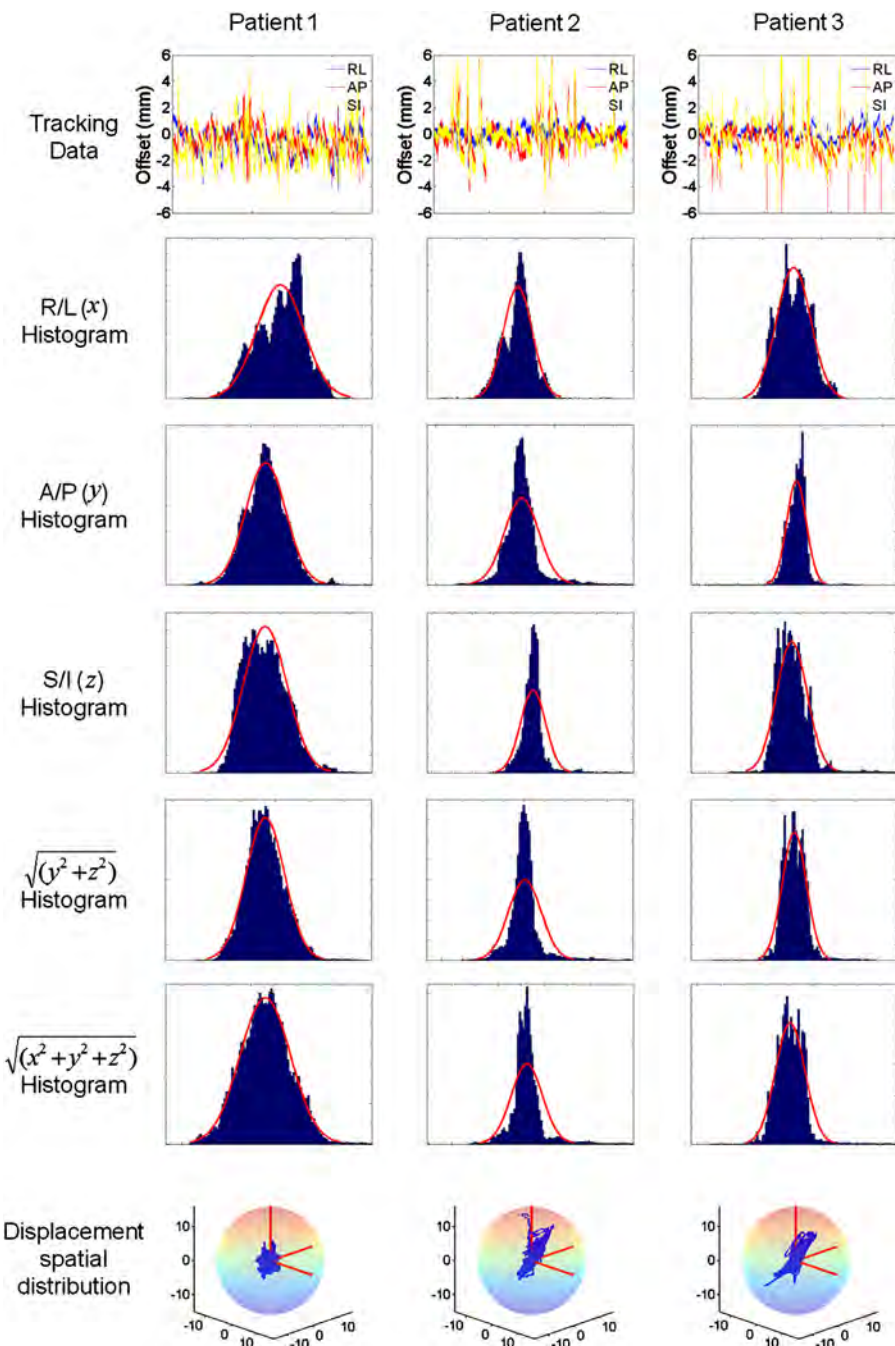


Fig. 2. Examples of prostate motion distribution analysis for individual patient including all fractions. (Row 1) Downsampled raw tracking data. (Rows 2-7) Histogram plot for right/left (RL), anteroposterior (AP), superoinferior (SI), oblique, and total directions. (Red line) Gaussian fit of the tracking data overlaid on the histogram. (Row 7) Spatial distribution of the transponder displacement. The upper limit of the x, y, and z axes are set to 12 mm.

Patient 1 (first column): This patient shows overall confined range of prostate motion throughout the treatment. The histograms revealed that the displacements in all directions are normally distributed except the RL direction. The 3-dimensional displacement spatial distribution shown in the last row indicates a uniformly distributed motion in all directions.

Patient 2 (second column): This patient shows higher range of motion. In contrast to patient 1, the histogram reveals that none of the displacements in any direction is normally distributed. Even though all the histogram is single peaked, the distribution fails to

satisfy the normality test based on the shape of the histogram. Accordingly, the spatial distribution of the transponder displacement shows an elongated distribution in oblique direction, indicating a larger range of motion in the AP and SI directions.

Patient 3 (third column): This patient has large range of motion. Although the histogram revealed the normal distribution in the RL and oblique directions, all the displacements in other directions do not have normal distribution. The spatial distribution of the transponder displacement again shows an elongated distribution in oblique direction.

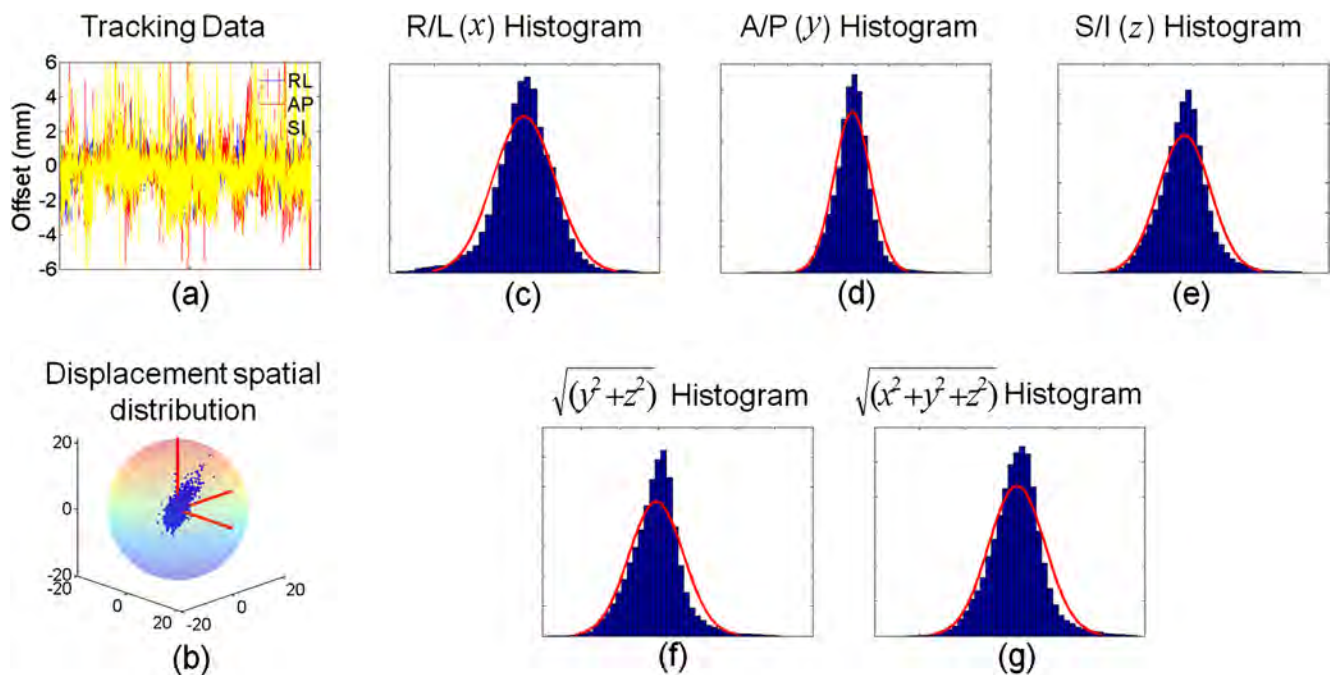


Fig. 3. Examples of the displacement analysis. (a) Downsampled raw tracking data. (b) Spatial distribution of the transponder displacement. The upper limit of the x, y, and z axes are set to 20 mm. (c-f) Histogram plot for right/left (RL), anteroposterior (AP), superoinferior (SI), oblique, and total directions. (Red line) Gaussian fit of the tracking data overlaid on the histogram.

Again, the non-Gaussian distribution is more common for all directions, and the RL direction has a higher percentage of Gaussian distribution than other directions. A total of 33% and 16.7% of all patients have normally distributed RL and total motion, respectively, and this ratio is approximately twice the percentage for individual fraction for each patient. The accumulative effect from all fractions may explain the increased percentage.

Prostate motion distribution measurement: total fractions from all patients

The results are shown in Figure 3. The number of tracking data is large and the plot in the first row is downsampled to select every hundredth data for presentation purpose. All the tracking data were combined to evaluate whether the Gaussian distribution is a good approximation at a population level. Even through all the histograms have only a single peak (Fig 3b), all of them failed the normality test. The 3-dimensional displacement plot clearly shows an elongated patterned in oblique direction, indicating this trend works at a population level.

Discussion

The intrafraction motion effect is normally modeled and included in the treatment planning as a Gaussian function with random distribution. Bortfeld et al have developed simulation tools and theoretically demonstrated the random motion effect (2, 12). This was also demonstrated using oscillating phantoms experimentally (13-15). Under this assumption, a Gaussian kernel was applied to account for the dose distribution blurring effect caused by organ motion (1, 16). With the 10-Hz real-time tracking data during

radiation therapy, we demonstrated that the simple Gaussian-shaped operator may need to be modified for prostate motion because of its specific characteristics. For instance, the higher magnitude of prostate motion is observed in AP and SI directions because of the oblique longitudinal movement of respiration on an organ sitting within the genitourinary diaphragm and confined by the bladder superiorly and the rectum inferiorly. It is also possible that the muscles making up the pelvic floor may limit prostate motion, mainly in the oblique direction. Indeed, this effect is also observed by other researchers previously. Using kV fluoroscopy, Adamson and Wu reported a population mean of 0.1-, 0.5-, and 0.6-mm motion in the RL, AP, and SI axes, respectively (17, 18). Using gold seed fiducial markers, Quan et al observed the mean intrafraction prostate displacements were -0.03, 0.21, and -0.86 mm in RL, AP, and SI directions, respectively (19). Using Calypso, Wiloughby et al reported prostate displacements of 0.9 ± 0.35 mm, 3.61 ± 3.13 mm, and 3.92 ± 4.32 mm in RL, AP, and SI directions, respectively (9). Our results are consistent with the previous clinical reports and suggest that a modified operator should be used to account for the spatial variation of organ motion.

The visual correlation of AP and SI directions has been reported using Calypso electromagnetic tracking system. Kupelian et al reported that a visual review of 1157 fractions of tracking data reveals that the longitudinal (SI direction) and vertical (AP direction) data tend to move together over the tracking session, consistent with the prostate motion being affected by bladder and rectum filling (8). Likewise, we quantified the level of correlation and found about 61% of the tracking data exhibiting strong to medium correlation in AP and SI directions. This conclusion demonstrated that PTV may be reduced in RL direction independently.

Our findings of non-Gaussian prostate motion on an individual and population level are likely a result of the anatomical design of the pelvic floor. The pelvic floor is constituted by the pelvic

diaphragm, which is shaped like a funnel, with muscular partitions caused by the levator ani and the coccygeus muscle. The levator ani is further subclassified into the iliococcygeus, pubococcygeus, and puborectalis muscles. All 3 of these muscles run horizontally from an AP direction and are situated laterally to the prostate to form a sling around the prostate (Appendix A, Fig 1). It is possible that because of this sling formation around the prostate motion, the prostate is limited to motion mainly in the AP and SI directions. Laterally, the muscles may limit this motion. The muscular construct of the pelvic floor is one possible explanation of our findings. It is likely that respiration causes motion of the prostate in the SI direction, whereas the anterior deflection of the rectum deflects this motion towards the SP direction. Another explanation may be that the bladder located superiorly and the rectum located posteriorly, both of which are compressible organs, may also allow for the SI directional movement of the prostate because of respiration to be deflected in an AP direction, especially if the bladder and rectum are full. Hence, this could also cause the prostate to exhibit more of an oblique motion as noted in our findings. Further work by our group is ongoing to assess the impact of respiration and may provide us with further insights about the physiological process that lead to the oblique motion patterns noted in our study.

Conclusion

Prostate motion cannot be accurately described using Gaussian distribution, disregarding the spatial characteristic of the organ motion. The high-frequency, real-time treatment tracking data indicate that the prostate motion is highly correlated in the AP and SI directions, indicating an oblique motion preference. In addition, the spatial distribution of prostate motion is elongated in an oblique direction at the individual fraction level, individual patient level, and population level. Future dosimetric kernel's modeling prostate motion will need to be modified.

References

1. van Herk M. Errors and margins in radiotherapy. *Semin Radiat Oncol* 2004;14:52-64.
2. Thomas B, Kimmo J, Michael G, et al. Effects of intra-fraction motion on IMRT dose delivery: Statistical analysis and simulation. *Phys Med Biol* 2002;47:2203.
3. Prostate motion during a course of IMRT: The value of daily ultrasound to guide portal localization and correct for random and systematic errors. *Radiother Oncol* 2000;56:S105.
4. Tanyi JA, He T, Summers PA, et al. Assessment of planning target volume margins for intensity-modulated radiotherapy of the prostate gland: Role of daily inter- and intrafraction motion. *Int J Radiat Oncol Biol Phys* 2010;78:1579-1585.
5. Webb S. Motion effects in (intensity modulated) radiation therapy: A review. *Phys Med Biol* 2006;51:R403.
6. Li HS, Chetty IJ, Enke CA, et al. Dosimetric consequences of intrafraction prostate motion. *Int J Radiat Oncol Biol Phys* 2008;71:801-812.
7. Curtis W, Khan M, Magnelli A, et al. Relationship of imaging frequency and planning margin to account for intrafraction prostate motion: Analysis based on real-time monitoring data. *Int J Radiat Oncol Biol Phys* 2013;85:700-706.
8. Kupelian P, Willoughby T, Mahadevan A, et al. Multi-institutional clinical experience with the Calypso System in localization and continuous, real-time monitoring of the prostate gland during external radiotherapy. *Int J Radiat Oncol Biol Phys* 2007;67:1088-1098.
9. Willoughby TR, Kupelian PA, Pouliot J, et al. Target localization and real-time tracking using the Calypso 4D localization system in patients with localized prostate cancer. *Int J Radiat Oncol Biol Phys* 2006;65:528-534.
10. Noel C, Parikh PJ, Roy M, et al. Prediction of intrafraction prostate motion: Accuracy of pre- and post-treatment imaging and intermittent imaging. *Int J Radiat Oncol Biol Phys* 2009;73:692-698.
11. Lilliefors HW. On the Kolmogorov-Smirnov test for the exponential distribution with mean unknown. *J Am Stat Assoc* 1969;64:387-389.
12. Bortfeld T, Jiang SB, Rietzel E. Effects of motion on the total dose distribution. *Semin Radiat Oncol* 2004;14:41-51.
13. Steve BJ, Cynthia P, Khaled MAJ, et al. An experimental investigation on intra-fractional organ motion effects in lung IMRT treatments. *Phys Med Biol* 2003;48:1773.
14. Li HSCI, Enke CA, Foster RD, et al. The dosimetric consequences of intra-fraction prostate motion in intensity modulation. *Int J Radiat Oncol Biol Phys* 2001;51:214.
15. Langen KM, Chauhan B, Siebers JV, et al. The dosimetric effect of intrafraction prostate motion on step-and-shoot intensity-modulated radiation therapy plans: Magnitude, correlation with motion parameters, and comparison with helical tomotherapy plans. *Int J Radiat Oncol Biol Phys* 2012;84:1220-1225.
16. van Herk M, Remeijer P, Lebesque JV. Inclusion of geometric uncertainties in treatment plan evaluation. *Int J Radiat Oncol Biol Phys* 2002;52:1407-1422.
17. Adamson J, Wu Q. Prostate intrafraction motion assessed by simultaneous kilovoltage fluoroscopy at megavoltage delivery I: Clinical observations and pattern analysis. *Int J Radiat Oncol Biol Phys* 2010;78:1563-1570.
18. Adamson J, Wu Q. Prostate intrafraction motion assessed by simultaneous kV fluoroscopy at MV delivery II: Adaptive strategies. *Int J Radiat Oncol Biol Phys* 2010;78:1323-1330.
19. Quon H, Loblaw DA, Cheung PCF, et al. Intra-fraction motion during extreme hypofractionated radiotherapy of the prostate using pre- and post-treatment imaging. *Clin Oncol* 2012;24:640-645.

Ultrasonic Nakagami-parameter characterization of parotid-gland injury following head-and-neck radiotherapy: A feasibility study of late toxicity

Xiaofeng Yang

Radiation Oncology, Emory University, Atlanta, Georgia 30322

Srini Tridandapani

Radiology and Imaging Sciences, Emory University School of Medicine, Atlanta, Georgia 30322;

School of Electrical and Computer Engineering, Georgia Institute of Technology, Atlanta, Georgia 30332;

and Winship Cancer Institute, Emory University, Atlanta, Georgia 30322

Jonathan J. Bejtler and David S. Yu

Radiation Oncology, Emory University, Atlanta, Georgia 30322 and Winship Cancer Institute, Emory University, Atlanta, Georgia 30322

Ning Wu and Yuefeng Wang

Radiation Oncology, Emory University, Atlanta, Georgia 30322

Deborah W. Bruner

Radiation Oncology, Emory University, Atlanta, Georgia 30322; Winship Cancer Institute, Emory University, Atlanta, Georgia 30322; and School of Nursing, Emory University, Atlanta, Georgia 30322

Walter J. Curran and Tian Liu^{a)}

Radiation Oncology, Emory University, Atlanta, Georgia 30322 and Winship Cancer Institute, Emory University, Atlanta, Georgia 30322

(Received 17 February 2013; revised 24 December 2013; accepted for publication 1 January 2014; published 28 January 2014)

Purpose: The study aims to investigate whether Nakagami parameters—estimated from the statistical distribution of the backscattered ultrasound radio-frequency (RF) signals—could provide a means for quantitative characterization of parotid-gland injury resulting from head-and-neck radiotherapy.

Methods: A preliminary clinical study was conducted with 12 postradiotherapy patients and 12 healthy volunteers. Each participant underwent one ultrasound study in which ultrasound scans were performed in the longitudinal, i.e., vertical orientation on the bilateral parotids. For the 12 patients, the mean radiation dose to the parotid glands was 37.7 ± 9.5 Gy, and the mean follow-up time was 16.3 ± 4.8 months. All enrolled patients experienced grade 1 or 2 late salivary-gland toxicity (RTOG/EORTC morbidity scale). The normal parotid glands served as the control group. The Nakagami-scaling and Nakagami-shape parameters were computed from the RF data to quantify radiation-induced parotid-gland changes.

Results: Significant differences in Nakagami parameters were observed between the normal and postradiotherapy parotid glands. Compared with the control group, the Nakagami-scaling parameter of the postradiotherapy group decreased by 25.8% ($p < 0.001$), and the Nakagami-shape parameter decreased by 31.3% ($p < 0.001$). The area under the receiver operating characteristic curve was 0.85 for the Nakagami-scaling parameter and was 0.95 for the Nakagami-shape parameter, which further demonstrated the diagnostic efficiency of the Nakagami parameters.

Conclusions: Nakagami parameters could be used to quantitatively measure parotid-gland injury following head-and-neck radiotherapy. Moreover, the clinical feasibility was demonstrated and this study provides meaningful preliminary data for future clinical investigation. © 2014 American Association of Physicists in Medicine. [<http://dx.doi.org/10.1118/1.4862507>]

Key words: ultrasonic tissue characterization, Nakagami imaging, radiation toxicity, parotid gland, xerostomia, head-and-neck cancer

1. INTRODUCTION

The Nakagami distribution is a statistical tool that has been applied in the context of ultrasonic imaging to characterize the biomechanical properties of backscattered radio-frequency (RF) signals from biological tissues. Relatively new, ultrasonic tissue characterization using Nakagami statistics has shown early success in the detection of organ abnormalities, such as those of the breast^{1,2} and liver.³ The purpose of this

study is to evaluate the ability of Nakagami statistics to noninvasively determine and quantify parotid-gland injury following head-and-neck cancer radiotherapy.

Parotid-gland injury is a prevalent side effect suffered by many patients receiving head-and-neck cancer radiotherapy. In the multidisciplinary approach to treating head-and-neck cancer, radiotherapy (RT) plays an essential role in improving locoregional tumor control and overall survival. However, radiotherapy is frequently associated with acute and

chronic complications.⁴ One of the most prevalent and distressing side effects is xerostomia (dry mouth), secondary to radiation-induced parotid-gland injury.⁵ Xerostomia causes pain, difficulty in speech and swallowing, and increased rates of dental caries and oral infection. Although recognized for decades, diagnostic tools to objectively measure radiation-induced parotid-gland injury are still limited in the clinic.

Several imaging studies have been conducted using CT, MRI, MR sialography, PET scintigraphy, and ultrasound to evaluate the severity of salivary-gland injury;⁶⁻¹³ each imaging modality shows some degree of success. Volume reduction of parotid glands after radiotherapy has been observed with CT and MRI. MR sialography was proposed as a functional imaging tool to assess the salivary ductal flow. Astrinidou *et al.* demonstrated, in a pilot study of nine patients, that MR sialography can depict radiation-induced changes to the salivary glands and ducts post-RT without the use of any contrast medium or stimulation. Wada *et al.* measured the salivary secretion function response to salivary secretion stimulation in a perspective study of 16 patients before and after head-and-neck cancer RT, and found irradiated salivary gland had strong influence on the clinical severity of xerostomia. Another promising imaging technology is salivary-gland scintigraphy with 99 mTc-pertechnetate. Salivary gland scintigraphy is a PET imaging technique that can provide a detailed functional evaluation of salivation as it measures the amount and speed of radioisotope uptake and excretion of the major glands. Buus *et al.* showed individual radiation response of parotid glands using dynamic PET. In recent years, several groups have reported ultrasound studies on radiation-induced parotid-gland injury. In conventional B-mode studies, increased heterogeneity was reported in the post-RT parotid glands.¹⁴ In the Doppler study of late toxicity in parotid glands, significant differences were demonstrated in the high peak systolic velocity, resistive index, and pulsatility between postirradiation and healthy parotid glands.^{7,15} Compared with CT, MR, MR sialography, and PET scintigraphy, ultrasound imaging of the parotid glands has its unique advantages, such as being the safest (nonradiation), fastest (5-10 min scan) and most cost-effective imaging modality.

Recently, our group conducted a series of ultrasound studies to explore statistical methods of quantitatively characterizing ultrasound images of parotid glands. Based on B-mode images, we demonstrated that first-order statistical features derived from the echo histogram¹⁶ and second-order statistical texture features based on the gray level co-occurrence matrix (GLCM) could provide quantitative measures of postradiotherapy parotid injury.¹⁷ Herein, we describe our current efforts in developing a Nakagami method based on analysis of the backscattered RF signals. Similar to previous B-mode based statistical methods, the Nakagami method provides quantitative measures of parotid changes induced by radiation. Distinct from the B-mode based methods, the Nakagami approach reveals the biomechanical properties of tissue microstructures, such as the arrangement and concentration of scatterers. In addition, Nakagami parameters are less dependent on system parameters, such as dynamic range and time-gain compensation.¹⁸

We have conducted a clinical study to test the feasibility of using Nakagami parameters to detect radiation-induced parotid-gland injury. This paper describes ultrasound examination of the parotid glands, summarizes the Nakagami statistical model, details the data processing procedures, and then presents the Nakagami parameter results of post-RT parotid glands. The Nakagami parameters of post-RT parotid glands were compared with a group of healthy controls.

2. MATERIALS AND METHODS

2.A. Patient population and treatment

Between January 2011 and March 2012, we enrolled 24 participants (including 12 healthy volunteers and 12 patients post-RT for head-and-neck malignancies). Our institutional review board approved this study, and written informed consent was obtained from all participants. The eligibility criteria for both healthy volunteers include: (1) Participants must be ≥ 18 years of age. (2) No prior radiotherapy to the head and neck or surgery to the head and neck for any reason. (3) No prior malignancies or chemotherapy. (4) No salivary gland malignancy. (5) No salivary gland disease, e.g., Sjögren's syndrome. The eligibility criteria for the post-RT patients include: (1) Participants must be ≥ 18 years of age; (2) Biopsy-confirmed histological diagnosis of squamous cell carcinoma of the oropharynx, hypopharynx, larynx, or patients with unknown primary tumor with unilateral metastases to the neck nodes; (3) Radiation volume $\geq 80\%$ of major salivary glands (parotids); (4) No salivary gland malignancy; (5) No salivary gland disease, e.g., Sjögren's syndrome; and (6) Clinically confirmed xerostomia.

All 12 patients developed Grade 1 (mild dry-mouth, eight patients) or Grade 2 (medium dry-mouth, four patients) post-RT xerostomia. Xerostomia was patient-reported and its level was evaluated using the standard RTOG/EORTC grading system. The 12 post-RT patients ranged in age from 41 to 65 years (mean: 55.4 ± 8.6 years). They include ten males and two females with primary tumor sites in the oral cavity (six patients), oropharynx (three patients), larynx (one patient), and nasopharynx (one patient). All patients had previously received RT for their primary tumors and the radiation regions involved the bilateral neck. The cross-sectional study is based on late toxicity, and all patients were scanned between 1 and 2 years post-RT.

Serving as the control group for the study, the healthy subjects (seven males and five females) ranged in age from 27 to 67 years (mean: 51.0 ± 12.0 years). The exclusion criteria for the control group included subjects with a clinical history of salivary gland diseases or head-and-neck cancers. Thus, the concept of using the Nakagami statistical model to evaluate radiation-induced parotid-gland injury was tested with a total of 24 post-RT and 24 normal parotid glands.

2.B. Data acquisition

Each participant underwent one ultrasound study of his/her right and left parotid glands. As described in the previous

report, we established a standardized protocol for ultrasound scanning of the parotid glands.¹⁷ All ultrasound studies were performed using a clinical scanner (SonixTouch, Ultrasonix, British Columbia, Canada) with a linear array transducer (L14-5/38 probe, 128 elements). All ultrasound data were acquired with the same settings: 10 MHz frequency, 1.00 cm focal length, 3 cm depth, 72% gain, and 80-dB dynamic range. The frequency bandwidth of the transducer is 14–5 MHz; its wavelength at 10 MHz is 0.154 mm; and the incident pulse length is around 0.3 mm. The time-gain-compensation (TGC) was set to the maximum value for all depths. All participants were scanned in the upright seated position, and ultrasound scans of the bilateral parotids were performed in the longitudinal (vertical) orientation. During the ultrasound scan, a thin layer of ultrasound gel was used to ensure good coupling between the face and the ultrasound probe. The probe was placed perpendicular to the scan surface with minimal pressure applied to the face.

During the ultrasound examination, B-mode images of the parotid glands and their corresponding RF echo signals were acquired simultaneously. All B-mode images were saved in 8-bit gray scale, with intensity ranging from 0 to 255. Each B-mode image contained 488 (width) \times 356 (depth) pixels, and the image size was 3.8 cm (width) \times 3.0 cm (depth). In this report, all B-mode images and corresponding parameter images were displayed to the depth of 2 cm since the thickness of the parotid gland was less than 1.5 cm. All RF data were acquired at 20 MHz sampling frequency. Each image frame contained 256 scan lines and 784 sample points/line. The Nakagami parameters were generated from the RF signals.

2.C. Data analysis—The Nakagami statistical model

The Nakagami analysis was applied to the envelope of the backscattered RF echo signals. The theoretical framework for Nakagami imaging relates statistical parameters to properties of the examined tissue.^{19–21} The formulation treats the backscattered ultrasound envelope signals as random signals. Our analysis characterizes tissue structures in terms of a stochastic probability distribution function (PDF) under the Nakagami statistical model. The PDFs of the ultrasonic backscattered envelope X under the Nakagami statistical model are given by

$$f(x) = \frac{2u^u}{\Gamma(u)\omega^u} x^{2u-1} \exp\left(-\frac{u}{\omega}x^2\right) \cdot W(x), \quad (1)$$

where $\Gamma(\cdot)$ is the gamma function and $W(\cdot)$ is the step function.

The Nakagami distribution has two parameters: a scaling parameter and a shape parameter. Let $E(\cdot)$ denote the statistical mean. The Nakagami scaling parameter ω is obtained from the following equation:

$$\omega = E(X^2). \quad (2)$$

The Nakagami shape parameter u is estimated from the second and fourth moments of the backscattered envelopes. The

Nakagami shape parameter u is obtained from the following equation:

$$u = \frac{E^2[X^2]}{E[X^2 - E^2(X^2)]^2}. \quad (3)$$

The Nakagami u is a shape parameter for the PDF. When $u = 1$, the Nakagami distribution reduces to a Rayleigh distribution. When $0 \leq u < 1$, the envelope distribution is considered to be pre-Rayleigh. When $u > 1$, the distribution conforms to post-Rayleigh. This property makes the Nakagami distribution a general model for ultrasonic backscattering.

When the region of interest (ROI) contains randomly located scatterers with varying scattering cross sections, the envelope statistics are likely to be pre-Rayleigh, and Nakagami-shape parameter u is typically between 0.5 and 1.²² Similarly, when some spatial periodicity exists among the scatterers within the resolution cell, then the envelope statistics are post-Rayleigh, and u becomes larger than unity.²³ Typically, u is used as a means to quantify the effective number of scatterers in the resolution cell. This interpretation can be obtained by noting that the random variable $Y = X^2$ follows a gamma distribution, and interpreting the physical relationships between u and the effective number obtained from the gamma distribution.²⁴

We have developed Nakagami statistical analysis procedures to quantitatively characterize the parotid glands. The procedures were carried out through an in-house MATLAB[®] (Mathworks, Inc., Natick, MA) software routine; Fig. 1 is a diagram showing the sequence of operations in our method.

- Step 1: The first step is a B-mode display either from the saved B-mode image file or a digital reconstruction of the B-mode image from the RF data. The B-mode image serves to identify the overall anatomic structures and guides the ROI selection.
- Step 2: The second step is to determine the ROI for the Nakagami analysis. The ROI could either be fixed or chosen by physicians based on their clinical judgment and need. In this proof of principle study, we used a fixed ROI, which is the region of the entire parotid gland contoured. For future studies, physicians could identify an

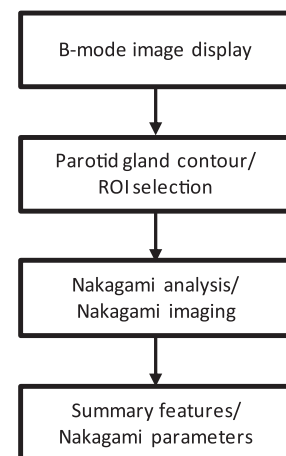


FIG. 1. Diagram showing Nakagami parameter characterization procedures.

ROI, e.g., in the high radiation dose region where radiation damages are expected. We note that the accuracy of the parotid-gland Nakagami imaging depends on the accuracy of parotid-gland contour. In this study, an experienced radiologist (S.T.) contoured all parotid glands on the B-mode images. The radiologist was blinded to the Nakagami-parameter images to eliminate any possible bias. The parotid glands are superficial structures wrapping around the mandibles and are often clear on the ultrasound B-mode images. In an earlier study, we demonstrated the interobserver and intraobserver reliability of manual contouring of the parotid glands.¹⁷

- Step 3: We reconstruct ultrasound envelope images by applying the Hilbert transform to the sampled RF signals. The ultrasonic Nakagami parameter images are generated using a square sliding window to process the envelope signals of the whole 2D ultrasound image. The window size is important in Nakagami parameter calculation and determines the resolution of the Nakagami images. There is a trade-off between the resolution and statistical stability of the Nakagami estimation. A previous study suggested that the appropriate sliding window length should be equal or higher than three times the pulse length of the incident ultrasound. In the context of evaluating parotid-gland injury, the resolution is not a major concern. The challenge presented here was to capture the subtle changes induced by radiation and the statistical stability was crucial. Therefore, we used a relatively larger sliding window size of $1.5 \text{ mm} \times 1.5 \text{ mm}$ (37 samples points by 10 lines) to generate Nakagami parameter images, which is 5 times the pulse length to ensure the statistical stability. The sliding window was moved at 1 pixel/point along the depth. With each sliding window, Nakagami scaling and shape parameters were computed through Eqs. (2) and (3).
- Step 4: We calculate the mean and standard deviation of the Nakagami scaling and shape parameters for the contoured ROI or the parotid gland. The performance of using the Nakagami parameters to discriminate the normal parotids and irradiated parotids were evaluated using the probability value (i.e., p value) calculated from the unpaired t -test.

3. RESULTS

We first present two illustrative cases, one healthy volunteer and one post-RT patient, to show how Nakagami parameters can be employed to assay radiation-induced parotid-gland changes. Figures 2(a) and 2(b) show the ultrasound images of the right and left parotid glands of a 40-year-old healthy volunteer. On the B-mode image, the parotid glands, contoured in dotted yellow lines, are visualized and exhibit homogeneous echo texture. Figures 3(a) and 3(b) show the B-mode images of the right and left parotid glands of a 63-year-old woman postradiotherapy. She received external beam radiation treatment between March and May 2009 for squamous cell carcinoma of the mandibular gingiva. The primary tumor received a total dose of 65.0 Gy. The mean radiation dose delivered to

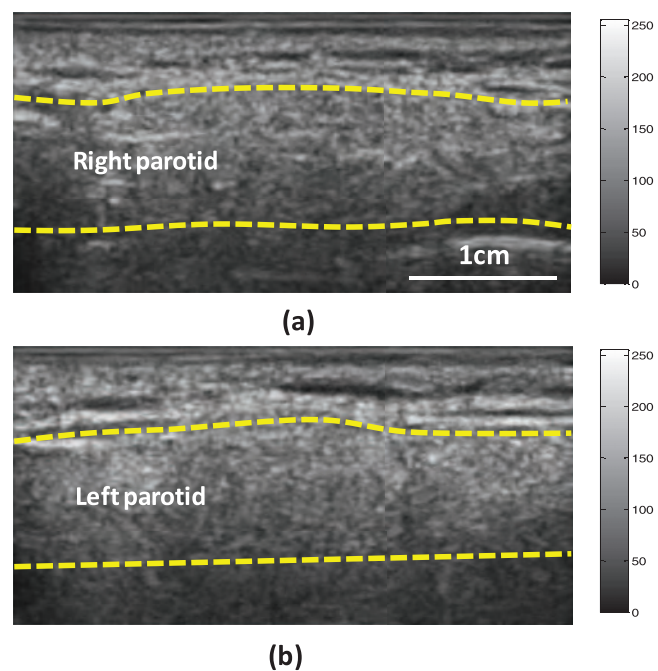


FIG. 2. Ultrasound images of normal parotid glands (between the dotted yellow lines). The B-mode images of the right parotid gland (a) and the left parotid gland (b) of a 40-year-old healthy volunteer show homogeneous echo texture.

the left parotid gland was 30.6 Gy, and to the right parotid gland was 28.9 Gy. She underwent ultrasound scanning 22 months after treatment completion. At the time of scanning, she was experiencing moderate (grade 2) xerostomia according to the physician's (J.J.B.) clinical assessment. In contrast to the normal parotid glands, the irradiated parotid glands

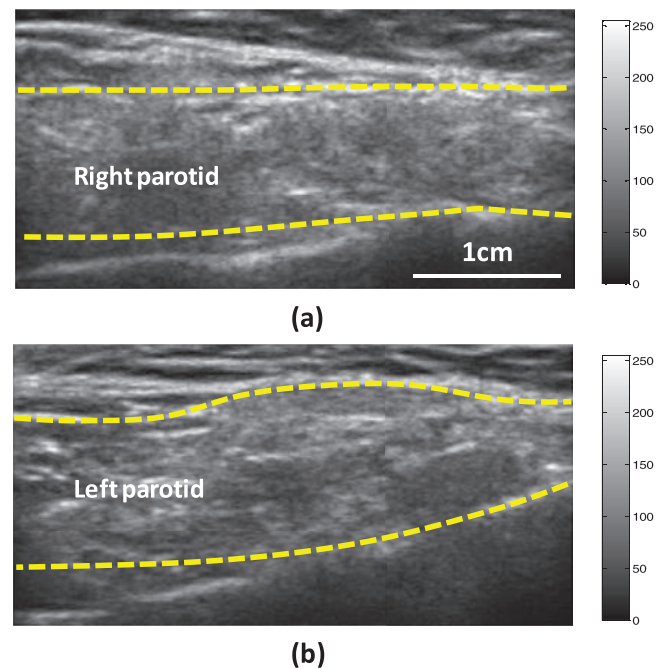


FIG. 3. Ultrasound images of the irradiated parotid glands (between the dotted yellow lines). The B-mode images of the right parotid gland (a) and the left parotid gland (b) of a 63-year-old woman 22 months post-RT show heterogeneous echo texture.

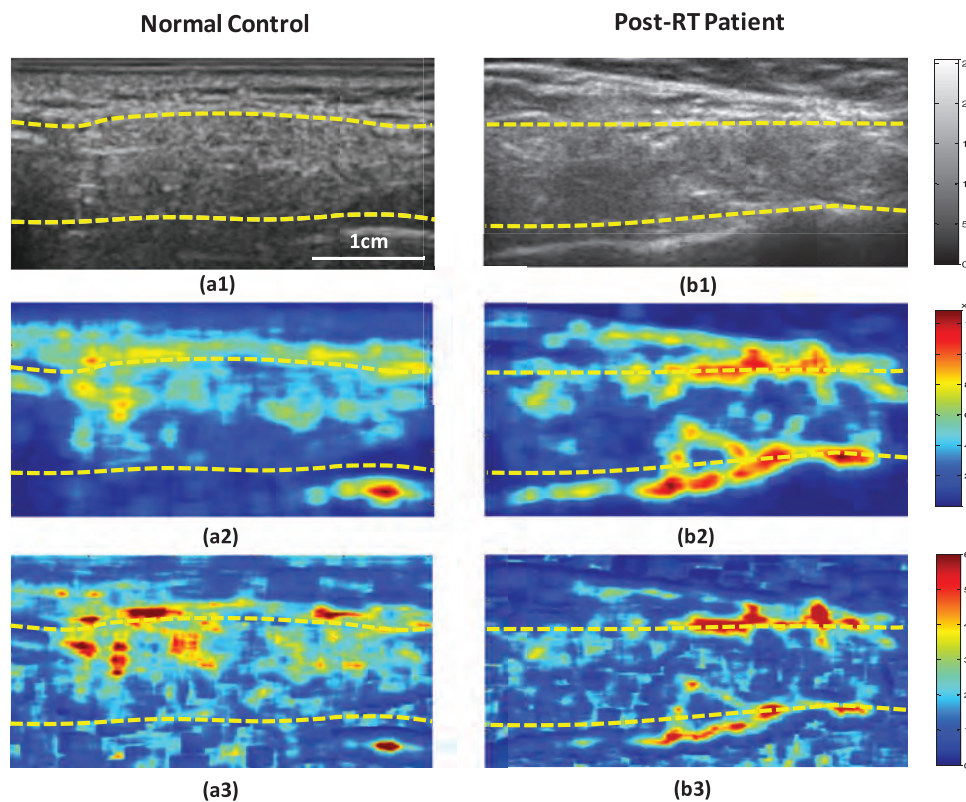


FIG. 4. Comparison of B-mode image and Nakagami parameter maps of a normal control and a post-RT patient (the parotid glands are between the dotted yellow lines). Left column (normal parotid gland): (a1) B-mode image of the parotid, (a2) Nakagami-scaling image, and (a3) Nakagami-shape image. Right column (post-RT parotid gland): (b1) B-mode image of the parotid, (b2) Nakagami-scaling image, and (b3) Nakagami-shape image. The maximum values of Nakagami scaling and shape parameters were assigned dark red shadings, which changed from blue to red with increasing value. Compared with the control, decreased Nakagami shape and scaling parameter values were observed in the post-RT patient.

revealed heterogeneity on the ultrasound images. Hypoechoic (darker) areas and hyperechoic (brighter) lines or spots are visible on the B-mode images of these parotid glands. The Nakagami-scaling and Nakagami-shape parameter images of the right parotid glands were generated according to the algorithmic procedure described above. The mean Nakagami-scaling parameter values were $(3.18 \pm 0.71) \times 10^8$ for the normal parotid glands, and $(2.36 \pm 0.56) \times 10^8$ for the irradiated parotid glands. The mean Nakagami-shape parameter values were 1.82 ± 0.26 for the normal parotid glands, and 1.25 ± 0.21 for the irradiated parotid glands. As shown in Fig. 4, a pseudocolor scale was applied to clearly reveal the information in the two Nakagami maps. The maximum values of u and ω were assigned a dark red shading, which changed from blue to red with increasing value. Decreases in Nakagami-scaling and Nakagami-shape parameter values of the post-RT can be seen on the Nakagami-shape and Nakagami-scaling maps.

We generated the Nakagami scaling and shape images for all the participants (22 post-RT and 24 normal parotid glands) and calculated the average and the standard deviation of the Nakagami parameters of the parotid glands. Since the well-known study by Eisbruch *et al.* reported that a mean dose of 26 Gy or above to the parotid glands resulted in significant decreases in the salivary flow upon stimulation, the mean dose of 26 Gy has been used as the threshold in radiotherapy.²⁵ Accordingly, we excluded two parotid glands which received a mean dose less than 26 Gy. Overall, the mean radiation dose of the 22 parotid glands was 37.7 Gy (range: 27.9–66.0 Gy). The mean follow-up period between the completion of RT and the ultrasound scan was 16.3 months (STD = 4.8 months, range 13.3–23.9 months). Table I shows the Nakagami-scaling and Nakagami-shape parameter values of the normal and post-RT groups. Compared with the control group, the Nakagami-scaling parameter of the post-RT group decreased by 25.8% ($p < 0.001$), and the Nakagami-shape

TABLE I. Nakagami parameters (mean \pm standard deviation) of the control and post-RT groups.

Nakagami parameters	Control group ($n = 24$)	Post-RT group ($n = 22$)	Percentage change	p value
Scaling parameters (10^8)	3.18 ± 0.71	2.36 ± 0.56	-25.8%	<0.001
Shape parameters	1.82 ± 0.26	1.25 ± 0.21	-31.3%	<0.001

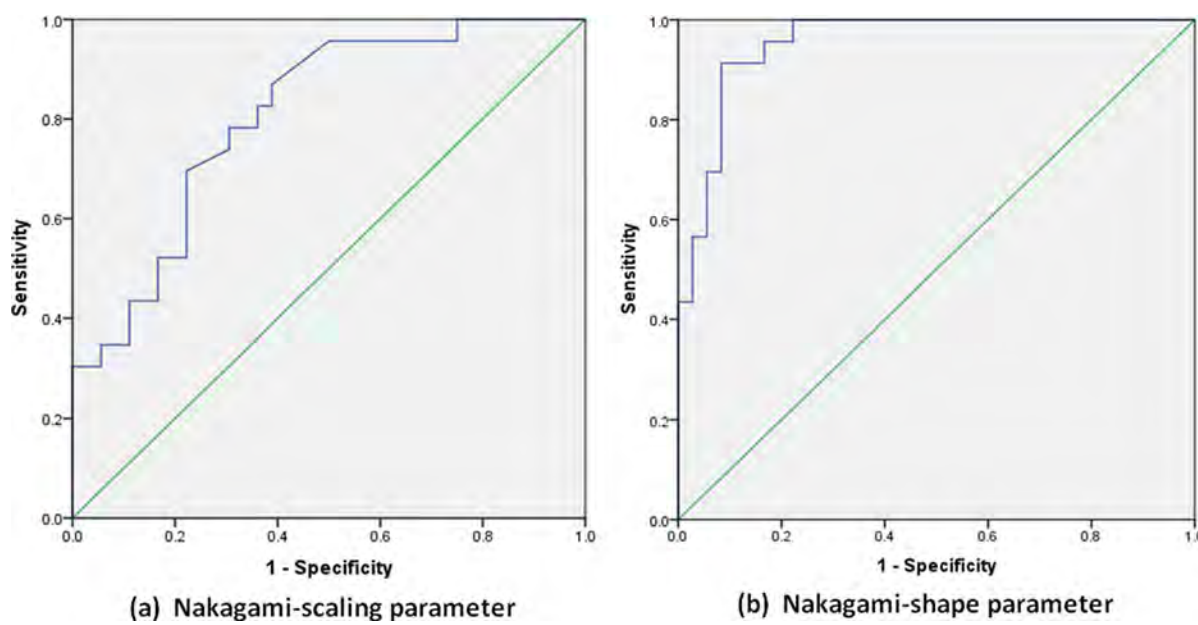


FIG. 5. ROC curves of the Nakagami-scaling parameter (a) and Nakagami-shape parameter (b).

parameter decreased by 31.3% ($p < 0.001$). Statistical analyses confirmed significant differences between post-RT and normal parotid glands in both Nakagami parameters.

The predictive discriminatory powers on the parotid gland injury of the two Nakagami parameters were further analyzed with receiver operating characteristic (ROC) curves. The diagnostic accuracy of Nakagami parameters was measured by calculating its sensitivity and specificity, as shown in Fig. 5. For the Nakagami-scaling parameter, the cutoff value in the ROC curves, estimated by maximizing both sensitivity and specificity, was 2.74×10^8 and its area under the ROC curve was 0.81. For the Nakagami-shape parameter, the cutoff value for the Nakagami-shape parameter was 1.57 and the area under the ROC curve was 0.95.

4. DISCUSSION

The use of radiotherapy to treat head-and-neck cancer often involves radiation exposure to the parotid glands, which frequently leads to the debilitating and long-term side effect xerostomia. In this study, we have developed Nakagami-statistical-analysis procedures to evaluate parotid-gland injury associated with head-and-neck cancer radiotherapy. The premise behind our Nakagami-parameter method is that high doses of radiation alter the structural and morphological characteristics of the parotid glands, and that these alterations can cause observable changes in the Nakagami parameters.

Nakagami-scaling and Nakagami-shape parameters, estimated from the statistical distribution of the ultrasonic RF signals backscattered from tissues, were employed as a means for characterizing the biomechanical properties of the parotid glands. In this pilot study of 24 participants, we have demonstrated its clinical efficacy in characterizing radiotherapy-associated parotid-gland injury. Compared with the control group, significant decreases in Nakagami-scaling and Nakagami-shape parameters were observed in irradiated

parotid glands. Histologically, normal parotid glands consist entirely of serous cells—with densely packed translucent secretory granules.^{5,26–29} These densely packed cells and granules provide uniform and highly reflective interfaces for the ultrasound beams,³⁰ accounting for the homogeneous and hyperechoic appearance of the normal parotid glands. Therefore, the Nakagami-scaling parameter, which is the power of the mean envelope intensity, is higher for the normal parotid gland than the irradiated gland. Following head-and-neck radiotherapy, radiation-induced chronic sialadenitis, with inflammatory infiltrate and fibrosis was reported in the irradiated parotid glands.^{27,31–33} Compared with normal tissues, fibrotic tissues are associated with increased sound speed and density, which make the scatterers exhibit a higher degree of variability. Previous studies have shown that fibrotic tissues tend to have the backscattered statistics of pre-Rayleigh distribution.^{3,34} With the higher intensity variation resulting from inflammation and fibrosis, the Nakagami-shape parameter shows a decreasing trend postradiation.

Despite large patient-to-patient variation, the Nakagami parameters were able to detect radiation-induced parotid-gland injury. With an area under the ROC curve of 0.81, the Nakagami-scaling parameter had good diagnostic accuracy in detecting radiation-induced parotid injury. With an area under the ROC of 0.95, the Nakagami-shape parameter had an excellent accuracy in the diagnosis of parotid-gland injury. One of the 12 enrolled patients was a 70-year male with squamous cell carcinoma of the oropharynx. Between November and December 2009, he received 70 Gy to the primary tumor; his right parotid gland received 0 Gy radiation while his left parotid gland received a mean dose of 27.2 Gy. He subsequently developed Grade 1 xerostomia and the parotid glands were scanned with ultrasound during his 1-year follow-up (Fig. 6). Compared with the nonirradiated right parotid gland, the Nakagami-scaling parameter of the irradiated left parotid gland decreased by 22% (right parotid: $\omega = 2.79 \times 10^8$, left

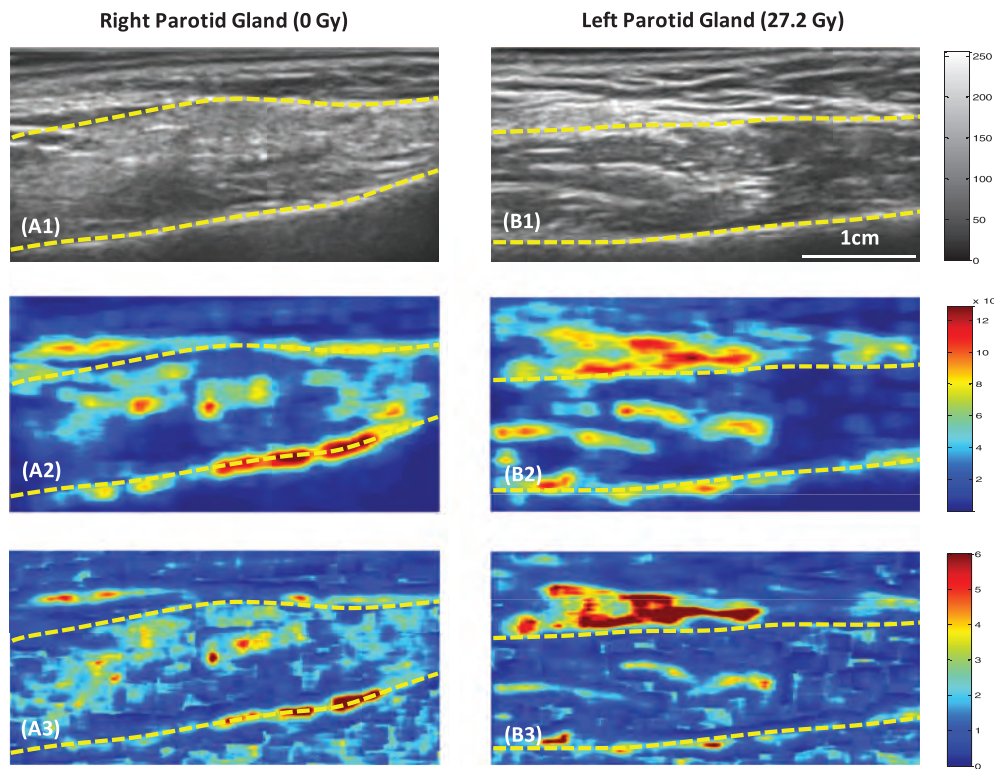


FIG. 6. A 70-year-old patient with squamous cell carcinoma of oropharynx cancer who has received 70 Gy to the primary tumor. The mean dose to the right parotid was 0 Gy and the mean dose to the left parotid gland was 27.2 Gy.

parotid: $\omega = 2.18 \times 10^8$) and the Nakagami-shape parameter of the left parotid gland decreased by 35% (right parotid: $u = 1.70$, left parotid: $u = 1.11$).

The Nakagami statistical analysis method utilizes RF signals obtained from the clinical ultrasound scanner, and this study's findings are consistent with those of previous B-mode based ultrasound studies.^{7, 14, 15, 35, 36} We should note that our Nakagami-parameter analysis, B-mode image and Doppler method are in general independent and complementary. B-mode image provides evidence of the anatomical changes and Power Doppler method provides evidence of the blood-vessel abnormalities of the parotid-gland. Yet Nakagami-parameter imaging has several advantages over the conventional B-mode based studies. As described in the theoretical framework,¹⁹ the backscattered ultrasound RF signals depend on the biomechanical properties (arrangement and concentrations) of the tissue microstructures. Nakagami distribution provides a general model that describes the RF signals; therefore Nakagami parameters provide measures of these biomechanical properties. Moreover, Nakagami distribution describes the statistics of ultrasound signals. Nakagami parameters yield more consistent measures that are independent of system factors such as dynamic range and system gain.¹⁸ Furthermore, Nakagami parameters enable extraction of the weak scattering information that may be lost in the conventional B-mode image interpretation.¹⁸ Such subtle changes may be critical in capturing radiation-induced tissue changes.

While this report has addressed parotid-gland toxicity assessment in head-and-neck radiotherapy, the underlying principles and analyses are applicable to assays of other or-

gans, such as the breast and prostate. For future work, we will continue to enroll patients in our clinical study, and we will investigate the correlations between Nakagami-parameter measured parotid injuries with treatment factors (i.e., radiation dose) and clinical endpoints (i.e., patient-reported xerostomia).

5. CONCLUSIONS

Nakagami statistical analysis, which complements conventional B-mode imaging, has the potential of providing key imaging signatures for ultrasonic characterization of radiation-induced changes in the parotid glands. These procedures remove measurement artifacts and provide objective quantitative, statistical descriptions of tissue microstructures. This pilot study demonstrated the clinical feasibility and significant differences in Nakagami-shape and Nakagami-scaling parameters of the parotid glands between healthy volunteers and post-RT groups. Ultrasound Nakagami parameters provide statistical features of the parotid tissues. Nakagami methods may provide a useful metric of parotid-gland injury secondary to radiation that can be further developed into a low-cost tool for normal-tissue assessment following head-and-neck radiotherapy.

ACKNOWLEDGMENTS

This research was supported in part by National Cancer Institute (NCI) Grant No. CA114313, DOD PCRP Award W81XWH-13-1-0269 and Georgia Cancer Coalition.

Dr. Srinivas Tridandapani's work was supported in part by National Institute of Biomedical Imaging and Bioengineering (NIBIB) Grant No. K23EB013221. The authors report no conflicts of interest in conducting the research.

- ^aAuthor to whom correspondence should be addressed. Electronic mail: tliu34@emory.edu; Telephone: (404)778-1848; Fax: (404)778-4139.
- ¹Y. Y. Liao, P. H. Tsui, and C. K. Yeh, "Classification of benign and malignant breast tumors by ultrasound B-scan and Nakagami-based images," *J. Med. Biol. Eng.* **30**, 307–312 (2010).
- ²Y. Y. Liao, C. H. Li, P. H. Tsui, C. C. Chang, W. H. Kuo, K. J. Chang, and C. K. Yeh, "Strain-compounding technique with ultrasound Nakagami imaging for distinguishing between benign and malignant breast tumors," *Med. Phys.* **39**, 2325–2333 (2012).
- ³M. C. Ho, J. J. Lin, Y. C. Shu, C. N. Chen, K. J. Chang, C. C. Chang, and P. H. Tsui, "Using ultrasound Nakagami imaging to assess liver fibrosis in rats," *Ultrasonics* **52**, 215–222 (2012).
- ⁴K. S. C. Chao, J. O. Deasy, J. Markman, J. Haynie, C. A. Perez, J. A. Purdy, and D. A. Low, "A prospective study of salivary function sparing in patients with head-and-neck cancers receiving intensity-modulated or three-dimensional radiation therapy: Initial results," *Int. J. Radiat. Oncol.* **49**, 907–916 (2001).
- ⁵A. Eisbruch, N. Rhodus, D. Rosenthal, B. Murphy, C. Rasch, S. Sonnis, C. Scarantino, and D. Brizel, "How should we measure and report radiotherapy-induced xerostomia?," *Semin. Radiat. Oncol.* **13**, 226–234 (2003).
- ⁶A. C. Houweling, T. Schakel, C. A. T. van den Berg, M. E. P. Philippens, J. M. Roesink, C. H. J. Terhaard, and C. P. J. Raaijmakers, "MRI to quantify early radiation-induced changes in the salivary glands," *Radiother. Oncol.* **100**, 386–389 (2011).
- ⁷M. Ying, V. W. C. Wu, and D. L. W. Kwong, "Comparison of sonographic appearance of normal and postradiotherapy parotid glands: A preliminary study," *Ultrasound Med. Biol.* **33**, 1244–1250 (2007).
- ⁸N. Gritzmann, T. Rettenbacher, A. Hollerweger, P. Macheiner, and E. Hubner, "Sonography of the salivary glands," *Eur. Radiol.* **13**, 964–975 (2003).
- ⁹E. Astreinidou, C. P. J. Raaijmakers, J. M. Roesink, C. H. J. Terhaard, J. J. W. Lagendijk, and L. W. Bartels, "3D MR sialography protocol for postradiotherapy follow-up of the salivary duct system," *J. Magn. Reson. Imaging* **24**, 556–562 (2006).
- ¹⁰A. Wada, N. Uchida, M. Yokokawa, T. Yoshizako, and H. Kitagaki, "Radiation-induced xerostomia: Objective evaluation of salivary gland injury using MR sialography," *Am. J. Neuroradiol.* **30**, 53–58 (2009).
- ¹¹A. Nomayr, M. Lell, R. Sweeney, W. Bautz, and P. Lukas, "MRI appearance of radiation-induced changes of normal cervical tissues," *Eur. Radiol.* **11**, 1807–1817 (2001).
- ¹²E. J. Bialek, W. Jakubowski, P. Zajkowski, K. T. Szopinski, and A. Osmolski, "US of the major salivary glands: Anatomy and spatial relationships, pathologic conditions, and pitfalls," *Radiographics* **26**, 745–764 (2006).
- ¹³S. Buus, C. Grau, O. L. Munk, A. Rodell, K. Jensen, K. Mouridsen, and S. Keiding, "Individual radiation response of parotid glands investigated by dynamic C-11-methionine PET," *Radiother. Oncol.* **78**, 262–269 (2006).
- ¹⁴S. C. H. Cheng, V. W. C. Wu, D. L. W. Kwong, and M. T. C. Ying, "Assessment of post-radiotherapy salivary glands," *Br. J. Radiol.* **84**, 393–402 (2011).
- ¹⁵S. C. Cheng, M. T. Ying, D. L. Kwong, and V. W. Wu, "Sonographic appearance of parotid glands in patients treated with intensity-modulated radiotherapy or conventional radiotherapy for nasopharyngeal carcinoma," *Ultrasound Med. Biol.* **37**, 220–230 (2011).
- ¹⁶X. Yang, S. Tridandapani, J. J. Beitler, D. S. Yu, E. J. Yoshida, W. J. Curran, and T. Liu, "Ultrasound GLCM texture analysis of radiation-induced parotid-gland injury in head-and-neck cancer radiotherapy: An in vivo study of late toxicity," *Med. Phys.* **39**, 5732–5740 (2012).
- ¹⁷X. Yang, S. Tridandapani, J. J. Beitler, D. S. Yu, E. J. Yoshida, W. J. Curran, and T. Liu, "Ultrasound histogram assessment of parotid gland injury following head-and-neck Radiotherapy: A feasibility study," *Ultrasound Med. Biol.* **38**, 1514–1521 (2012).
- ¹⁸P. H. Tsui and C. C. Chang, "Imaging local scatterer concentrations by the Nakagami statistical model," *Ultrasound Med. Biol.* **33**, 608–619 (2007).
- ¹⁹P. M. Shankar, "Ultrasonic tissue characterization using a generalized Nakagami model," *IEEE Trans. Ultrason. Ferroelectr.* **48**, 1716–1720 (2001).
- ²⁰P. H. Tsui, C. K. Yeh, Y. Y. Liao, C. C. Chang, W. H. Kuo, K. J. Chang, and C. N. Chen, "Ultrasonic Nakagami imaging: A strategy to visualize the scatterer properties of benign and malignant breast tumors," *Ultrasound Med. Biol.* **36**, 209–217 (2010).
- ²¹R. F. Wagner, M. F. Insana, and D. G. Brown, "Statistical properties of radio-frequency and envelope-detected signals with applications to medical ultrasound," *J. Opt. Soc. Am. A* **4**, 910–922 (1987).
- ²²P. M. Shankar, "A model for ultrasonic scattering from tissues based on the K distribution," *Phys. Med. Biol.* **40**, 1633–1649 (1995).
- ²³P. M. Shankar, "A general statistical model for ultrasonic backscattering from tissues," *IEEE Trans. Ultrason. Ferroelectr. Freq. Control* **47**, 727–736 (2000).
- ²⁴P. M. Shankar, V. A. Dumane, J. M. Reid, V. Genis, F. Forsberg, C. W. Piccoli, and B. B. Goldberg, "Classification of ultrasonic B-mode images of breast masses using Nakagami distribution," *IEEE Trans. Ultrason. Ferroelectr.* **48**, 569–580 (2001).
- ²⁵A. Eisbruch, R. K. Ten Haken, H. M. Kim, L. H. Marsh, and J. A. Ship, "Dose, volume, and function relationships in parotid salivary glands following conformal and intensity-modulated irradiation of head and neck cancer," *Int. J. Radiat. Oncol., Biol., Phys.* **45**, 577–587 (1999).
- ²⁶R. Henriksson, O. Frojd, H. Gustafsson, S. Johansson, C. Yi-Qing, L. Franzen, and L. Bjermer, "Increase in mast cells and hyaluronic acid correlates to radiation-induced damage and loss of serous acinar cells in salivary glands: The parotid and submandibular glands differ in radiation sensitivity," *Br. J. Cancer* **69**, 320–326 (1994).
- ²⁷L. Radfar and D. A. Sirois, "Structural and functional injury in minipig salivary glands following fractionated exposure to 70 Gy of ionizing radiation: An animal model for human radiation-induced salivary gland injury," *Oral Surg. Oral Med. Oral Pathol. Oral Radiol. Endod.* **96**, 267–274 (2003).
- ²⁸A. Eisbruch, "Clinical aspects of IMRT for head-and-neck cancer," *Med. Dosim.* **27**, 99–104 (2002).
- ²⁹A. L. Grehn, H. Gustafsson, L. Franzen, L. E. Thornell, and R. Henriksson, "Ultrastructural morphometry of parotid acinar cells following fractionated irradiation," *Oral Oncol.* **33**, 23–28 (1997).
- ³⁰P. Katz, D. M. Hartl, and A. Guerre, "Clinical ultrasound of the salivary glands," *Otolaryngol. Clin. North Am.* **42**, 973–1000 (2009).
- ³¹G. Seifert, "Etiology and differential diagnosis of sialadenitis," *Laryngorhinootologie* **74**, 274–281 (1995).
- ³²A. Teymoortash, N. Simolka, C. Schrader, M. Tiemann, and J. A. Werner, "Lymphocyte subsets in irradiation-induced sialadenitis of the submandibular gland," *Histopathology* **47**, 493–500 (2005).
- ³³A. W. T. Konings, H. Faber, F. Cotteleer, A. Vissink, and R. P. Coppen, "Secondary radiation damage as the main cause for unexpected volume effects: A histopathologic study of the parotid gland," *Int. J. Radiat. Oncol., Biol., Phys.* **64**, 98–105 (2006).
- ³⁴P. H. Tsui, C. C. Chang, M. C. Ho, Y. H. Lee, Y. S. Chen, C. C. Chang, N. E. Huang, Z. H. Wu, and K. J. Chang, "Use of Nakagami statistics and empirical mode decomposition for ultrasound tissue characterization by a nonfocused transducer," *Ultrasound Med. Biol.* **35**, 2055–2068 (2009).
- ³⁵D. C. Howlett, "High resolution ultrasound assessment of the parotid gland," *Br. J. Radiol.* **76**, 271–277 (2003).
- ³⁶V. W. C. Wu, M. T. C. Ying, and D. L. W. Kwong, "Evaluation of radiation-induced changes to parotid glands following conventional radiotherapy in patients with nasopharyngeal carcinoma," *Br. J. Radiol.* **84**, 843–849 (2011).

Diagnostic Accuracy of Ultrasonic Histogram Features to Evaluate Radiation Toxicity of the Parotid Glands:

A Clinical Study of Xerostomia Following Head-and-Neck Cancer Radiotherapy

Xiaofeng Yang, PhD, Srini Tridandapani, PhD, MD, Jonathan J. Bejtler, MD, David S. Yu, PhD, MD, Zhengjia Chen, PhD, Sungjin Kim, MS, Deborah W. Bruner, RN, PhD, FAAN, Walter J. Curran, MD, Tian Liu, PhD

Rationale and Objectives: To investigate the diagnostic accuracy of ultrasound histogram features in the quantitative assessment of radiation-induced parotid gland injury and to identify potential imaging biomarkers for radiation-induced xerostomia (dry mouth)—the most common and debilitating side effect after head-and-neck radiotherapy (RT).

Materials and Methods: Thirty-four patients, who have developed xerostomia after RT for head-and-neck cancer, were enrolled. Radiation-induced xerostomia was defined by the Radiation Therapy Oncology Group/European Organization for Research and Treatment of Cancer morbidity scale. Ultrasound scans were performed on each patient's parotids bilaterally. The 34 patients were stratified into the acute-toxicity groups (16 patients, ≤ 3 months after treatment) and the late-toxicity group (18 patients, > 3 months after treatment). A separate control group of 13 healthy volunteers underwent similar ultrasound scans of their parotid glands. Six sonographic features were derived from the echo-intensity histograms to assess acute and late toxicity of the parotid glands. The quantitative assessments were compared to a radiologist's clinical evaluations. The diagnostic accuracy of these ultrasonic histogram features was evaluated with the receiver operating characteristic (ROC) curve.

Results: With an area under the ROC curve greater than 0.90, several histogram features demonstrated excellent diagnostic accuracy for evaluation of acute and late toxicity of parotid glands. Significant differences ($P < .05$) in all six sonographic features were demonstrated between the control, acute-toxicity, and late-toxicity groups. However, subjective radiologic evaluation cannot distinguish between acute and late toxicity of parotid glands.

Conclusions: We demonstrated that ultrasound histogram features could be used to measure acute and late toxicity of the parotid glands after head-and-neck cancer RT, which may be developed into a low-cost imaging method for xerostomia monitoring and assessment.

Key Words: Xerostomia; ultrasound; parotid gland; radiation toxicity; sonographic features.

©AUR, 2014

Acad Radiol 2014; ■:1-10

From the Department of Radiation Oncology, Emory University, 1365 Clifton Rd NE, Atlanta, GA 30322 (X.Y., J.J.B., D.S.Y., W.J.C., T.L.); Department of Radiology and Imaging Sciences, Emory University School of Medicine, Atlanta, Georgia (S.T.); Winship Cancer Institute, Emory University, Atlanta, Georgia (S.T., J.J.B., D.S.Y., Z.C., S.K., D.W.B., W.J.C., T.L.); Department of Biostatistics and Bioinformatics, Rollins School of Public Health, Emory University, Atlanta, Georgia (Z.C.); and School of Nursing, Emory University, Atlanta, Georgia (D.W.B.). Received March 6, 2014; accepted May 13, 2014. Funding Sources: This study was funded by National Institutes of Health (CA114313), National Institute of Biomedical Imaging and Bioengineering (K23EB013221), U.S. Department of Defense (W81XWH-13-1-0269) and the Georgia Cancer Coalition. Address correspondence to: T.L. e-mail: tliu34@emory.edu

©AUR, 2014

<http://dx.doi.org/10.1016/j.acra.2014.05.017>

Xerostomia (dry mouth) is a common, often permanent, and debilitating morbidity of radiotherapy (RT) for head-and-neck malignancies (1,2). Patients with severe xerostomia have thick secretions, difficulty in swallowing and speaking, and are at high risk for oral infection and dental caries (3). This symptom burden impairs the quality of life (QoL) of many head-and-neck cancer survivors for months, even years, after treatment (4). It is well established that the main cause of RT-induced xerostomia is irradiation of parotid glands—the major salivary glands producing $\sim 60\%$ of total saliva (1). Recent clinical studies indicate that intensity-modulated radiotherapy (IMRT) provides a significant advantage in sparing the parotid glands

and reducing xerostomia. However, even with the new technology, 17%–30% of patients treated with IMRT still develop permanent xerostomia. There is substantial heterogeneity in parotid gland injury after radiation (5–7).

In the clinic, radiation-induced xerostomia is assessed using patient-based or physician-based grading systems. For example, the Radiation Therapy Oncology Group (RTOG) and the European Organization for Research and Treatment of Cancer (EORTC) established a morbidity scale to evaluate post-RT salivary glands. Specifically, salivary gland toxicity was divided into two categories: acute (≤ 3 months after RT) toxicity and late (> 3 months after RT) toxicity. Physicians assign a score of grade 1 (slight dryness) to grade 4 (necrosis or fibrosis) for acute or late salivary toxicity (8). Such subjective measures of radiation toxicity are prone to intraobserver and interobserver variability. In recent years, many groups have been investigating imaging technologies to evaluate parotid gland injury induced by radiation. Studies using computed tomography (CT), magnetic resonance imaging (MRI), MR sialography, and single-photon emission computed tomography scintigraphy have shown some degree of success in assessing the severity of parotid gland injury and documenting normal tissue response to RT (9–17). However, the high cost, the technical complexity, and the need for dedicated imaging expertise (CT, MRI, or nuclear medicine) preclude their use in routine clinical assessment of xerostomia.

The concept of ultrasound imaging to evaluate parotid gland injury is especially attractive because ultrasound is safe, portable, widely available, easy to use, and cost effective. In particular, because parotid glands are superficial structures wrapping around the mandible, they are readily amenable to ultrasound examination. Ultrasound, therefore, is the standard imaging modality in the assessment of salivary gland diseases such as neoplasms, Sjogren syndrome, sialadenitis, and sialolithiasis. However, there is limited information in the literature about evaluation of radiation-induced parotid gland injury or xerostomia using ultrasound (9). Previously, we have proposed an ultrasound technology based on quantitative analysis of echo-intensity histogram to assess RT-associated parotid gland injury (18). A family of sonographic features was derived from the echo histogram to quantify the echogenicity and heterogeneity of parotid glands, which is used to assess the morphologic and architectural integrity of post-RT parotids. In a pilot study of 12 patients, we demonstrated the clinical feasibility of using these echo histogram features in evaluating parotid gland toxicity after RT (18).

Another appealing factor of ultrasound histogram evaluation of RT-related parotid gland toxicity is that it could eliminate variations in subjective radiologic interpretations of ultrasound images. To further explore this ultrasound technology in the evaluation of RT-induced parotid gland injury, we embarked on this clinical study. The primary objective was to determine the diagnostic accuracy of echo-intensity histogram parameters in the assessment of RT-induced parotid gland injury. In addition, we compared the quantitative ultrasound examination with radiologists' evaluation of acute and

late toxicities of RT to parotid glands. Special emphasis was placed on acute toxicity for patients within 3 months of cancer treatment. We want to emphasize the importance of developing safe and easy ultrasound technology to detect acute toxicity because early detection of parotid gland injury could enable early interventions to minimize long-term morbidity.

MATERIALS AND METHODS

Study Population

The study was approved by our institutional review board and in compliance with the Health Insurance Portability and Accountability Act. The eligibility criteria for post-RT patients included 1) patients aged ≥ 18 years; 2) biopsy-confirmed histologic diagnosis of squamous cell carcinoma of oropharynx, hypopharynx, larynx, or patients with unknown primary tumor with unilateral metastases to neck lymph nodes; 3) radiation volume $\geq 80\%$ of major salivary glands (parotids) and ≥ 27 Gy delivered to parotid glands; 4) no salivary gland malignancy; 5) no salivary gland disease, for example, Sjogren syndrome; and 6) clinically confirmed xerostomia based on the RTOG/EORTC acute- and late-toxicity scoring scheme. We have also enrolled a normal control group, and the eligibility criteria for healthy volunteers included 1) participants aged ≥ 18 years; 2) no prior RT or surgery to head and neck for any reason; 3) no prior malignancies or chemotherapy; 4) no salivary gland malignancy; and 5) no salivary gland disease, for example, Sjogren syndrome.

We stratified our post-RT patients into the acute-toxicity and late-toxicity groups. In general, radiation toxicity is divided into two categories: acute (early) and chronic (late) toxicity (19). Acute toxicity is defined as toxicity occurring within the first 3 months of treatment completion, whereas late toxicity is defined as toxicity occurring beyond 3 months after treatment. RT-induced salivary injury is a complex process and evolves through phases (8). During the early course of RT (often 4–6 weeks), most patients may experience acute salivary gland swelling and pain. A reduction in salivary function can begin within 1 week of RT and usually persists afterward (20). For some patients, salivary function gradually recovers within 1–2 years after RT. And for others, acute salivary toxicity may progress to chronic radiation-induced sialadenitis and fibrosis.

Ultrasound Imaging Protocol

As described in previous reports, we established a standardized protocol for ultrasound scanning to facilitate quantitative evaluation of parotid glands (18,21). In brief, ultrasound studies were performed using a clinical scanner (SonixTouch; Ultrasonix, British Columbia, Canada) with a linear array transducer (L14-5/38 probe, 128 elements). All ultrasound B-mode images were acquired with the same settings: 10-MHz center frequency, 1.00-cm focal length, 3-cm depth, 72% gain, 31 frames per second, and 80-dB dynamic range.

The standard B-mode image consists of 256 levels in gray scale.

Each participant underwent one ultrasound study of the bilateral parotid glands. All participants were scanned in the upright seated position, and longitudinal (vertical) ultrasound scans were performed on the bilateral parotids. During the ultrasound scan, a thin layer of ultrasound gel was used to ensure good coupling between the face and the ultrasound probe. The probe was placed perpendicular to the scan surface with minimal pressure applied to the face.

Echo-Intensity Histogram Analysis of the Parotid Gland Ultrasound Image

The sonographic features were derived from the echo-intensity histograms to quantitatively characterize the integrity of the parotid glands. The echo histogram presents a graphical distribution of the pixel intensities within the region of interest. All parotid glands were contoured by a radiologist (S.T.). In a previous study, we have shown that interobserver and intraobserver agreement was excellent in contouring parotids (18). The echo-intensity histograms and sonographic features used to assess radiation damage to the parotid glands were generated by in-house signal processing software written in MatLab (Mathworks, Natick, MA).

As described in the previous article (18), six sonographic features were computed from the histogram to provide additional quantification of the echogenicity and heterogeneity of the parotid glands (Fig 1). These can be summarized briefly as follows: The I_{peak} is the peak intensity value of the histogram. $W_{-3 \text{ dB}}$ is the -3 dB intensity width of the histogram. W_{low} and W_{high} capture the width of the low-intensity ($<50\% I_{peak}$) and the high-intensity ($>50\% I_{peak}$) portions of the histogram, respectively. A_{low} and A_{high} characterize the area under the low-intensity and high-intensity portions of the curve. These sonographic features provide quantitative measures of the echogenicity (I_{peak}), homogeneity ($W_{-3 \text{ dB}}$), and heterogeneity (W_{low} , W_{high} , A_{low} , and A_{high}) of parotid glands. All histograms are normalized to the peak intensity I_{peak} . In other words, all probability distribution is divided by the maximum probability value at I_{peak} .

Subjective Radiologic Evaluation

An experienced radiologist (S.T. with over 10 years' experience), blinded to the ultrasound histogram findings, retrospectively evaluated all the ultrasound images and classified the echogenicity of the glands as hypoechoic (lower intensity), isoechoic, or hyperechoic (higher intensity) to adjacent musculature. The echotexture heterogeneity was assessed and classified as mild, moderate, or severe heterogeneity.

Statistical Analysis

Radiologic evaluations of the echogenicity and heterogeneity were compared using the chi-squared test among various

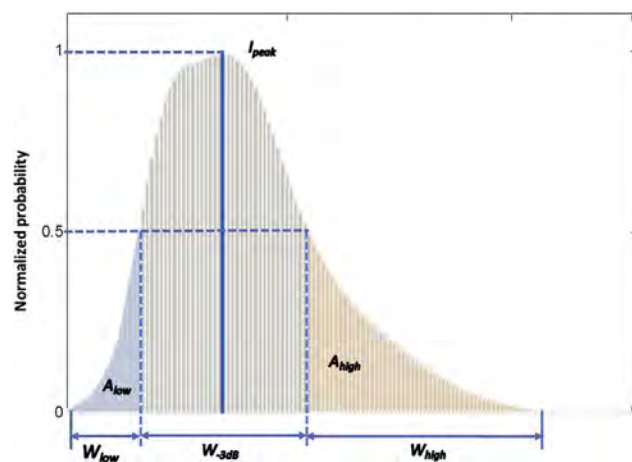


Figure 1. Echo-intensity histogram: histogram parameters quantify the intensity distribution of the parotid gland.

groups. Analysis of variance, Kruskal-Wallis test, or Wilcoxon rank sum test were used to compare each of the six sonographic features among various groups.

The predictive discriminatory powers on patient's toxicity status of the six sonographic features were further analyzed with receiver operating characteristic (ROC) analysis (22). The ability of these sonographic features to predict toxicity status was determined using ROC curves and measuring the area under the curve (AUC). Whether the AUCs of ROC curves were different from 0.5, which means no ability to predict toxicity, was tested with chi-squared tests. An AUC value between 0.8 and 0.9 indicates good accuracy, and an AUC between 0.9 and 1 indicates excellent accuracy in a diagnostic test. The diagnostic accuracy of a sonographic feature was measured by calculating its sensitivity and specificity. The cutoff value in the ROC curves was estimated while maximizing both sensitivity and specificity. The significance levels were set at .05 for all tests. The SAS statistical package V9.3 (SAS Institute, Inc., Cary, NC) was used for all data analysis.

RESULTS

A total of 47 subjects, consisting of 34 post-RT patients and 13 healthy volunteers, were included in this study. The control group consisted of 13 healthy volunteers (age, 51 ± 11 years). All enrolled patients had received IMRT for head-and-neck malignancies and were clinically diagnosed with grade 1 or grade 2 salivary gland toxicity. The 34 post-RT patients were further stratified into two groups. 1) Acute-toxicity group: sixteen patients received RT for head-and-neck malignancies within 3 months (age, 62 ± 7 years; follow-up time, 1.59 ± 0.79 months). For the acute-toxicity group, the mean dose to the primary tumor was 68.1 ± 3.7 Gy, and the mean dose to the parotid glands was 40.0 ± 14.8 Gy. All patients experienced RTOG grade 1 or 2 acute salivary gland toxicity. 2) Late-toxicity group: eighteen patients received RT for head-and-neck malignancies more than 3 months before imaging (age, 61 ± 7 years; follow-up time,

TABLE 1. Patient and Treatment Characteristics

Covariate	Level	Group, n (%) or Mean (\pm Standard Deviation)	
		Acute Toxicity Group (N = 16)	Late Toxicity Group (N = 18)
Age		62.3 (\pm 7.7)	60.7 (\pm 7.3)
Gender	Female	2 (12.5)	4 (22.2)
	Male	14 (87.5)	14 (77.8)
Primary tumor site	Head (orbit)	0 (0)	1 (5.6)
	Larynx	1 (6.3)	3 (16.7)
	Nasal cavity	1 (6.3)	0 (0)
	Oral cavity	1 (6.3)	2 (11.1)
	Pharynx	3 (18.8)	1 (5.6)
	Sinus	2 (12.5)	0 (0)
	Tongue	4 (25.0)	6 (33.3)
	Tonsil	3 (18.8)	4 (22.2)
	Unknown	0 (0)	1 (5.6)
	Vocal cord	1 (6.3)	0 (0)
Histology	Adenocarcinoma	2 (12.5)	1 (5.6)
	Squamous cell carcinoma	13 (81.3)	17 (94.4)
	Undifferentiated carcinoma	1 (6.3)	0 (0)
T stage	T1	2 (12.5)	3 (16.7)
	T2	6 (37.5)	5 (27.8)
	T3	2 (12.5)	2 (11.1)
	T4	6 (37.5)	6 (33.3)
	Tx	0 (0)	2 (11.1)
N stage	N0	3 (18.8)	1 (5.6)
	N1	1 (6.3)	2 (11.1)
	N2	11 (68.8)	11 (61.1)
	N3	1 (6.3)	3 (16.7)
	Nx	0 (0)	1 (5.6)
M stage	M0	14 (87.5)	18 (100)
	Mx	2 (12.5)	0 (0)
Concurrent chemotherapy	No	4 (25)	1 (5.6)
	Yes	12 (75)	17 (94.4)

20.14 \pm 10.36 months). All patients in this group experienced grade 1 or 2 late salivary gland toxicity. For the late-toxicity group, the median radiation dose to the primary tumor was 67.8 \pm 3.8 Gy, and the mean dose to the parotid glands was 36.3 \pm 11.3 Gy. The patient and treatment characteristics—age, follow-up time, gender, primary tumor site, histology, stage, and chemotherapy—are summarized in Table 1 for both acute- and late-toxicity groups.

Ultrasound Images and Histograms: Individual Subjects

Three representative cases were selected, one from each group, for presentation as shown in Figure 2.

- Normal case: This case of a 40-year-old healthy volunteer shows a normal parotid gland that appears homogeneous and has increased echogenicity relative to adjacent muscle on the ultrasound image. As described earlier, with the B-mode echo intensity ranges between 0 and 255, the histogram reveals a Gaussian (symmetric) distribution

centered at the peak intensity of 79. The narrow 3-dB bandwidth ($W_{-3 \text{ dB}} = 39$) indicates relatively homogenous distribution. The area under the low-intensity portion of the curve (ie, below A_{low}) is 5.4, and the area under the high-intensity portion of the curve (ie, above A_{high}) is 8.3; whereas the width of the low-intensity portion (W_{low}) is 39, and the width of the high-intensity portion (W_{high}) is 89.

- Case with acute toxicity: This case is a 58-year-old patient who had completed RT for his laryngeal cancer 1 month before imaging. He experienced mild xerostomia and was clinically diagnosed with RTOG grade 1 acute salivary gland toxicity. On the ultrasound image, the post-RT looks less homogeneous with multiple hypoechoic areas which may be due to patches of inflammatory infiltrate. The histogram reveals a non-Gaussian distribution with a peak intensity of 30. Compared to the normal parotid gland, the I_{peak} shifted to the lower intensity which may be mainly due to inflammatory response (darker area in the ultrasound image). The widened 3-dB bandwidth ($W_{-3 \text{ dB}} = 43$) indicates relatively heterogeneous

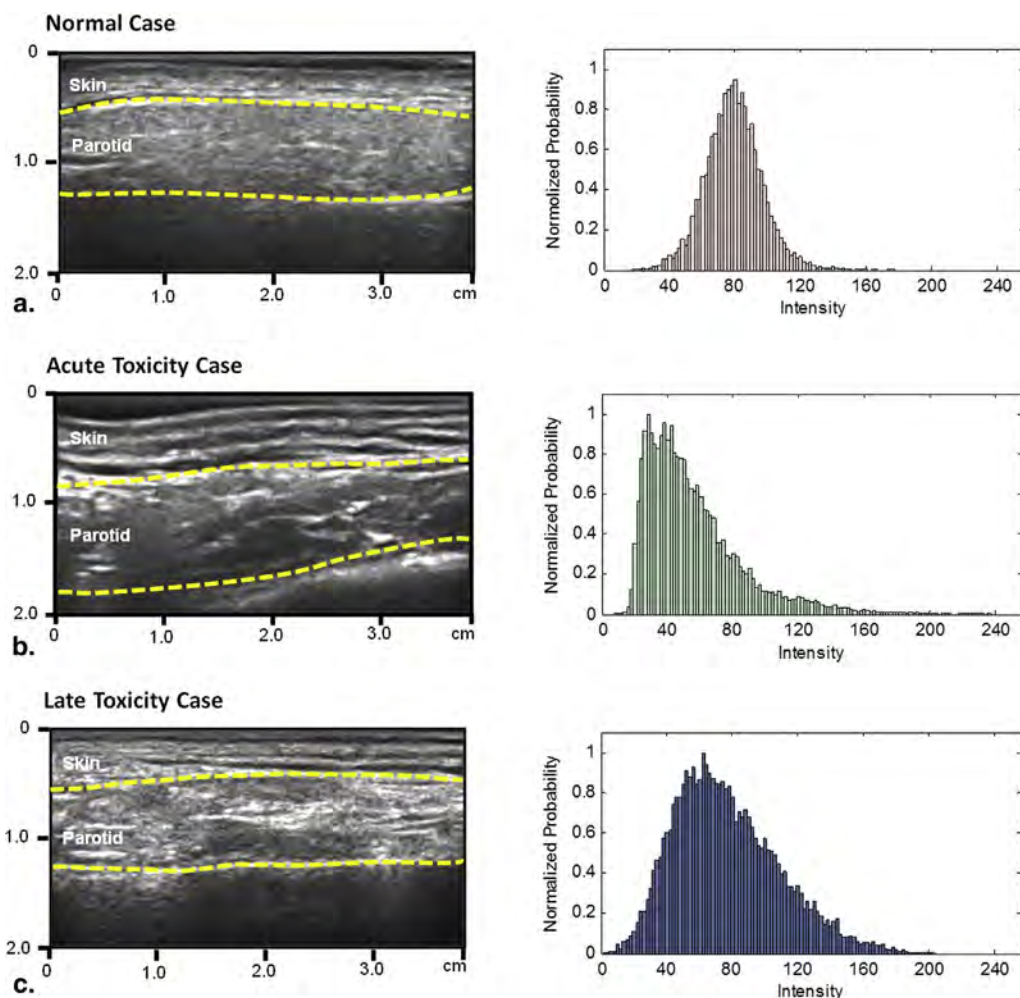


Figure 2. Parotid ultrasound images and histograms of three cases: **(a)** normal case of a 40-year-old healthy volunteer; **(b)** acute-toxicity case of a 58-year-old patient with laryngeal cancer, 1 month after radiotherapy (RT); **(c)** late-toxicity case of a 60-year-old laryngeal cancer patient, 18 months after RT. The dashed yellow lines delineate the parotid glands. Homogeneous texture was observed in the normal parotid gland **(a)** and heterogeneous textures in parotid glands with acute toxicity **(b)** and late toxicity **(c)**.

distribution. The area under the low-intensity portion of the curve (ie, below A_{low}) is 1.9, and the area under the high-intensity portion of the curve (ie, above A_{high}) is 13.0; whereas the width of the low-intensity portion (W_{low}) is 18, and the width of the high-intensity portion (W_{high}) is 179.

- Case with late toxicity: This case is a 60-year-old patient who had completed RT for laryngeal cancer 18 months before imaging. The patient experienced moderate xerostomia and was clinically diagnosed with RTOG grade 2 late toxicity of the salivary gland. On the ultrasound image, the parotid gland exhibits heterogeneous echotexture, isoechoic relative to the adjacent muscle, with multiple hyperechoic lines and spots interleaved with hypoechoic areas. The histogram reveals a non-Gaussian distribution with a peak intensity of 65. The further widened 3-dB bandwidth ($W_{3 \text{ dB}} = 75$) indicates heterogeneous distribution, which may be due to the existence of inflammatory and fibrotic areas. The area under the low-intensity portion of the

curve (ie, below A_{low}) is 4.1, and the area under the high-intensity portion of the curve (ie, above A_{high}) is 7.5; whereas the width of the low-intensity portion (W_{low}) is 33, and the width of the high-intensity portion (W_{high}) is 135.

Ultrasound Images and Histograms: Average for Three Groups

Echo histograms were generated for 26 parotid glands from the normal control group, 32 from the acute-toxicity group, and 36 from the late-toxicity group. The means and standard deviations of the six features from the histograms of the normal, acute-toxicity, and late-toxicity groups along with P values are listed in Table 2. All six sonographic features show significant difference among control, acute-, and late-toxicity groups; between the control and the acute-toxicity groups; between the control and the late-toxicity groups except for W_{low} (P value = .404); between the control and

TABLE 2. Ultrasound Histogram Features (Mean \pm Standard Deviation) of the Control, Acute-, and Late-Toxicity Groups

Group/Parameter	I_{peak}	$W_{-3 \text{ dB}}$	A_{low}	A_{high}	W_{low}	W_{high}
Comparing three groups						
Control ($N = 26$)	77.7 ± 4.6	37.9 ± 6.8	4.9 ± 0.7	7.3 ± 1.7	33.3 ± 5.7	75.2 ± 17.5
Acute toxicity ($N = 32$)	36.1 ± 10.4	45.5 ± 10.6	2.9 ± 1.0	13.9 ± 4.0	18.6 ± 5.7	158.5 ± 29.8
Late toxicity ($N = 36$)	61.1 ± 15.3	60.5 ± 15.7	4.1 ± 1.3	16.7 ± 4.5	31.58 ± 9.29	137.0 ± 26.0
P value*	<.001	<.001	<.001	<.001	<.001	<.001
Comparing control and irradiated (combined acute and late toxicity) groups						
Control ($N = 26$)	77.7 ± 4.6	37.9 ± 6.8	4.9 ± 0.7	7.3 ± 1.7	33.3 ± 5.7	75.2 ± 17.5
Toxicity ($N = 68$)	49.4 ± 18.2	53.4 ± 15.4	3.5 ± 1.3	15.4 ± 4.4	25.5 ± 10.1	147.1 ± 29.7
P value*	<.001	<.001	<.001	<.001	<.001	<.001
Comparing control and acute-toxicity group						
P value*	<.001	.008	<.001	<.001	<.001	<.001
Comparing control and late-toxicity group						
P value*	<.001	<.001	.012	<.001	0.404	<.001
Comparing acute- and late-toxicity groups						
P value*	<.001	<.001	<.001	.009	<.001	.002

$P \leq 0.05$ means statistically significant.

* P value is calculated by analysis of variance for A_{low} , W_{low} , and W_{high} ; Kruskal-Wallis test or Wilcoxon rank sum test for I_{peak} , $W_{-3 \text{ dB}}$, and A_{high} .

the irradiated groups (including acute- and late-toxicity groups); and between the acute- and the late-toxicity groups. Figure 3 shows that the average parotid gland echo histograms of the acute-toxicity group and the late-toxicity group are different from that of the control group.

Subject Radiologic Evaluations of the B-mode Images of the Parotid Glands

Subjective radiologic evaluation of the echogenicity and heterogeneity is listed in Table 3. Normal parotid glands have high echo intensity (isoechoic 38% or hyperechoic 62% to adjacent musculature); whereas the majority of post-RT glands are hypoechoic to adjacent musculature (50% among acute toxicity group and 33% among late toxicity group) or isoechoic (34% among acute-toxicity group and 47% among late-toxicity group). The majority of normal parotid glands look homogeneous (uniform); whereas the post-RT groups show a trend toward increased heterogeneity (nonuniform). The majority of normal parotid glands are mildly heterogeneous (92%), whereas the majority of post-RT groups are moderately heterogeneous (47% among acute-toxicity group and 33% among late-toxicity group) or severely heterogeneous (44% among acute-toxicity group and 39% among late-toxicity group). Echogenicity and heterogeneity are significantly different among control, acute-, and late-toxicity groups; between the control and the acute-toxicity groups; between the control and the late-toxicity groups; and between the control and irradiated groups (including acute- and late-toxicity groups; all P values $<.001$). Echogenicity and heterogeneity are similar between the acute-toxicity group and the late-toxicity group (P value, .375 for echogenicity and .144 for heterogeneity). Therefore, subjective radiologic evaluation cannot distinguish between the acute- and late-toxicity groups.

Efficiency of Histogram Features: ROC Curves

The ROC analyses to evaluate diagnostic accuracy of toxicity for the histogram parameters are summarized in Table 4. All histogram parameters, except for I_{peak} and $W_{-3 \text{ dB}}$, have AUCs greater than 0.94 and, therefore, have excellent diagnostic accuracy in classifying the acute-toxicity group and the control group. All histogram parameters except for A_{low} and W_{low} can differentiate the late-toxicity group from the control group. All histogram parameters are useful for correctly classifying patients with acute toxicity and patients with late toxicity; among them, I_{peak} , A_{high} , and W_{high} have excellent diagnostic accuracy. Overall, all parameters have abilities to predict patient toxicity (acute or late toxicity) versus normal controls.

DISCUSSION

In this study, we have investigated the diagnostic efficiency of sonographic features based on echo histograms to characterize parotid gland injury after RT. These sonographic features provide quantitative measures of the echo-intensity distributions of the parotid glands, echogenicity (I_{peak}), homogeneity ($W_{-3 \text{ dB}}$), and heterogeneity (W_{low} vs. W_{high} or A_{low} vs. A_{high}) of the parotid glands. Significant differences were observed in these six histogram features between the control and acute-toxicity groups, between the control and late-toxicity groups, and between the acute- and late-toxicity groups (Fig 4). Through the ROC method, we further demonstrated the ability of histogram parameters in differentiating radiation-induced acute toxicity and late toxicity in parotid glands. Among the sonographic features, W_{low} , W_{high} , A_{low} and A_{high} have excellent ($AUC \geq 0.90$) diagnostic accuracy in differentiating parotid glands with acute toxicity from normal glands; W_{high} and A_{high} have excellent diagnostic accuracy in

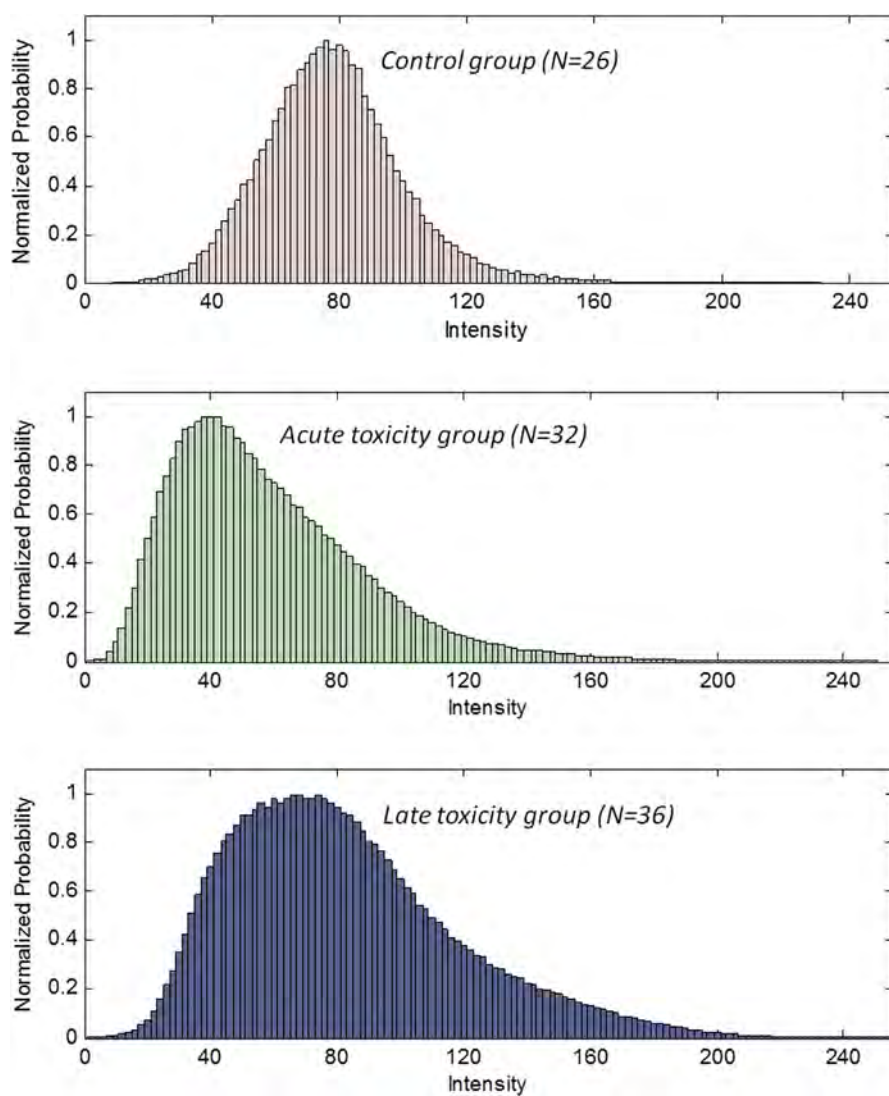


Figure 3. Average histograms of the control, acute-toxicity, and late-toxicity groups.

TABLE 3. Radiologic Evaluation of B-mode Images of the Control, Acute-, and Late-Toxicity Groups

Group	Echogenicity, n (%)				P Value*	Heterogeneity, n (%)			P Value*
	Hypoechoic	Isoechoic	Hyperechoic	Mild		Moderate	Severe		
Comparing three groups									
Control (N = 26)	0 (0)	10 (38.5)	16 (61.5)	24 (92.3)	<.001	2 (7.7)	0 (0)	<.001	
Acute toxicity (N = 32)	16 (50)	11 (34.4)	5 (15.6)	3 (9.4)		15 (46.9)	14 (43.8)		
Late toxicity (N = 36)	12 (33.3)	17 (47.2)	7 (19.4)	10 (27.8)		12 (33.3)	14 (38.9)		
Comparing control and toxicity groups									
Control (N = 26)	0 (0)	10 (38.5)	16 (61.5)	24 (92.3)	<.001	2 (7.7)	0 (0)	<.001	
Toxicity (N = 68)	28 (41.2)	28 (41.2)	12 (17.7)	13 (19.1)		27 (39.7)	28 (41.2)		
Comparing control and acute-toxicity Groups									
Control (N = 26)	0 (0)	10 (38.5)	16 (61.5)	24 (92.3)	<.001	2 (7.7)	0 (0)	<.001	
Toxicity (N = 68)	28 (41.2)	28 (41.2)	12 (17.7)	13 (19.1)		27 (39.7)	28 (41.2)		
Comparing control and late-toxicity Groups									
Control (N = 26)	0 (0)	10 (38.5)	16 (61.5)	24 (92.3)	<.001	2 (7.7)	0 (0)	<.001	
Toxicity (N = 68)	28 (41.2)	28 (41.2)	12 (17.7)	13 (19.1)		27 (39.7)	28 (41.2)		
Comparing acute- and late-toxicity groups									
Acute toxicity (N = 32)	16 (50)	11 (34.4)	5 (15.6)	3 (9.4)	<.001	15 (46.9)	14 (43.8)	<.001	
Late toxicity (N = 36)	12 (33.3)	17 (47.2)	7 (19.4)	10 (27.8)		12 (33.3)	14 (38.9)		

$P \leq 0.05$ means statistically significant.

*P value is calculated by chi-squared test.

differentiating parotid glands with late toxicity from normal glands; and I_{peak} and W_{low} have excellent diagnostic accuracy in differentiating acute from late toxicity.

The ultrasound studies that have demonstrated changes in the sonographic appearance of parotid glands exposed to radiation are mostly qualitative, or at best, semiquantitative

TABLE 4. Receiver Operating Characteristic (ROC) Analysis of Histogram Features for the Control, Acute-, and Late-Toxicity Groups

Parameter*	Area Under ROC Curve	Cutoff Value [†]	Sensitivity (%) [†]	Specificity (%) [†]	P Value [‡]
Probability modeled is group = "Acute Toxicity Group" compared to "Control Group"					
I_{peak}	1.00	—	—	—	—
$W_{-3 \text{ dB}}$	0.70	49.00	40.63	96.15	.003
A_{low}	0.94	3.86	84.38	88.46	<.001
A_{high}	0.98	10.61	87.50	100.00	<.001
W_{low}	0.97	26.00	93.75	92.31	<.001
W_{high}	0.99	110.00	96.88	100.00	<.001
Probability modeled is group = "Late Toxicity Group" compared to "Control Group"					
I_{peak}	0.86	74.00	77.78	80.77	<.001
$W_{-3 \text{ dB}}$	0.95	45.00	97.22	84.62	<.001
A_{low}	0.68	4.33	69.44	73.08	.012
A_{high}	0.99	10.77	91.67	100.00	<.001
W_{low}	0.61	27.00	36.11	92.31	.143
W_{high}	0.99	107.00	94.44	100.00	<.001
Probability modeled is group = "Acute Toxicity Group" compared to "Late Toxicity Group"					
I_{peak}	0.90	44.00	87.50	80.56	<.001
$W_{-3 \text{ dB}}$	0.79	43.00	50.00	97.22	<.001
A_{low}	0.77	3.26	71.88	75.00	<.001
A_{high}	0.68	13.94	62.50	75.00	.005
W_{low}	0.90	23.00	81.25	83.33	<.001
W_{high}	0.72	138.00	84.38	58.33	<.001
Probability modeled is group = "Toxicity Group" compared to "Control Group"					
I_{peak}	0.92	66.00	76.47	100.00	<.001
$W_{-3 \text{ dB}}$	0.83	45.00	75.00	84.62	<.001
A_{low}	0.80	3.89	66.18	88.46	<.001
A_{high}	0.98	10.61	89.71	100.00	<.001
W_{low}	0.78	27.00	63.24	92.31	<.001
W_{high}	0.99	107.00	95.59	100.00	<.001

$P \leq 0.05$ means statistically significant.

*Logistic regression model was used with each histogram parameter.

[†]Cutoff value is the value of each parameter as maximizing sum of the specificity and sensitivity.

[‡]P value is to examine if the area under the ROC curve (AUC) is different from 0.5 (AUC = 0.5 means the parameter has no ability to predict toxicity).

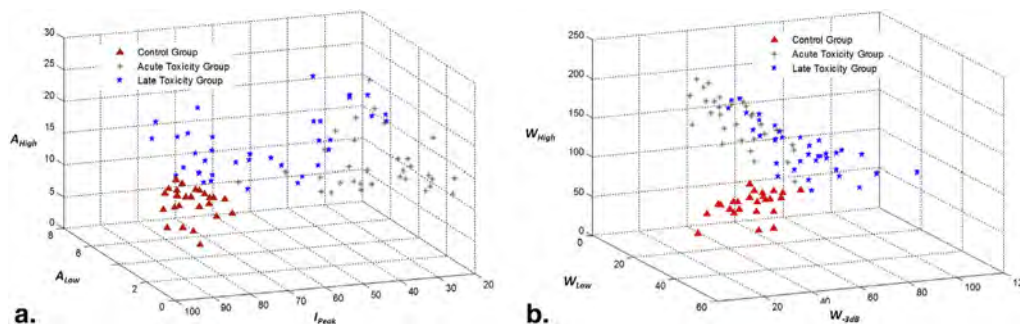


Figure 4. Scattergrams of histogram features demonstrate the separation between the control (red triangles), acute-toxicity (green stars), and late-toxicity groups (blue stars): (a) histogram features: A_{high} , A_{low} , and I_{peak} and (b) histogram features: W_{high} , W_{low} , and $W_{-3 \text{ dB}}$.

(23,24). In addition, previous studies were either on acute toxicity (24) or late toxicity (23). In our earlier studies (18,21), we demonstrated that histogram analysis could differentiate post-RT parotid glands with late toxicity from normal glands. In this study, we demonstrated significant differences in sonographic features between parotid glands with acute and late toxicities and normal parotid glands.

Homogeneous echotexture was observed in normal parotid glands, whereas heterogeneous texture was observed in the parotid glands of both acute- and late-toxicity groups. For the acute-toxicity group, the heterogeneous texture of post-RT parotid glands may be due to the presence of inflammatory infiltrates, which appear as hypoechoic (dark) areas (25–28). For the late-toxicity group, the heterogeneous

echotexture may be due to the presence of fibrosis, which appears as hyperechoic (bright) lines or spots (25–28). As shown in our study, physicians' subjective evaluations based on echogenicity and homogeneity of gray scale ultrasound images of the parotids were unable to distinguish between the acute-toxicity and late-toxicity groups. The echogenicity evaluation of the parotid gland is based on the comparison with the adjacent musculature. However, the adjacent muscles often receive the same dose of radiation as the parotid gland and may suffer from radiation-induced acute and late injury. For instance, the adjacent muscles may develop radiation-induced fibrosis and, therefore, may appear hyperechoic on the ultrasound scan.

The use of RT to treat head-and-neck cancer often involves radiation exposure of the parotid glands. As a result, many patients will develop xerostomia during the course of RT, a few weeks, months, or years after therapy. Xerostomia is commonly assessed through physicians' physical examination, patient-reported outcomes, and QoL instruments based on the symptoms (eg, altered taste or sensation of dryness) (29). The lack of objective evaluation or validated matrix for the assessment of parotid gland injury has slowed knowledge and treatment development and evaluation of xerostomia (20). We report our ultrasound study of parotid gland injury to highlight these problems and emphasize the importance of early recognition to minimize morbidity. Early detection of parotid gland injury would benefit patients by guiding physicians in modifying treatment regimen or providing early intervention.

One limitation of the sonographic histogram method is that the histogram of the images depends on many factors including time gain compensation and the nonlinear processing of the images (30). To overcome this limitation, we performed a pilot study to determine the optimal preset. All patients were scanned with this preset to facilitate relative comparison among patients. Another approach to overcome this limitation is through rigorous calibration procedures. For example, if two different settings are used for two patients, the settings need to be recorded. A correction map needs to be generated to normalize one image to the other.

Prospective validation of these ultrasound histogram features as convenient, quantitative imaging biomarkers of parotid injury is warranted. The pattern of toxicities changes with new RT treatment regimen alone or in combination with surgery and chemotherapy compared to conventional RT. Therefore, safe and cost-effective imaging methods to define and monitor new radiation-related toxicities are, thus, important in RT. The ongoing longitudinal study will enlarge the patient database and elucidate the trajectory of toxicity development using quantitative ultrasound. In addition, the predictive utility of the imaging method is continuously being refined and validated via patient-reported symptoms such as dry mouth and pain. These ultrasound parameters may provide a useful matrix of parotid gland injury secondary to radiation. The ultrasound technology could be further

developed into a low-cost imaging technique for parotid gland monitoring and assessment.

REFERENCES

1. Eisbruch A, Rhodus N, Rosenthal D, et al. How should we measure and report radiotherapy-induced xerostomia? *Semin Radiat Oncol* 2003; 13(3):226–234.
2. Meirovitz A, Murdoch-Kinch CA, Schipper M, et al. Grading xerostomia by physicians or by patients after intensity-modulated radiotherapy of head-and-neck cancer. *Int J Radiat Oncol Biol Phys* 2006; 66(2): 445–453.
3. Lin A, Kim HM, Terrell JE, et al. Quality of life after parotid-sparing IMRT for head-and-neck cancer: a prospective longitudinal study. *Int J Radiat Oncol* 2003; 57(1):61–70.
4. Bjordal K, Kaasa S, Mastekaasa A. Quality-of-life in patients treated for head and neck cancer—a follow-up study 7 to 11 years after radiotherapy. *Int J Radiat Oncol Biol Phys* 1994; 28(4):847–856.
5. Chao KSC, Ozigit G, Blanco AI, et al. Intensity-modulated radiation therapy for oropharyngeal carcinoma: impact of tumor volume. *Int J Radiat Oncol Biol Phys* 2004; 59(1):43–50.
6. Lee N, Xia P, Quivey JM, et al. Intensity-modulated radiotherapy in the treatment of nasopharyngeal carcinoma: an update of the UCSF experience. *Int J Radiat Oncol Biol Phys* 2002; 53(1):12–22.
7. de Arruda FF, Puri DR, Zhung J, et al. Intensity-modulated radiation therapy for the treatment of oropharyngeal carcinoma: the Memorial Sloan-Kettering Cancer Center experience. *Int J Radiat Oncol Biol Phys* 2006; 64(2):363–373.
8. Cox JD, Stetz J, Pajak TF. Toxicity criteria of the Radiation-Therapy Oncology Group (RTOG) and the European-Organization-for-Research-and-Treatment-of-Cancer (EORTC). *Int J Radiat Oncol Biol Phys* 1995; 31(5):1341–1346.
9. Cheng SCH, Wu VWC, Kwong DLW, et al. Assessment of post-radiotherapy salivary glands. *Br J Radiol* 2011; 84(1001):393–402.
10. Houweling AC, Schakel T, van den Berg CAT, et al. MRI to quantify early radiation-induced changes in the salivary glands. *Radiother Oncol* 2011; 100(3):386–389.
11. Ying M, Wu VWC, Kwong DLW. Comparison of sonographic appearance of normal and postradiotherapy parotid glands: a preliminary study. *Ultrasound Med Biol* 2007; 33(8):1244–1250.
12. Gritzmann N, Rettenbacher T, Hollerweger A, et al. Sonography of the salivary glands. *Eur Radiol* 2003; 13(5):964–975.
13. Astreinidou E, Raaymakers CPJ, Roesink JM, et al. 3D MR sialography protocol for postradiotherapy follow-up of the salivary duct system. *J Magn Reson Imaging* 2006; 24(3):556–562.
14. Wada A, Uchida N, Yokokawa M, et al. Radiation-induced xerostomia: objective evaluation of salivary gland injury using MR sialography. *Am J Neuroradiol* 2009; 30(1):53–58.
15. Nomayr A, Lell M, Sweeney R, et al. MRI appearance of radiation-induced changes of normal cervical tissues. *Eur Radiol* 2001; 11(9):1807–1817.
16. Blailek EJ, Jakubowski W, Zajkowski P, et al. US of the major salivary glands: anatomy and spatial relationships, pathologic conditions, and pitfalls. *Radiographics* 2006; 26(3):745–764.
17. Buus S, Grau C, Munk OL, et al. Individual radiation response of parotid glands investigated by dynamic C-11-methionine PET. *Radiother Oncol* 2006; 78(3):262–269.
18. Yang X, Tridandapani S, Beiter JJ, et al. Ultrasound histogram assessment of parotid gland injury following head-and-neck radiotherapy: a feasibility study. *Ultrasound Med Biol* 2012; 38(9):1514–1521.
19. Bentzen SA, Saunders MI, Dische S, et al. Radiotherapy-related early morbidity in head and neck cancer: quantitative clinical radiobiology as deduced from the CHART trial. *Radiother Oncol* 2001; 60(2):123–135.
20. Deasy JO, Moiseenko V, Marks I, et al. Radiotherapy dose-volume effects on salivary gland function. *Int J Radiat Oncol Biol Phys* 2010; 76(3): S58–S63.
21. Yang X, Tridandapani S, Beiter J, et al. Ultrasound GLCM texture analysis of radiation-induced parotid-gland injury in head-and-neck cancer radiotherapy: an in vivo study of late toxicity. *Medical Physics* 2012; 39(9):5732.
22. Metz CE. Basic principles of ROC analysis. *Semin Nucl Med* 1978; 8(4): 283–298.
23. Cheng SC, Ying MT, Kwong DL, et al. Sonographic appearance of parotid glands in patients treated with intensity-modulated radiotherapy or

- conventional radiotherapy for nasopharyngeal carcinoma. *Ultrasound Med Biol* 2011; 37(2):220–230.
- 24. Imanimoghaddam M, Rahrooh M, Tafakhori Z, et al. Changes of parotid and submandibular glands caused by radiotherapy—an ultrasound evaluation. *Dentomaxillofac Radiol* 2012.
 - 25. Grehn AL, Gustafsson H, Franzen L, et al. Ultrastructural morphometry of parotid acinar cells following fractionated irradiation. *Oral Oncol* 1997; 33(1):23–28.
 - 26. Henriksson R, Frojd O, Gustafsson H, et al. Increase in mast cells and hyaluronic acid correlates to radiation-induced damage and loss of serous acinar cells in salivary glands: the parotid and submandibular glands differ in radiation sensitivity. *Br J Cancer* 1994; 69(2):320–326.
 - 27. Konings AWT, Faber H, Cotteler F, et al. Secondary radiation damage as the main cause for unexpected volume effects: a histopathologic study of the parotid gland. *Int J Radiat Oncol Biol Phys* 2006; 64(1):98–105.
 - 28. Nagler RM. The enigmatic mechanism of irradiation-induced damage to the major salivary glands. *Oral Dis* 2002; 8(3):141–146.
 - 29. Henson BS, Inglehart MR, Eisbruch A, et al. Preserved salivary output and xerostomia-related quality of life in head and neck cancer patients receiving parotid-sparing radiotherapy. *Oral Oncology* 2001; 37(1):84–93.
 - 30. Yang X, Tridandapani S, Beiter JJ, et al. Ultrasonic Nakagami-parameter characterization of parotid-gland injury following head-and-neck radiotherapy: a feasibility study of late toxicity. *Med Phys* 2014; 41(2): 022903.

● *Original Contribution*

AUTOMATED SKIN SEGMENTATION IN ULTRASONIC EVALUATION OF SKIN TOXICITY IN BREAST CANCER RADIOTHERAPY

YI GAO,^{*1} ALLEN TANNENBAUM,[†] HAO CHEN,^{*} MYLIN TORRES,^{*§} EMI YOSHIDA,^{*} XIAOFENG YANG,^{*} YUEFENG WANG,^{*} WALTER CURRAN,^{*§} and TIAN LIU^{*§}

^{*}Department of Radiation Oncology, Emory University, Atlanta, Georgia, USA; [†]Department of Electrical and Computer Engineering, University of Alabama at Birmingham, Birmingham, Alabama, USA; and [§]Winship Cancer Institute, Emory University, Atlanta, Georgia, USA

(Received 23 August 2012; revised 8 January 2013; in final form 4 April 2013)

Abstract—Skin toxicity is the most common side effect of breast cancer radiotherapy and impairs the quality of life of many breast cancer survivors. We, along with other researchers, have recently found quantitative ultrasound to be effective as a skin toxicity assessment tool. Although more reliable than standard clinical evaluations (visual observation and palpation), the current procedure for ultrasound-based skin toxicity measurements requires manual delineation of the skin layers (*i.e.*, epidermis-dermis and dermis-hypodermis interfaces) on each ultrasound B-mode image. Manual skin segmentation is time consuming and subjective. Moreover, radiation-induced skin injury may decrease image contrast between the dermis and hypodermis, which increases the difficulty of delineation. Therefore, we have developed an automatic skin segmentation tool (ASST) based on the active contour model with two significant modifications: (i) The proposed algorithm introduces a novel dual-curve scheme for the double skin layer extraction, as opposed to the original single active contour method. (ii) The proposed algorithm is based on a geometric contour framework as opposed to the previous parametric algorithm. This ASST algorithm was tested on a breast cancer image database of 730 ultrasound breast images (73 ultrasound studies of 23 patients). We compared skin segmentation results obtained with the ASST with manual contours performed by two physicians. The average percentage differences in skin thickness between the ASST measurement and that of each physician were less than 5% ($4.8 \pm 17.8\%$ and $-3.8 \pm 21.1\%$, respectively). In summary, we have developed an automatic skin segmentation method that ensures objective assessment of radiation-induced changes in skin thickness. Our ultrasound technology offers a unique opportunity to quantify tissue injury in a more meaningful and reproducible manner than the subjective assessments currently employed in the clinic. (E-mail: tliu34@emory.edu) © 2013 World Federation for Ultrasound in Medicine & Biology.

Key Words: Skin segmentation, Radiation toxicity, Breast cancer radiotherapy, Breast ultrasound.

INTRODUCTION

Radiation-induced toxic effects on skin, including skin thickening, swelling and hardening, are the most common, debilitating, short-term and long-term side effects of breast cancer radiotherapy (Small and Woloschak 2006). Although recognized for decades, the assessment of skin toxicity is carried out subjectively by physicians through visual evaluation and palpation. We, along with other researchers (Huang et al. 2007; Liu et al. 2010; Warszawski et al. 1998; Zhou et al. 2009), have recently

reported that ultrasound can be used to quantitatively assess skin toxicity after radiotherapy for breast cancer. In particular, skin thickening was observed in almost all post-radiotherapy patients (Huang et al. 2007; Liu et al. 2010), making it an important parameter in ultrasonic evaluation of skin toxicity.

The major challenge in ultrasonic skin evaluation is accurate skin segmentation (delineation) on B-mode images. Human skin has two layers: the epidermis and the dermis. The tissue below the dermal layer is the hypodermis (subcutaneous tissue) (Fig. 1). On the 10-MHz-frequency ultrasound B-mode images (Fig. 2a), the normal epidermis and dermis have bright, well-defined boundaries; whereas the relatively thin epidermis appears as a single echo band. However, after breast radiotherapy, radiation-induced damage to the basal layers of dermal

Address correspondence to: Tian Liu, Department of Radiation Oncology, Emory University School of Medicine, 1365 Clifton Road NE, Atlanta, GA 30322, USA. E-mail: tliu34@emory.edu

¹Department of Electrical and Computer Engineering, University of Alabama at Birmingham, Birmingham, AL, USA

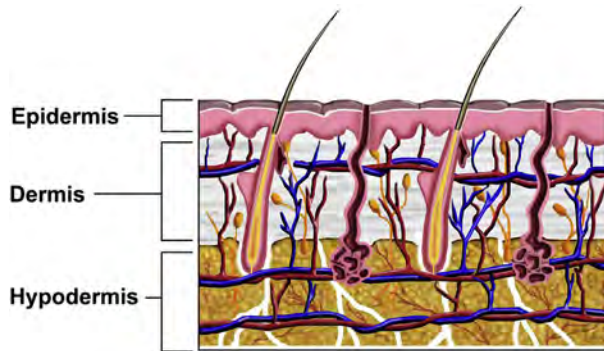


Fig. 1. Schematic diagram of the skin. Skin comprises two layers: epidermis and dermis. The hypodermis lies under the dermis.

cells (Archambeau *et al.* 1995; Fajardo *et al.* 2001) can often result in decreased contrast at the hypodermis interface, as shown in Figure 2b. Identification of this interface is a demanding task even for experienced physicians. In our previous skin toxicity studies, the skin was manually delineated, and inter-observer reliability was determined (Yoshida *et al.* 2012). Nevertheless, manual segmentation is time consuming. In addition, such extensive human interaction inevitably induces subjectivity into the process.

In this article, we report the development of an automatic skin segmentation tool (ASST) based on the active contour method with two major modifications. The active contour (snake) method has had a large audience in the image segmentation community since its proposal by Kass *et al.* (1988). To deal with skin segmentation, one major modification introduces a dual-curve evolution technique that is used to detect the epidermis-dermis and dermis-hypodermis interfaces. The other modification is that the proposed algorithm uses a geometric active contour framework as opposed to the previous parametric algorithm (Lagarde *et al.* 2005), which requires param-

eter input before segmentation. The main advantage of the proposed ASST algorithm is that it fully automates skin delineations on ultrasound breast images. Furthermore, we found that the ASST could accurately segment both normal skin and radiotherapy-damaged skin.

The remainder of the article is structured as follows. In the next section, Methods, we introduce our ASST algorithm and emphasize the modifications made to the active contour methods. In the Results section, we describe the findings of our clinical study of ASST using 73 breast ultrasound examinations (730 B-mode images), including 365 normal breast images and 365 post-radiotherapy breast images. The ASST results were compared with physicians' manual contours of the skin layers, and statistical analyses were conducted to evaluate the performance of the ASST. In the Discussion, we highlight the strength of the proposed automatic segmentation algorithm.

METHODS

Theory behind the automatic skin segmentation tool

The proposed skin segmentation algorithm, illustrated in Figure 3, consists of two major components. First, a Riemannian metric (Caselles *et al.* 1997; Kichenassamy *et al.* 1996; Siddiqi *et al.* 1998) is derived from the image information, and the curve is evolved by minimizing its length under the Riemannian metric, in order to converge to the desired epidermis-dermis interface. Next the dermis-hypodermis interface is identified through a two-step optimization process. The "center line" of the dermis is determined in the first step; the dermis-hypodermis interface is located in the second step.

Epidermis-dermis interface segmentation

In this section, we describe the method used to identify the interface between the epidermal and dermal layers. The intensity of the ultrasound image to be

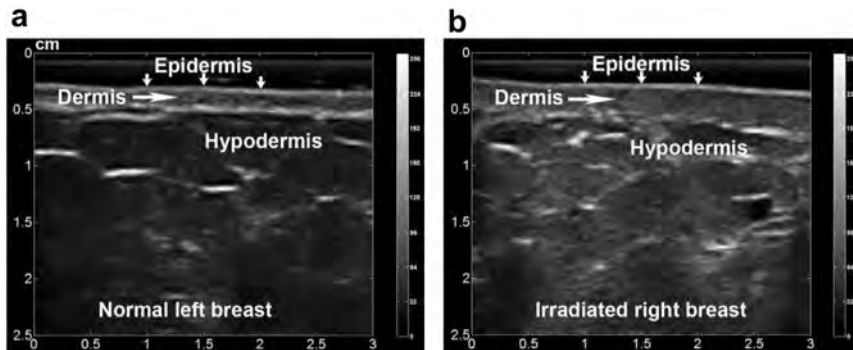


Fig. 2. Ultrasound B-mode images of (a) untreated (normal) breast and (b) irradiated breast. The two layers of the skin, epidermis and dermis, can be seen in both images. Radiation-induced skin injury is evidenced by the skin thickening and segmented dermis-hypodermis interface on the B-mode images.

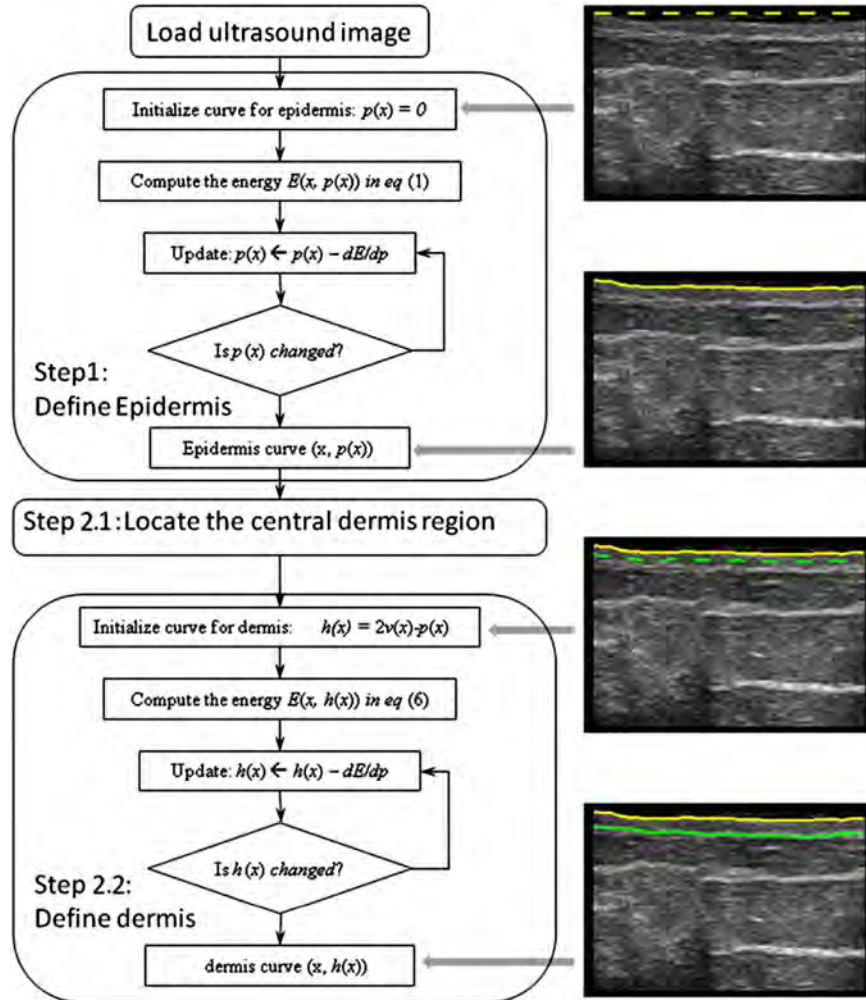


Fig. 3. Flowchart for the proposed method for automatic skin segmentation of ultrasound B-mode images. The block diagram on the left summarizes the two main steps of the skin segmentation algorithm. On the right are the intermediate segmentation curve positions corresponding to the block diagram.

segmented is denoted as $I(x, y)$, where x indicates the horizontal axis with a range of $[0, X]$, and y indicates the vertical axis with a range of $[0, Y]$. Because the breast skin does not fold, to preserve this condition, we wrote the curve of the skin layers as a graph $(x, p(x))$ of function $p: [0, X] \rightarrow [0, Y]$. The location of the epidermis-dermis interface usually corresponds to image regions with drastic intensity changes, which results in a high image gradient magnitude. Therefore, we expected the curve $(x, p(x))$ to pass through those high gradient locations. This is achieved within the framework of curve evolution under the Riemannian metric. Specifically, first, using the image intensity information, we define a Riemannian metric $f(x, y)$ as

$$f(x, y) := \frac{1}{1 + (S * G_\sigma(x, y) * I(x, y))^2} \quad (1)$$

where $G_s(x, y)$ is Gaussian kernel with standard deviation σ . In this application, σ is fixed at 3 to balance between image blurring and noise removal. It is also noted that the purpose of Gaussian filtering is to remove some non-smoothness in the segmentation cost function, rather than to improve the visual appearance of the ultrasound images, which, on its own, is an active research field (Hao et al. 1999; Michailovich and Tannenbaum 2006; Yu and Acton 2002). S is the Sobel edge operator, $S = (1, 2, 1; 0, 0, 0; -1, -2, -1)$, and the operator $*$ denotes 2-D convolution. The design of the discrete operator should take the sampling rate into consideration. This includes adjusting the size of the discrete operator and the values within the kernel for the given sample frequency and edge size. On the other hand, the prior Gaussian filtering is able to construct a nesting of scale space that is able to accommodate the original sampling

frequency. Therefore, we can fix the Sobel operator and adjust the Gaussian filtering for the given image and target. Therefore, the Sobel operator is fixed to its canonical form. The metric $f(x, y)$ is a positive function on the same domain as the original image. Wherever a high gradient edge region exists, the $f(x, y)$ value decreases. In Euclidean geometry, the infinitesimal curve length of the parametric curve $(x, p(x))$ at position x is $[1 + (p'(x))^2]^{1/2}$ (Hamming 2004). However, under this new Riemannian metric $f(x, y)$, the infinitesimal curve length at position x is $f(x, p(x))g[1 + (p'(x))^2]^{1/2}$. If the curve covers the skin regions, the total curve length would be small due to the effect of $f(x, y)$. Therefore, we modeled the epidermis-dermis interface curve as the function that minimizes the energy (Riemannian curve length):

$$p(x) = \operatorname{argmin}_x E(x, p(x))$$

$$E(x, p(x)) := \int_0^x f(x, p(x)) \sqrt{1 + (p'(x))^2} dx \quad (2)$$

Next, to solve for the optimal epidermis-dermis interface curve, the Euler-Lagrange equation of $E(x, p(x))$ in eqn (2) is computed. Denoting the Lagrangian as L , the Euler-Lagrange equation is computed as

$$\frac{\partial L}{\partial p} - \frac{d}{dx} \frac{\partial L}{\partial p'} = f_y \sqrt{1 + (p'(x))^2} - f_x \frac{p'(x)}{\sqrt{1 + (p'(x))^2}}$$

$$- f \frac{p''(x)}{\sqrt{1 + (p'(x))^2}} - f_y \frac{(p'(x))^2}{\sqrt{1 + (p'(x))^2}} + f \frac{p''(x)(p'(x))^2}{(\sqrt{1 + (p'(x))^2})^3} \quad (3)$$

We augment the curve $p(x)$ with an artificial time variable t , and the optimal curve can then be found by solving the initial-boundary-value problem:

$$\frac{\partial p}{\partial t} = \frac{\partial}{\partial x} \frac{\partial L}{\partial p'} - \frac{\partial L}{\partial p}$$

$$\frac{\partial p}{\partial x} \Big|_{x=0} = \frac{\partial p}{\partial x} \Big|_{x=X} = 0 \quad (4)$$

$$p(x, 0) = 0$$

At convergence, the curve would locate the expected epidermis-dermis interface corresponding to a minimal Riemannian length/energy.

Dermis-hypodermis interface segmentation

Compared with the epidermal-dermis interface, extracting the dermis-hypodermis interface poses a bigger challenge because of the contrast at the dermis-hypodermis interface. Moreover, for radiation-damaged skin, multiple fragments often appear on the dermis-hypodermis interface. Overall, the dermis-hypodermis interface should correspond to a minimal energy state under the same Riemannian metric created for the epidermis.

The energy defined in eqn (2) has at least two local minimal configurations. One corresponds to the epidermis-dermis interface and the other to the dermis-hypodermis interface. The curve in the center of the dermis has a high energy state. In solving eqn (2), we have already identified one energy minimization configuration for the epidermis-dermis interface; the finding of the dermis-hypodermis interface is modeled as a process that skips the epidermis-dermis interface and converges to the dermis-hypodermis interface. As one step toward that goal, previous researchers assumed a certain width for the dermis (Lagarde *et al.* 2005). Consequently, they initiated the dermis-hypodermis interface by moving a distance $p(x)$ and then fine-tuned the curve by minimizing the energy. However, two issues are associated with using this scheme in our skin toxicity assessment scenario. First, dermis thickness varies significantly in irradiated and non-irradiated patients. This creates technical difficulties in determining a pre-defined “jump distance.” Second, and more fundamentally, dermis thickness is a key parameter in measuring toxicity, but the pre-defined “jump distance” is an estimate for that value; hence, the estimate strongly biases the final results.

In this work, we propose a robust two-step scheme to identify the dermis-hypodermis interface, without the aforementioned assumptions and limitations.

In the first step, the optimization problem needs to be solved to find the center curve of the dermis:

$$v(x) = \operatorname{argmin}_x E(x, v(x))$$

$$E(x, v(x)) := \int_0^x \frac{1}{f(x, v(x))} \sqrt{1 + (v'(x))^2} dx \quad (5)$$

Here the initial position of $v(x)$ is $v(x) = p(x) + \epsilon$, and ϵ is a small positive value like 0.1 pixel that moves the epidermis curve down a short distance; the optimization then drives the curve further to the center position in the dermal layer. Essentially, the metric image $f(x, y)$ is placed in the denominator, and the energy function is effectively flipped: what used to be minimizer now becomes a maximizer, and vice versa. Previously (when $f(x, y)$ was in the numerator, as in eqn [2]), the two skin layer interfaces corresponded to a low-energy state, and the center curve of the dermis to a high-energy state. Now (as in eqn [5]), the center curve of the dermis has a low energy state and will be extracted by solving eqn (5). The reason for using the reciprocal, instead of negation, is that the reciprocal gives another metric that satisfies the positive definite requirement of being a Riemannian metric. However, by negation, such requirements would be violated and numerical instability would occur. The choice of the ϵ value would not bias the thickness computation. In the second step, with the

center curve located, the dermis-hypodermis interface curve is computed by solving

$$h(x) = \operatorname{argmin}_x E(x, h(x))$$

$$E(x, h(x)) := \int_0^x f(x, h(x)) \sqrt{1 + (h'(x))^2} dx \quad (6)$$

with the initial position of $h(x)$ $h(x)$ at $h(x) = 2v(x) - p(x)$. Equation (6) is structurally similar to eqn (2), but the initial condition differs. As a result, at convergence, the final position of $h(x)$ is located on the dermis-hypodermis interface.

Validation and reliability study

The ASST was tested and validated using our breast cancer radiotherapy ultrasound imaging database. Our study was conducted under institutional review board approval, and written, informed consent was obtained from all participants. Twenty-three patients with breast cancer who underwent breast conservation surgery (lumpectomy) and breast irradiation for early-stage breast cancer were included in this study (Liu et al. 2010). The median age was 56 (range: 44–74), and the median time elapsed between completion of radiotherapy and ultrasound examination was 22 mo (range: 6–92 mo). All patients received 50.0–50.4 Gy to the whole breast (1.8- or 2.0-Gy fractions); an electron boost of 10.0–16.0 Gy at the lumpectomy site followed. Doses were delivered using parallel and opposed 6-MV tangential fields. Beams were modulated using wedges to ensure dose homogeneity according to standard International Commissions on Radiation Units and Measurements 50 (ICRU-50) guidelines (ICRU 1993). Eighteen patients underwent one ultrasound exam, and the other 5 underwent multiple exams over a 1-y period. Overall, 73 ultrasound exams and 730 ultrasound images (365 normal breast images and 365 post-radiotherapy breast images) were analyzed in this study, and these gray-scale images have an intensity range of [0, 255]. (The ultrasound image is stored in a matrix of bytes. Each byte represents an 8-bit unsigned integer with 256 levels ranging from 0 to 255.) Ultrasound data acquisition has been reported previously and is briefly summarized here (Liu et al. 2010). Patients were scanned with a clinical ultrasound scanner in the supine position. Five ultrasound scans of each breast were obtained: left breast-upper (12:00), lateral (3:00), lower (6:00), medial (9:00) and tumor bed, and right breast-upper (12:00), medial (3:00), lower (6:00), lateral (9:00) and tumor bed. As a baseline measurement, we also scanned the same areas on the untreated (contralateral) breast. Ultrasound studies were performed using a clinical scanner (Sonix RP, Ultrasonix,

Richmond, BC, Canada) with a linear array transducer (L14-5/38 probe, 128 elements). All ultrasound data were acquired with the same settings: 10-MHz frequency, 1-cm focal length, 4-cm depth, 72% gain, 26 frames/s and 80-dB dynamic range. Ultrasonic B-mode images were acquired from the treated and contralateral normal breast.

The reliability study was conducted in two ways. First, we tested our skin segmentation algorithm by measuring skin thickness. Two observers were asked to independently contour the two skin layer interfaces on all 730 images. Observer 1 is an ultrasound expert, and observer 2 is a radiation oncologist. The skin thickness results obtained with our segmentation algorithm were compared with the manual contour results. Linear regressions were performed and correlation coefficients were calculated for assessment of consistency between the ASST and the observers. Furthermore, the accuracy of the segmentation of the two skin layers was evaluated using the absolute curve difference (ACD). For the two curves $c_1(x)$ and $c_2(x)$ with $x \in [0, X]$, the absolute curve difference $D_{1,2}(x)$ between them is defined as

$$D_{1,2}(x) := |c_1(x) - c_2(x)| \quad (7)$$

The ACD was computed between the ASST results and each observer's results and also between the two observers' results.

RESULTS

Skin segmentation with the ASST was performed on all 730 breast images, and the overall computation time was less than 5 min. Figure 4 is an example of a post-radiotherapy breast image, in which the skin was delineated by the ASST program and two physicians. This ultrasound image was obtained 1 y after treatment of a 55-y-old breast cancer patient with a radiation dose of 60.4 Gy. According to the physician's assessment, based on Radiation Therapy Oncology Group (RTOG) Late Morbidity Scoring Scheme, the patient developed mild (grade 1) late skin toxicity. On the ultrasound image, such radiation-induced skin damage was evidenced by the low contrast and segmented interface between the dermis and hypodermis. On visual inspection, the ASST skin segmentation is similar to the manual contours performed by the two experts.

Overall, the ASST skin segmentation results were close to the manual segmentation results, which are currently the gold standard in the clinic. For all 730 ultrasound images, percentage differences between skin thickness measurements made using the ASST algorithm and measurements by the two observers are summarized in Table 1. For the skin thickness, with similar variances, the average percentage differences between the ASST

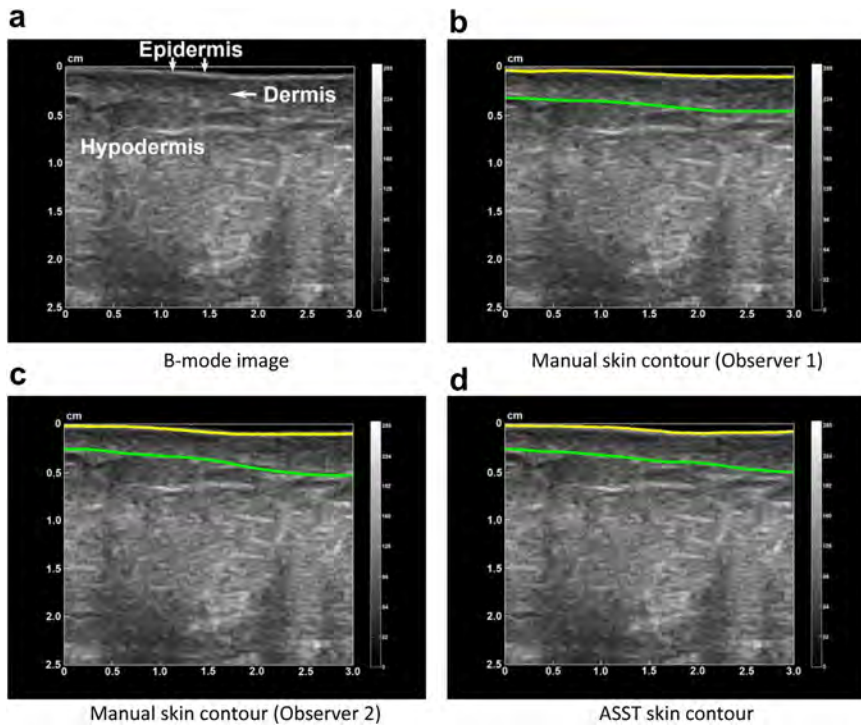


Fig. 4. Ultrasound breast images and skin segmentation. (a) Original ultrasound B-mode image. (b) Skin layers manually delineated by observer 1. (c) Skin layers manually contoured by observer 2. (d) Skin layers segmented by the proposed automatic skin segmentation algorithm (ASST).

and observers 1 and 2 were 4.8% and -3.8%, whereas the average percentage difference between the two observers was -9.9%. Figure 5 illustrates the linear regression of skin measurements between the ASST and each observer. The correlation coefficients, R^2 , were 0.74 for observer 1 and 0.70 for observer 2, demonstrating the accuracy of ASST skin segmentation.

Performance of the ASST was also evaluated separately for the normal breast and the treated breast. As seen in Figure 6, the differences between the ASST algorithm and each observer were larger for irradiated breasts than for normal breasts. The reason for this is that radiation injury increases the difficulty of skin segmentation. In addition, the ACDs were larger for the dermis than for the epidermis, not only for the ASST algorithm, but also for the two observers.

Table 1. Percentage differences in skin thickness measurements made with the proposed automatic skin segmentation tool (ASST) and two observers' manual segmentations

Comparison	Difference
ASST versus observer 1	4.8 ± 17.8%
ASST versus observer 2	-3.8 ± 21.1%
ASST versus observer 3	-9.9 ± 20.1%

DISCUSSION

We developed an ASST algorithm that automates skin segmentation on breast ultrasound images. The ability of the ASST to delineate normal as well as radiation-damaged skin was explored with a database of 730 ultrasound images, among which 365 were of normal (untreated) breasts and 365 were of radiation-treated breasts. In current clinical practice, skin contours on breast ultrasound images are performed manually by physicians. The proposed ASST method is more accurate and faster, compared with manual skin segmentations. Specifically, the average percentage differences between skin thickness measurements made using the ASST and measurements made by manual segmentation were less than 5%. Moreover, the two physicians each spent approximately 700 to 800 min to contour the skin layers for the 730 ultrasound images, whereas the ASST completed all segmentations within 5 min. Figure 7 illustrates three representative cases: normal breast, irradiated breast in a patient without toxicity and irradiated breast in a patient with toxicity. For all three cases, ASST skin segmentation results are similar to physicians' manual contours.

In 2005, Lagarde *et al.* proposed using the original active contour method to segment skin in various regions, including the arm, thigh, forehead and neck. A parametric

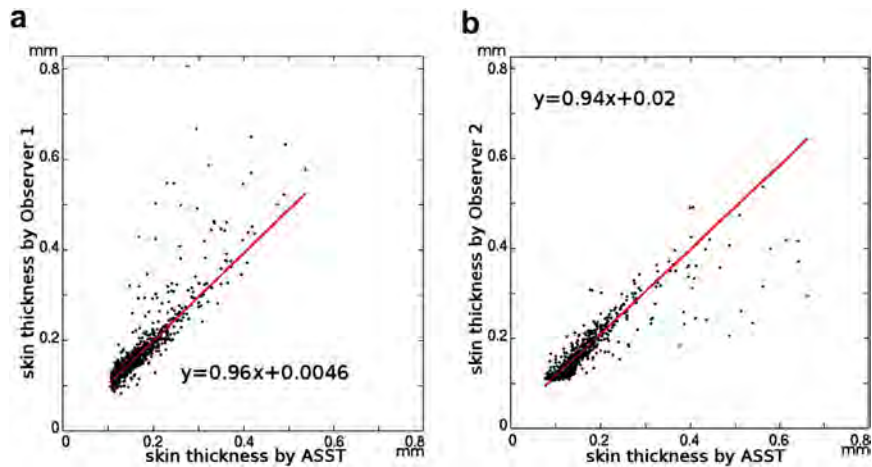


Fig. 5. Linear regressions comparing automatic skin segmentation tool (ASST)-computed skin thickness with human observer-delineated skin thickness. (a) ASST skin thickness versus observer 1. (b) ASST skin thickness versus observer 2.

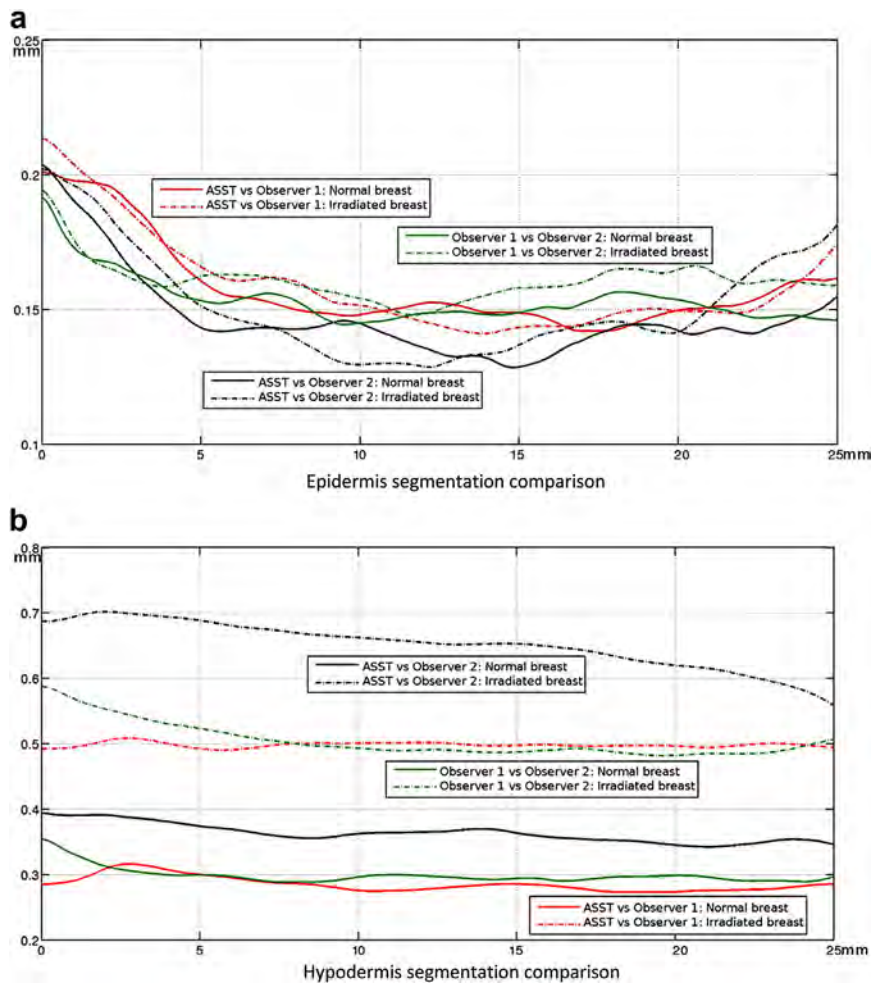


Fig. 6. Absolute curve differences in skin segmentation between results for the automatic skin segmentation method and manual results for the two observers. (a) Epidermis segmentation. (b) Dermis segmentations. Comparisons are made for normal and irradiated breasts.

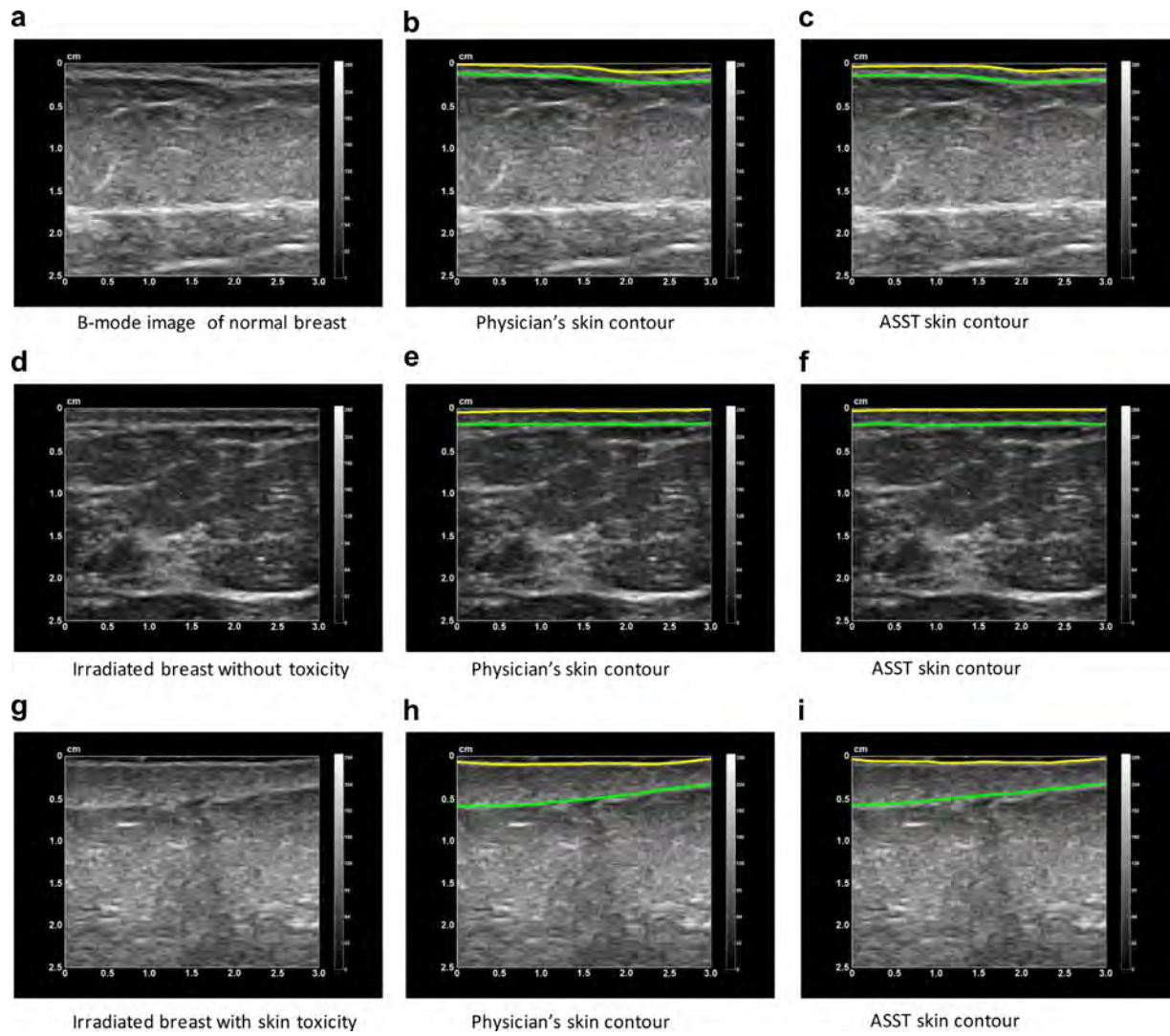


Fig. 7. Three representative data sets on the different cases observed: (a) normal breast image with (b) skin layers manually contoured by physician and (c) skin layers contoured with the automatic skin segmentation method. (d) Post-irradiation patient without toxicity with (e) skin layers manually contoured by physician and (f) skin layers contoured with the automatic skin segmentation method. (g) Post-irradiation patient with toxicity with (h) skin layers manually contoured by physician and (i) skin layers contoured with the automatic skin segmentation method.

model was used to represent the contour and its evolution with the local image gradient. Comparison of their automatic segmentation results with physicians' contours yielded R^2 values ranging from 0.01 to 0.61. In this study of breast skin segmentation, comparison of our automatic segmentation results with manual results for one physician yielded an R^2 value of 0.76, and for the other physician, 0.74, representing a significant improvement in consistency with the physicians' manual contours.

Although segmentation for ultrasound images has been studied extensively in organs (Noble and Boukerroui 2006) such as the heart (Mitchell *et al.* 2002) and prostate (Ladak *et al.* 2000; Zhan and Shen 2006), investigations on skin segmentation are limited

(Lagarde *et al.* 2005). To the best of our knowledge, this is the first segmentation study on breast skin after radiation treatment. To extract the two skin layers from the ultrasound image, we extended the well-known active contour method and designed an open-ended, dual-curve evolution technique. During skin layer extraction, our ASST method considers both the information from the ultrasound image information and skin properties, such as smoothness. More explicitly, a set of partial differential equations (PDEs) is derived for the position of the curve, so that the curve will be passing through the locations where the greatest change in image intensity occurs, which is the expected location of the skin layer. Although such a technique accurately locates the epidermis, because of

the decreased contrast and possible radiation damage, extraction of the dermis is often more challenging.

The other significant modification of the proposed ASST method was fully automatic detection of the dermis under the Riemannian geometry framework. Previous researchers usually extracted the dermis with a parametric algorithm (Lagarde et al. 2005). In the parametric method, on one hand, the curves are represented by spline nodes, which is numerically less stable. On the other hand, after the first curve (epidermis-dermis boundary) is located, an initial guess of a uniform shift ("jump distance") f is required to locate the second curve (dermis-hypodermis interface). Then, this shift is fine-tuned within a limited range from the initial position to capture the second boundary. Therefore, the final accuracy is strongly affected by the initial shift. The skin thickness measurement is also affected by the value of f , which implicitly induces subjectivity. In contrast, our ASST is a geometric-based method, where one set of PDEs moves the epidermis curve to the center of the dermis area. Then, another set of PDEs finally moves the center-of-dermis curve to the position of the dermis-hypodermis interface. The entire process is automatic, and more importantly, by using PDEs, we remove the subjectivity induced by the user-given parameter f .

We realize that other than the active contour framework employed in the present work, many other techniques may be able to solve skin segmentation problem. Noticeably, the mean shift algorithm proposed by Comaniciu and Meer (2002) gives a robust estimation of the centers of the modes among random samples in the feature space. The level-set algorithm seeks a contour to separate an image into two parts (Chan and Vese 2001). Although those algorithms tend to extract "blob"-shaped targets in the images, instead of curve-shaped objects, as needed for the skin, future studies will investigate how such algorithms could be used for a more accurate, more robust and faster algorithm for the clinical task.

In dermatology, skin is frequently imaged with 20-MHz high-frequency ultrasound, greatly improving the contrast between different layers of the skin (Foster et al. 2000; Harland et al. 2006; Hoffmann et al. 1991; Ritter et al. 2002; Vogt and Ermert 2005). In high-frequency ultrasound, the epidermis appears as a layer of certain width, as compared with our study in which the epidermis-dermis interface appeared fused as a single echo band. We used a frequency of 10 MHz to image the breast, because both skin and deeper glandular tissue are evaluated for radiation-induced damage.

In breast cancer radiotherapy, radiation toxicity is very common and routinely assessed through physical examinations. The drawbacks of physical examinations are subjectivity and imprecision. There is significant inconsistency in clinical assessments. We have conducted

a series of studies to introduce an ultrasound imaging tool into the diagnosis of post-irradiation breast tissue toxicity. This research tool would be useful in comparing skin toxicity after various treatment strategies, such as altered fractionation and external beam radiation versus brachytherapy, for example, Mammosite. The motivation is to develop an automatic, non-invasive and quantitative tool to measure normal tissue toxicity that has the potential to overcome the limitations of the current assessment tools in the clinic. In other words, our ultrasound tool may help distinguish good treatments from bad treatments, with respect to skin toxicity, and determine the effects of different types of treatment schemes in breast radiation. Toward this goal, the proposed ASST helps us move one step further—it will free physicians from tedious segmentation work and mitigate the subjectivity in skin delineation.

CONCLUSIONS

A fully automated skin segmentation algorithm based on the active contour method is described. The proposed ASST makes two contributions to the development of a non-invasive and quantitative imaging tool to assess radiation-induced tissue toxicity. First, the ASST program reduces physicians' manual work in skin delineation. More importantly, this program further reduces the subjectivity in radiation toxicity evaluation and provides more objective measurements of normal tissue injury in breast cancer radiotherapy. Although first clinically applied in breast cancer radiotherapy, our ASST program can also be used for other treatment sites, such as the head and neck.

Acknowledgments—This research was supported in part by National Cancer Institute Grant CA114313 and the Susan Komen for the Cure Foundation.

REFERENCES

- Archambeau J, Pezner R, Wasserman T. Pathophysiology of irradiated skin and breast. *Int J Radiat Oncol Biol Phys* 1995;315:1171–1185.
- Caselles V, Kimmel R, Sapiro G. Geodesic active contours. *Int J Computer Vision* 1997;221:61–79.
- Chan T, Vese L. Active contours without edges. *IEEE Trans Image Process* 2001;102:266–277.
- Comaniciu D, Meer P. Mean shift: A robust approach toward feature space analysis. *IEEE Trans Pattern Anal Machine Intell* 2002;245:603–619.
- Fajardo L, Berthrong M, Anderson R, Anderson R. *Radiation pathology*. New York: Oxford University Press; 2001.
- Foster F, Pavlin C, Harasiewicz K, Christopher D, Turnbull D. Advances in ultrasound biomicroscopy. *Ultrasound Med Biol* 2000;261:1–27.
- Hamming R. *Methods of mathematics applied to calculus, probability, and statistics*. Mineola, NY: Dover; 2004.
- Hao X, Gao S, Gao X. A novel multiscale non-linear thresholding method for ultrasonic speckle suppressing. *IEEE Trans Med Imaging* 1999;189:787.
- Harland C, Bamber J, Gusterson B, Mortimer P. High frequency, high resolution B-scan ultrasound in the assessment of skin tumours. *Br J Dermatol* 2006;1285:525–532.

- Hoffmann K, Gerbaulet U, El-Gammal S, Altmeyer P. 20-MHz B-mode ultrasound in monitoring the course of localized scleroderma (morphoea). *Acta Dermato-venereol Suppl* 1991;164:3.
- Huang Y, Zheng Y, Leung S, Choi A. High frequency ultrasound assessment of skin fibrosis: Clinical results. *Ultrasound Med Biol* 2007; 338:1191–1198.
- International Commission on Radiation Units & Measurements 50 (ICRU). Prescribing, recording and reporting photon beam therapy: Measurements. Bethesda, MD: ICRU; 1993. ICRU Report No. 50.
- Kass M, Witkin A, Terzopoulos D. Snakes: Active contour models. *Int J Computer Vision* 1988;14:321–331.
- Kichenassamy S, Kumar A, Olver P, Tannenbaum A, Yezzi A. Conformal curvature flows: From phase transitions to active vision. *Arch Rational Mech Anal* 1996;1343:275–301.
- Ladak H, Mao F, Wang Y, Downey D, Steinman D, Fenster A. Prostate boundary segmentation from 2-D ultrasound images. *Med Phys* 2000;27:1777.
- Lagarde J, George J, Soulcié R, Black D. Automatic measurement of dermal thickness from B-scan ultrasound images using active contours. *Skin Res Technol* 2005;112:79–90.
- Liu T, Zhou J, Yoshida E, Woodhouse S, Schiff P, Wang T, Lu Z, Pile-Spellman E, Zhang P, Kutcher G. Quantitative ultrasonic evaluation of radiation-induced late tissue toxicity: Pilot study of breast cancer radiotherapy. *Int J Radiat Oncol Biol Phys* 2010;783: 811–820.
- Michailovich O, Tannenbaum A. Despeckling of medical ultrasound images. *IEEE Trans Ultrason Ferroelectr Freq Control* 2006;531: 64–78.
- Mitchell S, Bosch J, Lelieveldt B, van der Geest R, Reiber J, Sonka M. 3-D active appearance models: Segmentation of cardiac MR and ultrasound images. *IEEE Trans Med Imaging* 2002;219:1167–1178.
- Noble J, Boukerroui D. Ultrasound image segmentation: A survey. *IEEE Trans Med Imaging* 2006;258:987–1010.
- Ritter T, Shroud T, Tutwiler R, Shung KA. 30-MHz piezo-composite ultrasound array for medical imaging applications. *IEEE Trans Ultrason Ferroelectr Freq Control* 2002;492:217–230.
- Siddiqi K, Lauziere Y, Tannenbaum A, Zucker S. Area and length minimizing flows for shape segmentation. *IEEE Trans Image Processing* 1998;73:433–443.
- Small W Jr, Woloschak G. Radiation toxicity: A practical guide. *Introduction. Cancer Treat Res* 2006;128:3.
- Vogt M, Ermert H. Development and evaluation of a high-frequency ultrasound-based system for *in vivo* strain imaging of the skin. *IEEE Trans Ultrason Ferroelectr Freq Control* 2005;523:375–385.
- Warszawski A, Röttinger E, Vogel R, Warszawski N. 20-MHz ultrasonic imaging for quantitative assessment and documentation of early and late postradiation skin reactions in breast cancer patients. *Radiother Oncol* 1998;473:241–247.
- Yoshida E, Chen H, Torres M, Andic F, Liu H, Chen Z, Sun X, Curran W, Liu T. Reliability of quantitative ultrasonic assessment of normal-tissue toxicity in breast cancer radiotherapy. *International J Radiat Oncol Biol Phys* 2012;82:724–731.
- Yu Y, Acton S. Speckle reducing anisotropic diffusion. *IEEE Trans Image Process* 2002;1111:1260–1270.
- Zhan Y, Shen D. Deformable segmentation of 3-D ultrasound prostate images using statistical texture matching method. *IEEE Trans Med Imaging* 2006;253:256–272.
- Zhou J, Zhang P, Osterman K, Woodhouse S, Schiff P, Yoshida E, Lu Z, Pile-Spellman E, Kutcher G, Liu T. Implementation and validation of an ultrasonic tissue characterization technique for quantitative assessment of normal-tissue toxicity in radiation therapy. *Med Phys* 2009;365:1643.

MR-TRUS Registration Based on Subject-Specific Biomechanical Model for Image-Guided Prostate Interventions

Xiaofeng Yang, Peter Rossi, Tomi Ogunleye, Ashesh B. Jani, Walter J. Curran, and Tian Liu

Department of Radiation Oncology, Winship Cancer Institute, Emory University, Atlanta, GA

ABSTRACT: The objective of this study is to develop a MR-TRUS prostate registration with a subject-specific biomechanical model, acquired from two US scans, to improve MR-targeted, US-guided prostate interventions (e.g., biopsy and radiotherapy) by incorporating the cancerous regions obtained from multiparametric MRI. The proposed registration method combines a novel subject-specific biomechanical model with a B-spline transformation to register the prostate gland of the MR image to the TRUS volume. The B-spline transformation is calculated by minimizing Euclidean distance between the normalized attribute vectors of landmarks on MR and TRUS prostate surfaces. The subject-specific biomechanical model is obtained through two US scans in which a 3D elasticity (strain) map of the prostate is generated. This biomechanical model is then used to constrain the B-spline-based transformation to predict and compensate for the internal prostate-gland deformation. This method is validated with a prostate-phantom experiment and a pilot study of 5 prostate-cancer patients. For the phantom study, the mean target registration error (TRE) was 1.29 mm. MR-TRUS registration was also successfully performed for 5 patients and the mean TRE was 1.71 ± 0.25 mm. The proposed registration method may provide an accurate and robust means of estimating internal prostate-gland deformation, and is therefore well-suited to a number of MR-targeted, US-guided prostate interventions.

Purpose: Prostate cancer is the major international health problem with a large and rising incidence in many parts of the world [1]. Transrectal ultrasound (TRUS) is the standard imaging modality for the image-guided interventions (e.g., biopsy and brachytherapy) due to its versatility and real-time capability. However, in these procedures, the cancerous regions often are not well-targeted because of the inability to reliably identify prostate cancer through TRUS. In the past decade, MR imaging has shown promise in visualizing prostate tumors with high sensitivity and specificity for the detection of early-stage prostate cancer [2]. A number of researchers have reported the use of multiparametric MRI for cancer detection in prostate with high rates of success [2, 3]. Therefore, the ability to incorporate MR-targeted cancer-bearing regions into TRUS-guided prostate procedures can provide extremely important benefits in terms of more successful prostate-cancer diagnosis and treatment.

To enable MR-targeted, TRUS-guided prostate intervention, MR-TRUS prostate registration is required to map the diagnostic MRI information onto the ultrasound images. MR-TRUS image registration is very challenging due to the intrinsic differences in grey-level intensity characteristics between the two image modalities and the presence of artifacts, particularly in the TRUS images. Hence, the standard intensity-based approaches, such as mutual information, often perform poorly since a probabilistic relationship between MR and TRUS voxel intensities usually does not exist. Recently, several non-intensity-based methods have been explored for MR-TRUS prostate registration. Bharatha *et al.* used an elastic finite element (FE) model to align pre- with intra-procedural images of the prostate [4]. Rishholm *et al.* described a probabilistic method for non-rigid registration of prostate images based on a biomechanical FE model which treats the prostate as an elastic material [5]. Davatzikos *et al.* [6] and Mohamed *et al.* [7] proposed to combine statistical motion modeling with FE analysis to generate 3D deformable models for MR-TRUS prostate image registration. Hu *et al.* used a FE-based statistical motion model trained by biomechanical simulations and registered the model to 3D TRUS images [8]. The purpose of this study is to develop a novel MR-TRUS registration method that combines a subject-specific biomechanical model with B-spline-based transformation.

Methods: The prostate gland is a heterogeneous organ with inter- and intra-patient variation in its physical and biological properties (for example, the calcification, cyst, and cancer regions have different stiffness with the normal tissue). The proposed registration method modeled the prostate tissue as an inhomogeneous elastic material. As shown in Fig. 1, our MR-TRUS registration method consists of three major components: (1) to calculate 3D prostate strain vector map obtained from two 3D TRUS scans under different probe-induced pressures, which is similar as US elastography; (2) to use surface-based registration between the MR and TRUS prostate surfaces to capture the prostate transformation based on the B-spline model; (3) to combine the strain vector map into the B-spline-based transformation to constrain the volumetric deformation of the prostate gland. The diagram of the proposed registration method is shown in Fig. 2.

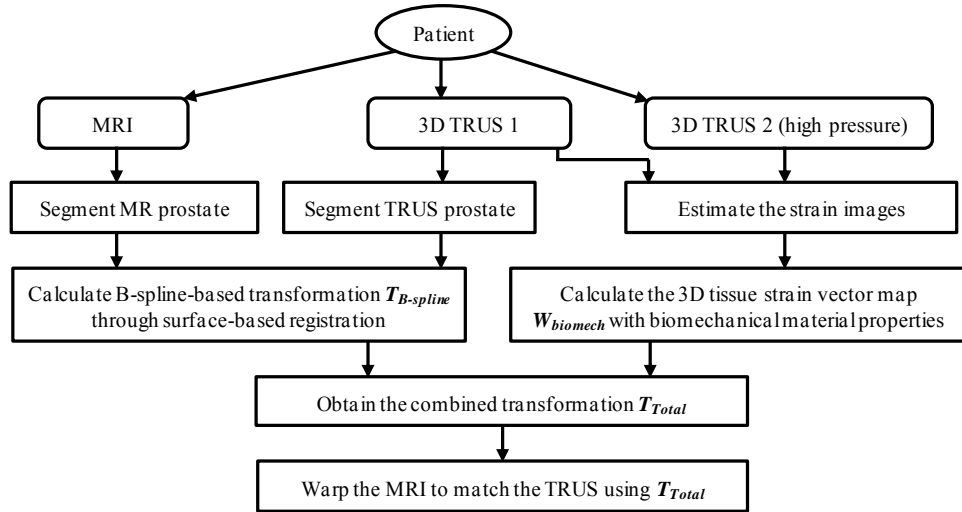


Figure 1. The flow chart of the MR-TRUS prostate registration.

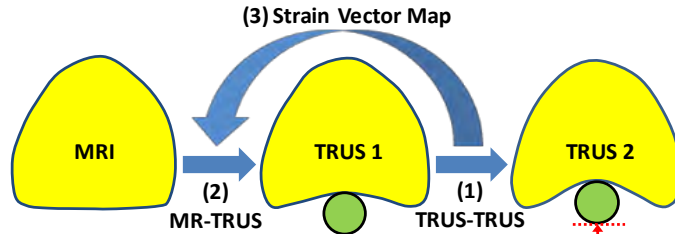


Figure 2. The MR-TRUS prostate registration diagram. Prostate gland is shown in yellow. The green circle represents the TRUS probe.

Biomechanical Model

In our study the two 3D TRUS images are captured with a clinical ultrasound scanner under the different TRUS probe-induced pressures (compression). In order to estimate the global and local displacement of the prostate tissue deformation between two TRUS images, we map the first 3D TRUS image to the second 3D TRUS images with high pressure using a rigid and non-rigid voxel-based registration algorithm [9]. Normalized Mutual Information (NMI) is used as the voxel-based similarity measure. Strain is defined as the deformation of an object, normalized to its original shape, which describes the compressibility of biological tissues. The deformation of the prostate is caused by probe-induced forces by compression and relaxation of the prostate tissue. The tissue at a point undergoes an actual displacement specified by a vector. The displacement vector contains three orthogonal components in our study. The strain tensors are obtained from the gradient of the local displacement at this point. Finally three strain tensors in each voxel are combined into a strain vector $W_{Biomech}$, which has subject-specific tissue biomechanical property.

B-Spline-based Transformation Model

We obtain the prostate tissue transformation $T_{B-spline}$ based on B-spline model through surface match. To perform surface registration, the prostate capsules are segmented from the MR and TRUS images. Then, a triangular mesh surface is generated for each prostate surface, with the vertices of the surface selected as the surface landmarks. Because each surface landmark is actually a vertex of the surface, its spatial relations with vertices in the neighborhood can be used to describe the geometric properties around the surface landmark [10]. Assuming x_i is a surface landmark under study, its geometric attribute is defined as the volume of the tetrahedron formed by x_i and its neighboring vertices. For each boundary landmark x_i , the volumes calculated from different neighborhood layers are stacked into an attribute vector $H(x_i)$, which characterizes the geometric features of x_i from a local to a global fashion. $H(x_i)$ can be further made into an affine-invariant as $\hat{H}(x_i)$, by normalizing it across the whole surface. By using this attribute vector, the similarity between two surface landmarks x_i and y_i , respectively, in MR and TRUS images, can be measured by a Euclidean distance between their normalized attribute vectors. The whole energy function is defined as

$$E(T_{B-spline}) = \sum_{i=1}^I \sum_{j=1}^J p_{ij} \left\| \hat{H}(y_j^{US}) - \hat{H}(T_{B-spline}(x_i^{MR})) \right\|^2 + \delta \sum_{i=1}^I \sum_{j=1}^J p_{ij} \log(p_{ij}) - \xi \sum_{i=1}^I \sum_{j=1}^J p_{ij} + \lambda \left\| \iiint_{(x,y,z) \in \Omega_M} \left(\frac{\partial^2 T_{B-spline}}{\partial x^2} + \frac{\partial^2 T_{B-spline}}{\partial y^2} + \frac{\partial^2 T_{B-spline}}{\partial z^2} \right)^2 dx dy dz \right\|^2$$

where p_{ij} is the fuzzy correspondence matrixes. And δ , λ and ξ are the weights for the energy terms.

Combined Transformation Model

The surface-based transformation using the B-spline model does not reflect the actual prostate tissue deformation because this model does not take into account the specific tissue elastic property. To incorporate tissue biomechanical property, the surface-based transformation $T_{B-spline}$ is regulated by the strain vector map $W_{biomech}$, to constrain the B-spline-based prostate-gland transformation. The prostate elastic property is weighted into the B-spline-based tissue deformation to obtain the accurate patient-specific volumetric deformation of the prostate gland. Contrast to the B-spline-based deformation model, our biomechanical model could capture accurate local deformation in heterogeneous tissue. Therefore, the transformation simultaneously estimates the surface and internal deformation.

Results: To validate the proposed registration method, we conducted an experiment with a prostate phantom, in which two markers and three lesions are imbedded. T1- and T2-weighted images of the prostate phantom were acquired using a 1.5T Philips MRI scanner. Two sets of 3D TRUS images were acquired with an Ultrasonix ultrasound scanner under two different probe-induced pressures. Our registration results were compared with the surface-based registration (Fig. 3). Contrast to the surface-based method which resulted in large mismatch of the internal structures such as the lesions and urethra, our registration achieved close match of the internal structures. Quantitative comparison of the two registration methods were demonstrated using the target registration error (TRE) of the markers. The averaged TRE was 3.09 ± 0.46 mm for the surface-based method, while 1.29 ± 0.11 mm for our proposed method. This demonstrates the proposed methods based on the inhomogeneous elasticity model improve the registration results by providing a physical regularization of the deformation map.

All patients' TRUS data were acquired using a Hitachi ultrasound machine and a 7.5MHz bi-plane probe. All MR images were acquired using a Philips 1.5T MR scanner and a pelvic phase-array coil. All prostates were contoured in T2-weighted MR and TRUS images by an experienced physician. For each patient, three to six landmarks were indentified in post-registration MR and TRUS images to facilitate

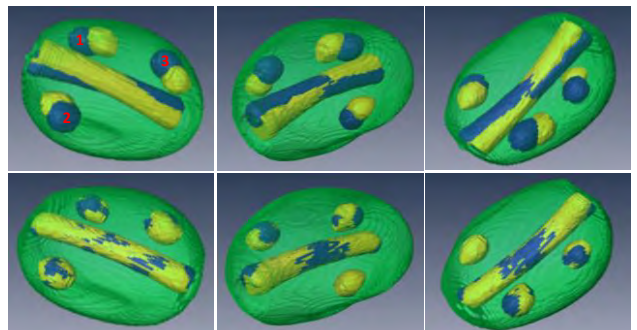


Figure 3. 3D comparison of registration results using surface-based and our methods. Top row (surface-based method): 3D visualization images of the post-registration MRI (yellow) and TRUS (blue). Bottom row (our method): 3D visualization images of the post-registration MRI (yellow) and TRUS (blue).

quantitative comparison. Again, we compared our registration results with the surface-based method. Figure 4 showed the registration results of a 65-year old prostate-cancer patient. Three cysts were identified as landmarks to compare the registration results (arrows) and our registration was able to achieve a close match of these landmarks. Table 1 shows the TRE of the 5 patients. The averaged TRE was 3.25 ± 0.51 mm for the surface-based method, while 1.71 ± 0.25 mm for our proposed method, which demonstrates the proposed methods based on the inhomogeneous elasticity model improve the registration results by providing a physical regularization of the deformation map.

New or breakthrough work to be presented: The main novelty of the proposed method is to construct a 3D biomechanical elasticity (strain) map of the prostate gland using two US scans. As compared with previous methods in which the constant elastic parameters of biological tissues were assigned, our approach can provide the precise and subject-specific biologic tissue elastic property of the prostate. This biomechanical model was used to constrain the B-spline-based deformation derived from the MR and TRUS prostate surface displacement to predict the prostate internal deformation.

Conclusion: In this report, we present a novel MR-TRUS registration method that combines a novel subject-specific biomechanical model with a B-spline transformation to register the prostate gland of the MR image to the TRUS volume. We have validated the accuracy of the proposed method with a prostate-phantom study and a pilot study of 5 prostate-cancer patients. The proposed registration method may provide an accurate and robust means of predicting internal prostate-gland deformation, and is therefore well-suited to a number of interventional applications where there is a need for deformation compensation. Successful integration of multi-parametric MR and TRUS prostate images could provide extremely important benefits in terms of more successful prostate-cancer diagnosis and treatment.

Acknowledgements: This research is supported in part by DOD PCRP Award W81XWH-13-1-0269, and National Cancer Institute (NCI) Grant CA114313.

References

- [1] Y. Sun, J. Yuan, M. Rajchl *et al.*, [Efficient Convex Optimization Approach to 3D Non-rigid MR-TRUS Registration] Springer Berlin Heidelberg, 25 (2013).
- [2] C. M. A. Hoeks, J. O. Barentsz, T. Hambrock *et al.*, “Prostate Cancer: Multiparametric MR Imaging for Detection, Localization, and Staging,” *Radiology*, 261(1), 46-66 (2011).
- [3] N. B. Delongchamps, F. Beuvon, D. Eiss *et al.*, “Multiparametric MRI is helpful to predict tumor focality, stage, and size in patients diagnosed with unilateral low-risk prostate cancer,” *Prostate Cancer and Prostatic Diseases*, 14(3), 232-237 (2011).
- [4] A. Bharatha, M. Hirose, N. Hata *et al.*, “Evaluation of three-dimensional finite element-based deformable registration of pre- and intraoperative prostate imaging,” *Medical Physics*, 28(12), 2551-2560 (2001).
- [5] P. Risholm, A. Fedorov, J. Pursley *et al.*, “Probabilistic Non-Rigid Registration of Prostate Images: Modeling and Quantifying Uncertainty,” *2011 8th Ieee International Symposium on Biomedical Imaging: From Nano to Macro*, 553-556 (2011).
- [6] C. Davatzikos, D. G. Shen, A. Mohamed *et al.*, “A framework for predictive modeling of anatomical deformations,” *Ieee Transactions on Medical Imaging*, 20(8), 836-843 (2001).
- [7] A. Mohamed, C. Davatzikos, and R. Taylor, [A Combined Statistical and Biomechanical Model for Estimation of Intra-operative Prostate Deformation] Springer Berlin Heidelberg, 57 (2002).
- [8] Y. P. Hu, H. U. Ahmed, Z. Taylor *et al.*, “MR to ultrasound registration for image-guided prostate interventions,” *Medical Image Analysis*, 16(3), 687-703 (2012).

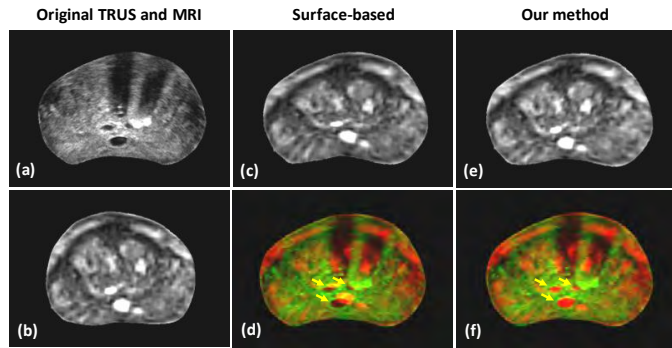


Figure 4. Comparison of prostate registration using the surface-based and our methods. Column 1: original TRUS (a) and MRI (b). Column 2 (surface-based method): post-registration MRI (c) and fusion image (d). Column 3 (our method): post-registration MRI (e) and fusion image (f). Three landmarks (yellow arrows) were identified to compare the registration accuracy.

Table1. TRE of 5 prostate-cancer patients.

Patient	P01	P02	P03	P04	P05	Mean	STD
Surface-based (mm)	2.47	3.25	2.13	3.63	3.78	3.25	0.51
Our method (mm)	1.61	1.74	1.34	1.87	1.97	1.71	0.25

- [9] D. Rueckert, L. I. Sonoda, C. Hayes *et al.*, “Nonrigid registration using free-form deformations: Application to breast MR images,” Ieee Transactions on Medical Imaging, 18(8), 712-721 (1999).
- [10] Y. Zhan, Y. Ou, M. Feldman *et al.*, “Registering histologic and MR images of prostate for image-based cancer detection,” Acad Radiol, 14(11), 1367-81 (2007).

A New CT Prostate Segmentation for CT-Based HDR Brachytherapy

Xiaofeng Yang*, Peter Rossi, Tomi Ogunleye, Ashesh B. Jani, Walter J. Curran, and Tian Liu

Department of Radiation Oncology, Winship Cancer Institute, Emory University,
Atlanta, GA 30322

*Corresponding author: xyang43@emory.edu

High-dose-rate (HDR) brachytherapy has become a popular treatment modality for localized prostate cancer. Prostate HDR treatment involves placing 10 to 20 catheters (needles) into the prostate gland, and then delivering radiation dose to the cancerous regions through these catheters. These catheters are often inserted with transrectal ultrasound (TRUS) guidance and the HDR treatment plan is based on the CT images. The main challenge for CT-based HDR planning is to accurately segment prostate volume in CT images due to the poor soft tissue contrast and additional artifacts introduced by the catheters. To overcome these limitations, we propose a novel approach to segment the prostate in CT images through TRUS-CT deformable registration based on the catheter locations. In this approach, the HDR catheters are reconstructed from the intra-operative TRUS and planning CT images, and then used as landmarks for the TRUS-CT image registration. The prostate contour generated from the TRUS images captured during the ultrasound-guided HDR procedure was used to segment the prostate on the CT images through deformable registration. We conducted two studies. A prostate-phantom study demonstrated a sub-millimeter accuracy of our method. A pilot study of 5 prostate-cancer patients was conducted to further test its clinical feasibility. All patients had 3 gold markers implanted in the prostate that were used to evaluate the registration accuracy, as well as previous diagnostic MR images that were used as the gold standard to assess the prostate segmentation. For the 5 patients, the mean gold-marker displacement was 1.2 mm; the prostate volume difference between our approach and the MRI was 7.2%, and the Dice volume overlap was over 91%. Our proposed method could improve prostate delineation, enable accurate dose planning and delivery, and potentially enhance prostate HDR treatment outcome.

Key words: Prostate, CT, segmentation, transrectal ultrasound (TRUS), ultrasound-guided, HDR, brachytherapy.

1. INTRODUCTION

In recent years, an increasing number of men, many of younger ages, are undergoing prostate high-dose-rate (HDR) brachytherapy instead of radical prostatectomy for localized prostate cancer [1, 2]. Prostate HDR treatment involves placing 10 to 20 catheters (needles) into the prostate gland, and then delivering radiation dose to the cancerous regions through these catheters. In CT-based prostate HDR brachytherapy, catheter insertions are commonly performed under the guidance of intra-operative transrectal ultrasound (TRUS), while treatment planning is based on post-operative CT images.

HDR prostate brachytherapy depends greatly on the precise delineation of the prostate gland on CT images. As is well known, it is challenging to define the prostate volume in CT images due to the poor soft-tissue contrast between the prostate and its surrounding tissue (background). This problem worsens in the HDR procedure, because the 10 to 20 HDR catheters inserted inside the prostate introduce significant artifacts to the prostate CT images.

Many segmentation methods have been proposed for prostate delineation in CT images. *Chowdhury et al.* proposed a linked statistical shape model (LSSM) that linked the shape variation of a structure of interest across MR and CT imaging modalities to concurrently segment prostate on pelvic CT images [3]. *Feng et al.* presented a deformable-model-based segmentation method using both shape and appearance information learned from the previous images to guide automatic segmentation of a new set of images [4]. *Ghosh et al.* combined the high-level-texture features and prostate-shape information with the genetic algorithm to identify the best matching region in the new to-be-segmented prostate CT image [5]. *Li et al.* presented an online-learning and patient-specific classification method based on the location-adaptive image context to achieve the segmentation of the prostate in CT images [6]. *Liao et al.* used a patch-based representation in the discriminative feature space with logistic sparse LASSO as the anatomical signature to deal with low contrast problems in prostate CT images, and designed a multi-atlases label fusion method formulated under sparse representation framework to segment the prostate [7]. *Chen et al.* proposed a Bayesian framework which considered anatomical constraints from bones and learnt appearance information to construct the deformable model [8]. These previous methods were all based on the appearance and texture of the prostate CT images, and therefore may not work well in the HDR procedure due to the strong artifacts generated by the HDR catheters which smear the boundary and texture of the prostate on CT images.

In this study, we propose a novel approach that deforms intra-operative TRUS-based prostate contours into the CT images for prostate segmentation through TRUS-CT registration using the catheter locations. Our segmentation approach was evaluated through two studies: a prostate-phantom study and a clinical study of 5 patients undergoing HDR brachytherapy for prostate cancer.

2. METHODS

Our prostate segmentation method for the HDR prostate brachytherapy consists of 5 major steps (Fig. 1).

- Step 1: 3D TRUS prostate images are captured after catheter insertion during the HDR procedure.
- Step 2: After the catheter insertion, each patient receives a post-operative CT scan.
- Step3: The prostate volume is contoured in the 3D TRUS images.
- Step 4: A TRUS-CT deformable registration is performed using the catheters as landmarks.
- Step 5: The TRUS-based prostate contour is integrated into the treatment planning CT images to segment the prostate for the HDR brachytherapy treatment.

Our approach requires acquisition of 3D TRUS prostate images in the operation room (OR) right after the HDR catheters are inserted, which takes 1-3 minutes. These TRUS images are then used to create prostate contours. The HDR catheters reconstructed from the intra-operative TRUS and post-operative CT images are used as landmarks for the TRUS-CT deformable registration based on a robust point match algorithm.

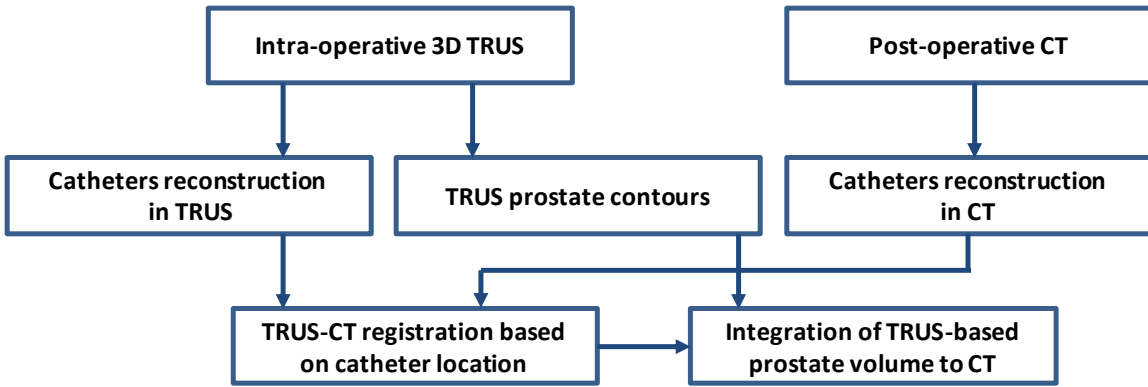


Fig. 1. Flow chart of prostate segmentation in TRUS-guided CT-based HDR brachytherapy.

The correspondences between the catheter landmarks are respectively described by a fuzzy correspondence matrixes P . The matrix $P = \{p_{ij}\}$ consists of two parts. The $I \times J$ inner submatrix define the correspondences of X and Y . It is worth noting that p_{ij} have real values between 0 and 1, which denote the fuzzy correspondences between landmarks [9, 10]. In order to perform TRUS-CT deformable registration we design an overall similarity function that integrates the similarities between catheter-type landmarks and smoothness constraints on the estimated transformation between catheters in CT and TRUS images.

$$\begin{aligned}
 E(f) = & \sum_{i=1}^I \sum_{j=1}^J p_{ij} (\|\hat{H}(y_j^{US}) - \hat{H}(f(x_i^{CT}))\|^2) + \alpha \sum_{i=1}^I \sum_{j=1}^J p_{ij} \log(p_{ij}) - \beta \sum_{i=1}^I \sum_{j=1}^J p_{ij} + \\
 & \lambda \left\| \iiint_{(x,y,z) \in \Omega_M} \left(\frac{\partial^2 f}{\partial x^2} + \frac{\partial^2 f}{\partial y^2} + \frac{\partial^2 f}{\partial z^2} \right)^2 dx dy dz \right\|^2
 \end{aligned}$$

α , β and λ are the weights for each energy term. The first, second and third terms are the similarity for catheter landmarks, and the forth term is the smoothness constraint term. α is called the temperature parameter and its weighted term is an entropy term comes from the deterministic annealing technique [11]. β is the weight for outlier rejection term. f denotes the transformation between CT and TRUS images. The overall similarity function can be minimized by an alternating optimization algorithm that successively updates the correspondences matrixes p_{ij} , and the transformation function f . The TRUS-based prostate volume is then deformed to the CT images to finish CT prostate segmentation for treatment planning after TRUS-CT registration.

3. RESULTS

3.1 Phantom study

Our prostate segmentation method was first tested with a prostate phantom (CIRS Model 053). In this phantom, a tissue-mimicking prostate along with the structures simulating the rectal wall, seminal vesicles and urethra is contained within an $11.5 \times 7.0 \times 9.5 \text{ cm}^3$ clear plastic container. To mimic a prostate

HDR procedure, 14 catheters were implanted into the prostate gland under the US guidance. In addition, three gold markers were implanted at the base, mid or apex of the prostate. After the prostate segmentation, the displacements of these gold markers between the CT and post-registration TRUS were used to test the accuracy of our registration. Because the phantom prostate boundary is clear on the CT images, we used the manually segmented CT prostate volume as the gold standard to evaluate the performance of our prostate segmentation.

Figure 2 shows the integration of TRUS-based prostate volume into the CT images. The phantom TRUS scan was captured with a transverse (axial) pixel size of $0.08 \times 0.08 \text{ mm}^2$ and a step size (slice thickness) of 0.5 mm. The phantom CT was scanned with a voxel size of $0.29 \times 0.29 \times 1.00 \text{ mm}^3$. The catheter artifacts are clearly displayed on the axial CT image. On the coronal images, the close match of a gold marker location between the post-registration US and CT is shown. The yellow dotted contour is the prostate transferred from the TRUS images after deformable registration between the TRUS and CT images.

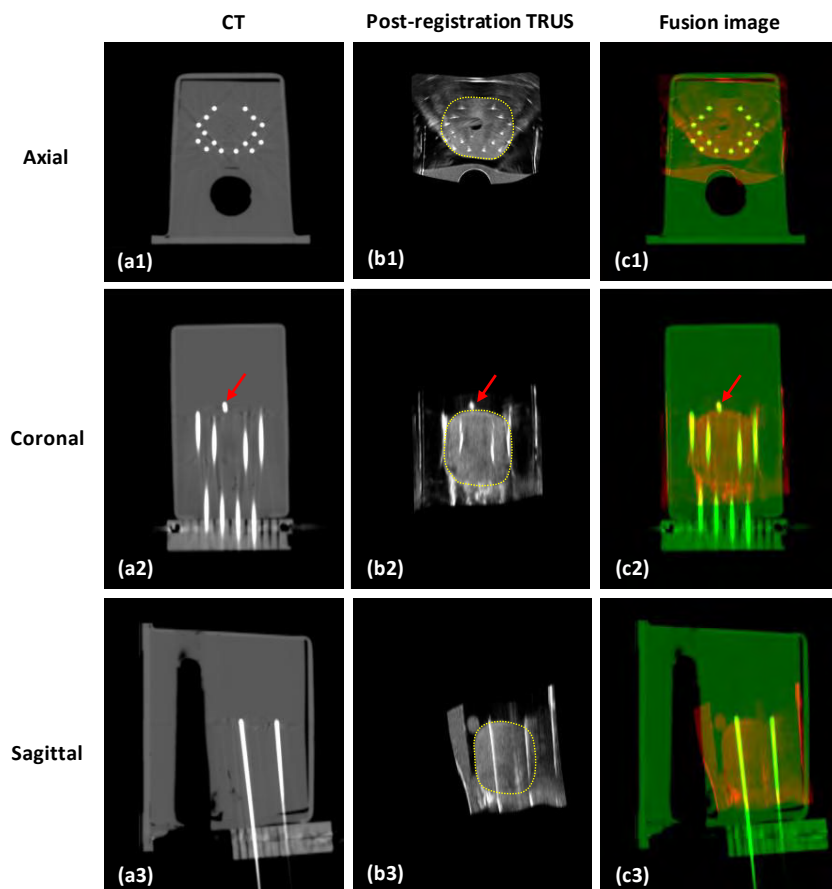


Fig. 2. Integration of TRUS-based prostate volume into CT images. a1-a3 are CT images of the prostate phantom; b1-b3 are the post-registration TRUS images; c1-c3 are the fusion images between CT and post-registration TRUS images. The close match between the gold markers (red arrows) in the CT and TRUS demonstrated the accuracy of our method.

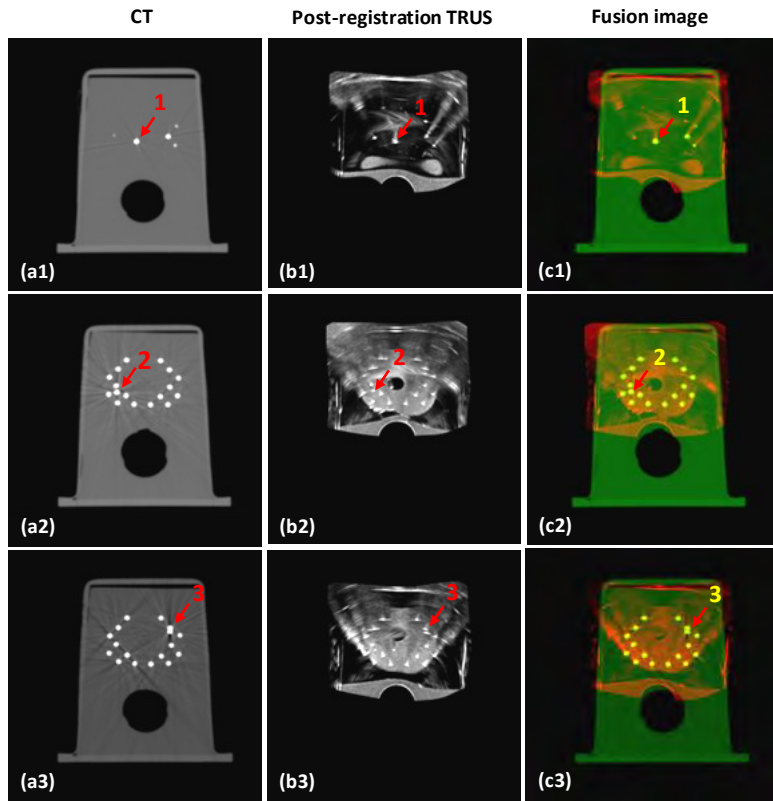


Fig. 3. Segmentation accuracy is demonstrated through 3 gold markers in the prostate phantom. a1-a3 are axial CT images of the prostate phantom; b1-b3 are its post-registration TRUS images; c1-c3 are the fusion images between the CT and post-registration TRUS images; and d1-d3 are the TRUS-CT fusion images, where the prostate volume is integrated. The close match between the 3 gold markers (red arrows) in the CT and TRUS demonstrated the accuracy of our registration.

Figure 3 shows the 3 gold markers on the CT, fusion and post-registration TRUS images. The 3 gold markers are located at the base, left mid and right mid of the prostate gland. Visually, we can see the locations of the gold markers on the post-registration TRUS and CT images are very close. Quantitatively, the displacements of the three gold markers between the post-registration TRUS and CT images were 0.51, 0.29 and 0.42 mm, respectively. The mean displacement of the 3 gold markers was less than 0.5 mm; therefore our registration between the CT and TRUS achieved sub-millimeter accuracy.

To evaluate the accuracy of our prostate segmentation, we compared our segmented prostate with the manually contoured prostate volume from the CT images. The volume difference between the CT and post-registration TRUS is an essential measurement in the morphometric assessment of anatomical structures. In this phantom study, the absolute volume difference and Dice volume overlap were 1.65% and 97.84%, respectively. The segmentation accuracy is demonstrated by the small volume difference and large volume overlap of the two prostate contours generated from the proposed method and the gold standard.

3.2 In vivo patient study

We conducted a retrospective clinical study of 5 patients, who had received HDR brachytherapy for localized prostate cancer. All treated patients received diagnostic Magnetic Resonance Imaging (MRI) scans before the HDR brachytherapy treatment. For the HDR brachytherapy, 14-18 catheters and 3 gold markers were implanted in each patient under the TRUS guidance. Three gold markers were placed at the base, middle and apex of the prostate. Therefore, each patient had a diagnostic MR scan, intra-operative 3D ultrasound scan and post-operative CT scan. The TRUS prostate image was scanned with 2 mm step and $0.07 \times 0.07 \text{ mm}^2$ transverse pixel size. The patient's CT image was captured with the voxel size of $0.68 \times 0.68 \times 1.00 \text{ mm}^3$, and the MR image was obtained with the voxel size of $1.0 \times 1.0 \times 2.0 \text{ mm}^3$.

In this clinical study, the prostate segmentation was successfully performed for all 5 patients. Figure 4 shows the prostate registration results between the CT and TRUS of a 58 year old patient. The accuracy of the CT-TRUS image registration was evaluated by the displacement of each gold marker on the CT and post-registration TRUS images. The mean displacement of the gold markers between CT and registered TRUS for each patient ranged between 1.1 to 1.6 mm. Overall, the mean displacement of the 3 gold markers of all patients was $1.2 \pm 0.3 \text{ mm}$. Therefore, the registration of the proposed method achieved millimeter accuracy.

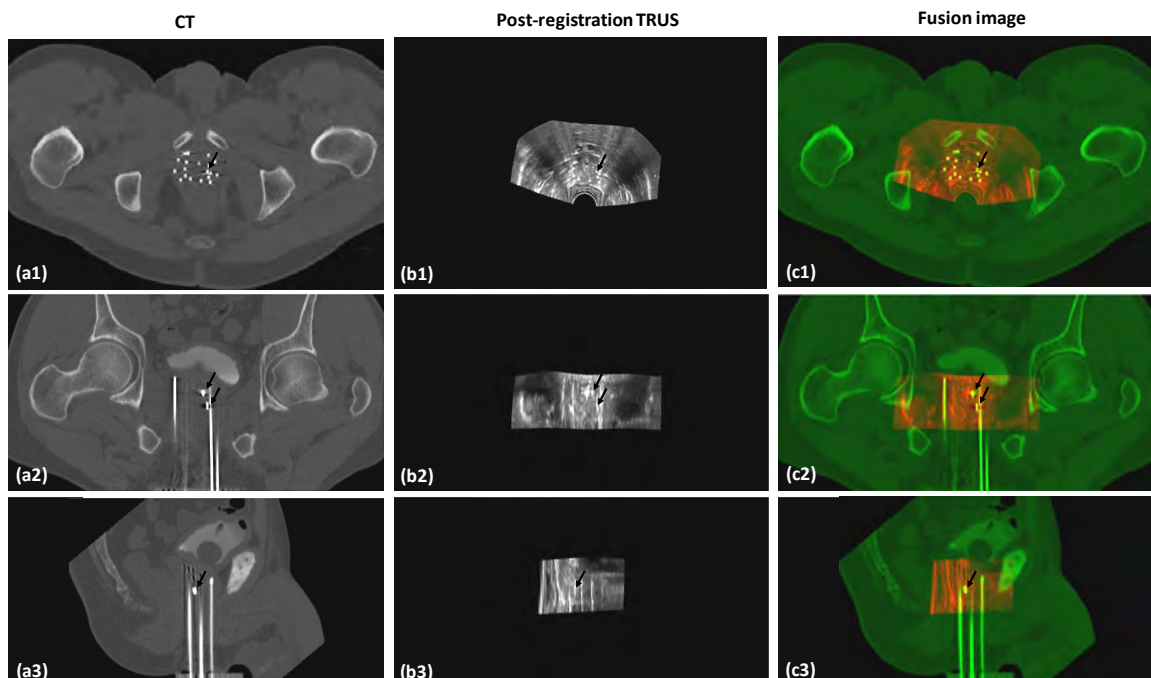


Fig. 4. TRUS-CT registration results. a1-a3 are CT images of a 58-year-old prostate-cancer patient; b1-b3 are his post-registration TRUS images; and c1-c3 are the fusion images between the CT and post-registration TRUS images. The close match between the gold markers (dark arrows) on the CT and TRUS demonstrated the accuracy of our registration method.

To evaluate the accuracy of our prostate segmentation, we used MRI-defined prostate volumes. Studies have shown that MRI has a high soft tissue contrast, and can provide accurate prostate delineation [12, 13]. Therefore we used prostate manually contoured from the MR images as the gold standard to evaluate our prostate segmentation. Due to variations in the patient's positions during the CT and MR scans, the prostate shape could be different between CT and MRI. Therefore, we transformed the MRI-defined prostate volumes onto CT images by MR-CT deformable registration [14-17]. Finally our segmented prostate volumes were compared with those defined from the MRIs.

Figure 5 shows the absolute volume difference and Dice volume overlap between the MRI-defined prostate contours and our prostate segmentation for all 5 patients. The average absolute prostate-volume difference between our approach and the corresponding MRI was $7.2 \pm 0.9\%$, and the average Dice volume overlap was $91.6 \pm 1.3\%$. The small prostate volume difference and large volume overlap demonstrated the robustness of our prostate segmentation method.

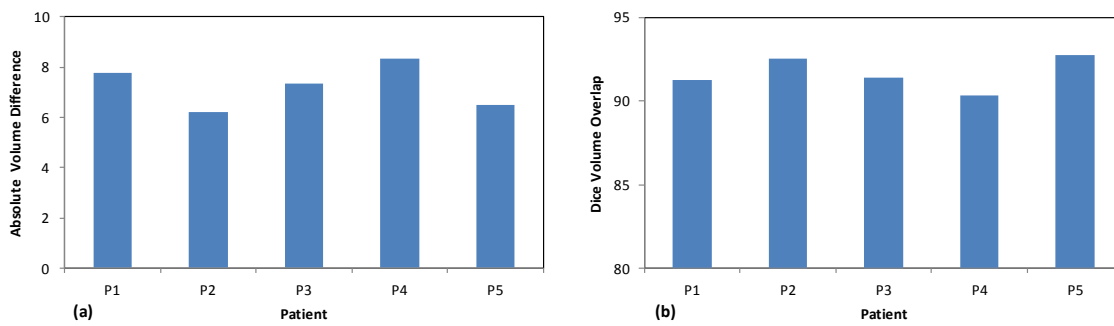


Fig. 5. Evaluation of our prostate segmentation accuracy. (a) Absolute volume difference and (b) Dice volume overlap between the corresponding prostate of TRUS and MR images of 5 prostate-cancer patients

4. CONCLUSION

In this study, we have proposed a novel CT prostate segmentation method through TRUS-CT deformable registration using the catheter locations for prostate HDR brachytherapy. While it is well known that accurate CT prostate segmentation is challenging, the 10-20 HDR catheters inserted inside the prostate worsens the problem by introducing significant artifacts in CT images. In our approach, we rely on the 3D TRUS images to provide accurate prostate delineation, and then use the HDR catheters as landmarks to register 3D TRUS prostate images to CT images. Therefore, our approach is not affected by the catheter artifacts, and can accurately segment the prostate volume in CT images. The proposed approach was evaluated through a prostate phantom study and a pilot clinical study of 5 patients. For future directions, we will incorporate automatic prostate segmentation methods into our 3D TRUS prostate segmentation to speed up the process [18-23]. Our prostate segmentation technology will improve prostate delineations, enable accurate dose planning and delivery, and potentially enhance prostate HDR treatment outcomes.

ACKNOWLEDGEMENTS

This research is supported in part by the Department of Defense (DoD) Prostate Cancer Research Program (PCRP) Award W81XWH-13-1-0269 and National Cancer Institute (NCI) Grant CA114313.

REFERENCES

- [1] C. J. Mettlin, G. P. Murphy, C. J. McDonald *et al.*, “The National Cancer Data base Report on increased use of brachytherapy for the treatment of patients with prostate carcinoma in the U.S.” *Cancer*, 86(9), 1877-82 (1999).
- [2] M. R. Cooperberg, D. P. Lubeck, M. V. Meng *et al.*, “The changing face of low-risk prostate cancer: trends in clinical presentation and primary management,” *J Clin Oncol*, 22(11), 2141-9 (2004).
- [3] N. Chowdhury, R. Toth, J. Chappelow *et al.*, “Concurrent segmentation of the prostate on MRI and CT via linked statistical shape models for radiotherapy planning,” *Medical Physics*, 39(4), 2214-2228 (2012).
- [4] Q. J. Feng, M. Foskey, W. F. Chen *et al.*, “Segmenting CT prostate images using population and patient-specific statistics for radiotherapy,” *Medical Physics*, 37(8), 4121-4132 (2010).
- [5] P. Ghosh, and M. Mitchell, “Prostate segmentation on pelvic CT images using a genetic algorithm,” *Medical Imaging 2008: Image Processing*, Pts 1-3, 6914, 91442-91442 (2008).
- [6] W. Li, S. Liao, Q. J. Feng *et al.*, “Learning image context for segmentation of the prostate in CT-guided radiotherapy,” *Physics in Medicine and Biology*, 57(5), 1283-1308 (2012).
- [7] S. Liao, Y. Z. Gao, J. Lian *et al.*, “Sparse Patch-Based Label Propagation for Accurate Prostate Localization in CT Images,” *Ieee Transactions on Medical Imaging*, 32(2), 419-434 (2013).
- [8] S. Q. Chen, D. M. Lovelock, and R. J. Radke, “Segmenting the prostate and rectum in CT imagery using anatomical constraints,” *Medical Image Analysis*, 15(1), 1-11 (2011).
- [9] H. Chui, and A. Rangarajan, “A new point matching algorithm for non-rigid registration,” *Computer Vision and Image Understanding*, 89(2-3), 114-141 (2002).
- [10] X. F. Yang, H. Akbari, L. Halig *et al.*, “3D Non-rigid Registration Using Surface and Local Salient Features for Transrectal Ultrasound Image-guided Prostate Biopsy,” *Medical Imaging 2011: Visualization, Image-Guided Procedures, and Modeling*, 7964, (2011).
- [11] A.L.Yuill, and J.J.Kosowsky, “Statistical Physics Algorithms That Converge,” *Neural Computation*, 6(3), 341-356 (1994).
- [12] J. S. Lee, and B. H. Chung, “Transrectal ultrasound versus magnetic resonance imaging in the estimation of prostate volume as compared with radical prostatectomy specimens,” *Urologia Internationalis*, 78(4), 323-327 (2007).
- [13] B. E. Weiss, A. J. Wein, S. B. Malkowicz *et al.*, “Comparison of prostate volume measured by transrectal ultrasound and magnetic resonance imaging: Is transrectal ultrasound suitable to determine which patients should undergo active surveillance?,” *Urologic Oncology-Seminars and Original Investigations*, 31(8), 1436-1440 (2013).
- [14] G. Cheng, X. Yang, N. Wu *et al.*, “Multi-atlas-based segmentation of the parotid glands of MR images in patients following head-and-neck cancer radiotherapy.” 8670, 86702Q-86702Q-7.
- [15] C. J. Dean, J. R. Sykes, R. A. Cooper *et al.*, “An evaluation of four CT-MRI co-registration techniques for radiotherapy treatment planning of prone rectal cancer patients,” *British Journal of Radiology*, 85(1009), 61-68 (2012).

- [16] A. Betgen, F. Pos, C. Schneider *et al.*, "Automatic registration of the prostate on MRI scans to CT scans for radiotherapy target delineation," *Radiotherapy and Oncology*, 84, S119-S119 (2007).
- [17] D. Levy, E. Schreibmann, B. Thorndyke *et al.*, "Registration of prostate MRI/MRSI and CT studies using the narrow band approach," *Medical Physics*, 32(6), 1895-1895 (2005).
- [18] X. Yang, and B. Fei, "3D prostate segmentation of ultrasound images combining longitudinal image registration and machine learning" *Proc. SPIE* 8316, 83162O (2012).
- [19] X. Yang, D. Schuster, V. Master *et al.*, "Automatic 3D segmentation of ultrasound images using atlas registration and statistical texture prior," *Proc. SPIE* 7964, 796432, (2011).
- [20] P. Yan, S. Xu, B. Turkbey *et al.*, "Adaptively learning local shape statistics for prostate segmentation in ultrasound," *IEEE Trans Biomed Eng*, 58(3), 633-41 (2011).
- [21] Y. Zhan, and D. Shen, "Deformable segmentation of 3-D ultrasound prostate images using statistical texture matching method," *IEEE Trans.Med.Imaging*, 25(3), 256-272 (2006).
- [22] J. A. Noble, and D. Boukerroui, "Ultrasound image segmentation: a survey," *IEEE Trans.Med.Imaging*, 25, 987-1010 (2006).
- [23] D. Shen, Y. Zhan, and C. Davatzikos, "Segmentation of prostate boundaries from ultrasound images using statistical shape model," *IEEE Trans.Med.Imaging*, 22(4), 539-551 (2003).

A New 3D Neurovascular Bundles (NVB) Segmentation Method based on MR-TRUS Deformable Registration

Xiaofeng Yang, Peter Rossi, Tomi Ogunleye, Ashesh B. Jani, Walter J. Curran, and Tian Liu

Department of Radiation Oncology, Winship Cancer Institute, Emory University, Atlanta, GA

ABSTRACT: In this paper we propose a 3D NVB segmentation method for ultrasound (US) image by integrating MR and transrectal ultrasound (TRUS) images through MR-TRUS deformable registration. First, 3D neurovascular bundles (NVB) are contoured in MR images captured before radiotherapy (RT) by a physician, and then 3D MR-defined NVB are transformed into US images by the MR-TRUS registration method, which models the prostate tissue as an elastic material, and jointly estimates the boundary deformation and the volumetric deformations under elastic constraint. This technique was validated with a clinical study of 7 patients undergoing RT treatment for prostate cancer. The accuracy of our approach was assessed through the locations of landmarks, as well as previous ultrasound Doppler images of patients. MR-TRUS registration was successfully performed for all patients. The mean displacement of the landmarks between the post-registration MR and TRUS images was 1.56 ± 0.37 mm, and the NVB volume Dice Overlap Coefficient was $92.1 \pm 3.2\%$. We have developed a new approach to improve 3D NVB segmentation through MR-TRUS registration for prostate RT, demonstrated its clinical feasibility, and validated its accuracy with ultrasound Doppler data. This technique could be a useful tool as we try to spare the NVB in prostate RT, monitor NVB response to RT, and potentially improve post-RT potency outcomes.

Purpose: In the United States, 2.36 million men have survived prostate cancer, and are currently living with cancer-affected life years. Erectile dysfunction (ED), or the loss of sexual potency, is the most common and debilitating side effect after radiotherapy for prostate cancer. The mechanism behind radiotherapy-related ED is not fully understood and one hypothesis is that neurovascular bundle (NVB) injury is correlated with the radiation-associated ED. However, the segmentation and localization of the NVB remains challenging in most prostate radiotherapy (RT) treatment planning. Currently, MRI is the best imaging modality for 3D visualization of the NVB. We propose to integrate MR into transrectal ultrasound (TRUS) images through MR-TRUS registration for accurate segment of 3D NVB in TRUS.

Methods: As shown in Figure 1, our segmentation approach evolves 5 major steps: 1) MR diagnostics prostate images are captured before the RT procedure; 2) Patient receives 2 3D TRUS ultrasound scans and ultrasound Doppler scan; 3) Physician contours NVB volumes using MR images; 4) MR-TRUS image registration is performed using a patient-specific biomechanical model; 5) Integration of MR-based NVB volumes into 3D TRUS images for treatment planning.

MR-TRUS registration

The key part of our proposed segmentation method is MR-TRUS registration. This paper uses a new MR-TRUS registration method that combines a subject-specific biomechanical model with B-spline-based transformation. As shown in Figure 2, our MR-TRUS registration method consists of three major components. First, we calculate 3D patient-specific prostate-gland elasticity map from two 3D TRUS scans under different probe-induced pressures, which is similar as ultrasound elastography. And then we use surface registration between the MR and TRUS prostate surfaces to capture the prostate transformation based on the B-spline model by minimizing the Euclidean distance between the normalized attribute vectors of surface landmarks of MR and TRUS prostate surfaces. Finally we combine the prior prostate-gland elasticity map into the surface-based transformation to constrain/guide the volumetric deformation of the prostate gland in MR-TRUS registration. The proposed registration method takes into account the wide variations among patients and within each prostate gland – normal

prostatic tissue, cysts, cancers and calcifications all have different elastic properties. This registration based on the inhomogeneous elasticity model could improve the prostate tissue deformation due to provide a physical regularization of the deformation map.

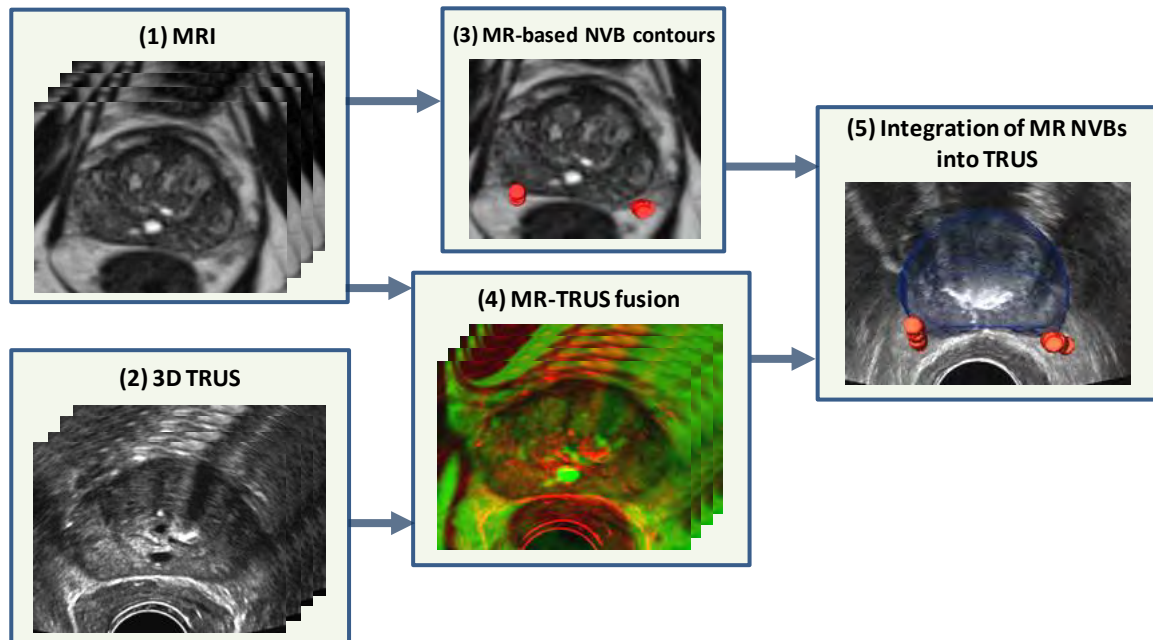


Figure 1. Flow chart of integrating MR-based 3D NVB into TRUS.

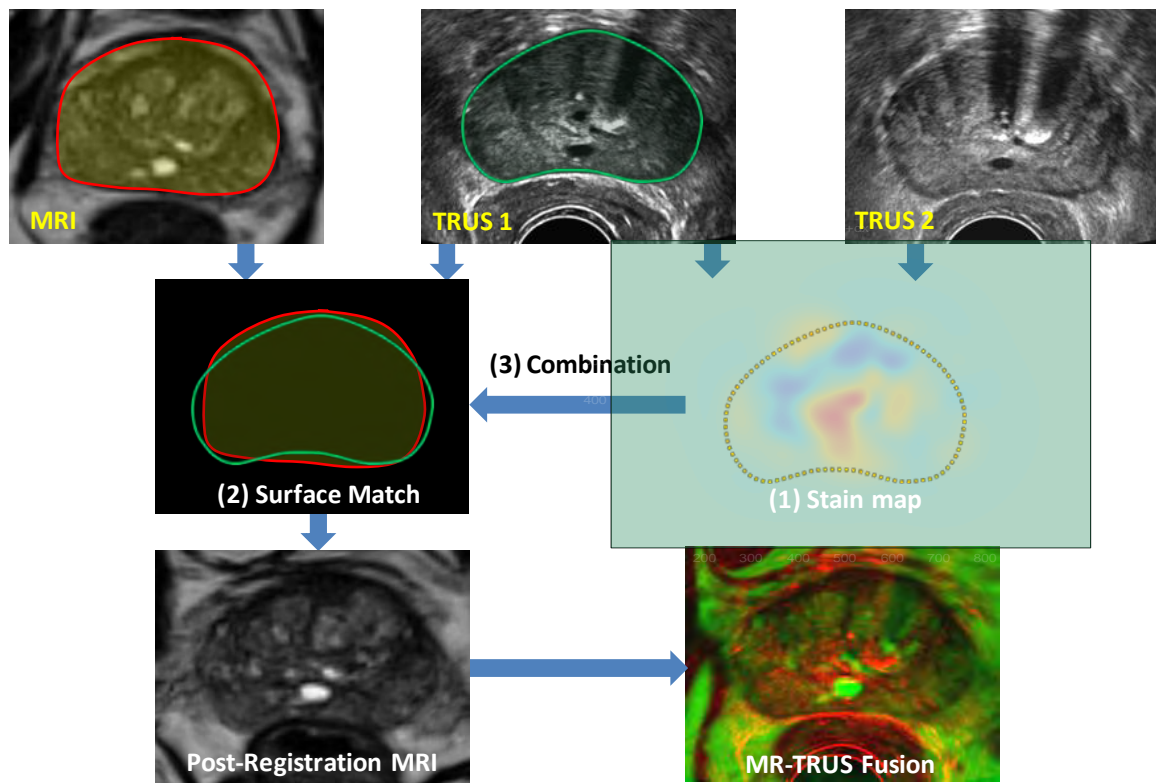


Figure 2. Flow chart of the MR-TRUS registration

NVB segmentation

This registration method used one-modality image registration between TRUS and TRUS to provide prior tissue deformation guidance for two-modality image registration between MR and TRUS to improve the accuracy the MR-TRUS registration. The NVB are composed of numerous nerve fibers superimposed on a scaffold of veins, arteries, and variable amounts of adipose tissue surrounding almost the entire lateral and posterior surfaces of the prostate. The accurate prostate tissue deformation provides the basis for the accurate TRUS segmentation of NVB surrounding the prostate surface. After the MR-TRUS deformable registration the MR-defined NVB can be transferred into TRUS image using the transformation obtained from this registration to achieve the 3D NVB segmentation in TRUS images.

Results: In order to validate the proposed registration method, we conducted a clinical study with 7 prostate cancer patients. All patients' TRUS data were acquired using a Hitachi ultrasound machine and a 7.5MHz bi-plane probe. Each 3D B-mode TRUS data sets consisted of $1024 \times 768 \times 75$ voxels and the voxel size was $0.10 \times 0.10 \times 1.00 \text{ mm}^3$. The ultrasound Doppler images were captured from the prostate base to apex at a 5-mm step. All MR images were acquired using a Philips 1.5T MR scanner and a pelvic phase-array coil. The 3D MRI data consisted of $320 \times 320 \times 92$ voxels and the voxel size was $0.63 \times 0.63 \times 1.00 \text{ mm}^3$. All prostate glands were contoured in T2-weighted MR and TRUS images by an experienced physician. For each patient, three to six landmarks were identified in post-registration MR and TRUS images to facilitate quantitative comparison. In addition, we used patients' ultrasound Doppler images to further validate our MR-based NVB segmentation.

We successfully performed the segmentation method for all enrolled 7 prostate-cancer patients. Figure 3 shows the NVB in MR image for a 65-year old prostate-cancer patient. Figure 4 indicates the integration of MR-based NVB into TRUS. Figure 5 demonstrates the ultrasound Doppler validation of our segmentation method. The red and blue regions are blood signal in Doppler images and the region within the yellow contour is the MR-defined NVB. The segmented NVB matches with Doppler signal very well. In addition, Though MR-TRUS registration, 3D visualization and blood flow information of the NVB are also obtained. The mean displacement of the landmarks between the post-registration MR and TRUS images was $1.56 \pm 0.37 \text{ mm}$, which demonstrated the precision of the registration based on the biomechanical model. Figure 6 shows the left and right NVB volume overlap between the segmented NVB and Ultrasound Doppler defined NVB for each patient. Overall the NVB volume Dice Overlap coefficient was $92.1 \pm 3.2\%$, which demonstrated the accuracy of the proposed registration-based segmentation method.

New or breakthrough work to be presented: MRI is the best imaging modality for 3D visualization of the NVB, while Doppler ultrasound can provide blood flow information of the NVB. We proposed a novel registration-based NVB segmentation method to combine its anatomical structures in MR images and its functional information in ultrasound Doppler imaging. Our method could not only provide the 3D visualization of the NVB, also provide its functional and dynamic property (blood flow). It will be very useful to spare the NVB in prostate RT, monitor NVB response to RT, and potentially improve post-RT potency outcomes.

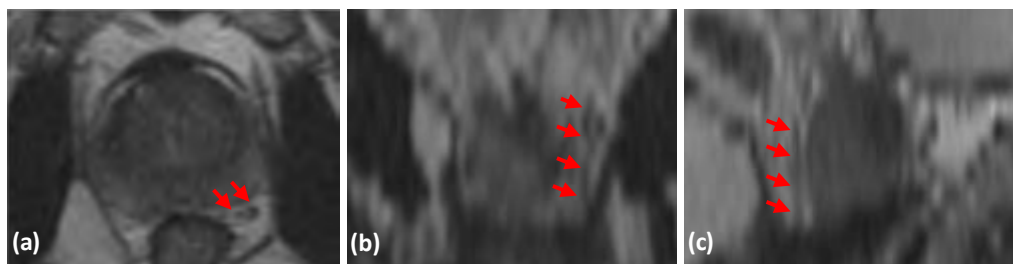


Figure 3. The NVB in MR image in axial (a), coronal (b) and sagittal (c) planes.

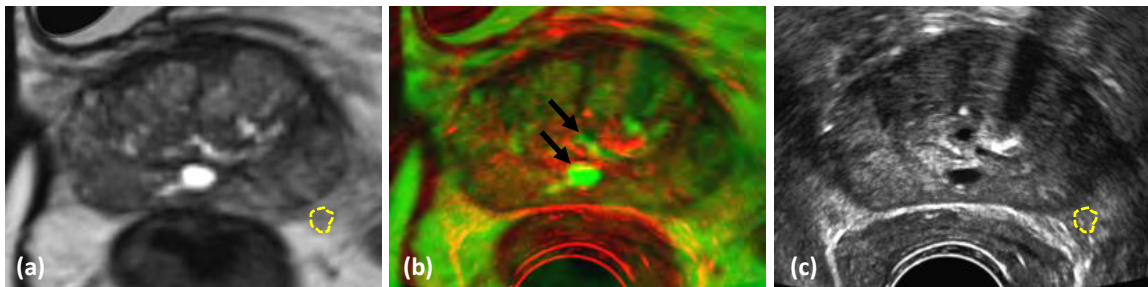


Figure 4. Integration of MR-based NVB into TRUS. (a) is MR; (c) is TRUS; (b) is MR-TRUS fusion images, where the NVB volume is integrated. The close match between the landmarks (black arrows) in fusion image demonstrated the accuracy of our method.

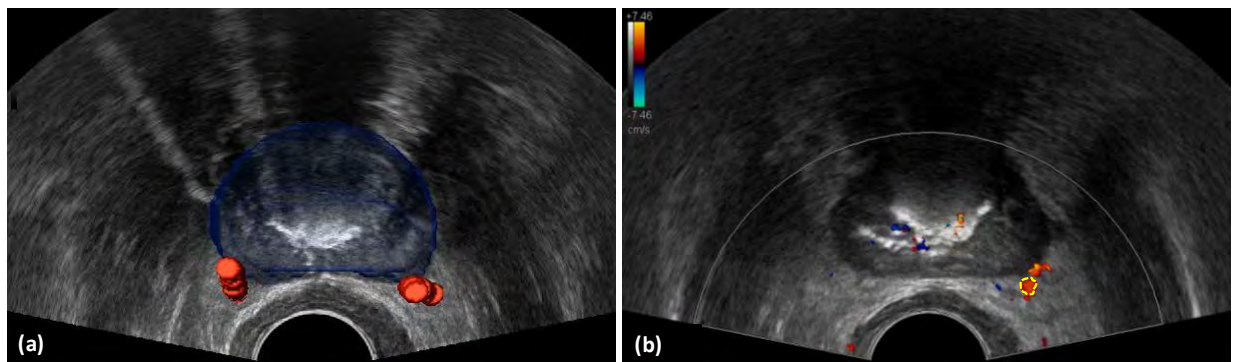


Figure 5. Ultrasound Doppler validation of our technology. 3D NVB in TRUS after MR-TRUS registration (a) and ultrasound Doppler image (b). Though MR-US registration, 3D visualization and blood flow information of the NVB are obtained.

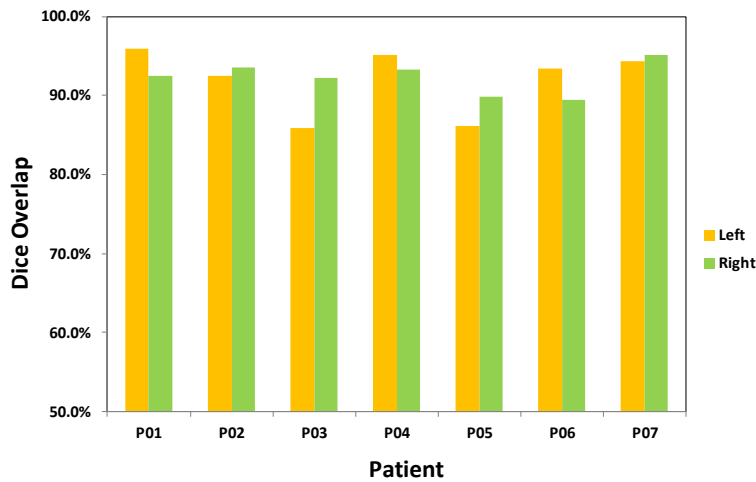


Figure 6. The left and right NVB volume overlap of each patient.

Conclusion: We have developed a novel approach to improve 3D NVB segmentation through MR-TRUS deformable registration for prostate RT, demonstrated its clinical feasibility, and validated its accuracy with ultrasound Doppler data. This technique could be a useful tool as we try to spare the NVB in prostate RT, monitor NVB response to RT, and potentially improve post-RT potency outcomes.

Acknowledgements: This research is supported in part by DOD PCRP Award W81XWH-13-1-0269, and National Cancer Institute (NCI) Grant CA114313.

3D Prostate Segmentation in Ultrasound Images Using Patch-Based Anatomical Feature

Xiaofeng Yang, Peter Rossi, Tomi Ogunleye, Ashesh B. Jani, Walter J. Curran, and Tian Liu

Department of Radiation Oncology, Winship Cancer Institute, Emory University, Atlanta, GA

Abstract: We propose a 3D segmentation method for transrectal ultrasound (TRUS) images based on patch-based anatomical feature. Patient-specific anatomical features are extracted from aligned training images and adopted as signatures for each voxel. The more robust and informative features are identified by the feature selection process to train the kernel support vector machine (KSVM). The well-trained KSVM was used to localize the prostate of the new patient. Our segmentation technique was validated with a clinical study of 10 patients. The accuracy of our approach was assessed using the manual segmentation. The mean volume Dice Overlap Coefficient was $89.7 \pm 2.3\%$. We have developed a new prostate segmentation approach based on the optimal feature learning framework, demonstrated its clinical feasibility, and validated its accuracy with manual segmentation (gold standard).

Purpose: Prostate cancer is the second leading cause of cancer death for U.S. male populations [1]. Transrectal ultrasound (TRUS) is the standard imaging modality for the image-guided prostate-cancer interventions (e.g., biopsy and brachytherapy) due to its versatility and real-time capability. Accurate segmentation of the prostate plays a key role in biopsy needle placement [2], treatment planning [3], and motion monitoring [4]. As ultrasound images have a relatively low signal-to-noise ratio (SNR), automatic segmentation of the prostate is difficult [5-8]. However, manual segmentation during biopsy or radiation therapy can be time consuming. We are developing an automated method to address this technical challenge.

Method: Our segmentation method consists of two major stages: the training stage and the segmentation stage. During the training stage, patch-based anatomical features are extracted from the registered training images with patient-specific information, because these training images have been mapped to the new patient's images, and the more informative anatomical features are selected to train the kernel support vector machine (KSVM). During the segmentation stage, the selected anatomical features are extracted from newly acquired image as the input of the well-trained KSVM and the output of this trained KSVM is the segmented prostate of this patient. Fig.1 shows a schematic flow chart of our method. The steps are briefly described below.

(1) Preprocessing and Registration

First of all, some preprocessing is performed for the training TRUS images in dataset, which includes reducing speckle noise, bias correction (AGC correction) and grayscale normalization. The same processing is also performed for the new patient's image that will be segmented. Such preprocessing steps are to improve the accuracy of the following registrations. During the alignment processing of training set, we first select one TRUS image as the template, detect probe center, position and radius, and align other TRUS images to the template image. And we use the corresponding transformation obtained from training image alignment to align the segmented prostates (binary mask) to the template prostate. Since the segmented prostate of each training image is available, in order to further optimize the alignment of training set we again align each training image to the template image by registering the binary segmentation prostates to the template prostate. A Gaussian filtering process is performed on the segmented binary prostates before conducting registration in order to enforce the proper optimization of the cost function during registration. The segmented prostates are binary mask volumes with relatively simple shapes; therefore the optimal deformable transformations to warp the binary prostates to the template prostate can be robustly estimated. When a newly acquired TRUS image comes, all aligned training TRUS images existed in training set are registered to this new image. The deformable registration methods [6, 8-10] are used to obtain the spatial deformation field between the new TRUS image and training TRUS images. The same transformations are applied to the segmented prostates in training set.

(2) Patch-based feature extraction

Patch-based representation has been widely used as voxel anatomical signature in computer vision and medical image analysis. The principle of the conventional patch-based representation is to first define a small image patch centered at each voxel and then use the voxel intensities of image patch as anatomical signature of each voxel. However, due to the low contrast and SNR, and also anatomical complexity of prostate ultrasound images, patch-based representation using voxel intensities alone may not be able to effectively distinguish prostate and non-prostate voxels. So we introduce to use patch-based anatomical features as signature for each voxel to characterize the image appearance. Three types of images features, namely, the Haar wavelet feature, the histogram of gradient (HOG) feature, and the local binary pattern (LBP) feature, are extracted from a small image patch (50×50) centered at each voxel of each aligned training image. Haar and HOG features can provide complementary anatomical information to each other, and LBP can capture texture information from the input image. The fourteen multiresolution Haar feature is used in this study. For the HOG feature, it is the 3×3 gradient orientation histogram, resulting in a 9D feature vector. The LBP feature is extracted in three resolution levels and it has a dimension 30. Therefore, for each voxel, it is represented by a 53 dimensional feature signature. Although the features are extracted from each 2D slice for each voxel normally due to the larger voxel size (1mm) along the sagittal direction than the size ($0.12 \times 0.12 \text{ mm}^2$) at transverse direction, the proposed framework is operated on 3D prostate TRUS images.

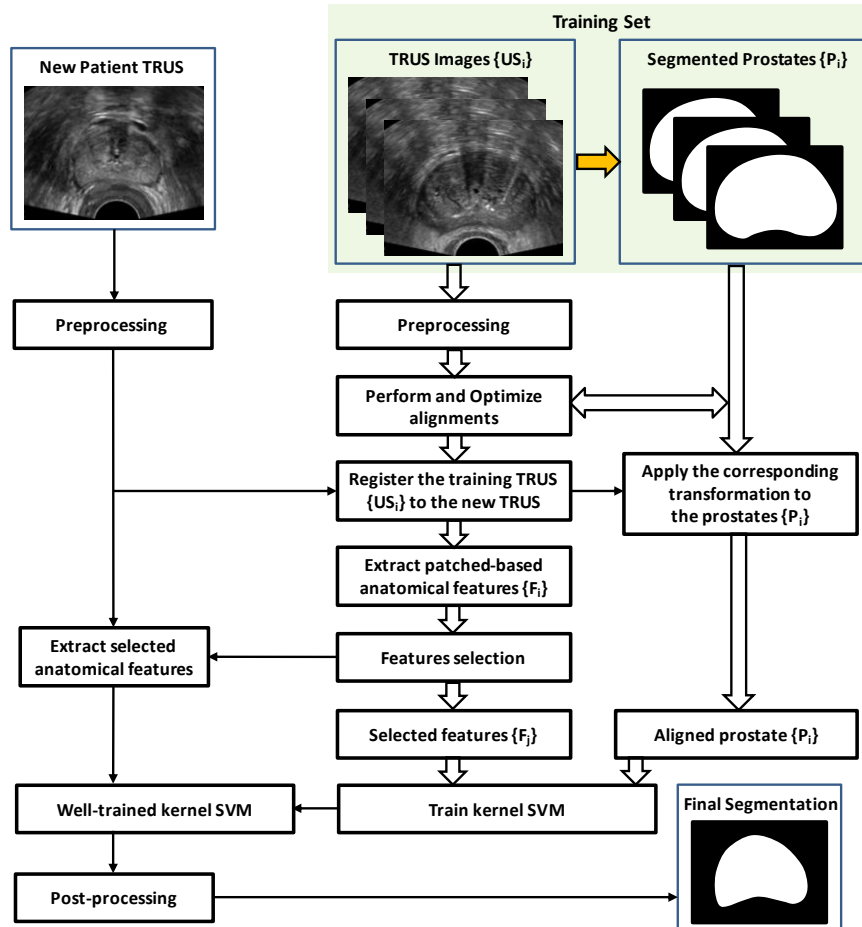


Figure 1. Schematic flow chart of the proposed algorithm for 3D segmentation of the prostate.

(3) Feature selection

Based on the above features, we can obtain patch-based representation of each voxel. It should be noted that the patch-based anatomical signature may contain noisy and redundant features which will finally affect the segmentation accuracy. Therefore, feature selection should be performed to identify the more

informative and salient features in the anatomical signature of each voxel. Here feature selection can also be viewed as a binary variable regression problem with respect to each dimension of the original feature. Therefore, the logistic function is used as the regression function. The logistic function [11] represents a conditional probability model defined by

$$P(y|\vec{\beta}, b, \vec{f}(\vec{x})) = \frac{1}{1 + \exp(-y(\vec{\beta}^T \vec{f}(\vec{x}) + b))} \quad (1)$$

where $\vec{f}(\vec{x})$ denotes the original feature signature of voxel \vec{x} , and y is a binary variable with $y=+1$ denoting that \vec{x} is belonging to the prostate region and $y=-1$ otherwise. $\vec{\beta}$ and b are parameters of the model.

Moreover, the aim of feature selection is to select a small subset of more informative feature as anatomical signature, which can be well accomplished by enforcing the sparsity constraint during the logistic regression process. Therefore, the feature selection problem can be finally formulated as a logistic sparse LASSO problem [12]. It is defined as,

$$J(\vec{\beta}, b) = \sum_{c=1}^P \log(1 + \exp(-L_c(\vec{\beta}^T \vec{f}(\vec{x}_c) + b))) + \lambda \|\vec{\beta}\|_1 \quad (2)$$

where $\vec{f}(\vec{x}_c)$ denotes the original feature signature of voxel \vec{x}_c . Label $L_c = +1$ denoting that \vec{x}_c is belonging to the prostate region and $L_c = -1$ otherwise. $\vec{\beta}$ is the sparse coefficient vector, $\|\cdot\|_1$ is the L_1 norm, b is the intercept scalar, and λ is the regularization parameter. The first term of (2) is obtained by inputting the label values of drawn samples and their original feature signatures to the logistic function in (1), and then take the logarithm for maximum likelihood estimation. The second term of (2) is the L_1 norm which aims to enforce the sparsity constraint for LASSO. Through minimizing the logistic sparse LASSO energy function (2) the features with superior discriminant power are selected. Based on the selected features, we can directly measure their discriminant power to separate prostate and non-prostate voxels quantitatively, based on the Fisher's score. The higher Fisher's score indicates the higher discriminative power of the representative feature.

(3) Support vector machine (SVM) training and segmentation

SVM is a popular supervised machine learning model with associated statistical learning algorithms that analyze data and recognize patterns for classification and regression analysis. The idea behind SVMs is to map the original data points from the input space to a high-dimensional (hyperplane) feature space such that the classification problem becomes simpler in the hyperplane space. The training phase of SVMs looks for a linear optimal separating hyperplane as a maximum margin classifier with respect to the training data [9]. Since the training data are not linearly separable, kernel-based SVM methods are employed to classify these features. We use the selected, more informative and salient features as well as the transformed prostate volumes (binary) to train the RBF kernel-based SVM. In order to segment the prostate for a newly acquired TRUS images, we extract the corresponding, more informative and salient features for each voxel of the new TRUS. These anatomical features of the new TRUS are the input of trained kernel-based SVM, and the well-trained SVM adaptively labels the prostate tissue based on its anatomical signature. The output of trained SVM is a binary volume consisting of many "0" (non-prostate tissues) and "1" (prostate tissue) points. After doing some morphological operations we can obtain the 3D segmented prostate.

Results: In order to test our segmentation method, we applied the segmentation method to 10 patients' TRUS images. All patients' TRUS data were acquired using a Hitachi ultrasound machine and a 7.5MHz bi-plane probe. Each 3D TRUS image consisted of $1024 \times 768 \times 75$ voxels and the voxel size was $0.12 \times 0.12 \times 1.00 \text{ mm}^3$. All prostate glands were contoured in TRUS images by an experienced physician. We used leave-one-out cross-validation method to evaluate the proposed segmentation algorithm. In other words, we used the 9 training images and segmented prostates as the training set and applied the proposed method to process the remaining subject. Our segmentations were compared with the manual results. In order to get a quantitative evaluation of this comparison, we calculated the Dice volume overlap between our and manual segmentations. We successfully performed the segmentation method for all enrolled patients. As demonstrated in Figure 2, the proposed segmentation method works well for 3D TRUS

images of the prostate and achieved similar results as compared to manual segmentation. Figure 3 shows Dice volume overlap for each patient. Overall the prostate volume Dice Overlap coefficient was $89.7 \pm 2.3\%$, which demonstrated the accuracy of the proposed segmentation method.

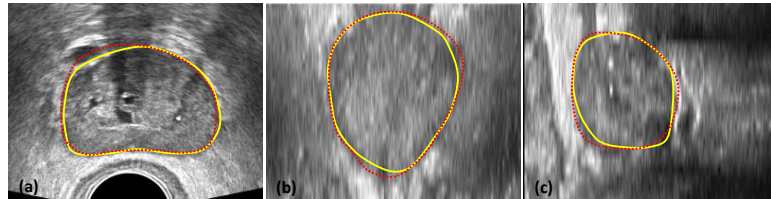


Figure 2. Comparison between the proposed method and manual segmentation. Images from left to right are in three orientations of the same TRUS image. The line in yellow is the manual segmentation result. The dashed line in red is the segmentation result of the proposed method.

New or breakthrough work to be presented:

Instead of using voxel intensity information alone, patch-based representation in the discriminative feature space with logistic sparse LASSO is used as anatomical signature to deal with low contrast and SNR problem in prostate ultrasound images. Based on the patch-based anatomical features training, a well-trained KSVM is designed to segment the prostate of a newly acquired TRUS.

Conclusion: In this study we report a novel 3D TRUS prostate segmentation method based on patch-based anatomical feature. Patient-specific anatomical features are extracted from aligned input images and adopted as signatures for each voxel. The more robust and informative features are identified by the feature selection process to train KSVM. The well-trained KSVM is used to help localize the prostate of the new patient. We have demonstrated its clinical feasibility, and validated its accuracy with manual segmentations. This segmentation technique could be a useful tool for image-guided interventions in prostate-cancer diagnosis and treatment.

Acknowledgements: This research is supported in part by DOD PCRP Award W81XWH-13-1-0269, and National Cancer Institute (NCI) Grant CA114313.

Reference

- [1] [Prostate Cancer Foundation, <http://www.prostatecancerfoundation.org>], (2008).
- [2] P. Yan, S. Xu, B. Turkbey *et al.*, “Discrete Deformable Model Guided by Partial Active Shape Model for TRUS Image Segmentation,” *Biomedical Engineering, IEEE Transactions on*, 99, 1-9 (2010).
- [3] K. K. Hodge, J. E. McNeal, M. K. Terris *et al.*, “Random systematic versus directed ultrasound guided transrectal core biopsies of the prostate,” *J.Urol.*, 142, 71-74 (1989).
- [4] D. Shen, Z. Lao, J. Zeng *et al.*, “Optimized prostate biopsy via a statistical atlas of cancer spatial distribution,” *Med.Image Anal.*, 8(2), 139-150 (2004).
- [5] F. Yang, J. Suri, and A. Fenster, “Segmentation of prostate from 3-D ultrasound volumes using shape and intensity priors in level set framework,” *Conf.Proc.IEEE Eng Med Biol.Soc.2006*, 1, 2341-2344 (2006).
- [6] X. Yang, H. Akbari, L. Halig *et al.*, “3D Non-rigid Registration Using Surface and Local Salient Features for Transrectal Ultrasound Image-guided Prostate Biopsy,” *Proc. SPIE* 7964, 79642V, (2011).
- [7] P. Yan, S. Xu, B. Turkbey *et al.*, “Adaptively learning local shape statistics for prostate segmentation in ultrasound,” *IEEE Trans Biomed Eng*, 58(3), 633-41 (2011).
- [8] X. Yang, D. Schuster, V. Master *et al.*, “Automatic 3D segmentation of ultrasound images using atlas registration and statistical texture prior,” *Proc. SPIE* 7964, 796432, (2011).
- [9] X. Yang, and B. Fei, “3D prostate segmentation of ultrasound images combining longitudinal image registration and machine learning ” *Proc. SPIE* 8316, 83162O (2012).
- [10] D. Rueckert, L. I. Sonoda, C. Hayes *et al.*, “Nonrigid registration using free-form deformations: application to breast MR images,” *Medical Imaging, IEEE Transactions on*, 18(8), 712-721 (1999).

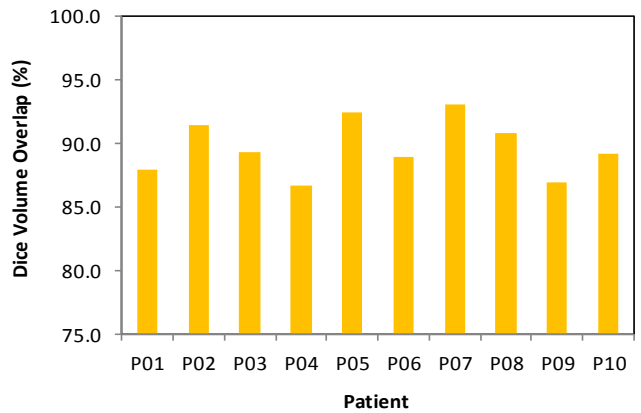


Figure 3. Dice volume overlaps between our and manual segmentations for each patient.

- [11] S. Liao, Y. Z. Gao, J. Lian *et al.*, “Sparse Patch-Based Label Propagation for Accurate Prostate Localization in CT Images,” *Ieee Transactions on Medical Imaging*, 32(2), 419-434 (2013).
- [12] S. Aseervatham, A. Antoniadis, E. Gaussier *et al.*, “A sparse version of the ridge logistic regression for large-scale text categorization,” *Pattern Recognition Letters*, 32(2), 101-106 (2011).

3D Ultrasound Nakagami Imaging for Radiation-Induced Vaginal Fibrosis

Xiaofeng Yang, Peter Rossi, Joseph Shelton, Deborah Bruner, Srinivasa Tridandapani, Tian Liu*

Department of Radiation Oncology and Winship Cancer Institute, Emory University,
Atlanta, GA 30322

*Corresponding author: tliu34@emory.edu

Radiation-induced vaginal fibrosis is a debilitating side-effect affecting up to 80% of women receiving radiotherapy for their gynecological (GYN) malignancies. Despite the significant incidence and severity, little research has been conducted to identify the pathophysiologic changes of vaginal toxicity. In a previous study, we have demonstrated that ultrasound Nakagami shape and PDF parameters can be used to quantify radiation-induced vaginal toxicity. These Nakagami parameters are derived from the statistics of ultrasound backscattered signals to capture the physical properties (e.g., arrangement and distribution) of the biological tissues. In this paper, we propose to expand this Nakagami imaging concept from 2D to 3D to fully characterize radiation-induced changes to the vaginal wall within the radiation treatment field. A pilot study with 5 post-radiotherapy GYN patients was conducted using a clinical ultrasound scanner (6 MHz) with a mechanical stepper. A serial of 2D ultrasound images, with radio-frequency (RF) signals, were acquired at 1 mm step size. The 2D Nakagami shape and PDF parameters were calculated from the RF signal envelope with a sliding window, and then 3D Nakagami parameter images were generated from the parallel 2D images. This imaging method may be useful as we try to monitor radiation-induced vaginal injury, and address vaginal toxicities and sexual dysfunction in women after radiotherapy for GYN malignancies.

Keywords: Ultrasound, Nakagami imaging, vaginal fibrosis, radiation toxicity

1. INTRODUCTION

Radiation-induced vaginal fibrosis is a debilitating side-effect, affecting 80% of women post pelvic or vaginal radiotherapy. Despite the significant incidence and severity, little research has been conducted to identify the pathophysiologic changes of vaginal toxicity. This paucity of data is largely due to the lack of an easy, reliable tool able to assess radiation-induced vaginal changes. This study's purpose is to develop ultrasound Nakagami imaging technique to quantitatively evaluate vaginal fibrosis in a 3D manner.

The Nakagami imaging method utilizes the radio-frequency (RF) signals obtained from a clinical ultrasound scanner. These RF signals are dependent on the physical properties (e.g. shape, size, and density) of the scatterers inside the biological tissue [1]. The Nakagami distribution, initially proposed to

describe the statistics of the radar echoes, is applied to analyze the statistics of the ultrasonic backscattered signals [2, 3]. The Nakagami parameters have been demonstrated to be useful for distinguishing various scatterer concentrations and arrangements in tissues [4-6]. The Nakagami statistical model has received considerable attention because the Nakagami distribution is highly consistent with the statistics of the backscattered ultrasound data, with the corresponding Nakagami parameter varying with the backscattering-envelope statistics [7, 8].

2. METHODS

The theoretical framework for Nakagami imaging relates statistical parameters to properties of the examined tissue. The analysis applies to the backscattered envelope signals of the “raw” radio-frequency echo signals, not to ultrasound B-mode image data. The formulation treats the backscattered ultrasound envelope signals as random signals. Our analysis characterizes tissue structures in terms of a stochastic probability density function (PDF) under the Nakagami statistical model [9]. The PDF of the ultrasonic backscattered envelope x under the Nakagami statistical model is define as,

$$f(x) = \frac{2u^u}{\Gamma(u)\omega^u} x^{2u-1} \exp(-\frac{u}{\omega} x^2) \cdot W(x) \quad (1)$$

where (\cdot) is the gamma function and $W(\cdot)$ is the weight function. The parameter ω is the scaling parameter, whereas u is the Nakagami parameter. Let $E(\cdot)$ denote the statistical mean, then scaling parameter ω and Nakagami parameter u associated with the Nakagami distribution can be obtained from the following equations:

$$\omega = E(X^2) \quad (2)$$

$$u = \frac{E^2[X^2]}{Var[X^2]} \quad (3)$$

$$Var[X^2] = E^2[X^2 - E(X^2)] \quad (4)$$

$$W(x) = \begin{cases} 0, & x > T \\ 1, & x \leq T \end{cases} \quad (5)$$

where $E(\cdot)$ is the expected value operator and T is a threshold. The likelihood ratio was obtained by assuming that every envelope value within the region of interest (ROI) was independently and identically distributed. Then, the parameters ω and u were found by maximizing the likelihood ratio using an ascent algorithm [10].

The Nakagami parameter u is a shape parameter for the PDF. When u equals 1, the Nakagami distribution reduces to a Rayleigh distribution. When u is between 0 and 1, the envelope distribution is said to be pre-Rayleigh [11]. When $u > 1$, the distribution conforms to post-Rayleigh, as shown in Fig.1 [12]. This property makes the Nakagami distribution a good general model for ultrasonic backscattering. When the ROI contains randomly located scatterers with varying scattering cross sections, the envelope

statistics are likely to be pre-Rayleigh and u is typically between 0.5 and 1[13]. Similarly, when some spatial periodicity exists among scatterers within the resolution cell, then the envelope statistics are post-Rayleigh, and u becomes larger than unity [12]. Typically, u is used as a means to quantify the effective number of scatterers in the resolution cell. This interpretation can be obtained by noting that the random variable $Y = X^2$ follows a gamma distribution and interpreting the physical relationships between u and the effective number obtained from the gamma distribution [4].

Note that the window size determines the resolution of the Nakagami parameter image. The principle notion in image formation is the resolution which describes the ability of a system to resolve the smallest details in an object. There is a trade-off between resolution and statistical power. As the window size decreases, the resolution of the Nakagami u image is improved. However, a small window has fewer envelope data points, leading to an unstable estimation of the parameter. In the evaluation of radiation toxicity, the area of treatment is large, and the irradiated tissues typically range from 5 cm to 15 cm. Therefore, resolution is not a problem in the evaluation of post-RT tissues. The principle challenge in imaging radiation toxicity is to detect early changes that might be subtle. Hence, we selected a relatively big window size of 39 sample points (beam direction) and 15 scan lines (lateral direction) to improve the statistical power. At the probe surface, the actual window size is 1.50 mm (beam) by 1.26 mm (lateral). Because of the fan shape of the beam, the lateral width increases with depth.

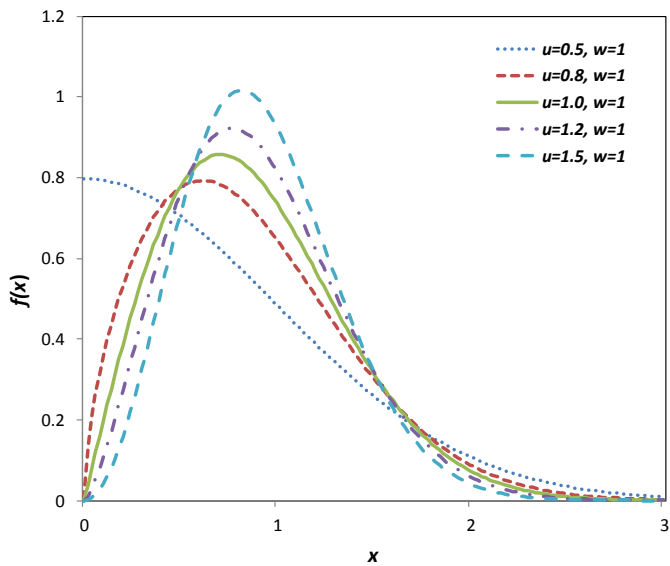


Fig. 1. Nakagami distributions for different Nakagami parameters.

Nakagami u images and Nakagami PDF images are generated using a 3D sliding box. The Nakagami parameters ω and u are commonly used parameters, which are computed from Eqs. (2) and (3). From Eq. (1), we subsequently calculated a PDF value for the central point of the sliding box from the corresponding envelope intensity value. The sliding box is moved through the entire RF envelope image point by point, line by line and slice by slice to generate the 3D Nakagami parameter images. This sliding box method could reduce the sub-resolvable effect at the locations of the strong reflectors (e.g. tissue interface or point target) in a scattering medium. In other words, when the sliding box moves onto the strong reflector, the box not only covers the signals from the strong reflector but also contains those from

the tissue background. Because there is a large difference in the echo intensity between the reflector and the background, the backscattered envelopes acquired by the box would tend to be extremely pre-Rayleigh distributed, rendering the Nakagami u parameter very small. From the Nakagami PDF and Nakagami u images, Nakagami PDF and u parameters were calculated based on the physicians' contours of the vaginal wall.

3. RESULTS

In this study, 10 participants (5 post-radiation patients and 5 normal controls) were enrolled. The 5 patients all have received radiotherapy for their GYN malignancies (follow-up time: 20.5 ± 7.1 months). Each subject underwent one transvaginal ultrasound study (6 MHz). Three-dimensional transverse images of the anterior vaginal wall were acquired in a 1 mm step size from the apex (vaginal cuff) to the introitus (vagina opening).

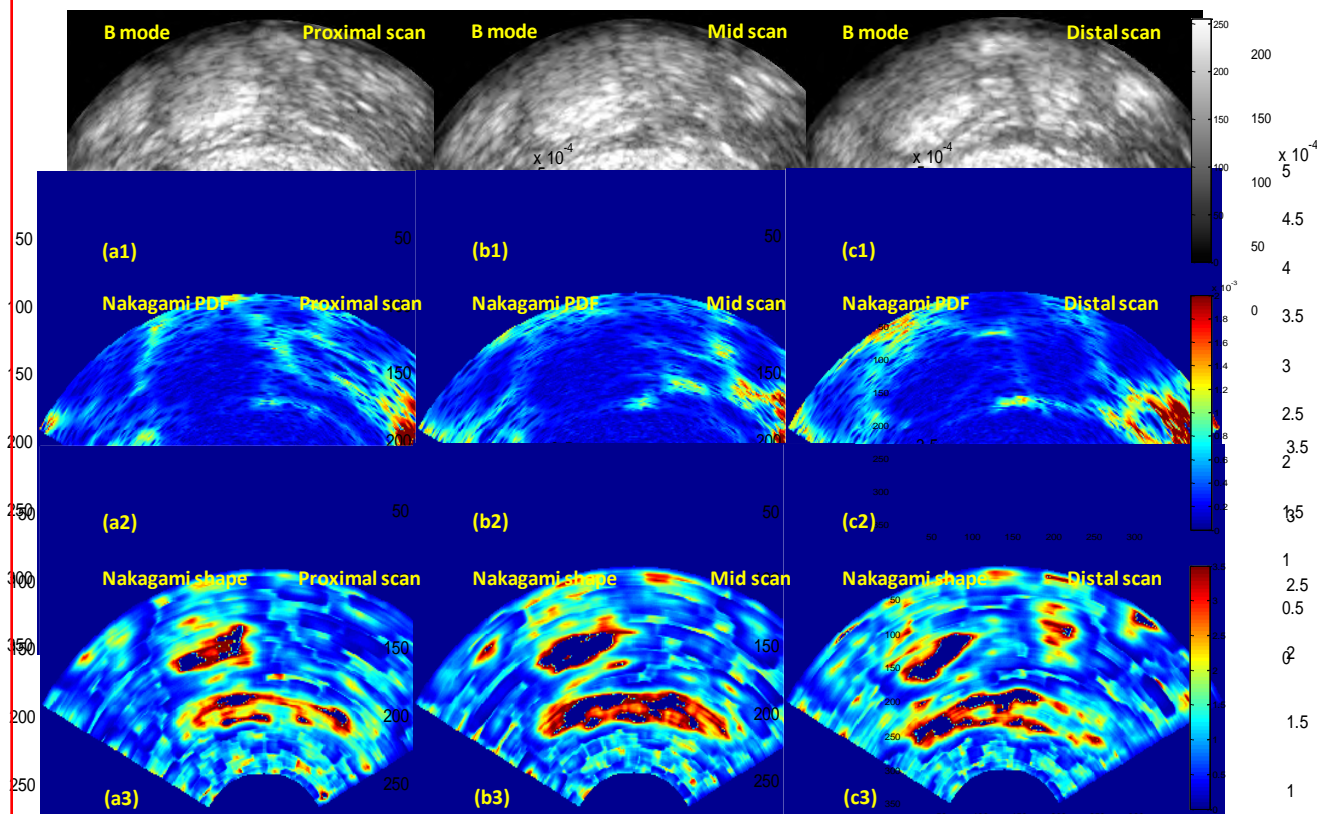


Fig. 2. Tranvaginal ultrasound B-mode and corresponding Nakagami parameter images at the proximal, mid and distal locations of the vagina.

Here, the 3D Nakagami imaging method is illustrated through a case of a 54-year-old patient who had received 54 Gy external beam radiation for her early-stage endometrial cancer. At her 2-year follow-up visit, a clinical examination showed a Grade 1 vaginal fibrosis. Transvaginal ultrasound B-mode images showed increased vaginal wall thickness at the proximal, mid and distal locations of the

vagina (Figure 2, top row). The corresponding 2D Nakagami PDF images are shown in the 2nd row of Figure 2, and 2D Nakagami shape images are shown in the 3rd row of Figure 2. Figure 3 show the 3D Nakagami shape and PDF image of the anterior vaginal wall.

Figure 4 shows the Nakagami parameters for the normal and post-radiotherapy groups. The significant separations between the two groups indicated that the Nakagami method was capable of distinguishing the control from the post-RT vaginal walls. The increased Nakagami shape and PDF parameters may be related to the increases in the concentration of scatterers and periodic structures, which may be resulted from the fibrotic development and increased collagen content in the vaginal wall.

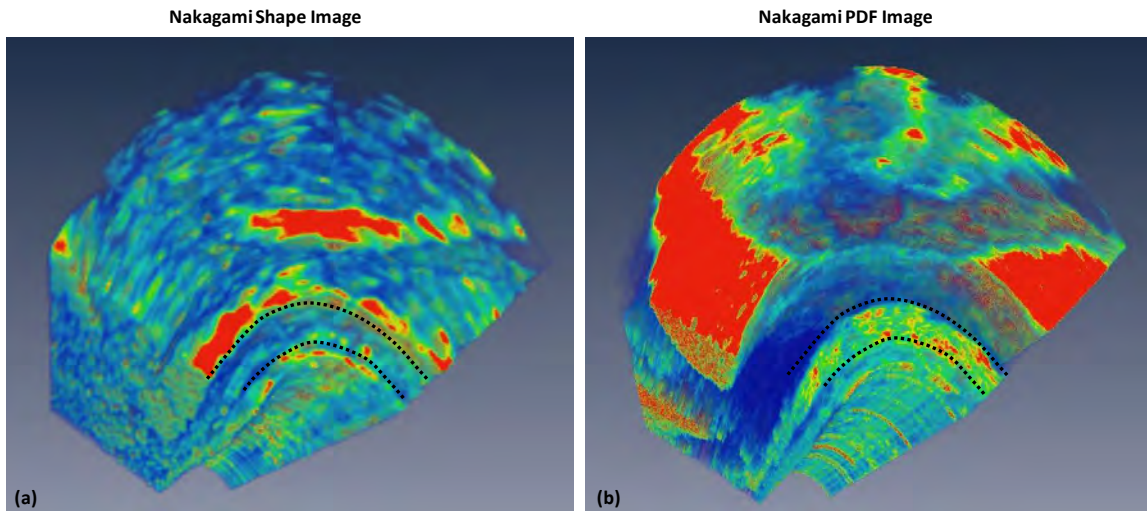


Fig. 3. 3D Nakagami shape and PDF image of a post-RT patient.

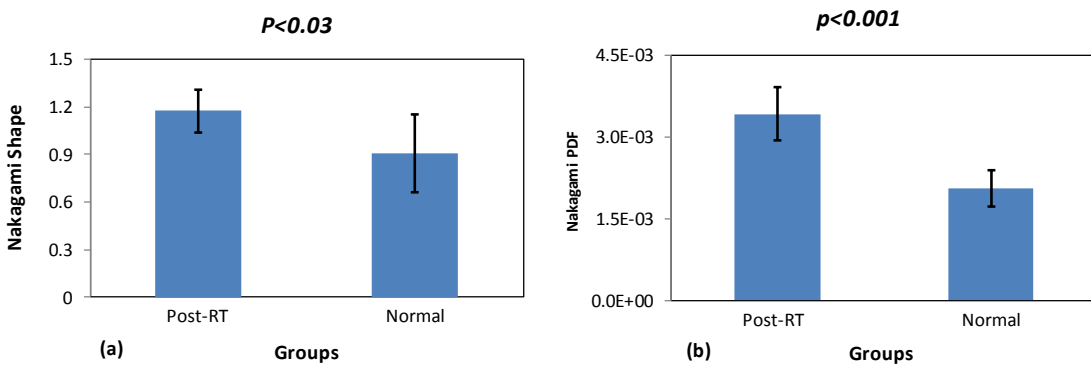


Fig. 4. Comparison of the control and post-RT groups. (a) Nakagami shape parameter (b) Nakagami PDF.

4. DISCUSSION AND CONCLUSION

This pilot study demonstrated that 3D Nakagami imaging is a promising imaging tool for the quantitative evaluation of radiation-induced vaginal fibrosis. In this study, we proposed a new 3D Nakagami parameter imaging, to assess post-RT vaginal toxicity *in vivo*. Conventional B-mode imaging, generated from the intensity of the backscattered echoes, provides the anatomy and intensity of the vaginal wall. In contrast, the Nakagami parameter image, constructed using the raw RF signals, reflects the arrangements and distributions of the vaginal tissue (microstructures). The separations on the scatter grams indicated that the 3D Nakagami imaging method was capable of distinguishing the control from the post-RT vaginal walls.

Traditionally, vaginal toxicity is assessed through the physicians' visual and tactile examination. Such assessment is subjective and, hence, potentially inconsistent. Quantitative ultrasound is an attractive alternative that could provide clinicians with a simple visualization and quantitative assessment of the vaginal injury. Computed from the statistics of the enveloped backscattered signals, the Nakagami parameters can be used to characterize various scatterer concentrations and arrangements of the biological tissues.

So far, imaging has played a negligible role in the evaluation of vaginal toxicity, and this is the first ultrasound study on post-RT vaginal fibrosis using 3D Nakagami imaging. We should note that the B-mode image method and the Nakagami-parameter method are independent and complementary [14]. The advantage of utilizing ultrasound B-mode image is its wide availability in the clinic [15, 16]. The Nakagami parameter image is constructed using the raw RF signals, and the same diagnostic ultrasound system is used in the current investigation. The Nakagami parameter estimated from the ultrasonic backscattered signals depend on the statistical distribution of echo waveform and not affected by the echo amplitude and, thus, Nakagami imaging is less operator-dependent.

In this study, we demonstrated that 3D Nakagami imaging has the potential to serve as a functional imaging tool to enhance the study of vaginal fibrosis. This imaging tool could provide greater insight into structural changes that lead to vaginal toxicity, and potentially lay the groundwork for outcome metrics of interventions to prevent and treat vaginal toxicity.

ACKNOWLEDGEMENTS

This research is supported in part by DOD PCRP Award W81XWH-13-1-0269, and National Cancer Institute (NCI) Grant CA114313.

REFERENCES

- [1] M. F. Insana, R. F. Wagner, D. G. Brown et al., "Describing Small-Scale Structure in Random-Media Using Pulse-Echo Ultrasound," *Journal of the Acoustical Society of America*, 87(1), 179-192 (1990).

- [2] P. M. Shankar, "A general statistical model for ultrasonic backscattering from tissues," *Ieee Transactions on Ultrasonics Ferroelectrics and Frequency Control*, 47(3), 727-736 (2000).
- [3] M. P. Wachowiak, R. Smolikova, G. D. Tourassi et al., "General ultrasound speckle models in determining scatterer density," *Medical Image 2002: Ultrasonic Imaging and Signal Processing*, 4687, 285-295 (2002).
- [4] P. M. Shankar, V. A. Dumane, J. M. Reid et al., "Classification of ultrasonic B-mode images of breast masses using Nakagami distribution," *Ieee Transactions on Ultrasonics Ferroelectrics and Frequency Control*, 48(2), 569-580 (2001).
- [5] P. M. Shankar, "A compound scattering pdf for the ultrasonic echo envelope and its relationship to K and Nakagami distributions," *IEEE Transactions on Ultrasonics Ferroelectrics and Frequency Control*, 50(3), 339-343 (2003).
- [6] P.-H. Tsui, and S.-H. Wang, "The effect of transducer characteristics on the estimation of Nakagami parameter as a function of scatterer concentration," *Ultrasound in Medicine & Biology*, 30(10), 1345-1353 (2004).
- [7] P. H. Tsui, C. W. Hsu, M. C. Ho et al., "Three-dimensional ultrasonic Nakagami imaging for tissue characterization," *Physics in Medicine and Biology*, 55(19), 5849-5866 (2010).
- [8] Y.-Y. Liao, C.-H. Li, P.-H. Tsui et al., "Strain-compounding technique with ultrasound Nakagami imaging for distinguishing between benign and malignant breast tumors," *Medical Physics*, 39(5), 2325-2333 (2012).
- [9] X. Yang, P. Rossi, D. W. Bruner et al., "Noninvasive evaluation of vaginal fibrosis following radiotherapy for gynecologic malignancies: A feasibility study with ultrasound B-mode and Nakagami parameter imaging" *Med. Phys.*, 40(2), 7 (2013).
- [10] J. Mamou, A. Coron, M. L. Oelze et al., "Three-Dimensional High-Frequency Backscatter and Envelope Quantification of Cancerous Human Lymph Nodes," *Ultrasound in Medicine and Biology*, 37(3), 345-357 (2011).
- [11] H. C. Holzman, [Statistical Methods on Radio Wave Propagation (New York: Pergamon)] RAND Corporation, New York(1960).
- [12] P. Mohana Shankar, "A general statistical model for ultrasonic backscattering from tissues," *IEEE Trans Ultrason Ferroelectr Freq Control*, 47(3), 727-36 (2000).
- [13] P. M. Shankar, "A model for ultrasonic scattering from tissues based on the K distribution," *Physics in Medicine and Biology*, 40(10), 1633-49 (1995).
- [14] X. Yang, S. Tridandapani, J. Beitzler et al., "Ultrasonic Nakagami-parameter characterization of parotid-gland injury following head-and-neck radiotherapy: A feasibility study of late toxicity," *Medical Physics*, 41(2), (2014).
- [15] X. F. Yang, S. Tridandapani, J. J. Beitzler et al., "Ultrasound Histogram Assessment of Parotid Gland Injury Following Head-and-Neck Radiotherapy: A Feasibility Study," *Ultrasound in Medicine and Biology*, 38(9), 1514-1521 (2012).
- [16] X. F. Yang, S. Tridandapani, J. J. Beitzler et al., "Ultrasound GLCM texture analysis of radiation-induced parotid-gland injury in head-and-neck cancer radiotherapy: An in vivo study of late toxicity," *Medical Physics*, 39(9), 5732-5739 (2012).

Ultrasound 2D Strain Estimator Based on Image Registration for Ultrasound Elastography

Xiaofeng Yang, Mylin Torres, Stephanie Kirkpatrick, Walter J. Curran, Tian Liu*

Department of Radiation Oncology, Winship Cancer Institute, Emory University,
Atlanta, GA 30322

*Corresponding author: tliu34@emory.edu

In this paper, we present a new approach to calculate 2D strain through the registration of the pre- and post-compression (deformation) B-mode image sequences based on an intensity-based non-rigid registration algorithm (INRA). Compared with the most commonly used cross-correlation (CC) method, our approach is not constrained to any particular set of directions, and can overcome displacement estimation errors introduced by incoherent motion and variations in the signal under high compression. This INRA method was tested using phantom and *in vivo* data. The robustness of our approach was demonstrated in the axial direction as well as the lateral direction where the standard CC method frequently fails. In addition, our approach copes well under large compression (over 6%). In the phantom study, we computed the strain image under various compressions and calculated the signal-to-noise (SNR) and contrast-to-noise (CNS) ratios. The SNR and CNS values of the INRA method were much higher than those calculated from the CC-based method. Furthermore, the clinical feasibility of our approach was demonstrated with the *in vivo* data from patients with arm lymphedema.

Key words: Ultrasound, elastography, strains imaging, image registration.

1. INTRODUCTION

Ultrasound elasticity imaging describes the compressibility of biological tissues [1]. Changes in tissue stiffness often correlate with pathological phenomena, and can be indicators of diseases, such as cancer or cardiovascular illness [2]. In elasticity (strain) imaging, the displacement or deformation of tissue is estimated using pre- and post-compression image data. The resulting strain measurement could provide insight into the elastic properties of tissues [3].

Most elastography techniques estimate tissue displacements based on an amplitude correlation [4, 5] or a phase correlation of the radio-frequency (RF) echoes [6, 7]. Such cross-correlation (CC) provides an accurate and effective estimator of the similarities between the echo fields, and is capable of tracking small displacements even when very low strains (less than 2%) are involved. However, elastography is often degraded by decorrelation noise, especially when incoherent motion [4, 7-9], and non-rigid tissue deformation [10, 11] between the pre- and post-compression (deformation) are present. In fact, incoherent motion and variations in the signal from scatterers at high compression lead to displacement estimation errors [12] and ambiguities in the determination of the motion vectors [13].

Attempts have been made to adapt the correlation algorithm to provide sub-sample accuracy and multi-level estimation stability [14-18]. These approaches proved to be valuable, however, the motion is estimated in sub-windows where it is supposed to be linear [19] or constant [20], and the continuity of the motion field in the whole domain. When the continuity assumption is violated, a tracking algorithm might not only fail to find the correct displacement at any particular point, but also propagate this incorrect estimate into other parts of the image, producing so-called drop-outs. To avoid this problem, incorrect displacement estimates can be detected and replaced by values interpolated from nearby points before they get a chance to propagate [18, 21]. While most previously mentioned methods use tissue motion continuity to confine the search range for the neighboring windows, the displacement of each window is calculated independently, and hence is sensitive to signal decorrelation.

In this paper, we developed a new approach to measure 2D strain at high compression by registration of pre-stress and post-stress B-mode image sequences, which combines the advantages of intensity-based similarity measures with a non-rigid transformation model.

2. METHODS

To be able to calculate the strain of the biological tissue, the displacement (deformation) of the tissue from pre-stress to post-stress has to be determined. This is equivalent to finding the corresponding point before and after compression for each point of the tissue. Elasticity image reconstructions are considered as a non-rigid image registration problem. We use a hierarchical transformation model which captures the global and local transformation for the displacement estimation of tissue under compression. The global displacement of the tissue is modeled by an affine transformation, while the local transformation is described by a non-rigid deformation based on B-splines [22]. Since the intensity and contrast between the pre-compression and post-compression may change, we will use voxel-based similarity measures based on normalized mutual information.

2.1 Transform Model

The overall displacement of the tissue is described using the global displacement model. Compared with a rigid transformation, which is parameterized by 6 degrees of freedom, describing the rotations and translations of the tissue, an affine transformation is a more general class of transformations, and it has six additional degrees of freedom, describing scaling and shearing. It is defined as:

$$Affine(x, y) = \begin{bmatrix} a_{11} & a_{12} & a_{13} \\ a_{21} & a_{22} & a_{23} \\ 0 & 0 & 1 \end{bmatrix} \begin{bmatrix} x \\ y \\ 1 \end{bmatrix} \quad (1)$$

where the coefficients a parameterize the 6 degrees of freedom of the transformation.

Because of the difference in tissue elasticity characteristics, the regional deformation in the tissue can vary significantly under loaded external pressure. Therefore, it is difficult to describe the regional deformation via parameterized transformations [23]. Instead, a multi-level B-splines deformation model [24-26] has been applied to displacement analysis in this paper. The resulting deformation controls the shape of the object and produces a smooth and continuous transformation. A hierarchical multi-resolution approach [22] has been applied, in which the resolution of the control mesh is increased, along with the image resolution, in a coarse to fine style. At each level of resolution the spacings between the control points in the x and y directions are denoted by δ_x and δ_y , respectively. By moving the control points independently of each other, the space between them is deformed non-rigidly. At any position (x, y) of

each level the deformation is computed from the positions of the surrounding 4×4 neighborhood of control points. The regional transformation F_{FFD}^c at level c of resolution is defined by each control mesh Φ^c , and the corresponding spline-based transformation, and their sum of the regional transformation F_{FFD} is defined as

$$F_{Deformable}(x, y) = \sum_{c=1}^C \sum_{i=0}^3 \sum_{j=0}^3 \beta_i(s) \beta_j(t) \Phi_{l+i, m+j}^c \quad (2)$$

Here, l and m denote the index of the control point cell containing (x, y) , and s and t are the relative positions of x and y , respectively, inside that cell in the two dimensions, $l = \lfloor x/\delta_x \rfloor - 1$, $m = \lfloor y/\delta_y \rfloor - 1$, $s = x/\delta_x - (l + 1)$, and $t = y/\delta_y - (m + 1)$. The function β_i represents the i th basis function of the B-spline

$$\beta_0(s) = \frac{(1-s)^3}{6}, \beta_1(s) = \frac{(3s^3-6s^2+4)}{6}, \beta_2(s) = \frac{(-3s^3+3s^2+3s+1)}{6}, \beta_3(s) = \frac{s^3}{6} \quad (3)$$

Here the regional transformation is represented as a combination of B-spline deformation s at increasing resolutions of the control point mesh. The control point mesh at level c is refined by inserting new control points to create the control point mesh at level $c + 1$, and the values of the new control points Φ^{c+1} can be calculated directly from those of Φ^c [27]. The control points Φ^c are parameters of the B-spline deformation, and the degree of non-rigid displacement that can be modeled depends essentially on the resolution of the mesh of control points Φ^c . The large lattice spacing δ permits the representation of non-rigid displacements of the whole image, whereas the fine lattice allows for modeling highly regional non-rigid displacements.

The goal of the displacement estimation in ultrasound elastography is to obtain a 2D map of the tissue's mechanical properties, that is, to find the optimal transformation F which maps any point in the post-deformation image into its corresponding point in the pre-deformation reference image. Finally a combined transformation F consisting of a global and regional transformation has been applied

$$F(x, y) = F_{Affine}(x, y) + F_{Deformable}(x, y) \quad (4)$$

2.2 Smoothness Constraint

To constrain the smoothness of the spline-based transformation, a penalty term is introduced, which is based on the bending energy of a thin plate of metal that is subjected to bending deformations [28]. It is composed of second-order derivatives of the deformation

$$E_{Smooth}(F) = \frac{1}{V} \int_0^X \int_0^Y \left[\left(\frac{\partial^2 F}{\partial x^2} \right)^2 + \left(\frac{\partial^2 F}{\partial y^2} \right)^2 + 2 \left(\frac{\partial^2 F}{\partial xy} \right)^2 \right] dx dy \quad (5)$$

where V denotes the volume of the image domain. This regularization term penalizes only non-affine transformations. The second-order derivatives of the B-spline transformation are computed by substituting the appropriate derivatives for the corresponding polynomials. Mixed second-order derivatives with respect to the two different variables are computed by substituting two B-spline polynomials with their respective first-order derivatives.

2.3 Similarity Measure

Central to mutual information (MI) is the Shannon entropy [29], H , which relates to the average information supplied by a given set of parameters, v , whose probabilities are given by $P(v)$. The expression for the Shannon entropy with respect to a discrete parameter probability is

$$H = - \sum_q P(v_q) \log (P(v_q)) \quad (6)$$

In order to relate a post-deformation image to the pre-deformation reference image, a similarity criterion which measures the degree of alignment between both images, must be defined. Because the image intensity and contrast (the amplitude of RF signals) might change after a large compression, a direct comparison (i.e. cross correlation) of image intensities cannot be used as a similarity measure. By characterizing two images using the probability distribution function (PDF) based on the joint histogram and minimizing the joint entropy correlates with better image-to-image alignment. An alternative voxel-based similarity measure is MI [30, 31], and it is based on the concept of information theory and expresses the amount of information that a pre-deformation image I_{Pre} contains about a post-deformation image I_{Post} . The MI will be maximized when both images are aligned. MI relies on the overlap between the two images [32]; to avoid any dependency on the amount of image overlap, NMI as a measure of image alignment is proposed and it is written as

$$E_{NMI}(I_{Pre}, I_{Post}) = \frac{H(I_{Pre}) + H(I_{Post})}{H(I_{Pre}, I_{Post})} \quad (7)$$

where $H(I_{Pre})$ and $H(I_{Post})$ denotes the marginal entropies of I_{Pre} and I_{Post} and $H(I_{Pre}, I_{Post})$ denotes their joint entropy, which is calculated from the joint histogram of I_{Pre} and I_{Post} .

2.4 Optimization

In order to find the optimal transformation, we minimize a cost function associated with the global and regional transformation parameters. In addition to the NMI similarity measure E_{NMI} , our registration method incorporates an additional penalty term E_{Smooth} to constrain the deformation of the coordinate space. The cost function comprises two competing goals. A user-defined weighting factor $\tau (0 \leq \tau < 1)$ controls the relative influence of E_{NMI} and E_{Smooth} , combining both into the overall cost function E_{Total} as follows:

$$E_{Total}(a, \Phi) = (\tau - 1)E_{NMI}[I_{Pre}(x, y, z), \mathbf{F}(I_{Post}(x, y, z))] + \tau E_{Smooth}(\mathbf{F}) \quad (8)$$

Here, τ is the weighting parameter which defines the tradeoff between the alignment of the two images and the smoothness of the transformation. Finding the parameters of the nonrigid transformation that optimize the joint cost function requires an efficient and robust optimization algorithm. The optimization proceeds include two stages. During the first stage, the affine transformation parameters a are optimized. Since the smoothness term of the cost function is zero ($\tau = 0$) for any affine transformation, this step is equivalent to maximizing the image similarity. During the second stage, the non-rigid transformation parameters Φ are optimized as a function in the cost function. In each stage the gradient of the cost function is computed, and a line search is performed for the optimum parameters along the gradient direction [22]. This procedure is repeated until the cost function cannot be improved any further.

3. EXPERIMENTS AND RESULTS

In order to validate our non-rigid registration based elastography method, we conducted a phantom and *in vivo* ultrasound studies using a clinical scanner (SonixTouch, Ultrasonix, British Columbia, Canada). The elastography phantom (Model 059, CIRS) and *in-vivo* human hand were scanned using the L14-5/38 linear probe (128 elements) at 10 MHz center frequency. The *in-vivo* arm data were acquired using the BPL9-5/55 probe (256 elements) at 6.5 MHz center frequency. For the CC-based method, 4 levels from coarse to fine were used. We used $\tau = 0.01$ for the cost function and 3×3 grid spaces for our registration-based method.

This phantom includes several dense masses (lesions). The elasticity (stiffness) of the each dense mass is at least two times greater than the elasticity of the background, which has an elastic modulus of $20 \text{ kPa} \pm 5 \text{ kPa}$. For phantom results we calculate the signal-to-noise ratio (SNR) and contrast to noise ratio (CNR) to assess the performance of our method according to

$$CNR = \frac{Contrast}{Noise} = \sqrt{\frac{2(m_b - m_t)^2}{\sigma_b^2 + \sigma_t^2}}, \quad SNR = \frac{Signal}{Noise} = \frac{m}{\sigma} \quad (9)$$

where m_t and m_b are the spatial strain average of the target and background, σ_t^2 and σ_b^2 are the spatial strain variance of the target and background, and m and σ are the spatial average and variance of a window in the strain image, respectively.

Figures 1 shows the comparison of the elastography results of the INRA and CC-based methods along the axial direction of the elastography phantom. The breast lesion is clearly visualized on the strain and B-mode fusion image of the INRA method, yet is not clear on the fusion image of the CC-based method. Figure 2 shows the comparison of the elastography results of the INRA and CC-based method along the lateral direction of the elastography phantom. The breast lesion is still clear on the B-mode and strain fusion image of the INRA method, and is not visible on the fusion image of the CC-based method. Compared with the INRA method, the CC-based block match has more artifacts in the axial strain image and the breast lesion in phantom almost cannot be seen in lateral strain images. However, the INRA method can detect the lesion in both the axial and lateral strain images.

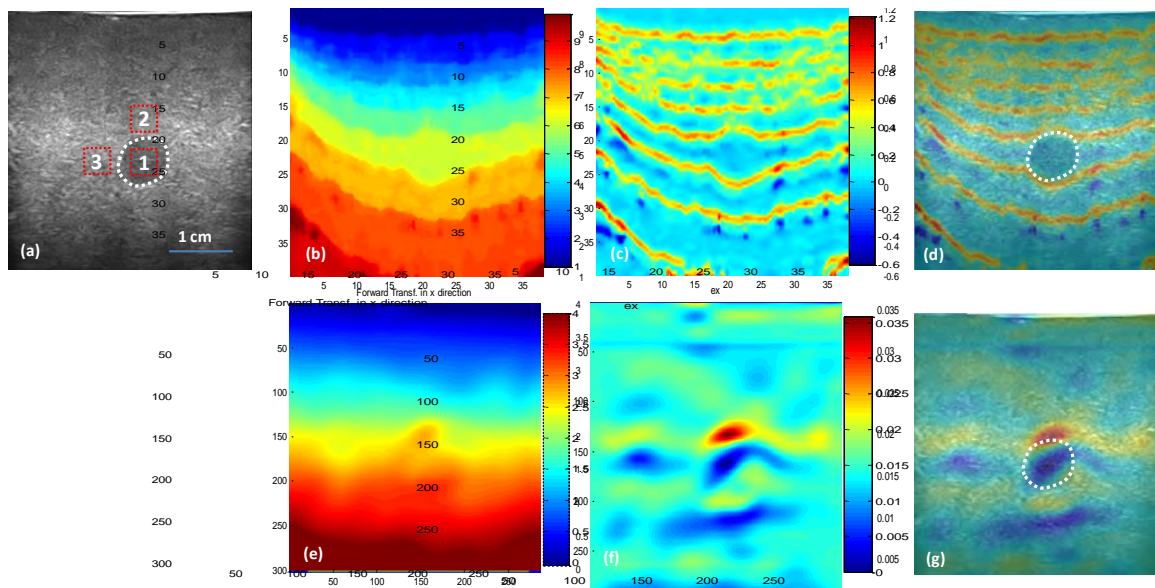


Fig. 1. Phantom experiment results – axial direction. (a) B-mode image of the breast phantom with a lesion (white dotted line); CC-based elastography results (top row): (b) Displacement, (c) Strain, and (d) Strain and B-mode fused image; INRA-based elastography results (bottom row): (e) Displacement, (f) Strain, and (g) Strain and B-mode fused image.

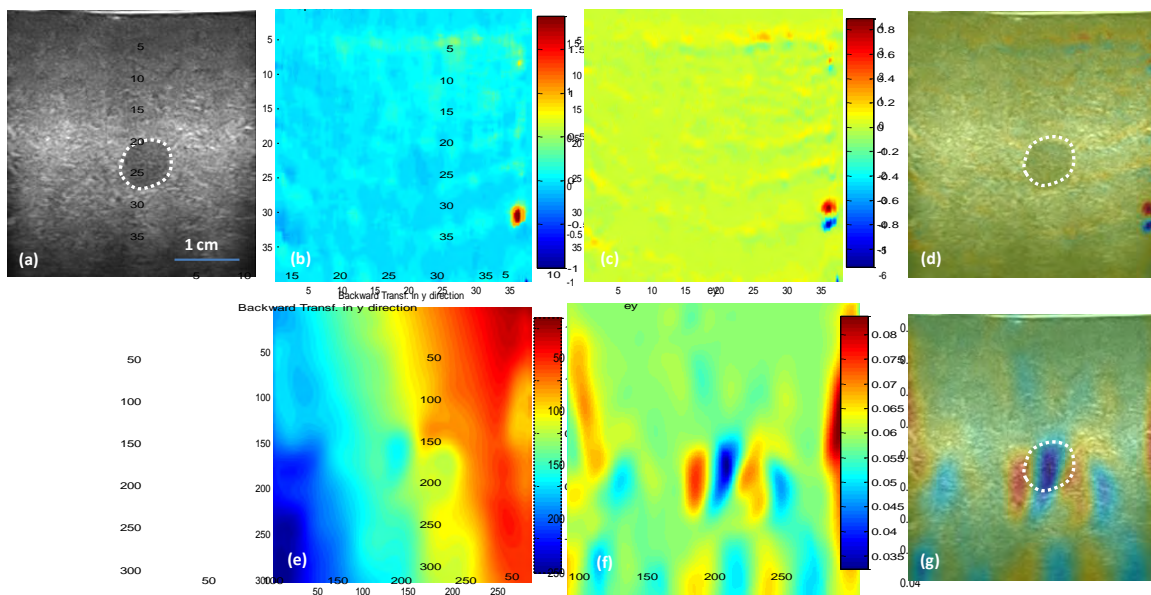


Fig. 2. Phantom experiment results – lateral direction. (a) B-mode image of the breast phantom with a lesion; CC-based elastography results (top row): (b) Displacement, (c) Strain, and (d) Strain and B-mode fused image; INRA-based elastography results (bottom row): (e) Displacement, (f) Strain, and (g) Strain and B-mode fused image.

In order to quantitatively compare the INRA method with the traditional CC-based method, we used Eq. (9) to calculate the CNR and SNR in the axial and lateral strain images. We captured 90 frames of B-mode images and RF data while the pressure was evenly loaded by the probe. We used the first frame as the reference frame, and selected every 10th frame (10th, 20th, 30th, 40th, and etc.) as the floating frames to compare the CNR and SNR under various pressure deformations. The region of interest (ROI) 1 shown in Fig. 2 was used as the target. ROIs 2 and 3 were used as the background. ROIs 1 and 2 were used to calculate the CNR in the axial strain images, and ROIs 1 and 3 were used to calculate the CNR in the lateral strain images. Figures 3 and 4 illustrate the comparison of CNR and SNR between the two methods in the axial and lateral strains at different pressures (frames).

For the both methods, the CNR and SNR in the axial strain were higher than the lateral strain. The CNR and SNR at corresponding directions of our INRA method were significantly higher than the CC-based method. The CNRs for both methods at two directional strains finally decreased along the pressure (deformation) increase, while the SNRs increased along the pressure increase. The INRA method was better than the CC-based method in the CNR and SNR. In particular, the proposed INRA method can work well under high pressure and large deformation.

In the *in-vivo* study, the CC-based method failed due to the large pressure and motion (over 6% strain). Figure 5 shows the INRA-based results from the *in vivo* palm data and Fig. 6 shows the results from *in vivo* arm data. Our method detected the soft tissue (white arrows) as shown red regions in Fig. 4(e) and 5(e). From these two experiments we proved when we gave a large pressure to a probe, the intensity in the B-mode or the amplitude in RF will have a big deference. But we apply the NMI to calculate the similarity, so the intensity or amplitude changes will not affect our method and make our method robust.

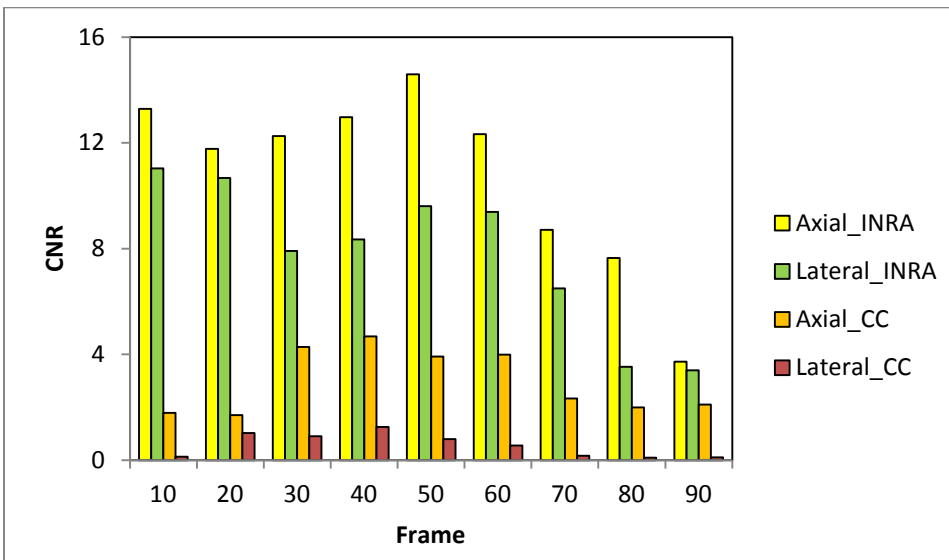


Fig. 3. Comparison of the axial and lateral CNR.

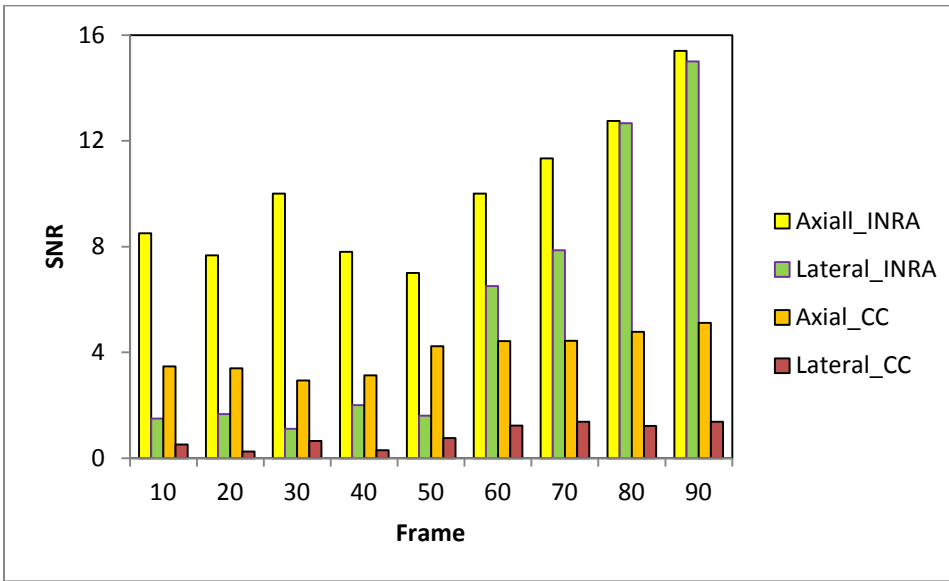


Fig. 4. Comparison of the axial and lateral SNR.

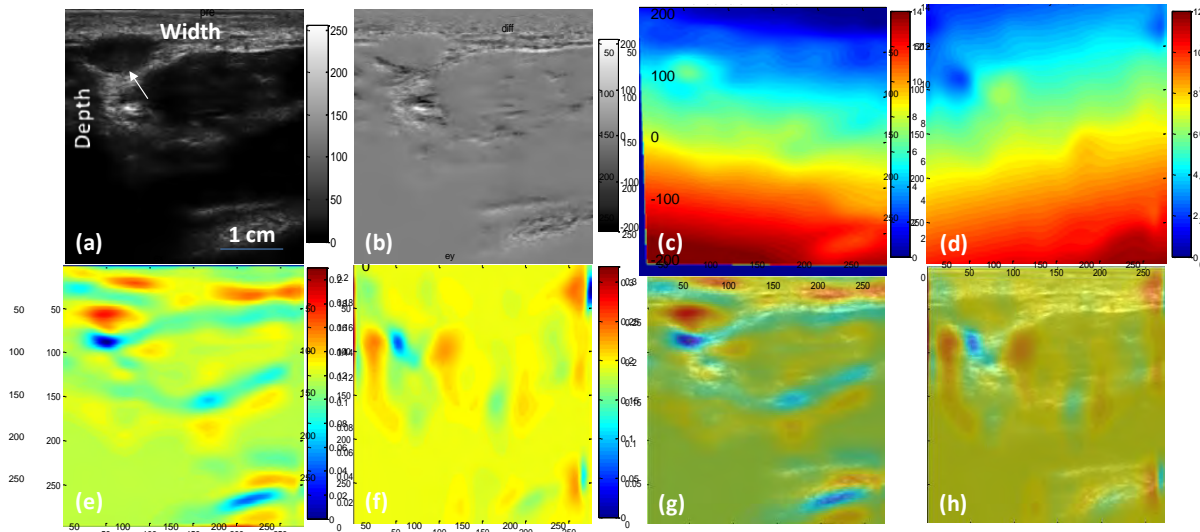


Fig. 5. In vivo results of the palm. (a) Pre-compression B-mode image of the palm, (b) B-mode intensity difference between pre- and post-compression, (c) Axial displacement, (d) Lateral displacement, (e) Axial strain image from the INRA method, (f) Lateral strain image from the INRA method, (g) Axial fusion image of the B-mode and strain images, and (h) Lateral fusion image of the B-mode and strain images.

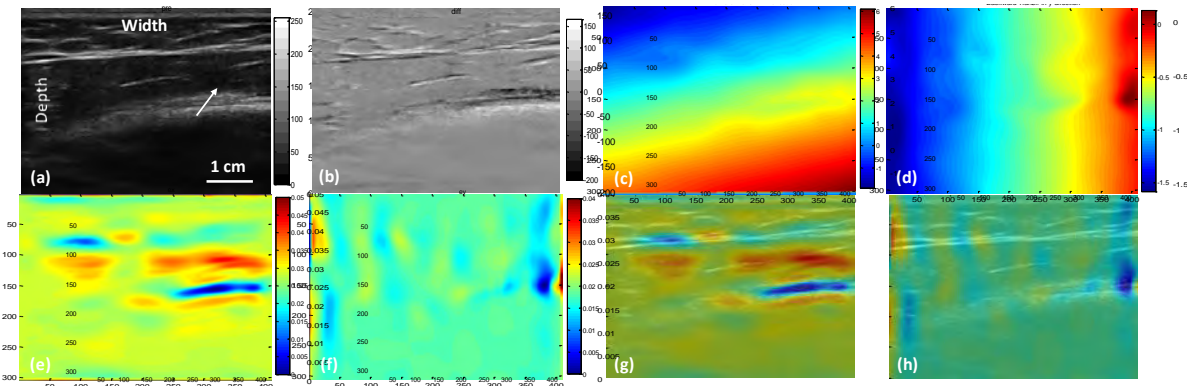


Fig. 6. In vivo results of the arm. (a) Pre-compression B-mode image of the arm, (b) B-mode intensity difference between pre- and post-compression, (c) Axial displacement, (d) Lateral displacement, (e) Axial strain image from INRA method, (f) Lateral strain image from INRA method, (g) Axial fusion image of the B-mode and strain images, and (h) Lateral fusion image of the B-mode and strain images.

4. CONCLUSIONS

We have described a novel 2D strain estimation technology using intensity-based non-rigid registration for ultrasonic elasticity imaging. This method is an alternative approach towards 2D or 3D displacement estimation, which combines the advantages of voxel-based similarity measures with a non-rigid transformation model of tissue. The INRA-based strain estimation is not constrained to any particular set of directions, is insensitive to nonlinear and incoherent motion as well as large signal variations under

high pressure (big compression). The preliminary investigation suggests the robustness of this INRA method in phantom and *in vivo* data sets; this method could become useful in many clinical applications, such as arm lymphedema.

ACKNOWLEDGEMENTS

This research is supported in part by DOD PCRP Award W81XWH-13-1-0269, and National Cancer Institute (NCI) Grant CA114313.

REFERENCES

- [1] K. J. Parker, M. M. Doyley, and D. J. Rubens, "Imaging the elastic properties of tissue: the 20 year perspective," *Phys Med Biol*, 56(1), R1-R29 (2011).
- [2] P. N. T. Wells, and H. D. Liang, "Medical ultrasound: imaging of soft tissue strain and elasticity," *Journal of the Royal Society Interface*, 8(64), 1521-1549 (2011).
- [3] J. Ophir, S. K. Alam, B. Garra *et al.*, "Elastography: ultrasonic estimation and imaging of the elastic properties of tissues," *Proceedings of the Institution of Mechanical Engineers Part H-Journal of Engineering in Medicine*, 213(H3), 203-233 (1999).
- [4] F. Viola, and W. F. Walker, "A comparison of the performance of time-delay estimators in medical ultrasound," *IEEE Trans Ultrason Ferroelectr Freq Control*, 50(4), 392-401 (2003).
- [5] J. F. Greenleaf, M. Fatemi, and M. Insana, "Selected methods for imaging elastic properties of biological tissues," *Annual Review of Biomedical Engineering*, 5, 57-78 (2003).
- [6] A. Pesavento, C. Perrey, M. Krueger *et al.*, "A time-efficient and accurate strain estimation concept for ultrasonic elastography using iterative phase zero estimation," *IEEE Transactions on Ultrasonics Ferroelectrics and Frequency Control*, 46(5), 1057-1067 (1999).
- [7] J. E. Lindop, G. M. Treece, A. H. Gee *et al.*, "Pulse-based ultrasonic deformation estimation," *IEEE Transactions on Ultrasonics Ferroelectrics and Frequency Control*, 55(1), 94-111 (2008).
- [8] T. J. Hall, Y. N. Zhu, and C. S. Spalding, "In vivo real-time freehand palpation imaging," *Ultrasound in Medicine and Biology*, 29(3), 427-435 (2003).
- [9] G. Treece, J. Lindop, L. J. Chen *et al.*, "Real-time quasi-static ultrasound elastography," *Interface Focus*, 1(4), 540-552 (2011).
- [10] H. Rivaz, E. M. Boctor, M. A. Choti *et al.*, "Real-Time Regularized Ultrasound Elastography," *IEEE Transactions on Medical Imaging*, 30(4), 928-945 (2011).
- [11] F. Yeung, S. F. Levinson, and K. J. Parker, "Multilevel and motion model-based ultrasonic speckle tracking algorithms," *Ultrasound in Medicine and Biology*, 24(3), 427-441 (1998).
- [12] M. F. Insana, L. T. Cook, and P. C. Aturvedi, "Analytical study of bioelasticity ultrasound systems," *Information Processing in Medical Imaging, Proceedings*, 1613, 1-14 (1999).
- [13] P. C. Aturvedi, M. F. Insana, and T. J. Hall, "Testing the limitations of 2-D companding for strain imaging using phantom," *Ultrasonics, Ferroelectrics and Frequency Control, IEEE Transactions on*, 45(4), 1022-1031 (1998).
- [14] J. Bai, C. X. Ding, and Y. Fan, "A multi-scale algorithm for ultrasonic strain reconstruction under moderate compression," *Ultrasonics*, 37(7), 511-519 (1999).
- [15] T. Vargese, M. Bilgen, and J. Ophir, "Multiresolution imaging in elastography," *IEEE Transactions on Ultrasonics Ferroelectrics and Frequency Control*, 45(1), 65-75 (1998).

- [16] J. Dey, J. J. Mai, and M. F. Insana, "Multi-resolution approach to strain imaging," 2000 IEEE Ultrasonics Symposium Proceedings, Vols 1 and 2, 1853-1856 (2000).
- [17] H. R. Saito and T. Vargas, "Two-dimensional multi-level strain estimation for discontinuous tissue," *Physics in Medicine and Biology*, 52(2), 389-401 (2007).
- [18] Y. N. Zhu, and T. J. Hall, "A modified block matching method for real-time freehand strain imaging," *Ultrasonic Imaging*, 24(3), 161-176 (2002).
- [19] R. L. Maurice, and M. Bertrand, "Lagrangian speckle model and tissue-motion estimation--theory," *IEEE Trans Med Imaging*, 18(7), 593-603 (1999).
- [20] C. Pellet-Barakat, F. Frouin, M. F. Insana *et al.*, "Ultrasound elastography based on multiscale estimations of regularized displacement fields," *Medical Imaging, IEEE Transactions on*, 23(2), 153-163 (2004).
- [21] J. Jiang, and T. J. Hall, "A parallelizable real-time motion tracking algorithm with applications to ultrasonic strain imaging," *Physics in Medicine and Biology*, 52(13), 3773-3790 (2007).
- [22] D. Rueckert, L. I. Sonoda, C. Hayes *et al.*, "Nonrigid registration using free-form deformations: Application to breast MR images," *IEEE Transactions on Medical Imaging*, 18(8), 712-721 (1999).
- [23] X. F. Yang, H. Akbari, L. Halig *et al.*, "3D Non-rigid Registration Using Surface and Local Salient Features for Transrectal Ultrasound Image-guided Prostate Biopsy," *Medical Imaging 2011: Visualization, Image-Guided Procedures, and Modeling*, 7964, (2011).
- [24] S. Lee, G. Wolberg, and S. Y. Shin, "Scattered data interpolation with multilevel B-splines," *IEEE Transactions on Visualization and Computer Graphics*, 3(3), 228-244 (1997).
- [25] T. Rohlfing, C. R. Maurer, Jr., D. A. Bluemke *et al.*, "Volume-preserving nonrigid registration of MR breast images using free-form deformation with an incompressibility constraint," *Medical Imaging, IEEE Transactions on*, 22(6), 730-741 (2003).
- [26] E. Bardinet, L. D. Cohen, and N. Ayache, "Tracking and motion analysis of the left ventricle with deformable superquadrics," *Med Image Anal*, 1(2), 129-49 (1996).
- [27] D. R. Forsey, and R. H. Bartels, "Hierarchical B-spline refinement," *SIGGRAPH Comput. Graph.*, 22(4), 205-212 (1988).
- [28] F. L. Bookstein, "Principal Warps - Thin-Plate Splines and the Decomposition of Deformations," *IEEE Transactions on Pattern Analysis and Machine Intelligence*, 11(6), 567-585 (1989).
- [29] C. E. Shannon, "A Mathematical Theory of Communication," *Bell System Technical Journal*, 27(4), 623-656 (1948).
- [30] A. Collignon, F. Maes, D. Delaere *et al.*, "Automated multi-modality image registration based on information theory," *Information Processing in Medical Imaging*, 3, 263-274 (1995).
- [31] P. Viola, and W. M. Wells, "Alignment by maximization of mutual information," *Fifth International Conference on Computer Vision, Proceedings*, 16-23 (1995).
- [32] C. Studholme, D. L. G. Hill, and D. J. Hawkes, "An overlap invariant entropy measure of 3D medical image alignment," *Pattern Recognition*, 32(1), 71-86 (1999).